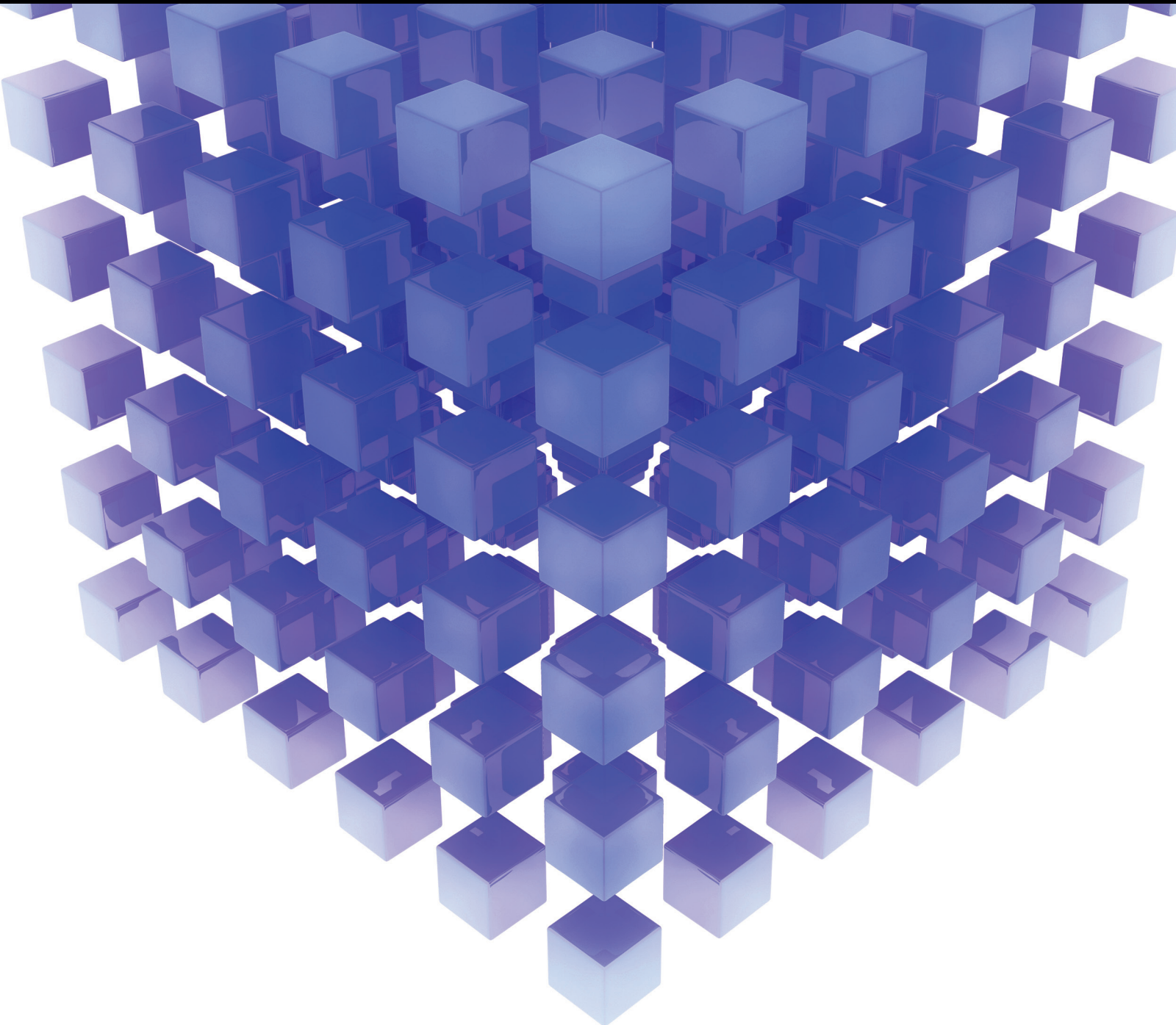


Mathematical Problems in Engineering

Computational Methods for Fracture

Guest Editors: Timon Rabczuk, Stéphane P. A. Bordas, and Goangseup Zi





Computational Methods for Fracture

Mathematical Problems in Engineering

Computational Methods for Fracture

Guest Editors: Timon Rabczuk, Stéphane P. A. Bordas,
and Goangseup Zi



Copyright © 2014 Hindawi Publishing Corporation. All rights reserved.

This is a special issue published in “Mathematical Problems in Engineering.” All articles are open access articles distributed under the Creative Commons Attribution License, which permits unrestricted use, distribution, and reproduction in any medium, provided the original work is properly cited.

Editorial Board

Mohamed Abd El Aziz, Egypt
Eihab M. Abdel-Rahman, Canada
Rashid K. Abu Al-Rub, USA
Sarp Adali, South Africa
Salvatore Alfonzetti, Italy
Igor Andrianov, Germany
Sebastian Anita, Romania
W. Assawinchaichote, Thailand
Erwei Bai, USA
Ezzat G. Bakhoum, USA
José Manoel Balthazar, Brazil
R. K. Bera, India
Christophe Bérenguer, France
Jonathan N. Blakely, USA
Stefano Boccaletti, Spain
Stephane P.A. Bordas, USA
Daniela Boso, Italy
M. Boutayeb, France
Michael J. Brennan, UK
Salvatore Caddemi, Italy
Piermarco Cannarsa, Italy
Jose E. Capilla, Spain
Carlo Cattani, Italy
Marcelo Moreira Cavalcanti, Brazil
Diego J. Celentano, Chile
Mohammed Chadli, France
Arindam Chakraborty, USA
Yong-Kui Chang, China
Michael J. Chappell, UK
Kui Fu Chen, China
Xinkai Chen, Japan
Kue-Hong Chen, Taiwan
Jyh-Horng Chou, Taiwan
Slim Choura, Tunisia
Cesar Cruz-Hernandez, Mexico
Swagatam Das, India
Filippo de Monte, Italy
Antonio Desimone, Italy
Yannis Dimakopoulos, Greece
Baocang Ding, China
Joao B. R. Do Val, Brazil
Daoyi Dong, Australia
B. Dubey, India
Horst Ecker, Austria
M. Onder Efe, Turkey
Elmetwally Elabbasy, Egypt
A. Elías-Zúñiga, Mexico
Anders Eriksson, Sweden
Vedat S. Erturk, Turkey
Moez Feki, Tunisia
Ricardo Femat, Mexico
Robertt A. Fontes Valente, Portugal
Claudio R. Fuerte-Esquivel, Mexico
Zoran Gajic, USA
Ugo Galvanetto, Italy
Xin-Lin Gao, USA
Furong Gao, Hong Kong
Behrouz Gatmiri, Iran
Oleg V. Gendelman, Israel
Didier Georges, France
Paulo Batista Gonçalves, Brazil
Oded Gottlieb, Israel
Fabrizio Greco, Italy
Quang Phuc Ha, Australia
M. R. Hajj, USA
Tony Sheu Wen Hann, Taiwan
Thomas Hanne, Switzerland
K. R. (Stevanovic) Hedrih, Serbia
M.I. Herreros, Spain
Wei-Chiang Hong, Taiwan
Jaromir Horacek, Czech Republic
Gordon Huang, Canada
Huabing Huang, China
Chuangxia Huang, China
Yi Feng Hung, Taiwan
Hai-Feng Huo, China
Asier Ibeas, Spain
Anuar Ishak, Malaysia
Reza Jazar, Australia
Zhijian Ji, China
Jun Jiang, China
J. J. Judice, Portugal
Tadeusz Kaczorek, Poland
Tamas Kalmar-Nagy, USA
Tomasz Kapitaniak, Poland
Hamid Reza Karimi, Norway
Metin O. Kaya, Turkey
Nikolaos Kazantzis, USA
Farzad Khani, Iran
Kristian Krabbenhoft, Australia
Ren-Jieh Kuo, Taiwan
Jurgen Kurths, Germany
Claude Lamarque, France
Usik Lee, Korea
Marek Lefik, Poland
Stefano Lenci, Italy
Roman Lewandowski, Poland
Shihua Li, China
Ming Li, China
Jian Li, China
Shanling Li, Canada
Teh-Lu Liao, Taiwan
Panos Liatsis, UK
Jui-Sheng Lin, Taiwan
Yi-Kuei Lin, Taiwan
Shueei M. Lin, Taiwan
Wanquan Liu, Australia
Yuji Liu, China
Bin Liu, Australia
Paolo Lonetti, Italy
Vassilios C. Loukopoulos, Greece
Junguo Lu, China
Chien-Yu Lu, Taiwan
Alexei Mailybaev, Brazil
Manoranjan K. Maiti, India
Oluwole Daniel Makinde, South Africa
Rafael Martinez-Guerra, Mexico
Driss Mehdi, France
Roderick Melnik, Canada
Xinzhu Meng, China
Yuri Vladimirovich Mikhlin, Ukraine
Gradimir Milovanovic, Serbia
Ebrahim Momoniat, South Africa
Trung Nguyen Thoi, Vietnam
Hung Nguyen-Xuan, Vietnam
Ben T. Nohara, Japan
Sotiris K. Ntouyas, Greece
Gerard Olivar, Colombia
Claudio Padra, Argentina
Bijaya Ketan Panigrahi, India
Francesco Pellicano, Italy
Matjaz Perc, Slovenia
Vu Ngoc Phat, Vietnam
Maria do Rosário Pinho, Portugal
Alexander Pogromsky, The Netherlands

Seppo Pohjolainen, Finland
Stanislav Potapenko, Canada
Sergio Preidikman, USA
Carsten Proppe, Germany
Hector Puebla, Mexico
Justo Puerto, Spain
Dane Quinn, USA
K. R. Rajagopal, USA
Gianluca Ranzi, Australia
Sivaguru Ravindran, USA
G. Rega, Italy
Pedro Ribeiro, Portugal
J. Rodellar, Spain
Rosana Rodriguez-Lopez, Spain
Alejandro J. Rodriguez-Luis, Spain
Ignacio Romero, Spain
Hamid Ronagh, Australia
Carla Roque, Portugal
Rubén Ruiz García, Spain
Manouchehr Salehi, Iran
Miguel A. F. Sanjuán, Spain
Ilmar Ferreira Santos, Denmark
Nickolas S. Sapidis, Greece
Evangelos J. Sapountzakis, Greece
Bozidar Sarler, Slovenia
Andrey V. Savkin, Australia
Massimo Scalia, Italy
Mohamed A. Seddeek, Egypt
Alexander P. Seyranian, Russia
Leonid Shaikhet, Ukraine
Cheng Shao, China
Bo Shen, Germany
Zhan Shu, UK
Jian-Jun Shu, Singapore
Dan Simon, USA
Luciano Simoni, Italy
Grigori M. Sisoiev, UK
Christos H. Skiadas, Greece
Davide Spinello, Canada
Sri Sridharan, USA
Rolf Stenberg, Finland
Changyin Sun, China
Jitao Sun, China
Xi-Ming Sun, China
Andrzej Swierniak, Poland
Yang Tang, Germany
Allen Tannenbaum, USA
Cristian Toma, Romania
Irina N. Trendafilova, UK
Alberto Trevisani, Italy
Jung-Fa Tsai, Taiwan
Kuppalapalle Vajravelu, USA
Victoria Vampa, Argentina
Josep Vehi, Spain
Stefano Vidoli, Italy
Xiaojun Wang, China
Dan Wang, China
Youqing Wang, China
Cheng C. Wang, Taiwan
Yijing Wang, China
Yongqi Wang, Germany
Moran Wang, China
Gerhard-Wilhelm Weber, Turkey
Jeroen A.S. Witteveen, The Netherlands
Kwok-Wo Wong, Hong Kong
Ligang Wu, China
Zhengguang Wu, China
Gongnan Xie, China
Wang Xing-yuan, China
Xuping Xu, USA
Xi Frank Xu, USA
Jun-Juh Yan, Taiwan
Xing-Gang Yan, UK
Suh-Yuh Yang, Taiwan
Mahmoud T. Yassen, Egypt
Mohammad I. Younis, USA
Bo Yu, China
Huang Yuan, Germany
S.P. Yung, Hong Kong
Ion Zaballa, Spain
Ashraf M. Zenkour, Saudi Arabia
Jianming Zhan, China
Xu Zhang, China
Yingwei Zhang, China
Lu Zhen, China
Liancun Zheng, China
Jian Guo Zhou, UK
Zexuan Zhu, China
Mustapha Zidi, France

Contents

Computational Methods for Fracture, Timon Rabczuk, Stéphane P. A. Bordas, and Goangseup Zi
Volume 2014, Article ID 593041, 2 pages

Stable Cracking Particles Method Based on Stabilized Nodal Integration and Updated Lagrangian Kernel, S. Xu
Volume 2014, Article ID 646514, 10 pages

Error Estimate and Adaptive Refinement in Mixed Discrete Least Squares Meshless Method, J. Amani, A. Saboor Bagherzadeh, and T. Rabczuk
Volume 2014, Article ID 721240, 16 pages

A Meshless Local Petrov-Galerkin Shepard and Least-Squares Method Based on Duo Nodal Supports, Xiaoying Zhuang and Yongchang Cai
Volume 2014, Article ID 806142, 11 pages

A Coupled Thermo-Hydro-Mechanical Model of Jointed Hard Rock for Compressed Air Energy Storage, Xiaoying Zhuang, Runqiu Huang, Chao Liang, and Timon Rabczuk
Volume 2014, Article ID 179169, 11 pages

Dynamic Fracture in Thin Shells Using Meshfree Method, Y. Shie
Volume 2014, Article ID 262494, 8 pages

Evaluating the Applicability of Fracture Criteria to Predict the Crack Evolution Path of Dolomite Based on SCB Experiments and FEM, Cunbao Li, Lingzhi Xie, Li Ren, Heping Xie, and Jun Wang
Volume 2013, Article ID 959806, 13 pages

POD for Real-Time Simulation of Hyperelastic Soft Biological Tissue Using the Point Collocation Method of Finite Spheres, Suleiman Banihani, Timon Rabczuk, and Thakir Almomani
Volume 2013, Article ID 386501, 9 pages

Homotopy Iteration Algorithm for Crack Parameters Identification with Composite Element Method, Ling Huang, Zhongrong Lv, Weihuan Chen, and Jike Liu
Volume 2013, Article ID 524562, 10 pages

An Efficient Approach for Identifying Constitutive Parameters of the Modified Oyane Ductile Fracture Criterion at High Temperature, Sergei Alexandrov, Yusof Mustafa, and Mohd Yazid Yahya
Volume 2013, Article ID 514945, 4 pages

Study on Analog Theory of Rock Mass Simulation and Its Engineering Application, Sun Shaorui, Lu Yexu, Xu Yuanyuan, Liu Jin, and Wei Jihong
Volume 2013, Article ID 491069, 11 pages

Explicit Dynamic Finite Element Method for Failure with Smooth Fracture Energy Dissipations, Jeong-Hoon Song, Thomas Menouillard, and Alireza Tabarraei
Volume 2013, Article ID 293861, 12 pages

Explicit Dynamic Finite Element Method for Predicting Implosion/Explosion Induced Failure of Shell Structures, Jeong-Hoon Song, Patrick Lea, and Jay Oswald
Volume 2013, Article ID 957286, 11 pages

Editorial

Computational Methods for Fracture

Timon Rabczuk,^{1,2} Stéphane P. A. Bordas,^{3,4} and Goangseup Zi²

¹ *Bauhaus Universität Weimar, 99423 Weimar, Germany*

² *Korea University, Seoul 136-701, Republic of Korea*

³ *Faculty of Science, Technology and Communication, Research Unit in Engineering Science, University of Luxembourg, Campus Kirchberg, G 007, 6 rue Richard Coudenhove-Kalergi, 1359 Luxembourg, Luxembourg*

⁴ *Cardiff School of Engineering, Cardiff University, Room W2.43, Queen's Buildings, The Parade, Cardiff 24 3AA, UK*

Correspondence should be addressed to Timon Rabczuk; timon.rabczuk@uni-weimar.de

Received 15 May 2014; Accepted 15 May 2014; Published 20 July 2014

Copyright © 2014 Timon Rabczuk et al. This is an open access article distributed under the Creative Commons Attribution License, which permits unrestricted use, distribution, and reproduction in any medium, provided the original work is properly cited.

The numerical study of fracture has far-reaching applications throughout engineering and science. Its importance is becoming even more significant that engineers and materials scientists are thriving to devise new lighter and stronger materials from the bottom up.

Simulating fracture requires devising suitable models, discretizing the resulting partial differential equations, and solving them numerically. Each of those three steps poses its own difficulties which have been tackled in various ways, both academically and for practical applications.

This special issue deals with a range of such models: discretization and solution methods applied to a number of problems ranging from rock mechanics to surgical simulation requiring tackling various loading spectra, ranging from fast dynamics to quasistatic loading, and leading to a number of different failure modes, from brittle to ductile fracture.

The topics of this issue can be decomposed into five groups:

Models have been developed with special emphasis on rock mechanics and multi-field problems in fracture [1, 2] with applications, for example to coupled thermohydro-mechanical model of jointed hard rock for compressed air energy storage, and to rock failure [3].

Discretization methods have been heavily investigated, to address the difficulties faced by the standard finite element method [4], in particular, associated with remeshing as the cracks evolve. The issue discusses recent developments in meshless methods, including a posteriori error estimation and adaptive methods.

Dynamic fracture is in itself a wide field of study. Papers in this issue focus on explicit dynamics and tackle, in particular, the issue of energy dissipation during crack growth and the simulation of fracture in thin shells due to dynamic and implosive or explosive loading.

Model reduction methods have recently been developed for fracture simulations. Algebraic model reduction such as the proper orthogonal decomposition (POD) is not inherently well-suited to such problems [5–8]. This issue discusses one possibility relying on the combination of POD with meshfree methods.

Parameter identification in fracture mechanics is a topic of special interest in practical applications and a necessary step to provide convincing and predictive modeling and simulation tools. Two methods are discussed in this issue, both for crack parameter identification and multifield problems in fracture.

Through these five topics, we believe the issue gives a fair reflection of the current state of the art, with a heavy focus on modeling and simulation methods, although covering the whole spectrum of applications and methodologies would require a much more substantial volume.

*Timon Rabczuk
Stéphane P. A. Bordas
Goangseup Zi*

References

- [1] X. Zhuang, C. Augarde, and S. Bordas, "Accurate fracture modelling using meshless methods, the visibility criterion and level sets: Formulation and 2D modelling," *International Journal for Numerical Methods in Engineering*, vol. 86, no. 2, pp. 249–268, 2011.
- [2] X. Zhuang, C. E. Augarde, and K. M. Mathisen, "Fracture modeling using meshless methods and levels sets in 3D: framework and modeling," *International Journal for Numerical Methods in Engineering*, vol. 92, no. 11, pp. 969–998, 2012.
- [3] H. Zhu, X. Zhuang, Y. Cai, and G. Ma, "High rock slope stability analysis using the enriched meshless Shepard and least squares method," *International Journal of Computational Methods*, vol. 8, no. 2, pp. 209–228, 2011.
- [4] Y. Cai, X. Zhuang, and C. Augarde, "A new partition of unity finite element free from the linear dependence problem and possessing the delta property," *Computer Methods in Applied Mechanics and Engineering*, vol. 199, no. 17–20, pp. 1036–1043, 2010.
- [5] P. Kerfriden, P. Gosselet, S. Adhikari, and S. P. A. Bordas, "Bridging proper orthogonal decomposition methods and augmented Newton-Krylov algorithms: an adaptive model order reduction for highly nonlinear mechanical problems," *Computer Methods in Applied Mechanics and Engineering*, vol. 200, no. 5–8, pp. 850–866, 2011.
- [6] P. Kerfriden, J. C. Passieux, and S. P. A. Bordas, "Local/global model order reduction strategy for the simulation of quasi-brittle fracture," *International Journal for Numerical Methods in Engineering*, vol. 89, no. 2, pp. 154–179, 2012.
- [7] P. Kerfriden, O. Goury, T. Rabczuk, and S. P. A. Bordas, "A partitioned model order reduction approach to rationalise computational expenses in nonlinear fracture mechanics," *Computer Methods in Applied Mechanics and Engineering*, vol. 256, pp. 169–188, 2013.
- [8] P. Kerfriden, K. M. Schmidt, T. Rabczuk, and S. P. A. Bordas, "Statistical extraction of process zones and representative subspaces in fracture of random composites," *International Journal for Multiscale Computational Engineering*, vol. 11, no. 3, pp. 253–287, 2013.

Research Article

Stable Cracking Particles Method Based on Stabilized Nodal Integration and Updated Lagrangian Kernel

S. Xu

School of Mechanical Engineering, Jiangnan University, China

Correspondence should be addressed to S. Xu; ssxu@windowslive.com

Received 27 November 2013; Revised 27 January 2014; Accepted 17 February 2014; Published 7 May 2014

Academic Editor: Goangseup Zi

Copyright © 2014 S. Xu. This is an open access article distributed under the Creative Commons Attribution License, which permits unrestricted use, distribution, and reproduction in any medium, provided the original work is properly cited.

A stable cracking particles method (CPM) based on updated Lagrangian kernels is proposed. The idea of CPM is to model the crack topology by a set of cracked particles. Hence no representation of the crack surface is needed making the method useful for problems involving complex fracture patterns as they occur in dynamics and under fast loading conditions. For computational efficiency, nodal integration is exploited in the present paper. In order to avoid instabilities, a scheme is presented to stabilize the integration. Moreover, a set of simple cracking rules are proposed in order to prevent numerical fracture. The method is applied to two benchmark problems and shows good accuracy.

1. Introduction

Meshless methods have been a competitor to finite element method due to their ability to add particles and model large deformations, dynamic fracture, and fragmentation with ease [1–14]. In contrast to finite element methods that require the deletion of elements for complex dynamic fracture problems involving penetration and perforation, meshless methods [14–20] treat such problems quite naturally. However, meshless methods are computationally expensive. Moreover, numerical fracture is reported when fracture and material modelling is not accounted for carefully [21–23]. Recently developed efficient methods such as finite element methods with edge rotations [24–27], phase-field models [28, 29], and partition-of-unity enriched finite element [30–44] and meshless methods have been widely applied to fracture problems with a few number of cracks [23, 45–52]. However, their application to complex dynamic fracture and fragmentation remains a major challenge. A powerful method for complex fracture is the cracking particles method (CPM) [53, 54] that is based on enriching nodes with step-enrichment function once a fracture criterion is met. The crack's topology is modeled by discrete plane crack segments and the well-posedness of the initial boundary value problem is restored by means of cohesive zone models. The advantage of the CPM is its robustness and efficiency. Complex fracture is modeled

naturally with relatively coarse discretizations as the process zone does not need to be smeared over several particles. The CPM has been applied to numerous challenging problems [55–59]. However, due to the “discontinuous” representation of the crack surface, stresses might be transferred over the opening crack leading to spurious cracking [60–63].

In this paper, we present a stabilized nodal integrated CPM based on updated Lagrangian kernels that alleviates several shortcomings of the original CPM. In particular, the following occurs.

- (i) We propose a set of simple cracking rules according to [64] in order to avoid spurious cracking in the CPM. The original CPM shows suffering from spurious cracking adjacent to the crack surface that might artificially increase the dissipated energy.
- (ii) We combine for the first time the stabilized nodal integration and the CPM. CPM was only used in combination with computationally expensive Gauss quadrature, stress-point integration and nodal integration. Nodal integration is computationally very efficient but suffers from instabilities. Stress-point integration eliminates these instabilities but cracks are restricted to cross nodes—not stress points. Moreover, there is still the need to update the position of the stress points. Therefore, we employ the stabilized

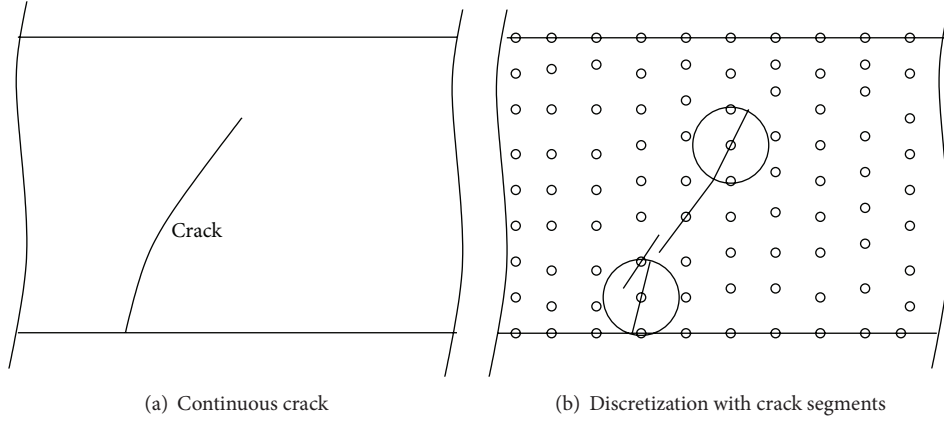


FIGURE 1: (a) Continuous crack and (b) representation of the crack with discrete cohesive crack segments.

conforming nodal integration [65] also used in the smoothed finite element method [66–70].

- (iii) While the original CPM employs a Lagrangian kernel that is only applicable to moderate deformations, an updated Lagrangian kernel formulation is proposed here for the first time. It guarantees the applicability of the method to extremely large deformation.

The paper is organized as follows. First, we present the CPM. Then, the weak form is stated and the discrete equations are derived. Subsequently, the fracture model and the cohesive zone models are discussed before the paper ends with examples and conclusions.

2. CPM

The key idea of the CPM is to decompose the displacement field into two parts: the continuous part \mathbf{u}^C , sometimes also referred to as the “usual” part, and the discontinuous or “enriched” part \mathbf{u}^D :

$$\mathbf{u}(\mathbf{X}, t) = \mathbf{u}^C(\mathbf{X}, t) + \mathbf{u}^D(\mathbf{X}, t). \quad (1)$$

The discretization of the continuous part of the displacement field is based on moving least squares (MLS) shape functions [71] of linear completeness:

$$\mathbf{u}^C(\mathbf{X}, t) = \sum_{I \in \mathcal{N}} N_I(\mathbf{X}) \mathbf{u}_I(t), \quad (2)$$

where $N_I(\mathbf{X})$ are the meshless shape functions of node I at position \mathbf{X} and $\mathbf{u}_I(t)$ are nodal parameters at time t . Note that (1) the nodal parameters are not the true physical displacement values at node I and (2) the shape functions are expressed in terms of material coordinates \mathbf{X} . It can be shown that the shape functions are given by

$$N_I(\mathbf{X}) = \mathbf{p}^T(\mathbf{X}) \mathbf{A}^{-1}(\mathbf{X}) \mathbf{D}_I(\mathbf{X}) \quad (3)$$

with

$$\begin{aligned} \mathbf{D}_I(\mathbf{X}) &= w(\mathbf{X} - \mathbf{X}_I, h) \mathbf{p}^T(\mathbf{X}_I), \\ \mathbf{A}_I(\mathbf{X}) &= \sum_{I \in \mathcal{N}} w(\mathbf{X} - \mathbf{X}_I, h) \mathbf{p}(\mathbf{X}_I) \mathbf{p}^T(\mathbf{X}_I), \end{aligned} \quad (4)$$

where $w(\mathbf{X} - \mathbf{X}_I, h)$ denotes the kernel function and h its support size; $\mathbf{p}(\mathbf{X}) = (1, X, Y)$ is a linear polynomial basis. We point out again that the kernel function is expressed in terms of material coordinates and therefore is called Lagrangian kernel [22]. It was shown by [22] that a Lagrangian kernel avoids numerical fracture often observed for simulations based on Eulerian kernels. However, the Lagrangian kernel formulation limits the amount of large deformations. Therefore, we update the kernel functions every n th time step referring to a new reference configuration and hence call this kernel an updated Lagrangian kernel. A similar approach was mentioned in [54].

The discontinuous part of the displacement field is obtained by simply multiplying the shape function with enrichment functions accounting for the jump in the displacement field (see Figure 2):

$$\mathbf{u}(\mathbf{X}, t) = \sum_{I \in \mathcal{N}_c} N_I(\mathbf{X}) \mathcal{H}_{\Gamma_c}(\mathbf{X}) \mathbf{q}_I(t). \quad (5)$$

\mathcal{N}_c being the set of cracking particles $\mathbf{q}_I(t)$ are additional degrees of freedom (DOF) and the enrichment function is the step function

$$\mathcal{H}(\mathbf{X}) = \frac{\mathbf{X} \cdot \mathbf{n}_{\Gamma_c}}{\|\mathbf{X} \cdot \mathbf{n}_{\Gamma_c}\|}. \quad (6)$$

The key strength of the CPM is that it does not require any representation of the crack’s topology. In the CPM, the crack topology is described as a set of crack segments as illustrated in Figure 1 allowing the simulation of very complex crack patterns with ease.

It is advantageous to write the approximation of the displacement field in vector matrix notation:

$$\mathbf{d} = \mathbf{N} \mathbf{D} \quad (7)$$

and store the “standard” and enriched shape functions in the matrix \mathbf{N} ; the DOFs of the “standard” and enriched part of the displacement field are stored in the vector \mathbf{D} . Moreover, we can define the matrix $[[\mathbf{N}]]$ and the matrix containing the derivatives of the meshless shape functions \mathbf{B} needed later.

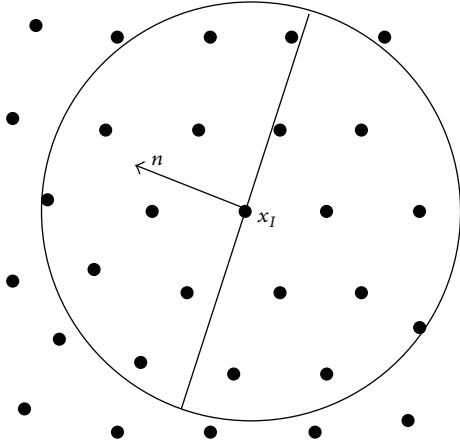


FIGURE 2: Normal of the crack segment.

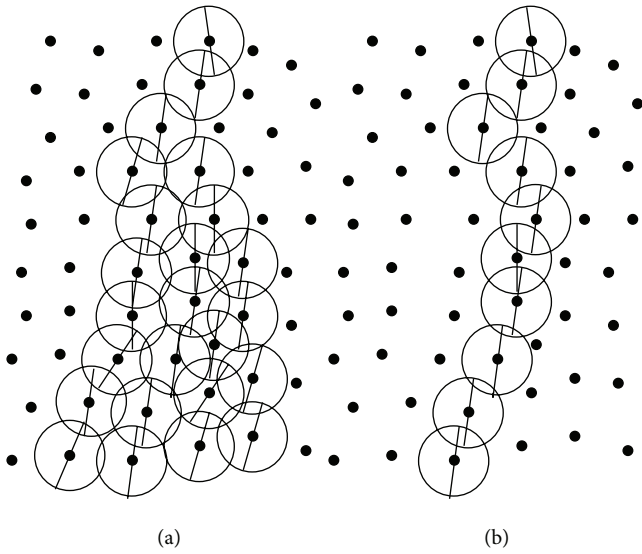


FIGURE 3: (a) Spurious cracking during crack propagation and (b) crack propagation without spurious cracking.

Though the CPM can handle complex crack patterns, it might lead to spurious cracking adjacent to the crack that can be avoided by a set of simple rules as shown in [64]. We propose similar rules and firstly distinguish between propagation and initiating cracks by a simple criterion based on a circular support domain. When a cracking particle does not find another cracking particle within the circular domain of size αh , then a new crack is initiated. The factor α is chosen to be 1.1 in all simulations. Secondly, we define a zone adjacent to a crack surface where no new cracks can evolve; see Figure 3.

As such a criterion might prevent crack branching, these rules need to be adjusted at the crack tip. Since the crack surface is not continuous in the CPM, we employ the following simple algorithm to detect the crack tip for branching cracks: crack branching occurs when the angle of existing and newly created particles at the crack tip exceeds

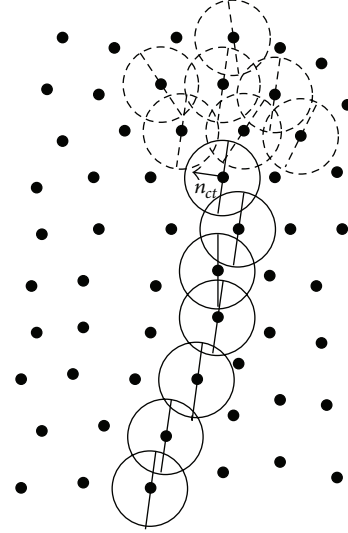
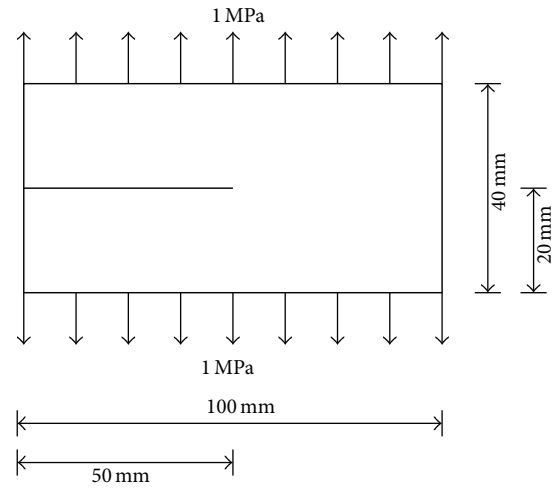

 FIGURE 4: Crack with crack tip node (solid line) at time n and nodes that meet cracking criterion at time $n + 1$ (dashed line).


FIGURE 5: Plate with a horizontal initial notch under tensile tractions.

a prescribed tolerance. According to Figure 4, the deviation in this angle is calculated by

$$\gamma_{\max} = \max_{I \in \widetilde{\mathcal{N}}_c} (\mathbf{n}_{ct} \cdot \mathbf{n}_I) \quad \forall I \in \widetilde{\mathcal{N}}_c, \quad (8)$$

$$\gamma_{\min} = \min_{I \in \widetilde{\mathcal{N}}_c} (\mathbf{n}_{ct} \cdot \mathbf{n}_I) \quad \forall I \in \widetilde{\mathcal{N}}_c$$

$\widetilde{\mathcal{N}}_c \subset \mathcal{N}_c$ being the set of new cracking particles. Crack branching is assumed when $\gamma_{\max} - \gamma_{\min} \geq \text{TOL}$.

3. Weak Form and Discretization

The linear momentum equation is

$$\nabla \cdot \mathbf{P} + \rho \mathbf{b} = \rho \ddot{\mathbf{u}}, \quad \mathbf{X} \in \Omega, \quad (9)$$

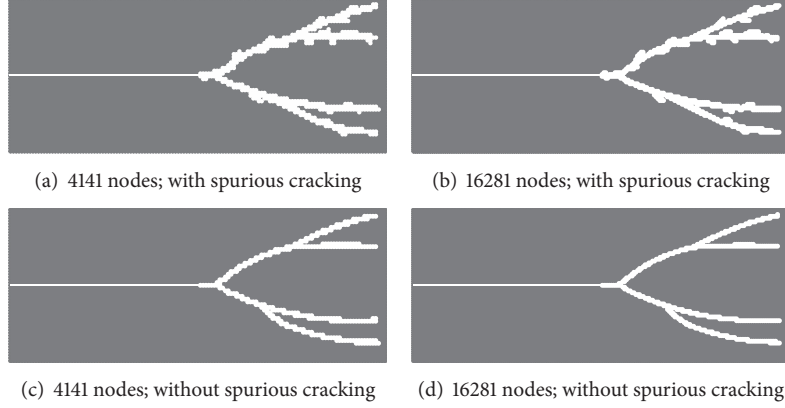


FIGURE 6: Crack pattern for the crack branching problem.

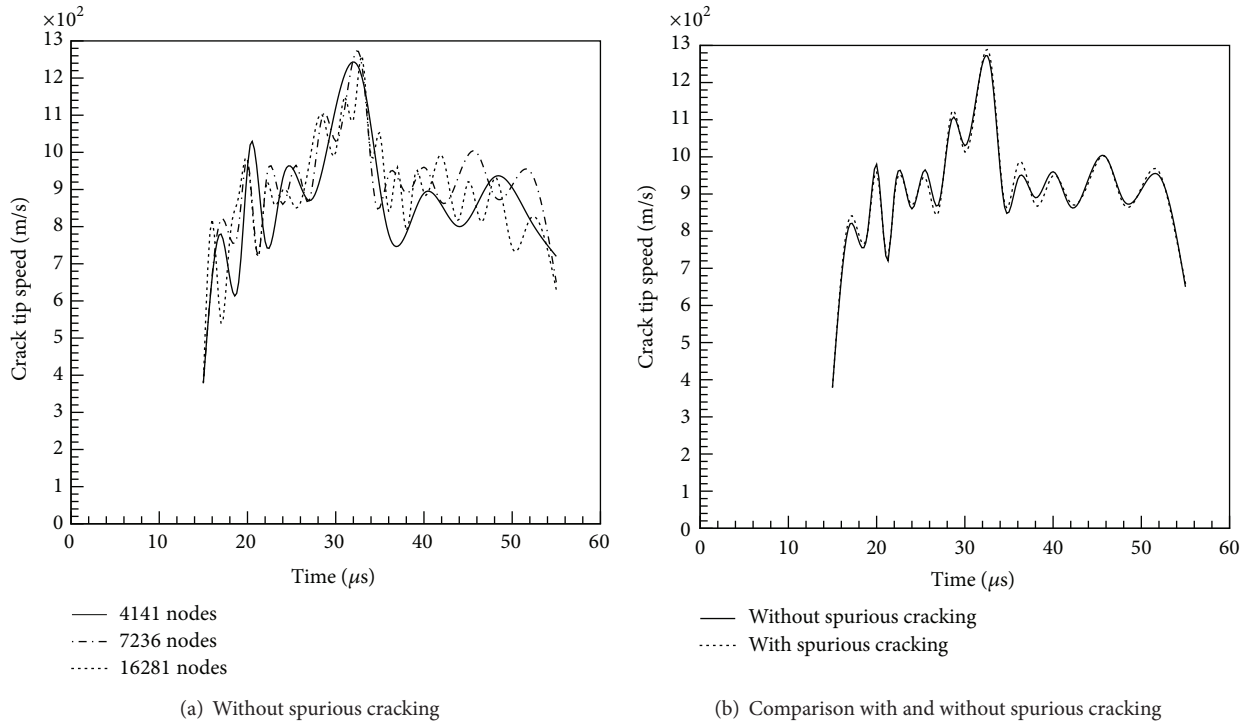


FIGURE 7: Crack tip speed for the crack branching problem.

where \mathbf{P} is the nominal stress tensor, ρ is the density, \mathbf{b} are body forces, and the superimposed dots denote material time derivatives. The displacement and traction boundary conditions are

$$\begin{aligned} \mathbf{u} &= \bar{\mathbf{u}}, & \mathbf{X} &\in \Gamma_u \\ \mathbf{n}_t \cdot \mathbf{P} &= \bar{\mathbf{t}}, & \mathbf{X} &\in \Gamma_t \\ \mathbf{n}_c \cdot \mathbf{P} &= \mathbf{t}_c([\![\mathbf{u}]\!]]) , & \mathbf{X} &\in \Gamma_c, \end{aligned} \quad (10)$$

where the index c refers to the crack, the index t refers to traction boundaries, and the index u refers to displacement boundaries.

We solve the equation of motion in weak form that can be stated in variational form. Find the displacement field $\mathbf{u} \in \mathcal{U} \forall \delta \mathbf{u} \in \mathcal{V}$ such that the first variation in the energy is zero:

$$\begin{aligned} \delta W &= \delta W_{\text{int}} - \delta W_{\text{ext}} + \delta W_{\text{inertia}} - \delta W_{\text{coh}} = 0 \\ &\forall \delta \mathbf{u} \in \mathcal{U}_0 \end{aligned} \quad (11)$$

with

$$\begin{aligned} \delta W_{\text{int}} &= \int_{\Omega} \nabla \delta \mathbf{u} : \mathbf{P} \, d\Omega, \\ \delta W_{\text{ext}} &= \int_{\Gamma_t} \delta \mathbf{u} \cdot \bar{\mathbf{t}} \, d\Gamma + \int_{\Omega} \rho \delta \mathbf{u} \cdot \mathbf{b} \, d\Omega, \end{aligned}$$

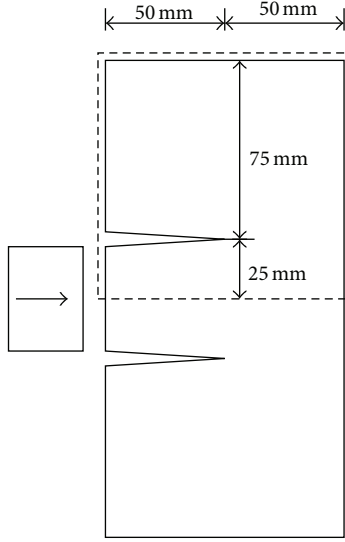


FIGURE 8: The Kalthoff problem.

$$\begin{aligned}\delta W_{\text{inertia}} &= \int_{\Omega} \rho \delta \mathbf{u} \cdot \ddot{\mathbf{u}} \, d\Omega, \\ \delta W_{\text{coh}} &= \int_{\Gamma_c} \delta [[\mathbf{u}]] \cdot \mathbf{t}_c \, d\Gamma.\end{aligned}\quad (12)$$

The approximation spaces \mathcal{U} and \mathcal{U}_0 are given by

$$\begin{aligned}\mathcal{U} &= \left\{ \mathbf{u}(\mathbf{X}, t) \mid \mathbf{u} \in H^1, \mathbf{u} = \bar{\mathbf{u}} \text{ on } \Gamma_u, \right. \\ &\quad \left. \mathbf{u} \text{ discontinuous on } \Gamma_c \right\}, \\ \mathcal{U}_0 &= \left\{ \delta \mathbf{u} \mid \delta \mathbf{u} \in H^1, \delta \mathbf{u} = 0 \text{ on } \Gamma_u, \right. \\ &\quad \left. \delta \mathbf{u} \text{ discontinuous on } \Gamma_c \right\}.\end{aligned}\quad (13)$$

The essential and natural boundary conditions are given by

$$\begin{aligned}\mathbf{u} &= \bar{\mathbf{u}}, \quad \mathbf{X} \in \Gamma_u \\ \mathbf{n}_t \cdot \mathbf{P} &= \bar{\mathbf{t}}, \quad \mathbf{X} \in \Gamma_t \\ \mathbf{n}_c \cdot \mathbf{P} &= \mathbf{t}_c ([[\mathbf{u}]]), \quad \mathbf{X} \in \Gamma_c,\end{aligned}\quad (14)$$

the index c referring to crack boundaries, the index t to natural boundaries, and the index u to essential boundaries.

By substituting the approximation of the displacement field \mathbf{u} and the virtual displacement field $\delta \mathbf{u}$ into the weak form (11), the discrete system of equations is obtained:

$$\begin{aligned}\sum_{j=1}^n \int_{\Omega_j} \nabla \delta \mathbf{u}_j : \mathbf{P} \, d\Omega - \sum_{j=1}^n \int_{\Gamma_{t,j}} \delta \mathbf{u} \cdot \bar{\mathbf{t}} \, d\Gamma \\ - \sum_{j=1}^n \int_{\Omega_j} \rho \delta \mathbf{u} \cdot \mathbf{b} \, d\Omega + \int_{\Gamma_{c,j}} \delta [[\mathbf{u}]] \cdot \mathbf{t}_c \, d\Gamma \\ + \sum_{j=1}^n \int_{\Omega_j} \rho \delta \mathbf{u} \cdot \ddot{\mathbf{u}} \, d\Omega = 0\end{aligned}\quad (15)$$

or in vector-matrix form:

$$\mathbf{M}_{IJ} \mathbf{D}_J = \mathbf{F}_I^{\text{ext}} - \mathbf{F}_I^{\text{int}} \quad (16)$$

with

$$\begin{aligned}\mathbf{F}_I^{\text{ext}} &= \int_{\Gamma_t} (\mathbf{N}_I)^T \mathbf{t} \, d\Gamma + \int_{\Omega} (\mathbf{N}_I)^T \mathbf{b} \, d\Omega + \int_{\Gamma_c} [[(\mathbf{N}_I)^T]] \mathbf{t}_c \, d\Gamma, \\ \mathbf{F}_I^{\text{int}} &= \int_{\Omega} (\mathbf{B}_I)^T \mathbf{P} \, d\Omega, \\ \mathbf{M}_{IJ} &= \int_{\Omega} \rho \mathbf{N}_I \mathbf{N}_J^T \, d\Omega.\end{aligned}\quad (17)$$

For computational efficiency, nodal integration is employed. Nodal integration does not drastically reduce the number of quadrature points; it was shown, for example, by [72] that the critical time step is increased by orders of magnitude; care has to be taken in the existence of cracks [73]. However, nodal integration leads to instabilities due to rank deficiency. Therefore, we employ the stabilized conforming nodal integration technique as mentioned previously. Stabilized conforming nodal integration has also shown great performance for fracture problems in the context of the finite element method; see [74–80]. The explicit central difference time integration scheme is used (for the time integration).

4. Fracture Criterion and Cohesive Zone Model

Fracture is governed by the maximum principal stress. The crack is introduced perpendicular to the direction of the maximum principal stress. Complex crack patterns are obtained automatically as the method does not require any representation of the crack's topology. There is no need to distinguish between crack nucleation and crack propagation and complex crack patterns including crack branching are natural outcome of the simulation.

The cohesive zone model related the jump in the displacement field $[[\mathbf{u}]]$ to the cohesive traction at the crack surface. The discontinuous displacement field can be split into a part acting perpendicular and another tangential to the crack surface:

$$\begin{aligned}\delta_n &= [[\mathbf{u}]] \cdot \mathbf{n} \\ \delta_t &= |[[\mathbf{u}]] - \delta_n \mathbf{n}|.\end{aligned}\quad (18)$$

Defining an effective crack opening displacement as suggested by [81]

$$\delta = \sqrt{\beta^2 \delta_t^2 - \delta_n^2} \quad (19)$$

an effective cohesive zone model can be derived by

$$t = \frac{t_{\text{max}}}{\delta_{\text{max}}} \delta \quad \text{if } \delta \leq \delta_{\text{max}} \text{ or } \dot{\delta} < 0. \quad (20)$$

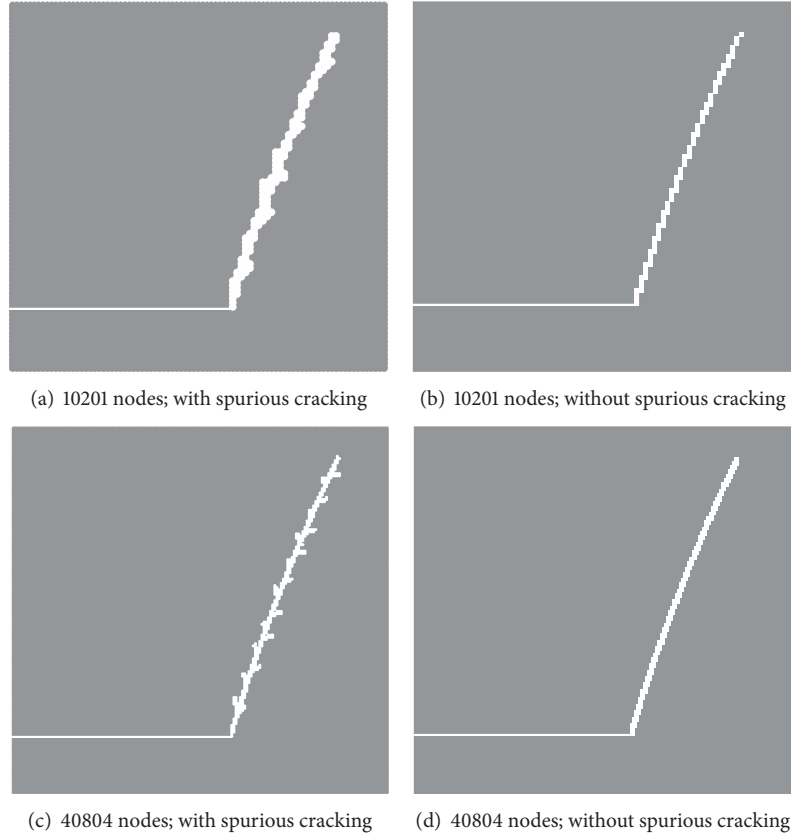


FIGURE 9: Final crack path of the Kalthoff problem.

The traction vector is then obtained by

$$\mathbf{t} = \frac{t}{\delta} (\beta^2 \delta_t + \delta_n \mathbf{n}), \quad (21)$$

where β determines the amount of tangential and normal tractions.

5. Results

5.1. Crack Branching. Let us consider a specimen with initial crack as illustrated in Figure 5. It is subjected to uniaxial tensile loading of $\sigma = 1$ MPa at the top and bottom. This classical benchmark problem of dynamic fracture has been studied by several people to test the accuracy and robustness of their computational method [39, 53, 82, 83]. Also, experimental data can be found for such type of problems; see, for example, [84–86]. The material properties for this example are modulus of elasticity $E = 32,000$ MPa and Poisson's ratio $\nu = 0.20$. The maximum crack speed is restricted by the Rayleigh wave speed $c_R = 2119.0$ m/s. Discretizations ranging from only 4000 nodes up to more than 16000 nodes are investigated. Also the influence of the cracking rules will be demonstrated in this section.

The fracture patterns at various time steps are depicted in Figure 6. Spurious cracks adjacent to the “main” crack are observed when no cracking rules are applied. The velocity of

the propagating crack is illustrated in Figure 7. We note the following.

- (i) The cracking rules do not influence the crack speed indicating that much less energy is dissipated in the spurious cracks.
- (ii) The crack propagates faster just before it branches.
- (iii) The maximum crack speed is far below the Raleigh wave speed. This agrees well with experimental observations of the microbranch instability problem as reported by [84–86]. The ability to capture this physical behaviour naturally is one advantage of the CPM over other methods with continuous crack surface [23, 39, 51, 87].

5.2. The Kalthoff Experiment. The second classical benchmark example studied here is the Kalthoff problem [88]. Therefore consider the double-notched specimen under impact loading ($v = 20$ m/s) as illustrated in Figure 8. The impact leads to mode I dominated fracture with a crack propagating almost orthogonal to the impact loading.

We exploit the symmetry of the model and carry out simulations of discretizations ranging from 10,000 to 40,000 particles. According to [89], the modulus of elasticity in these experiments is $E = 190$ GPa, the initial density is $\rho_0 = 8000$ kg/m³, and Poisson's ratio is $\nu = 0.3$. Figure 9 shows the final fracture pattern that matches the experimental

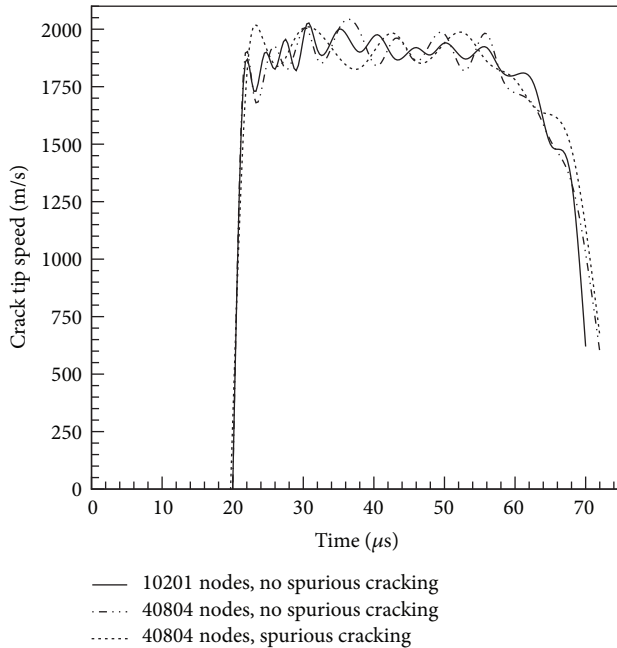


FIGURE 10: Crack tip speed and cohesive fracture energy of the Kalthoff problem.

data. Figure 10 reveals that the crack speed here is also not influenced by the cracking rules. However, the crack looks more erratic without using the cracking rules.

6. Conclusions

In conclusion, a cracking particles method based on nodal integration and updated Lagrangian kernels was proposed where a set of simple cracking rules was suggested in order to avoid spurious cracking. The stabilized nodal integration guarantees the computational efficiency of the method while maintaining the stability. Moreover, the updated Lagrangian kernel ensures that the method remains applicable also for extremely large deformations.

The method was applied to two benchmark examples where the performance of the method was demonstrated.

Conflict of Interests

The author declares that there is no conflict of interests regarding the publication of this paper.

References

- [1] S. Li and W. K. Liu, "Meshfree and particle methods and their applications," *Applied Mechanics Reviews*, vol. 55, no. 1, pp. 1–34, 2002.
- [2] S. Li and W. K. Liu, *Meshfree Particle Methods*, Springer, 2004.
- [3] S. Li and D. C. Simkins Jr., "Conserving Galerkin weak formulations for computational fracture mechanics," *Communications in Numerical Methods in Engineering*, vol. 18, no. 12, pp. 835–850, 2002.
- [4] S. Li and B. C. Simonson, "Meshfree simulation of ductile crack propagation," *International Journal of Computational Methods in Engineering Science and Mechanics*, vol. 6, pp. 1–19, 2003.
- [5] S. Li and B. C. Simonson, "Meshfree simulation of ductile crack propagation," *International Journal of Computational Methods in Engineering Science and Mechanics*, vol. 60, no. 8, pp. 1425–1450, 2004.
- [6] S. Li, W. Hao, and W. K. Liu, "Mesh-free simulations of shear banding in large deformation," *International Journal of Solids and Structures*, vol. 37, no. 48, pp. 7185–7206, 2000.
- [7] S. Li, W. Hao, and W. K. Liu, "Numerical simulations of large deformation of thin shell structures using meshfree methods," *Computational Mechanics*, vol. 25, no. 2, pp. 102–116, 2000.
- [8] S. Li, W. K. Liu, A. J. Rosakis, T. Belytschko, and W. Hao, "Mesh-free Galerkin simulations of dynamic shear band propagation and failure mode transition," *International Journal of Solids and Structures*, vol. 39, no. 5, pp. 1213–1240, 2002.
- [9] A. G. Petschek and L. D. Libersky, "Cylindrical smoothed particle hydrodynamics," *Journal of Computational Physics*, vol. 109, no. 1, pp. 76–83, 1993.
- [10] T. Rabczuk and J. Eibl, "Modelling dynamic failure of concrete with meshfree methods," *International Journal of Impact Engineering*, vol. 32, no. 11, pp. 1878–1897, 2006.
- [11] T. Rabczuk and J. Eibl, "Simulation of high velocity concrete fragmentation using SPH/MLSPH," *International Journal for Numerical Methods in Engineering*, vol. 56, no. 10, pp. 1421–1444, 2003.
- [12] T. Rabczuk, J. Eibl, and L. Stempniewski, "Numerical analysis of high speed concrete fragmentation using a meshfree Lagrangian method," *Engineering Fracture Mechanics*, vol. 71, no. 4–6, pp. 547–556, 2004.
- [13] T. Rabczuk, S. P. Xiao, and M. Sauer, "Coupling of mesh-free methods with finite elements: Basic concepts and test results," *Communications in Numerical Methods in Engineering*, vol. 22, no. 10, pp. 1031–1065, 2006.
- [14] P. W. Randles and L. D. Libersky, "Recent improvements in SPH modeling of hypervelocity impact," *International Journal of Impact Engineering*, vol. 20, no. 6–10, pp. 525–532, 1997.
- [15] T. Belytschko, Y. Y. Lu, L. Gu, and M. Tabbara, "Element-free galerkin methods for static and dynamic fracture," *International Journal of Solids and Structures*, vol. 32, no. 17–18, pp. 2547–2570, 1995.
- [16] T. Belytschko, Y. Krongauz, D. Organ, M. Fleming, and P. Krysl, "Meshless methods: an overview and recent developments," *Computer Methods in Applied Mechanics and Engineering*, vol. 139, no. 1–4, pp. 3–47, 1996.
- [17] W. K. Liu, S. J. Jun, and Y. F. Zhang, "Reproducing kernel particle methods," *International Journal for Numerical Methods in Fluids*, vol. 20, no. 8–9, pp. 1081–1106, 1995.
- [18] V. P. Nguyen, T. Rabczuk, S. Bordas, and M. Duflot, "Meshless methods: a review and computer implementation aspects," *Mathematics and Computers in Simulation*, vol. 79, no. 3, pp. 763–813, 2008.
- [19] T. Rabczuk and T. Belytschko, "Adaptivity for structured mesh-free particle methods in 2D and 3D," *International Journal for Numerical Methods in Engineering*, vol. 63, no. 11, pp. 1559–1582, 2005.
- [20] P. W. Randles and L. D. Libersky, "Normalized SPH with stress points," *International Journal for Numerical Methods in Engineering*, vol. 48, no. 10, pp. 1445–1462, 2000.

- [21] T. Belytschko, Y. Guo, W. K. Liu, and S. P. Xiao, "A unified stability analysis of meshless particle methods," *International Journal for Numerical Methods in Engineering*, vol. 48, no. 9, pp. 1359–1400, 2000.
- [22] T. Rabczuk, T. Belytschko, and S. P. Xiao, "Stable particle methods based on Lagrangian kernels," *Computer Methods in Applied Mechanics and Engineering*, vol. 193, no. 12–14, pp. 1035–1063, 2004.
- [23] T. Rabczuk, S. Bordas, and G. Zi, "A three dimensional meshfree method for static and dynamic multiple crack nucleation/propagation with crack path continuity," *Computational Mechanics*, vol. 40, no. 3, pp. 473–495, 2007.
- [24] P. Areias and T. Rabczuk, "Finite strain fracture of plates and shells with configurational forces and edge rotations," *International Journal for Numerical Methods in Engineering*, vol. 94, no. 12, pp. 1099–1122, 2013.
- [25] P. Areias, D. Dias da Costa, J. M. Sargado, and T. Rabczuk, "Element-wise algorithm for modeling ductile fracture with the rousselier yield function," *Computational Mechanics*, vol. 52, no. 6, pp. 1429–1443, 2013.
- [26] P. Areias, T. Rabczuk, and P. P. Camanho, "Initially rigid cohesive laws and fracture based on edge rotations," *Computational Mechanics*, vol. 52, no. 4, pp. 931–947, 2013.
- [27] P. Areias, T. Rabczuk, and D. Dias da Costa, "Element-wise fracture algorithm based on rotation of edges," *Engineering Fracture Mechanics*, vol. 110, pp. 113–137, 2013.
- [28] C. Miehe, M. Hofacker, and F. Welschinger, "A phase field model for rate-independent crack propagation: Robust algorithmic implementation based on operator splits," *Computer Methods in Applied Mechanics and Engineering*, vol. 199, no. 45–48, pp. 2765–2778, 2010.
- [29] C. Miehe, F. Welschinger, and M. Hofacker, "Thermodynamically consistent phase-field models of fracture: variational principles and multi-field FE implementations," *International Journal for Numerical Methods in Engineering*, vol. 83, no. 10, pp. 1273–1311, 2010.
- [30] F. Armero and K. Garikipati, "Recent advances in the analysis and numerical simulation of strain localization in inelastic solids," in *Proceedings of the 4th Computational Plasticity: Fundamentals and Applications Conference (COMPLAS '00)*, pp. 635–640, 2000.
- [31] T. Belytschko and T. Black, "Elastic crack growth in finite elements with minimal remeshing," *International Journal for Numerical Methods in Engineering*, vol. 45, no. 5, pp. 601–620, 1999.
- [32] T. Belytschko, H. Chen, J. Xu, and G. Zi, "Dynamic crack propagation based on loss of hyperbolicity and a new discontinuous enrichment," *International Journal for Numerical Methods in Engineering*, vol. 58, no. 12, pp. 1873–1905, 2003.
- [33] T. Chau-Dinh, G. Zi, P.-S. Lee, T. Rabczuk, and J.-H. Song, "Phantom-node method for shell models with arbitrary cracks," *Computers & Structures*, vol. 92–93, pp. 242–246, 2012.
- [34] G. A. Dilts, "Moving-least-squares-particle hydrodynamics. I. Consistency and stability," *International Journal for Numerical Methods in Engineering*, vol. 44, no. 8, pp. 1115–1155, 1999.
- [35] G. A. Dilts, "Moving least-squares particle hydrodynamics. II. Conservation and boundaries," *International Journal for Numerical Methods in Engineering*, vol. 48, no. 10, pp. 1503–1524, 2000.
- [36] C. Linder and F. Armero, "Finite elements with embedded strong discontinuities for the modeling of failure in solids," *International Journal for Numerical Methods in Engineering*, vol. 72, no. 12, pp. 1391–1433, 2007.
- [37] N. Moës, J. Dolbow, and T. Belytschko, "A finite element method for crack growth without remeshing," *International Journal for Numerical Methods in Engineering*, vol. 46, no. 1, pp. 131–150, 1999.
- [38] S. S. Nanthakumar, T. Lahmer, and T. Rabczuk, "Detection of flaws in piezoelectric structures using extended FEM," *International Journal for Numerical Methods in Engineering*, vol. 96, no. 6, pp. 373–389, 2013.
- [39] J.-H. Song, P. M. A. Areias, and T. Belytschko, "A method for dynamic crack and shear band propagation with phantom nodes," *International Journal for Numerical Methods in Engineering*, vol. 67, no. 6, pp. 868–893, 2006.
- [40] T. Strouboulis, K. Copps, and I. Babuška, "The generalized finite element method: An example of its implementation and illustration of its performance," *International Journal for Numerical Methods in Engineering*, vol. 47, no. 8, pp. 1401–1417, 2000.
- [41] G. Ventura, E. Budyn, and T. Belytschko, "Vector level sets for description of propagating cracks in finite elements," *International Journal for Numerical Methods in Engineering*, vol. 58, no. 10, pp. 1571–1592, 2003.
- [42] G. Zi and T. Belytschko, "New crack-tip elements for XFEM and applications to cohesive cracks," *International Journal for Numerical Methods in Engineering*, vol. 57, no. 15, pp. 2221–2240, 2003.
- [43] G. Zi, J.-H. Song, E. Budyn, S.-H. Lee, and T. Belytschko, "A method for growing multiple cracks without remeshing and its application to fatigue crack growth," *Modelling and Simulation in Materials Science and Engineering*, vol. 12, no. 5, pp. 901–915, 2004.
- [44] G. Zi, H. Chen, J. Xu, and T. Belytschko, "The extended finite element method for dynamic fractures," *Shock and Vibration*, vol. 12, no. 1, pp. 9–23, 2005.
- [45] F. Amiri, C. Anitescu, M. Arroyo, S. P. A. Bordas, and T. Rabczuk, "XLME interpolants, a seamless bridge between XFEM and enriched meshless methods," *Computational Mechanics*, vol. 53, no. 1, pp. 45–57, 2014.
- [46] S. Bordas, T. Rabczuk, and G. Zi, "Three-dimensional crack initiation, propagation, branching and junction in non-linear materials by an extended meshfree method without asymptotic enrichment," *Engineering Fracture Mechanics*, vol. 75, no. 5, pp. 943–960, 2008.
- [47] T. Rabczuk and P. Areias, "A meshfree thin shell for arbitrary evolving cracks based on an extrinsic basis," *Computer Modeling in Engineering and Sciences*, vol. 16, no. 2, pp. 115–130, 2006.
- [48] T. Rabczuk, G. Zi, S. Bordas, and H. Nguyen-Xuan, "A geometrically non-linear three-dimensional cohesive crack method for reinforced concrete structures," *Engineering Fracture Mechanics*, vol. 75, no. 16, pp. 4740–4758, 2008.
- [49] T. Rabczuk, S. Bordas, and G. Zi, "On three-dimensional modelling of crack growth using partition of unity methods," *Computers & Structures*, vol. 88, no. 23–24, pp. 1391–1411, 2010.
- [50] T. Rabczuk, R. Gracie, J.-H. Song, and T. Belytschko, "Immersed particle method for fluid-structure interaction," *International Journal for Numerical Methods in Engineering*, vol. 81, no. 1, pp. 48–71, 2010.
- [51] G. Ventura, J. X. Xu, and T. Belytschko, "A vector level set method and new discontinuity approximations for crack growth by EFG," *International Journal for Numerical Methods in Engineering*, vol. 54, no. 6, pp. 923–944, 2002.

- [52] G. Zi, T. Rabczuk, and W. Wall, "Extended meshfree methods without branch enrichment for cohesive cracks," *Computational Mechanics*, vol. 40, no. 2, pp. 367–382, 2007.
- [53] T. Rabczuk and T. Belytschko, "Cracking particles: a simplified meshfree method for arbitrary evolving cracks," *International Journal for Numerical Methods in Engineering*, vol. 61, no. 13, pp. 2316–2343, 2004.
- [54] T. Rabczuk and T. Belytschko, "A three-dimensional large deformation meshfree method for arbitrary evolving cracks," *Computer Methods in Applied Mechanics and Engineering*, vol. 196, no. 29–30, pp. 2777–2799, 2007.
- [55] T. Rabczuk and P. M. A. Areias, "A new approach for modelling slip lines in geological materials with cohesive models," *International Journal for Numerical and Analytical Methods in Geomechanics*, vol. 30, no. 11, pp. 1159–1172, 2006.
- [56] T. Rabczuk and T. Belytschko, "Application of particle methods to static fracture of reinforced concrete structures," *International Journal of Fracture*, vol. 137, no. 1–4, pp. 19–49, 2006.
- [57] T. Rabczuk and E. Samaniego, "Discontinuous modelling of shear bands using adaptive meshfree methods," *Computer Methods in Applied Mechanics and Engineering*, vol. 197, no. 6–8, pp. 641–658, 2008.
- [58] T. Rabczuk, P. M. A. Areias, and T. Belytschko, "A meshfree thin shell method for non-linear dynamic fracture," *International Journal for Numerical Methods in Engineering*, vol. 72, no. 5, pp. 524–548, 2007.
- [59] T. Rabczuk, J.-H. Song, and T. Belytschko, "Simulations of instability in dynamic fracture by the cracking particles method," *Engineering Fracture Mechanics*, vol. 76, no. 6, pp. 730–741, 2009.
- [60] L. Chen and Y. Zhang, "Dynamic fracture analysis using discrete cohesive crack method," *International Journal for Numerical Methods in Biomedical Engineering*, vol. 26, no. 11, pp. 1493–1502, 2010.
- [61] Y. Dong, S. Wu, S. S. Xu, Y. Zhang, and S. Fang, "Analysis of concrete fracture using a novel cohesive crack method," *Applied Mathematical Modelling*, vol. 34, no. 12, pp. 4219–4231, 2010.
- [62] N. Sageresan and R. Drathi, "Crack propagation in concrete using meshless method," *Computer Modeling in Engineering and Sciences*, vol. 32, no. 2, pp. 103–112, 2008.
- [63] H. X. Wang and S. X. Wang, "Analysis of dynamic fracture with cohesive crack segment method," *Computer Modeling in Engineering & Sciences*, vol. 35, no. 3, pp. 253–274, 2008.
- [64] T. Rabczuk, G. Zi, S. Bordas, and H. Nguyen-Xuan, "A simple and robust three-dimensional cracking-particle method without enrichment," *Computer Methods in Applied Mechanics and Engineering*, vol. 199, no. 37–40, pp. 2437–2455, 2010.
- [65] J. S. Chen, C. T. Wu, S. Yoon, and Y. You, "A stabilized conforming nodal integration for galerkin meshfree-methods," *International Journal for Numerical Methods in Engineering*, vol. 50, pp. 435–466, 2001.
- [66] G. R. Liu, T. T. Nguyen, K. Y. Dai, and K. Y. Lam, "Theoretical aspects of the smoothed finite element method (SFEM)," *International Journal for Numerical Methods in Engineering*, vol. 71, no. 8, pp. 902–930, 2007.
- [67] T. Nguyen-Thoi, H. C. Vu-Do, T. Rabczuk, and H. Nguyen-Xuan, "A node-based smoothed finite element method (NS-FEM) for upper bound solution to visco-elastoplastic analyses of solids using triangular and tetrahedral meshes," *Computer Methods in Applied Mechanics and Engineering*, vol. 199, no. 45–48, pp. 3005–3027, 2010.
- [68] T. Nguyen-Thoi, P. Phung-Van, T. Rabczuk, H. Nguyen-Xuan, and C. Le-Van, "Free and forced vibration analysis using the n-sided polygonal cellbased smoothed finite element method (ncs-fem)," *International Journal of Computational Methods*, vol. 10, no. 1, Article ID 13400082, 2013.
- [69] H. Nguyen-Xuan, T. Rabczuk, T. Nguyen-Thoi, T. N. Tran, and N. Nguyen-Thanh, "Computation of limit and shakedown loads using a node-based smoothed finite element method," *International Journal for Numerical Methods in Engineering*, vol. 90, no. 3, pp. 287–310, 2012.
- [70] C. H. Thai, H. Nguyen-Xuan, N. Nguyen-Thanh, T.-H. Le, T. Nguyen-Thoi, and T. Rabczuk, "Static, free vibration, and buckling analysis of laminated composite Reissner-Mindlin plates using NURBS-based isogeometric approach," *International Journal for Numerical Methods in Engineering*, vol. 91, no. 6, pp. 571–603, 2012.
- [71] T. Belytschko, Y. Y. Lu, and L. Gu, "Element-free Galerkin methods," *International Journal for Numerical Methods in Engineering*, vol. 37, no. 2, pp. 229–256, 1994.
- [72] M. A. Puso, J. S. Chen, E. Zywickz, and W. Elmer, "Meshfree and finite element nodal integration methods," *International Journal for Numerical Methods in Engineering*, vol. 74, no. 3, pp. 416–446, 2008.
- [73] H. Talebi, C. Samaniego, E. Samaniego, and T. Rabczuk, "On the numerical stability and mass-lumping schemes for explicit enriched meshfree methods," *International Journal for Numerical Methods in Engineering*, vol. 89, no. 8, pp. 1009–1027, 2012.
- [74] P. Baiz, S. Natarajan, S. Bordas, P. Kerfriden, and T. Rabczuk, "Linear buckling analysis of cracked plates by sfem and xfem (smxfem)," *Journal of Mechanics of Materials and Structures*, vol. 6, no. 9–10, pp. 1213–1238, 2011.
- [75] S. P. A. Bordas, T. Rabczuk, N.-X. Hung et al., "Strain smoothing in FEM and XFEM," *Computers & Structures*, vol. 88, no. 23–24, pp. 1419–1443, 2010.
- [76] S. P. A. Bordas, S. Natarajan, P. Kerfriden et al., "On the performance of strain smoothing for quadratic and enriched finite element approximations (XFEM/GFEM/PUFEM)," *International Journal for Numerical Methods in Engineering*, vol. 86, no. 4–5, pp. 637–666, 2011.
- [77] L. Chen, T. Rabczuk, S. P. A. Bordas, G. R. Liu, K. Y. Zeng, and P. Kerfriden, "Extended finite element method with edge-based strain smoothing (ESm-XFEM) for linear elastic crack growth," *Computer Methods in Applied Mechanics and Engineering*, vol. 212, no. 4, pp. 250–265, 2012.
- [78] H. Nguyen-Xuan, G. R. Liu, S. Bordas, S. Natarajan, and T. Rabczuk, "An adaptive singular ES-FEM for mechanics problems with singular field of arbitrary order," *Computer Methods in Applied Mechanics and Engineering*, vol. 253, pp. 252–273, 2013.
- [79] N. Vu-Bac, H. Nguyen-Xuan, L. Chen et al., "A node-based smoothed extended finite element method (NS-XFEM) for fracture analysis," *Computer Modeling in Engineering and Sciences*, vol. 73, no. 4, pp. 331–355, 2011.
- [80] N. Vu-Bac, H. Nguyen-Xuan, L. Chen et al., "A phantom-node method with edge-based strain smoothing for linear elastic fracture mechanics," *Journal of Applied Mathematics*, vol. 2013, Article ID 978026, 12 pages, 2013.
- [81] A. Pandolfi, P. Krysl, and M. Ortiz, "Finite element simulation of ring expansion and fragmentation: the capturing of length and time scales through cohesive models of fracture," *International Journal of Fracture*, vol. 95, no. 1–4, pp. 279–297, 1999.
- [82] T. Rabczuk, G. Zi, A. Gerstenberger, and W. A. Wall, "A new crack tip element for the phantom-node method with arbitrary

- cohesive cracks," *International Journal for Numerical Methods in Engineering*, vol. 75, no. 5, pp. 577–599, 2008.
- [83] X.-P. Xu and A. Needleman, "Numerical simulations of fast crack growth in brittle solids," *Journal of the Mechanics and Physics of Solids*, vol. 42, no. 9, pp. 1397–1434, 1994.
- [84] J. Fineberg, E. Sharon, and G. Cohen, "Crack front waves in dynamic fracture," *International Journal of Fracture*, vol. 121, no. 1-2, pp. 55–69, 2003.
- [85] K. Ravi-Chandar, "Dynamic fracture of nominally brittle materials," *International Journal of Fracture*, vol. 90, no. 1-2, pp. 83–102, 1998.
- [86] E. Sharon, S. P. Gross, and J. Fineberg, "Local crack branching as a mechanism for instability in dynamic fracture," *Physical Review Letters*, vol. 74, no. 25, pp. 5096–5099, 1995.
- [87] T. Rabczuk and G. Zi, "A meshfree method based on the local partition of unity for cohesive cracks," *Computational Mechanics*, vol. 39, no. 6, pp. 743–760, 2007.
- [88] J. F. Kalthoff and S. Winkler, "Failure mode transition at high rates of shear loading," in *Proceedings of the International Conference on Impact Loading and Dynamic Behavior of Materials*, vol. 1, pp. 185–195, 1987.
- [89] J. F. Kalthoff, "Modes of dynamic shear failure in solids," *International Journal of Fracture*, vol. 101, no. 1-2, pp. 1–31, 2000.

Research Article

Error Estimate and Adaptive Refinement in Mixed Discrete Least Squares Meshless Method

J. Amani,¹ A. Saboor Bagherzadeh,¹ and T. Rabczuk^{1,2}

¹ Institute of Structural Mechanics, Bauhaus-University Weimar, Marienstrasse 15, 99423 Weimar, Germany

² School of Civil, Environmental and Architectural Engineering, Korea University, Seoul, Republic of Korea

Correspondence should be addressed to A. Saboor Bagherzadeh; saboorbagherzadeh.a@gmail.com

Received 3 October 2013; Accepted 29 December 2013; Published 16 February 2014

Academic Editor: Stephane P. A. Bordas

Copyright © 2014 J. Amani et al. This is an open access article distributed under the Creative Commons Attribution License, which permits unrestricted use, distribution, and reproduction in any medium, provided the original work is properly cited.

The node moving and multistage node enrichment adaptive refinement procedures are extended in mixed discrete least squares meshless (MDLSM) method for efficient analysis of elasticity problems. In the formulation of MDLSM method, mixed formulation is accepted to avoid second-order differentiation of shape functions and to obtain displacements and stresses simultaneously. In the refinement procedures, a robust error estimator based on the value of the least square residuals functional of the governing differential equations and its boundaries at nodal points is used which is inherently available from the MDLSM formulation and can efficiently identify the zones with higher numerical errors. The results are compared with the refinement procedures in the irreducible formulation of discrete least squares meshless (DLSM) method and show the accuracy and efficiency of the proposed procedures. Also, the comparison of the error norms and convergence rate show the fidelity of the proposed adaptive refinement procedures in the MDLSM method.

1. Introduction

Adaptivity needs appropriate numerical solutions of problems in order to describe high gradient regions and an anisotropic behavior of the solution. In an adaptive procedure, a good error estimator plays a very important role. The error estimation in numerical methods is obviously as old as the numerical computations themselves. The earliest paper by Richardson [1] proposed an error estimation procedure to use in finite difference method. This was followed in finite element method (FEM) [2]. A particular strength of the FEM is the well-developed theories of error estimation and adaptivity. Three h-refinement procedures, namely, mesh movement, mesh enrichment, and remeshing have been proposed for adaptivity [3]. In the mesh movement, the total number of nodes remains constant, but the location of the nodes can change in order to achieve a better overall distribution of the error. In the mesh enrichment, the original nodes hold fix and hierarchical nodes or simply more nodes add to the problem domain based on error distribution. In the remeshing, a completely new nodes is constructed based

on the information acquired from the previous computation, and hence, it is required to implement a suitable node generator. on one hand, the mesh movement is more suitable than mesh enrichment because the problem scale remains constant, and on the other hand, its interpolations become too distort in the mesh-based methods [4].

In order to avoid these problems, an alternative approach, known as meshless methods (MMs), has been developed in recent decades to discretize a continuum body only by a finite number of nodes. In MMs the unknowns are interpolated from the nodal values that constitute the problem degrees-of-freedom. The main advantage of MMs is the fact that the interpolation accuracy is much less affected by the nodal distribution. Many meshless methods have been introduced since Gingold and Monaghan [5] proposed smoothed particle hydrodynamics (SPH) method. Nayroles et al. [6] implemented the diffuse element method (DEM). Belytschko et al. [7] presented the Element-Free Galerkin (EFG) method. Liu et al. [8] suggested the reproducing kernel particle method (RKPM). The other meshless methods that have been developed in recent years are the Finite Point (FP)

method [9], the HP clouds method [10], the meshless local Petrov-Galerkin (MLPG) method [11], the local boundary integral equation (LBIE) method [12], the finite cloud (FC) method [13] and the discrete least squares meshless (DLSM) method [14].

Researchers used the advantages of MMs for developing efficient error estimate and adaptivity procedures. Rabczuk and Belytschko [15, 16] proposed an adaptive continuum/discrete crack approach for meshfree particle methods and also an adaptivity procedure for structured meshfree particle methods in 2D and 3D problems. Yoon et al. [17] worked on enriched meshfree collocation method with diffuse derivatives for elastic fracture. Zi et al. [18] investigated extended meshfree methods without branch enrichment for cohesive cracks. Bordas et al. [19] proposed enriched meshfree methods without asymptotic enrichment for 3D nonlinear fracture mechanics. Rabczuk and Samaniego [20] worked on discontinuous modelling of shear bands using adaptive meshfree methods. Zhuang et al. [21–23] investigated error control in the EFG method and adaptivity for structured meshfree particle methods in 2D and 3D problems. The DLSM method was extended for error estimate and adaptivity in solid [24, 25] and fluid [26] problems.

Two different formulations, namely irreducible and mixed formulations have been introduced and used for the solution of engineering problems. With the mixed formulation, the continuity requirement decreases by one order compared to the irreducible formulation [27]. Use of mixed formula may result in an improved approximation, in particular, for the gradient variables, which in turn could result in higher accuracy than possible with the irreducible formulation [27]. In the standard mixed FEM, in order to obtain a coefficient matrix which leads to the system of equations with a unique and stable solution, the polynomial functions chosen for approximation of stresses and displacements must satisfy the Ladyzhenskaya-Babuška-Brezzi (LBB or inf-sup) condition [28, 29]. The stability of mixed discretization does not allow FEM to choose independently the approximation spaces, so these spaces are restricted in the stability condition which is known as the LBB condition. However, the least squares approximation has the advantage that it does not require satisfying the LBB condition [30–32]. Hence, this advantage was used by Amani et al. [33] to implement a mixed meshless method named mixed discrete least squares Meshless (MDLSM) method which is formulated based on the least squares residuals functional of the governing partial differential equations of planar elasticity problem and its boundary conditions at the nodal points, and hence, it is stable and is not required to satisfy the LBB condition between the displacements and stresses approximations. Hence, the approximation spaces of the displacements and stresses can be chosen independently while they are obtained simultaneously.

In this paper, the MDLSM method is extended for the residual based error estimation and for the two types of adaptive refinement procedures. The node moving adaptive refinement procedure based on the spring analogy [24] and the node enrichment adaptive refinement procedure [25] are formulated and used in the MDLSM method for efficient analysis of the elasticity problems.

The present paper is organized as follows. Formulation of the mixed discrete least squares meshless method for solving the planar elasticity problems is given in Section 2. In Section 3, an error estimator based on the least square functional residuals is formulated for the MDLSM method to use in the node moving and node enrichment adaptive refinement procedures. In Section 4, we present some numerical benchmark examples which illustrate the proposed adaptive refinement process as well as the efficiency of the error estimator. Finally, some concluding remarks are addressed in Section 5.

2. Formulation of Mixed Discrete Least Squares Meshless Method for Elasticity

Consider the following two-dimensional linear elasticity problem

$$-\mu\Delta\mathbf{u} + (\lambda + \mu)\nabla(\nabla\cdot\mathbf{u}) = \mathbf{f} \quad \text{in } \Omega, \quad (1)$$

with displacement and traction boundary conditions as follow:

$$\begin{aligned} \mathbf{u} &= \bar{\mathbf{u}}, & \mathbf{v} &= \bar{\mathbf{v}}, & \text{in } \Gamma_u, \\ \sigma_x n_x + \tau_{xy} n_y &= \bar{t}_x, & \tau_{xy} n_x + \sigma_y n_y &= \bar{t}_y, & (2) \\ & & & & \text{in } \Gamma_t, \end{aligned}$$

where Ω is a bounded domain representing the region occupied by an elastic body, and λ, μ are the Lamé constants which are defined as

$$\mu = \frac{E}{2(1+\nu)} > 0, \quad \lambda = \frac{E\nu}{(1-2\nu)(1+\nu)} > 0, \quad (3)$$

where ν is the Poisson ratio, E is the Young modulus, and Γ_u, Γ_t are the displacement and traction boundaries, respectively. $\bar{\mathbf{u}}, \bar{\mathbf{v}}, \bar{t}_x,$ and \bar{t}_y prescribed respectively the displacements and tractions in the x and y directions and n_x, n_y are direction cosines of the normal vector to the boundary.

By using the following definition of stresses in terms of the displacement components:

$$\begin{aligned} \sigma_x &= (\lambda + 2\mu) \frac{\partial u}{\partial x} + \lambda \frac{\partial v}{\partial y}, \\ \sigma_y &= \lambda \frac{\partial u}{\partial x} + (\lambda + 2\mu) \frac{\partial v}{\partial y}, \\ \tau_{xy} &= \mu \left(\frac{\partial u}{\partial y} + \frac{\partial v}{\partial x} \right), \end{aligned} \quad (4)$$

we can rewrite (1) in term of stresses as

$$\begin{aligned} \frac{\partial \sigma_x}{\partial x} + \frac{\partial \tau_{xy}}{\partial y} &= -f_x \quad \text{in } \Omega, \\ \frac{\partial \tau_{xy}}{\partial x} + \frac{\partial \sigma_y}{\partial y} &= -f_y \quad \text{in } \Omega. \end{aligned} \quad (5)$$

The compact form of (1) can be written by substituting (4)-(5) into the second-order problem of (1) in the form of

$$\mathbf{L}(\boldsymbol{\phi}) + \mathbf{f} = \mathbf{0}, \quad (6)$$

where $\mathbf{L}(\cdot)$ is a first-order differential operator defined as

$$\mathbf{L}(\cdot) = \mathbf{L}_1(\cdot)_x + \mathbf{L}_2(\cdot)_y + \mathbf{L}_3(\cdot), \quad (7)$$

and $\boldsymbol{\phi}$ is the vector of unknowns defined as

$$\boldsymbol{\phi} = [u \quad v \quad \sigma_x \quad \sigma_y \quad \tau_{xy}]^T, \quad (8)$$

and vector \mathbf{f} contains the forcing terms which has the form

$$\mathbf{f} = [0 \quad 0 \quad 0 \quad -f_x \quad -f_y]^T. \quad (9)$$

In (7), \mathbf{L}_1 , \mathbf{L}_2 , and \mathbf{L}_3 are defined by the following matrices:

$$\mathbf{L}_1 = \begin{pmatrix} \lambda + 2\mu & 0 & 0 & 0 & 0 \\ \lambda & 0 & 0 & 0 & 0 \\ 0 & \mu & 0 & 0 & 0 \\ 0 & 0 & 1 & 0 & 0 \\ 0 & 0 & 0 & 0 & 1 \end{pmatrix},$$

$$\mathbf{L}_2 = \begin{pmatrix} 0 & \lambda & 0 & 0 & 0 \\ 0 & \lambda + 2\mu & 0 & 0 & 0 \\ \mu & 0 & 0 & 0 & 0 \\ 0 & 0 & 0 & 0 & 1 \\ 0 & 0 & 0 & 1 & 0 \end{pmatrix},$$

$$\mathbf{L}_3 = \begin{pmatrix} 0 & 0 & -1 & 0 & 0 \\ 0 & 0 & 0 & -1 & 0 \\ 0 & 0 & 0 & 0 & -1 \\ 0 & 0 & 0 & 0 & 0 \\ 0 & 0 & 0 & 0 & 0 \end{pmatrix}. \quad (10)$$

The displacement and traction boundary conditions (2) can be written in terms of the unknown vector $\boldsymbol{\phi}$ as

$$\mathbf{D}\boldsymbol{\phi} - \bar{\mathbf{f}} = \mathbf{0}, \quad (11)$$

where \mathbf{D} and $\bar{\mathbf{f}}$ are defined as follow:

$$\mathbf{D} = \begin{pmatrix} 1 & 0 & 0 & 0 & 0 \\ 0 & 1 & 0 & 0 & 0 \\ 0 & 0 & n_x & 0 & n_y \\ 0 & 0 & 0 & n_y & n_x \end{pmatrix}, \quad \bar{\mathbf{f}} = \begin{pmatrix} \bar{u} \\ \bar{v} \\ \bar{t}_x \\ \bar{t}_y \end{pmatrix}. \quad (12)$$

The plane elasticity problem is now defined as solving the first-order differential equation subjected only to the Dirichlet type boundary condition

$$\mathbf{L}_1(\boldsymbol{\phi})_x + \mathbf{L}_2(\boldsymbol{\phi})_y + \mathbf{L}_3(\boldsymbol{\phi}) + \mathbf{f} = \mathbf{0}, \quad \text{in } \Omega, \quad (13)$$

$$\mathbf{D}\boldsymbol{\phi} - \bar{\mathbf{f}} = \mathbf{0}, \quad \text{on } \Gamma.$$

The application of the proposed MDLSM method for solving problem of (13) starts with the definition of residuals as follows:

$$\mathcal{R}_\Omega = \mathbf{L}(\boldsymbol{\phi}) + \mathbf{f} \quad \text{in } \Omega, \quad (14)$$

$$\mathcal{R}_\Gamma = \mathbf{D}\boldsymbol{\phi} - \bar{\mathbf{f}} \quad \text{on } \Gamma,$$

where \mathcal{R}_Ω and \mathcal{R}_Γ are domain and boundary residuals, respectively.

Now the penalty approach is used to form the least square residuals functional which is defined as

$$\mathbf{I} = \sum_{k=1}^{M_d} \mathcal{R}_\Omega^T \mathcal{R}_\Omega + \alpha \sum_{k=1}^{M_b} \mathcal{R}_\Gamma^T \mathcal{R}_\Gamma, \quad M = M_d + M_b, \quad (15)$$

where M is the total number of sampling (or collocation) points, M_d is total number of domain sampling points, M_b is total number of boundary sampling points, and the penalty coefficient α is a positive scalar constant that must be large enough in order to impose the essential boundary condition with the desired accuracy. A note should be made here regarding the value of the penalty parameters. To impose the boundary conditions exactly, the penalty factor must be infinite, which is not possible in practical numerical analysis. Therefore, the boundary conditions could not be satisfied exactly but only approximately. In general, the use of a larger penalty factor will lead to better enforcement of the constraint. The proper value of the penalty parameter is determined prior to the main calculation via a trial and error process and it is problem dependent.

Minimizing the functional in (15) with respect to the nodal unknown vector $\boldsymbol{\phi}$ leads to the following system of equation:

$$\mathbf{K} \boldsymbol{\Phi} = \mathbf{F}, \quad (16)$$

where

$$\mathbf{K}_{ij} = \sum_{\ell=1}^{M_d} [\mathbf{L}(\mathbf{N}_i)]_\ell^T [\mathbf{L}(\mathbf{N}_j)]_\ell + \alpha \sum_{\ell=1}^{M_b} [\mathbf{D}(\mathbf{N}_i)]_\ell^T [\mathbf{D}(\mathbf{N}_j)]_\ell,$$

$$\mathbf{F}_i = \sum_{\ell=1}^{M_d} [\mathbf{L}(\mathbf{N}_i)]_\ell^T \mathbf{f}_\ell + \alpha \sum_{\ell=1}^{M_b} [\mathbf{D}(\mathbf{N}_i)]_\ell^T \bar{\mathbf{f}}_\ell, \quad (17)$$

and $\boldsymbol{\Phi}$ is unknown matrix that contains displacements and stresses of all nodes. \mathbf{F} is the right hand side vector and the stiffness matrix \mathbf{K} in (16) is $n_{\text{DOF}} \times n_{\text{DOF}}$ square matrix where n_{DOF} is the number of unknowns per each node and \mathbf{N} is the moving least squares (MLS) shape functions. The proposed MDLSM method has 2.5 times unknowns compared to the irreducible DLSM method with only displacements as unknowns. This should drastically reduce the computational efficiency by $(2.5)^\beta$ (where β depends on the type of linear solver used) times. But, since matrix \mathbf{K} is symmetric and positive definite, therefore, the final system of equation can be solved directly via efficient solvers. The MDLSM formulation for the plane elasticity problem has the following advantages that increase its efficiency [33].

- (1) The order of shape function derivatives is reduced by one order, thus complex and costly second-order derivative calculations of the MLS shape function in the irreducible DLSM method are avoided.

- (2) The stresses are obtained directly, while calculation of stresses in the irreducible DLSSM method requires some postprocessing.
- (3) Only a linear complete polynomial basis is needed to construct the MLS shape functions, while in the irreducible DLSSM formulation, the second order polynomial basis is required to achieve second-order consistency due to the presence of second-order derivatives in the irreducible formulation. This leads to lower computational effort for mixed method in construction of MLS shape functions and its derivatives compared to irreducible one. Furthermore, this in turn leads to the smaller number of points to be included in the support domain for the construction of the MLS shape functions in the mixed method and hence, less computational effort.
- (4) Both the displacement and stress boundary conditions are of the Dirichlet type which requires the specification of a single penalty parameter if a penalty method is used to enforce them as used in this work. In the irreducible DLSSM method both Dirichlet and Neumann type boundary conditions are required for the determination of two types of penalty coefficient.
- (5) The mixed formulation, when used with the standard weighted residual methods both mesh-based and meshless forms, requires the LBB condition because the resulting problem is a saddle point problem. The least squares method, however, is a minimization method and therefore is not subject to the LBB condition.

3. Error Estimator and Adaptive Refinement

3.1. Error Estimator. In numerical methods, a problem is solved by discretization of the problem domain into the subdomains, hence, the governing equations only apply into these subdomains, so numerical methods always come with discretization error. Discretization error is one of the most important challenges in the numerical methods. Discretization error is theoretically decreased by refining the discretization domain but perfunctory refinement imposes the heavy computational cost without supplying the expected accuracy. Adaptive refinement methods mean balances between refinement procedure and its computational cost. These methods only refine locally the regions of the domain which has higher error. Adaptive procedure has two main parts: error estimation and adaptive refinement. Any success adaptive refinement needs a reliable error estimation procedure. Real error distribution can not be practicably used because the exact solution is not available for any practical problems. Several methods are used for error estimation with different numerical methods and these methods are categorized into two classes, namely, the residual based method [34] and recovery based method [35]. In residual based method, the residuals of differential equation and its boundaries are used as a criterion of error. The gradient of the solutions is used in recovery based method as the error criterion.

In this paper, the relative least square residuals functional for each node is defined as follows:

$$e = \sqrt{\frac{\mathbf{I}}{(\mathbf{U}_t^T \mathbf{U}_t)}}, \quad (18)$$

where \mathbf{I} is the least square residuals functional in (15) and \mathbf{U}_t is unknowns obtained from the main solution. It is noticed that most of the computations of the least square residuals functional can be obtained from the main solution of the MDLSSM method.

3.2. Adaptive Refinement Procedures

3.2.1. Node Moving. Mesh movement strategy can be easily and efficiently used with meshless methods since no element distortion is associated with the method. It should be noted that the mesh movement technique can be used in conjunction with the MDLSSM method to adaptively adjust nodal points to improve the quality of the solution obtained with a prespecified number of nodal points. Here, a nodal refinement procedure is used that is called node moving adaptive refinement approach. When a node refinement is required, springs of prescribed stiffness are placed between each pair of nodes belonging to the same subdomain and the nodes are then moved until the spring system is in equilibrium.

In the node moving procedure, first, all nodes are connected with springs in which the neighbor nodes are defined using Voronoi diagram [36] (see Figure 1). Voronoi diagram is defined as

$$\mathbb{T}_i = \{x \in \mathbb{R} : d(x, x_i) < d(x, x_j), j \neq i\}, \quad (19)$$

where $d(x, x_i)$ is Euclidean distance between x and x_i . The above equation means that neighbor nodes to node i are the closest nodes to the node i rather than other nodes.

Spring forces are defined as

$$b_{ij} = c_{ij}(x_i - x_j), \quad (20)$$

where c_{ij} is stiffness of spring between i, j and x_i, x_j are coordinates of i, j in equilibrium, respectively. The free body diagram is shown in Figure 2.

Spring stiffness is defined as a function of errors between two points i, j as follows:

$$c_{ij} = \frac{(e_i + e_j)}{d_{ij}}, \quad (21)$$

where e_i and e_j are the values of the error estimators obtained from (18) at nodes i and j , respectively, and d_{ij} is distance between these two connected nodes. In matrix form we have

$$\begin{pmatrix} c_{ij} & 0 & -c_{ij} & 0 \\ 0 & c_{ij} & 0 & -c_{ij} \\ -c_{ij} & 0 & c_{ij} & 0 \\ 0 & -c_{ij} & 0 & c_{ij} \end{pmatrix} \begin{pmatrix} x_i \\ y_i \\ x_j \\ y_j \end{pmatrix} = \begin{pmatrix} b_x^i \\ b_y^i \\ b_x^j \\ b_y^j \end{pmatrix}, \quad (22)$$

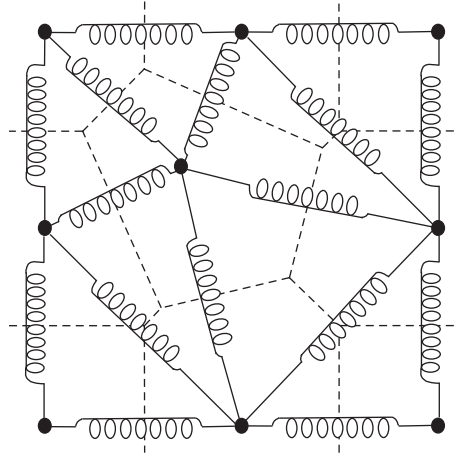


FIGURE 1: Voronoi diagram of neighboring nodes and spring connections.

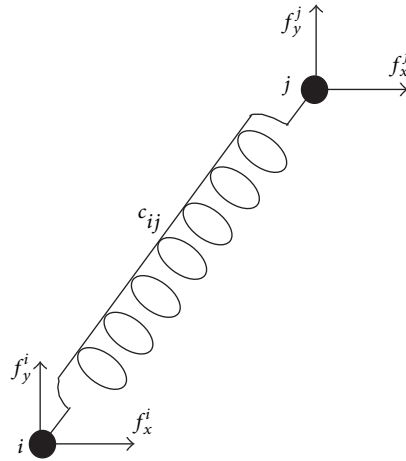


FIGURE 2: Free body diagram between two nodes i and j .

where b_x^i and b_y^i are the components of the force exerted at node i in x and y directions, respectively, and x_i and y_i are the coordinates of node i in x and y directions, respectively. The spring systems work as a two-dimensional truss such that nodes and springs are points and elements of truss, respectively. We mention that the system of algebraic equations (22) can be assembled in its standard finite element concept to yield global force vector for whole system of springs as follows:

$$\mathbf{CX} = \mathbf{B}, \tag{23}$$

where \mathbf{C} is the stiffness matrix of the system calculated by assembling the stiffness matrices of all the springs defined in the system and \mathbf{B} represents the vector of nodal forces. In the equilibrium condition, the vector \mathbf{B} of assembled spring forces should be equal to zero. This requirement leads to the following system of algebraic equation which should be solved for the unknown vector of nodal position \mathbf{X} , that is, solve

$$\mathbf{CX} = \mathbf{0}. \tag{24}$$

It is obvious that the equation system defined in (24) is singular before any boundary conditions are considered. The boundary conditions used here for solving this system of equations are defined by the requirement that the boundary nodes should not be allowed to move perpendicularly to the boundaries. In other words, boundary nodes only can be displaced along the boundaries which they have been placed on. Mathematical representation of these boundary conditions can be defined as

$$\begin{aligned} \Delta \mathbf{X}_i^T \mathbf{n}_i &= (\Delta x_i \ \Delta y_i) \begin{pmatrix} n_x^i \\ n_y^i \end{pmatrix} \\ &= ((x_i - \bar{x}_\ell) \ (y_i - \bar{y}_\ell)) \begin{pmatrix} n_x^i \\ n_y^i \end{pmatrix} = 0, \end{aligned} \tag{25}$$

where \bar{x}_ℓ and \bar{y}_ℓ are the initial coordinates of boundary node i ; x_i and y_i represent the displaced final position of node i and \mathbf{n} is outward unit vector normal to the boundary at node i . This condition guarantees that the nodes initially located at the intersection of two boundary lines must remain on its initial position. Boundary conditions for a simple net of springs are shown in Figure 3.

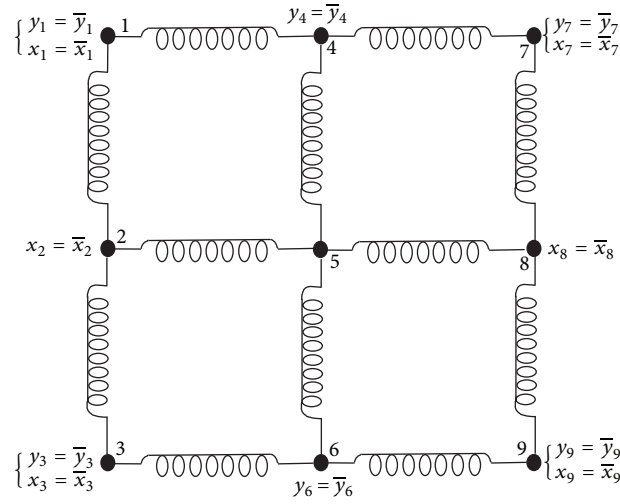


FIGURE 3: Boundary conditions of spring system.

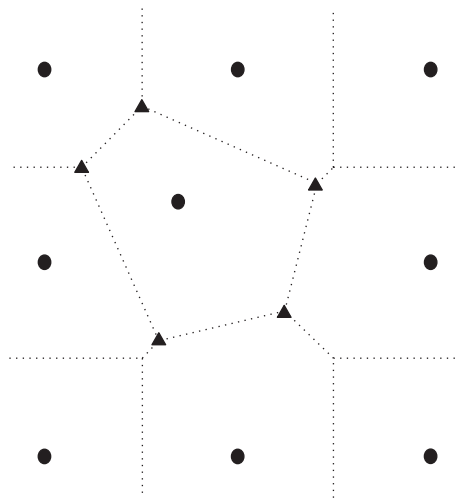


FIGURE 4: The node enrichment using Voronoi diagram (• initial nodes, ▲ new added nodes).

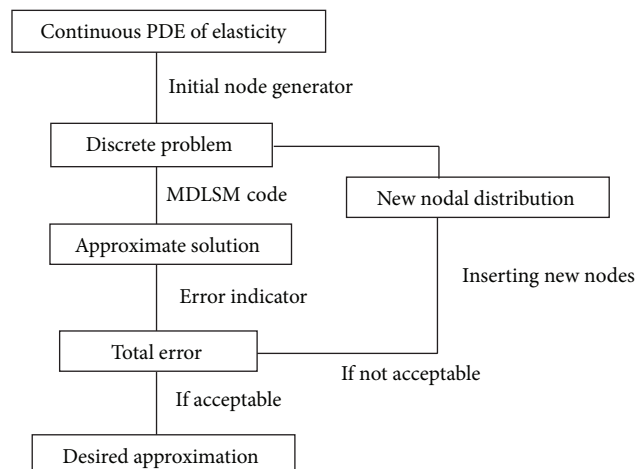


FIGURE 5: The node enrichment procedure in MDLSM method.

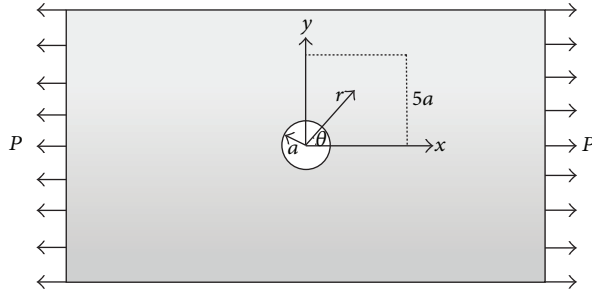


FIGURE 6: An infinite plate with a circular hole under a uniaxial load P (Example 1).

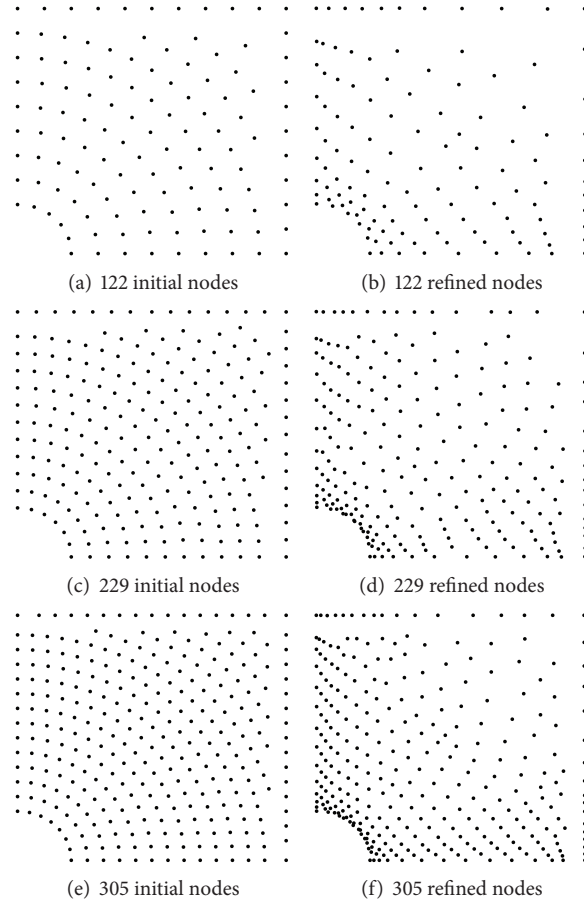


FIGURE 7: Initial and refined (node moving) nodal configurations (Example 1).

Upon solving the system of equations with appropriate boundary conditions, the refined position of nodes is obtained leading to substantial reduction of the local and global error of the numerical solution in the subsequent analysis. The efficiency and effectiveness of the proposed adaptive refinement technique is verified in the next section by its application to benchmark test examples in plane elasticity.

3.2.2. Node Enrichment. With the meshless methods, the enrichment strategy only requires that the locations of new nodes to be added are determined without requiring to define the connectivity of the resulting configuration. Different

methods can be thought to be defining the location of the nodes to be added to the current nodal configuration. Here the new nodes are added in the neighborhood of existing nodal points defined by a Voronoi diagram.

Once the Voronoi cells are defined, the vertices of Voronoi cells corresponding to the nodes with higher error than the average error over the domain are considered as the new nodes to be added to the current nodal configuration. The method is schematically illustrated in Figure 4. The value of average error e_{avg} over the domain is obtained by

$$e_{\text{avg}} = \frac{\sum_{\ell=1}^M e_{\ell}}{M}. \tag{26}$$

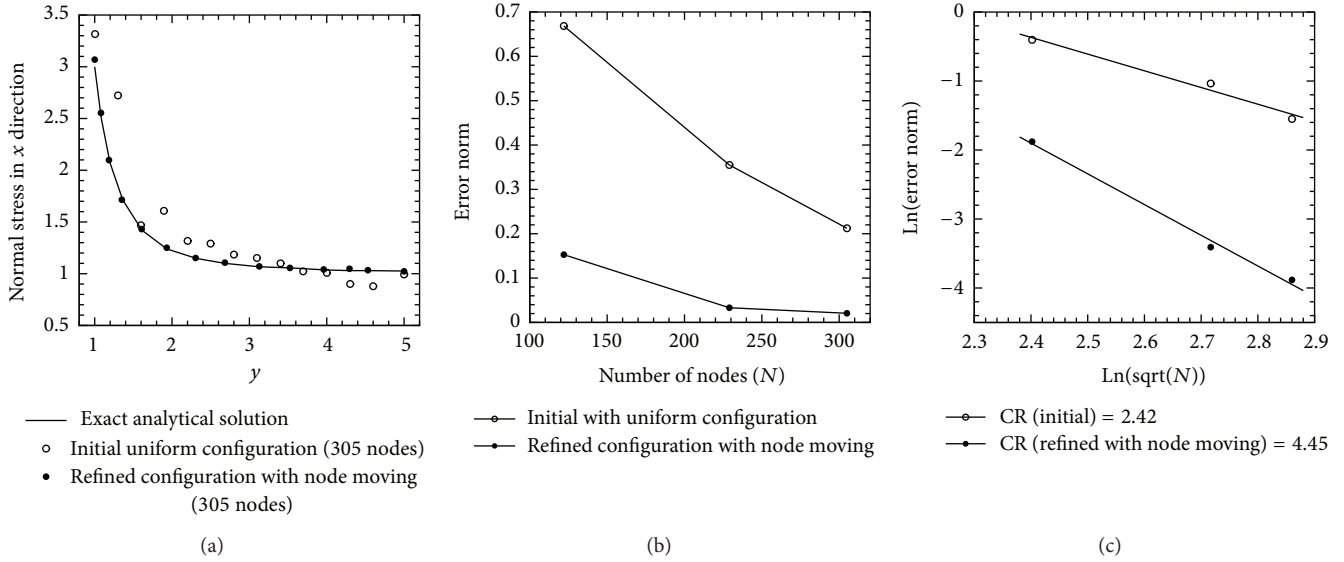


FIGURE 8: (a) Normal stress σ_x at $x = 0$. (b) Convergence curve of node moving procedure. (c) Convergence rate of node moving procedure.

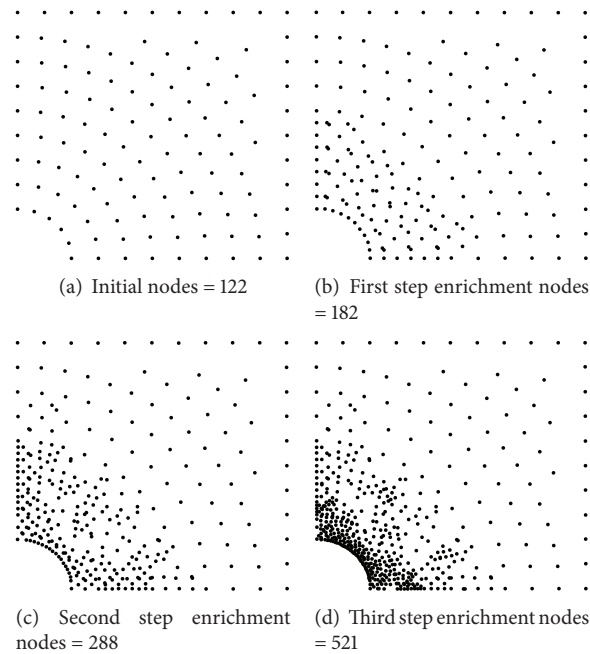


FIGURE 9: Initial and refined (node enrichment) nodal configurations (Example 1).

The above node enrichment adaptive refinement procedure based on error estimation is schematically shown in Figure 5.

4. Numerical Experiments

In this section, we are solving the benchmark examples by using the proposed node moving and node enrichment refinement procedures for the MDLSM method and comparing the results with the refinement procedure in the

irreducible DLSSM method and the exact analytical solutions or finite element results with very fine mesh.

Example 1 (an infinite plate with a circular hole). In the first example, consider the case of an infinite plate with a circular hole subjected to a uniaxial traction P at infinity, as shown in Figure 6. Due to symmetry, only the upper right square quadrant of the plate is modeled. The edge length of the square is $5a$, where a is the radius of the circular hole. This example is chosen because the exact analytical solution is available from Timoshenko and Goodier [37]. The solutions

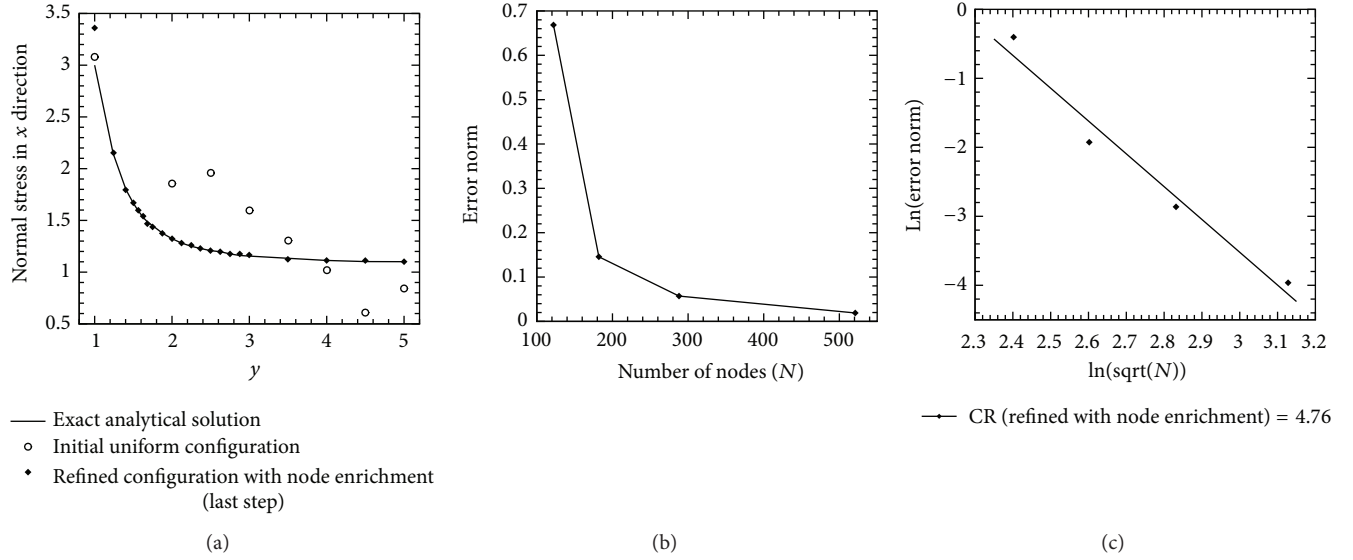


FIGURE 10: (a) Normal stress σ_{xx} at $x = 0$. (b) Convergence curve for node enrichment procedure. (c) Convergence rate for node enrichment procedure.

TABLE 1: Comparison of the error norms for initial and refined (using node moving) nodal configurations (Example 1).

Number of nodes	Norm of error for initial nodes	Norm of error for refined nodes
122	0.6684	0.1528
229	0.3550	0.0331
305	0.2123	0.0206

for the displacements and the stresses under a unit uniaxial stress along the x axis are given as follows:

$$\begin{aligned}\sigma_x &= t \left(1 - \frac{a^2}{r^2} \left(\frac{3}{2} \cos(2\theta) + \cos(4\theta) \right) + \frac{3a^4}{2r^4} \cos(4\theta) \right), \\ \sigma_y &= - \left(\frac{a^2}{r^2} \left(\frac{1}{2} \cos(2\theta) - \cos(4\theta) \right) + \frac{3a^4}{2r^4} \cos(4\theta) \right), \\ \tau_{xy} &= -t \left(\frac{a^2}{r^2} \left(\frac{1}{2} \sin(2\theta) + \sin(4\theta) \right) - \frac{3a^4}{2r^4} \sin(4\theta) \right), \\ u_r &= \frac{t}{4G} \left(r \left(\frac{\kappa - 1}{2} + \cos(2\theta) \right) + \frac{a^2}{r} (1 + (1 + \kappa) \cos(2\theta)) \right. \\ &\quad \left. - \frac{a^4}{r^3} \cos(2\theta) \right), \\ u_\theta &= \frac{t}{4G} \left((1 - \kappa) \frac{a^2}{r} - r - \frac{a^4}{r^3} \right) \sin(2\theta),\end{aligned}\quad (27)$$

which G is the shear modulus and $\kappa = (3 - \nu)/(1 + \nu)$ where ν is the Poissons ratio. In this example, the constant values are $a = 1$, $t = 1$, and $E = 1000$ and $\nu = 0.3$.

For the node moving procedure, initial and refined nodal configurations with 122, 229, and 305 nodes are shown in Figure 7. The nodal points are refined with respect to the

TABLE 2: Error norms in initial nodal configuration and in different steps of multistage node enrichment procedure (Example 1).

Number of nodes	Norm of the error
122	0.6684
182	0.1457
288	0.0571
521	0.0190

proposed error estimator based on the least square residuals functional. In Figure 8(a) numerical results of normal stress σ_x on the left edge is compared with the exact analytical solution. Figures 8(b) and 8(c) compare the convergence curve and the convergence rate of the MDLSM method for the node moving adaptive refinement strategy and plotted using the error norms in Table 1.

Also, the node enrichment adaptive refinement strategy is applied to the MDLSM method for obtaining accurate results. As shown in Figure 9, first the problem domain is discretized by using 122 initial nodal distributions, and then the nodal points are enriched in three steps (182, 288, and 521 nodes) on the region determined by the error indicator. Figure 10(a) compares the numerical results of normal stress σ_x on the left edge with exact analytical solution. The error norms in Table 2 are used for plotting and comparison of the convergence curve and the convergence rate of the node enrichment

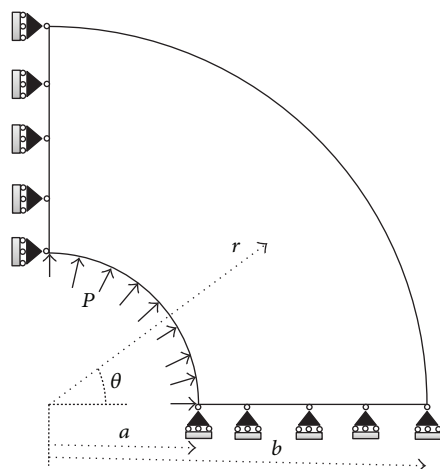


FIGURE 11: A cylinder subjected to an internal pressure and its boundary conditions.

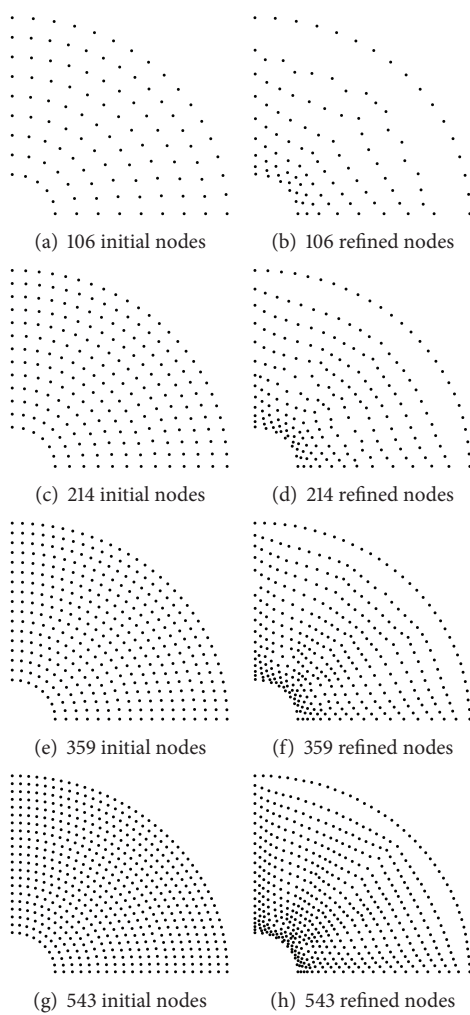


FIGURE 12: Initial and refined (node moving) nodal configurations (Example 2).

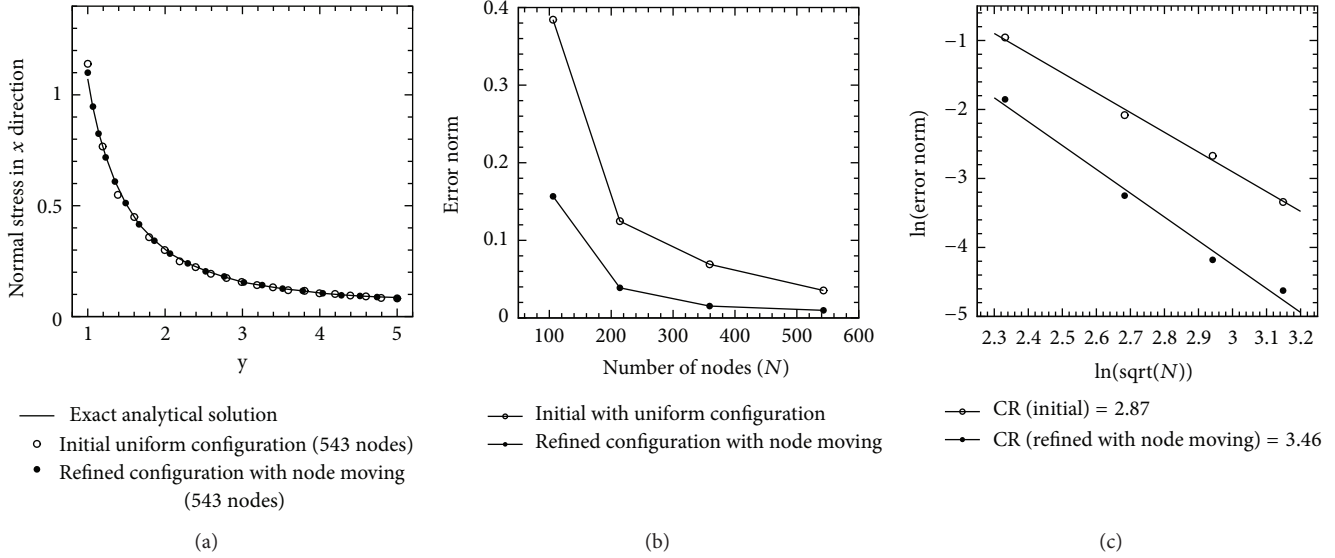


FIGURE 13: (a) Normal stress σ_x at $x = 0$. (b) Convergence curve of node moving procedure. (c) Convergence rate of node moving procedure.

TABLE 3: Comparison of the error norms for initial and refined (using node moving) nodal configurations (Example 2).

Number of nodes	Norm of error for initial nodes	Norm of error for refined nodes
106	0.3843	0.1567
214	0.1247	0.0388
359	0.0691	0.0153
543	0.0354	0.0098

procedure for the MDLSM method (see Figures 12(b) and 12(c)). The results clearly show that the node moving and multistage node enrichment adaptive refinement strategies in the MDLSM method are more efficient compared to the refinement procedures in the DLSM method. Figures 8(b) and 8(c), 10(b), and 10(c) indicate that by using the node moving and the node enrichment adaptive refinement procedures, the convergence rate of the MDLSM method is increased.

Example 2 (a cylinder subjected to an internal pressure). As a second elastostatic benchmark example a cylinder subjected to an internal pressure is considered. Due to the symmetry, only a quarter of the cylinder is modeled; see Figure 11. The boundary conditions are illustrated in Figure 11. The exact analytical solution of this problem is

$$\begin{aligned}\sigma_r &= \frac{a^2 P}{b^2 - a^2} \left(1 - \frac{b^2}{r^2} \right), \\ \sigma_\theta &= \frac{a^2 P}{b^2 - a^2} \left(1 + \frac{b^2}{r^2} \right),\end{aligned}\quad (28)$$

where the constant values are $a = 1$, $b = 5$, $P = 1$, $\nu = 0.3$, and $E = 10^7$. As shown in Figure 12, four types of nodal distributions with 106, 214, 359, and 543 nodes are distributed to solve and refine the nodes in the problem domain.

TABLE 4: Error norms in initial nodal configuration and in different steps of multistage node enrichment procedure (Example 2).

Number of nodes	Norm of the error
106	0.3843
164	0.0808
276	0.0501
491	0.0191

Figure 13(a) compares the normal stress σ_x at $x = 0$ for initial and refined nodal configurations with 543 nodes. It is clear that the result of refined nodal configuration is more similar to the exact analytical solution than initial nodal configuration. Table 3 compares the error norms of the node moving procedure for the initial and refined nodal configurations and Figures 13(b) and 13(c) compare the convergence curve and the convergence rate, respectively.

In Figure 14, the initial and refined nodal distributions for the node enrichment strategy are shown. Figure 15(a) compares the normal stress σ_x at $x = 0$ for initial and last steps refined with 543 nodal distributions. In Table 4 the error norm of the node enrichment refinement procedure is shown. Figures 15(b) and 15(c) compare the convergence curve and the convergence rate of the node enrichment adaptive refinement strategy.

Example 3 (a reservoir fully filled with water). In this example, consider that the wall of a reservoir fully filled with water is

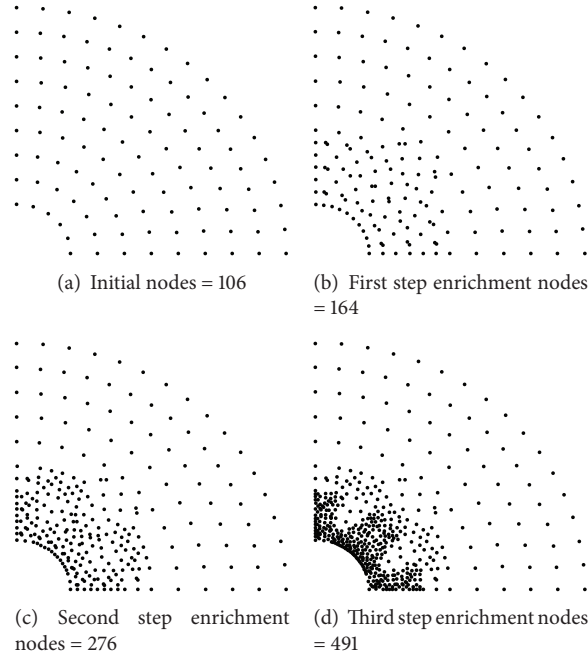


FIGURE 14: Initial and refined (node enrichment) nodal configurations (Example 2).

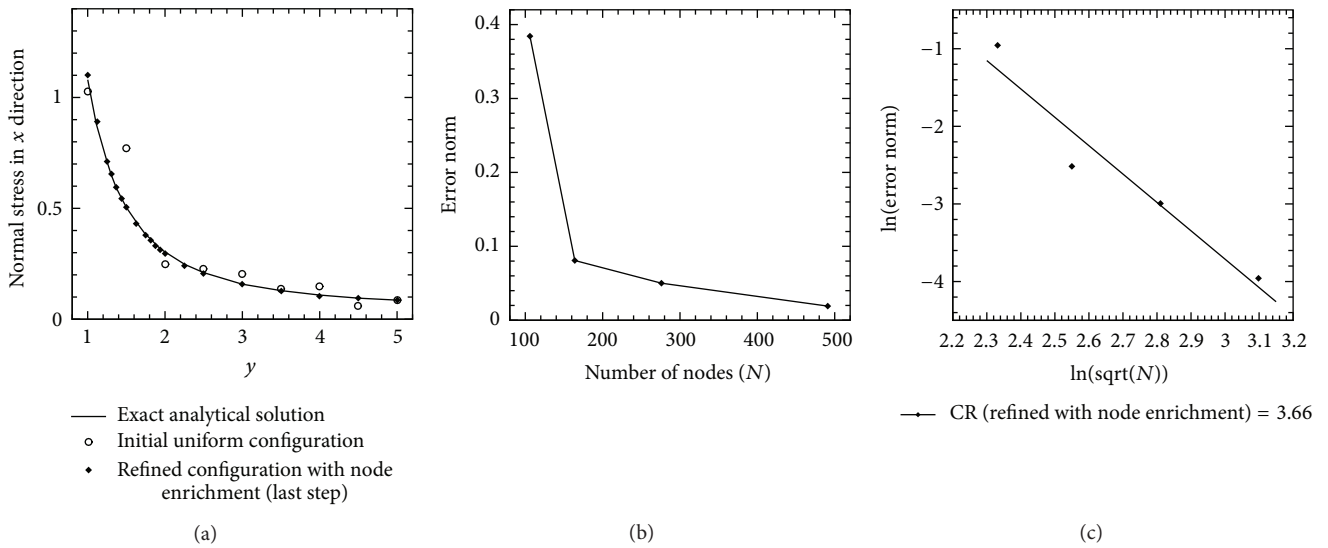


FIGURE 15: (a) Normal stress σ_x at $x = 0$. (b) Convergence curve for node enrichment procedure. (c) Convergence rate for node enrichment procedure.

investigated. The geometry of the wall is irregular as given in Figure 16. The material properties of the wall are given as Young's modulus $E = 10^7$ and Poissons ratio $\nu = 0.3$. The bottom of the wall is fixed and the curved edge of the wall is subjected to a hydrostatic pressure $P = -9800(H - y)$ MPa. Since the analytical solution of this problem is not available, a very fine mesh (with 59,400 linear triangular elements) FEM solution will be considered as our reference solution.

As shown in Figure 17, four types of nodal distribution with 84, 138, 218, and 299 nodes are distributed to solve

and refine the points in the problem domain. Figure 18(a) compares the displacement in y -direction along the vertical edge for initial and refined configurations. Table 5 compares the error norms of the node moving procedures based on MDLSM method and Figures 18(a) and 18(b) compare the convergence curve and convergence rate, respectively. For node enrichment adaptive refinement procedure, the problem domain is discretized with initial 84 points and is refined in three steps near high gradient error norm and is solved with 120, 181, and 284 nodes, respectively (see Figure 19). Figure 20(a) compares the displacement in y -direction

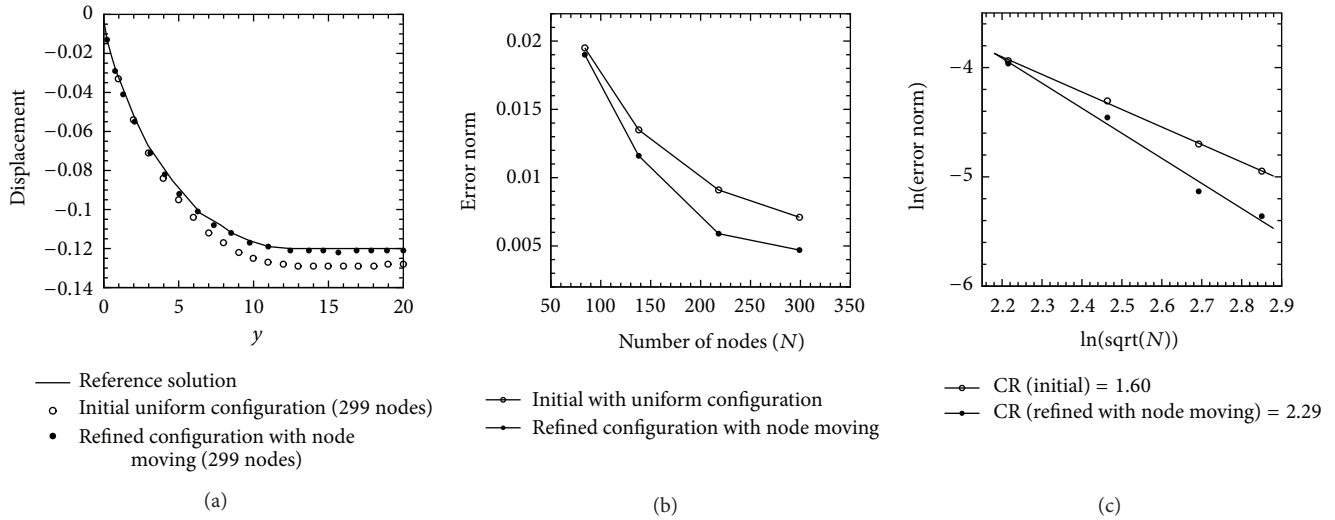


FIGURE 18: (a) Displacement in y -direction along the vertical edge. (b) Convergence curve of node moving procedure. (c) Convergence rate of node moving procedure.

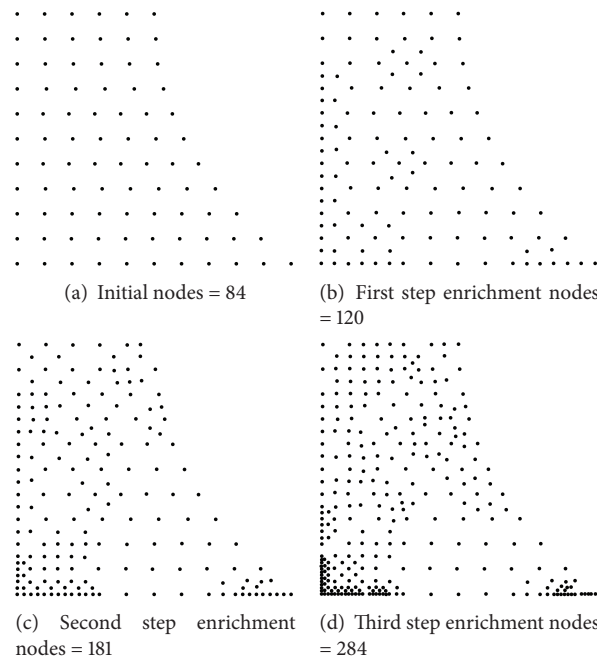


FIGURE 19: Initial and refined (node enrichment) nodal configurations (Example 3).

along the vertical edge for initial and refined configurations. In Table 6 the error norms of the node enrichment refinement procedure is used to plot the convergence curve and convergence rate in Figures 20(b) and 20(c).

5. Conclusion

A mixed discrete least squares meshless method was extended for node moving and node enrichment adaptive refinements for efficient analysis of the planar elasticity problem. For the refinement procedures an error estimator based

on least square residuals functional was formulated and used. Voronoi diagram was extended in the refinement procedures to find the neighbor nodes (node moving) and the position of the new nodes (node enrichment). For the moving node procedure, spring analogy was used to construct a system for computing the new place of each node after the refinement procedure. The efficiency and effectiveness of the proposed node moving and node enrichment adaptive refinement techniques in the MDLSM method by their application to the benchmark examples in the elasticity problems were verified. Results show that the proposed refinement methods are accurate and straightforward.

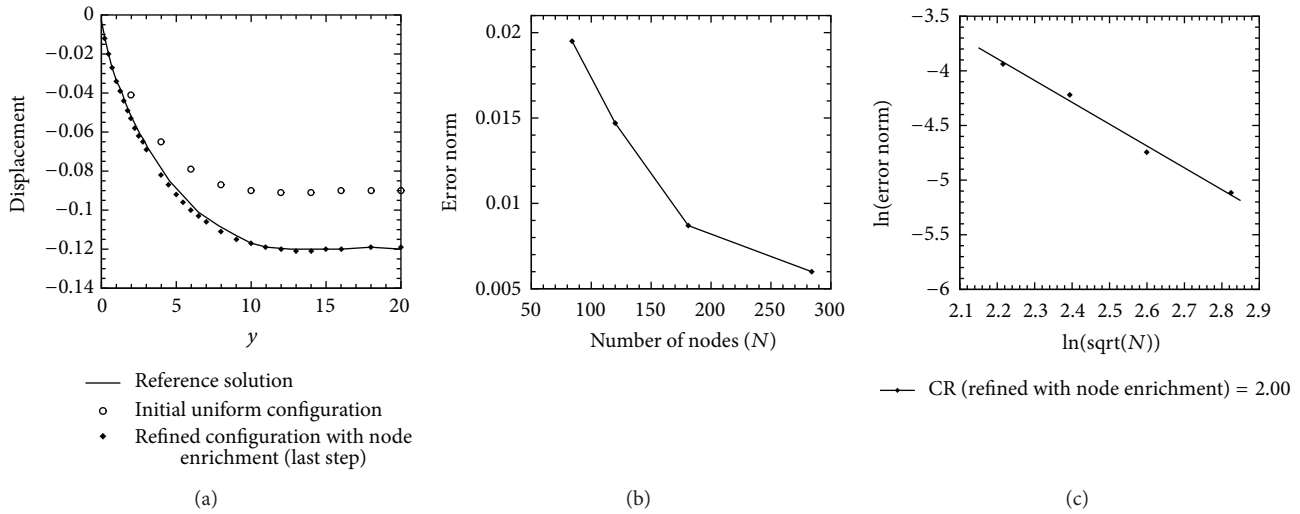


FIGURE 20: (a) Displacement in y -direction along the vertical edge. (b) Convergence curve for node enrichment procedure. (c) Convergence rate for node enrichment procedure.

TABLE 5: Comparison of the error norms for initial and refined (using node moving) nodal configurations (Example 3).

Number of nodes	Norm of error for initial nodes	Norm of error for refined nodes
84	0.0195	0.0190
138	0.0135	0.0116
218	0.0091	0.0059
299	0.0071	0.0047

TABLE 6: Error norms in initial nodal configuration and in different steps of multistage node enrichment procedure (Example 3).

Number of nodes	Norm of the error
84	0.0195
120	0.0147
181	0.0087
284	0.0060

Conflict of Interests

The authors declare that there is no conflict of interest regarding the publication of this paper.

References

- [1] L. F. Richardson, “The approximate arithmetical solution by finite differences of physical problems,” *Transactions of the Royal Society A*, vol. 210, pp. 307–357, 1910.
- [2] O. C. Zienkiewicz, “The background of error estimation and adaptivity in finite element computations,” *Computer Methods in Applied Mechanics and Engineering*, vol. 195, no. 4–6, pp. 207–213, 2006.
- [3] O. C. Zienkiewicz, *The Finite Element Method*, McGraw Hill, London, UK, 1977.
- [4] I. Babuška and A. K. Aziz, “On the angle condition in the finite element method,” *SIAM Journal on Numerical Analysis*, vol. 13, no. 2, pp. 214–226, 1976.
- [5] R. A. Gingold and J. J. Monaghan, “Smoothed particle hydrodynamics: theory and applications to non-spherical stars,” *Monthly Notices of the Royal Astronomical Society*, vol. 181, pp. 375–389, 1977.
- [6] B. Nayroles, G. Touzot, and P. Villon, “Generalizing the finite element method: diffuse approximation and diffuse elements,” *Computational Mechanics*, vol. 10, no. 5, pp. 307–318, 1992.
- [7] T. Belytschko, Y. Y. Lu, and L. Gu, “Element-free Galerkin methods,” *International Journal for Numerical Methods in Engineering*, vol. 37, no. 2, pp. 229–256, 1994.
- [8] W. K. Liu, S. Jun, and Y. F. Zhang, “Reproducing kernel particle methods,” *International Journal for Numerical Methods in Fluids*, vol. 20, no. 8–9, pp. 1081–1106, 1995.
- [9] E. Oñate, S. Idelsohn, O. C. Zienkiewicz, and R. L. Taylor, “A finite point method in computational mechanics. Applications to convective transport and fluid flow,” *International Journal for Numerical Methods in Engineering*, vol. 39, no. 22, pp. 3839–3866, 1996.
- [10] S. N. Atluri and T. Zhu, “A new Meshless Local Petrov-Galerkin (MLPG) approach in computational mechanics,” *Computational Mechanics*, vol. 22, no. 2, pp. 117–127, 1998.
- [11] S. N. Atluri and T. Zhu, “A new meshless local Petrov-Galerkin (MLPG) approach in computational mechanics,” *Computational Mechanics*, vol. 22, no. 2, pp. 117–127, 1998.
- [12] T. Zhu, J.-D. Zhang, and S. N. Atluri, “A local boundary integral equation (LBIE) method in computational mechanics, and a meshless discretization approach,” *Computational Mechanics*, vol. 21, no. 3, pp. 223–235, 1998.
- [13] N. R. Aluru and L. Gang, “Finite cloud method: a true meshless technique based on a fixed reproducing kernel approximation,”

- Journal for Numerical Methods in Engineering*, vol. 50, pp. 2373–2410, 2001.
- [14] H. Arzani and M. H. Afshar, “Solving Poisson’s equations by the discrete least square meshless method,” in *Boundary Elements and Other Mesh Reduction Methods XXVIII*, vol. 42 of *WIT Transactions on Modelling and Simulation*, pp. 23–32, WIT Press, Southampton, UK, 2006.
- [15] T. Rabczuk and T. Belytschko, “An adaptive continuum/discrete crack approach for mesh-free particle methods,” *Latin American Journal of Solids and Structures*, vol. 1, pp. 141–166, 2003.
- [16] T. Rabczuk and T. Belytschko, “Adaptivity for structured mesh-free particle methods in 2D and 3D,” *International Journal for Numerical Methods in Engineering*, vol. 63, no. 11, pp. 1559–1582, 2005.
- [17] Y.-C. Yoon, S.-H. Lee, and T. Belytschko, “Enriched meshfree collocation method with diffuse derivatives for elastic fracture,” *Computers & Mathematics with Applications*, vol. 51, no. 8, pp. 1349–1366, 2006.
- [18] G. Zi, T. Rabczuk, and W. Wall, “Extended meshfree methods without branch enrichment for cohesive cracks,” *Computational Mechanics*, vol. 40, pp. 367–382, 2007.
- [19] S. Bordas, G. Zi, and T. Rabczuk, “Three-dimensional non-linear fracture mechanics by en-riched meshfree methods without asymptotic enrichment,” *Solid Mechanics and Its Applications*, vol. 5, pp. 21–36, 2007.
- [20] T. Rabczuk and E. Samaniego, “Discontinuous modelling of shear bands using adaptive meshfree methods,” *Computer Methods in Applied Mechanics and Engineering*, vol. 197, no. 6–8, pp. 641–658, 2008.
- [21] X. Zhuang and C. Augarde, “Aspects of the use of orthogonal basis functions in the element-free Galerkin method,” *International Journal for Numerical Methods in Engineering*, vol. 81, no. 3, pp. 366–380, 2010.
- [22] X. Zhuang, C. Heaney, and C. Augarde, “On error control in the element-free Galerkin method,” *Engineering Analysis with Boundary Elements*, vol. 36, no. 3, pp. 351–360, 2012.
- [23] X. Zhuang, H. Zhu, and C. Augarde, “An improved meshless Shepard and least square method possessing the delta property and requiring no singular weight function,” *Computational Mechanics*, vol. 53, no. 2, pp. 343–357, 2014.
- [24] M. H. Afshar, M. Naisipour, and J. Amani, “Node moving adaptive refinement strategy for planar elasticity problems using discrete least squares meshless method,” *Finite Elements in Analysis and Design*, vol. 47, no. 12, pp. 1315–1325, 2011.
- [25] M. H. Afshar, J. Amani, and M. Naisipour, “A node enrichment adaptive refinement in discrete least squares meshless method for solution of elasticity problems,” *Engineering Analysis with Boundary Elements*, vol. 36, no. 3, pp. 385–393, 2012.
- [26] A. R. Firoozjaee and M. H. Afshar, “Error estimate and adaptive refinement for incompressible Navier-Stokes equations using the discrete least squares meshless method,” *International Journal for Numerical Methods in Fluids*, vol. 70, no. 1, pp. 56–70, 2012.
- [27] F. Brezzi and M. Fortin, *Mixed and Hybrid Finite Element Methods*, vol. 15 of *Springer Series in Computational Mathematics*, Springer, New York, NY, USA, 1991.
- [28] F. Brezzi and K.-J. Bathe, “A discourse on the stability conditions for mixed finite element formulations,” *Computer Methods in Applied Mechanics and Engineering*, vol. 82, no. 1–3, pp. 27–57, 1990.
- [29] K.-J. Bathe, “The inf-sup condition and its evaluation for mixed finite element methods,” *Computers & Structures*, vol. 79, no. 2, pp. 243–252, 2001.
- [30] F. Brezzi, “On the existence, uniqueness and approximation of saddle-point problems arising from Lagrangian multipliers,” *Revue Française d’Automatique, Informatique, Recherche Opérationnelle. Analyse Numérique*, vol. 8, no. R-2, pp. 129–151, 1974.
- [31] Z. Cai, R. Lazarov, T. A. Manteuffel, and S. F. McCormick, “First-order system least squares for second-order partial differential equations. I,” *SIAM Journal on Numerical Analysis*, vol. 31, no. 6, pp. 1785–1799, 1994.
- [32] X. Ye, “Domain decomposition for a least-square finite element method for second order elliptic problem,” *Applied Mathematics and Computation*, vol. 91, no. 2–3, pp. 233–242, 1998.
- [33] J. Amani, M. H. Afshar, and M. Naisipour, “Mixed discrete least squares meshless method for planar elasticity problems using regular and irregular nodal distributions,” *Engineering Analysis with Boundary Elements*, vol. 36, no. 5, pp. 894–902, 2012.
- [34] I. Babuska and W. C. Rheinboldt, “A posteriori error estimates for the finite element method,” *International Journal for Numerical Methods in Engineering*, vol. 12, pp. 1597–1615, 1978.
- [35] O. C. Zienkiewicz, B. Boroomand, and J. Z. Zhu, “Recovery procedures in error estimation and adaptivity. I. Adaptivity in linear problems,” *Computer Methods in Applied Mechanics and Engineering*, vol. 176, no. 1–4, pp. 111–125, 1999.
- [36] Q. Du and D. Wang, “Tetrahedral mesh generation and optimization based on centroidal Voronoi tessellations,” *International Journal for Numerical Methods in Engineering*, vol. 56, no. 9, pp. 1355–1373, 2003.
- [37] S. Timoshenko and J. N. Goodier, *Theory of Elasticity*, McGraw-Hill Book, New York, 2nd edition, 1951.

Research Article

A Meshless Local Petrov-Galerkin Shepard and Least-Squares Method Based on Duo Nodal Supports

Xiaoying Zhuang and Yongchang Cai

National Key Laboratory of Disaster Reduction and Protection, Department of Geotechnical Engineering, Tongji University, Shanghai 200092, China

Correspondence should be addressed to Yongchang Cai; yccai@tongji.edu.cn

Received 28 September 2013; Accepted 14 October 2013; Published 23 January 2014

Academic Editor: Timon Rabczuk

Copyright © 2014 X. Zhuang and Y. Cai. This is an open access article distributed under the Creative Commons Attribution License, which permits unrestricted use, distribution, and reproduction in any medium, provided the original work is properly cited.

The meshless Shepard and least-squares (MSLS) interpolation is a newly developed partition of unity- (PU-) based method which removes the difficulties with many other meshless methods such as the lack of the Kronecker delta property. The MSLS interpolation is efficient to compute and retain compatibility for any basis function used. In this paper, we extend the MSLS interpolation to the local Petrov-Galerkin weak form and adopt the duo nodal support domain. In the new formulation, there is no need for employing singular weight functions as is required in the original MSLS and also no need for background mesh for integration. Numerical examples demonstrate the effectiveness and robustness of the present method.

1. Introduction

Meshless methods have prospered both in theory and application in engineering problems in the past two decades as they offer the possibility of a discretised approach without the occurrence of mesh entanglement requiring remeshing. A wide range of meshless methods have been proposed as outlined in recent surveys [1–3]. Remarkable successes have been reported in applying these methods for analyzing challenging engineering problems, namely, fracture modeling [4–7], plate and shell analysis [8–15], three-dimensional problems [16–18], fluid structure interaction analysis [19], strain localization problems [20], large deformation problems [21], and other applications [22–29].

Some currently popular meshless approximations are the moving least-squares (MLS) approximation, Shepard shape functions, partition of unity (PU), radial basis functions (RBF), reproducing kernel particle method (RKPM), point interpolation (PI), and Kriging interpolation (KI). Among them, the MLS approximation [30] is one of the most widely used approximations at present due to its global continuity, completeness, and robustness. However, the MLS approximation suffers from a number of problems that practically

limit its application, namely, the high computational cost in obtaining the shape functions and their derivatives, difficulty in retaining accuracy with respect to nodal arrangement, and also the difficulty with which essential boundary conditions can be imposed due to the lack of the Kronecker delta property. Efforts have been made to address these problems by various means. Breitkopf et al. [31] developed the analytical forms for computing shape functions and diffuse derivatives of shape functions by assuming that some terms are constant and complete derivatives of shape functions. However, these formulations are dependent on the number of nodes and the formulation grows unwieldy when there are a large number of nodes in the support domain. Orthogonal basis functions pertaining to MLS for efficient and accurate computation of shape functions are investigated in [32, 33]. Singular weight functions are introduced by Kaljević and Saigal [34] to produce an interpolatory MLS approximation for the direct imposition of essential boundary conditions. Chen and Wang [35] developed a matrix transformation method for the imposition of boundary conditions; however, the formulation is complicated for implementation. The Shepard and least square (MSLS) interpolation developed by the authors [36] satisfactorily keeps the consistency of the Shepard shape

functions up to the order of basis function and satisfies the delta property. However, singular weight functions have to be used to enforce the interpolating property of shape functions, which results in the loss of the smoothness of the interpolation as well as local oscillation. To eliminate this problem, an improved MSLS interpolation possessing the delta property without using singular weight functions as PU was proposed in [37].

Apart from the interpolation, the integration scheme of the weak form is also an important factor affecting the solution accuracy, which has been the problem for many meshless methods. Background cells have usually been used to integrate the weak form as has been the case with the EFGM, RKPM, and PIM [38]. Due to the complexity of the shape functions, a large number of integration points are needed to avoid the underestimation of the weak form, which is computationally expensive but still not adequate to give accurate solutions. Furthermore when an irregular nodal arrangement is used, the background mesh has to be refined where nodes are densely distributed [39]. To remove this difficulty, the nodal integration scheme which is free from the background cell was proposed in [40] and later used in [41, 42]. However, the performance of this scheme is unstable and also reduces the accuracy of the results. The MLPG-type meshless methods well solved this problem in a natural way by partitioning the local domain into a number of subdomains that may or may not overlap. In this way, integration of high order accuracy can be obtained for the global stiffness matrix [43] without background mesh. A similar but conceptually different approach was developed in [44] using the partition of unity quadrature scheme. However, the algorithms are complicated and more computationally demanding compared to the classical quadrature on subcells. Although many different approaches have been carried out for the weak form integration, finding a simple, efficient, and accurate integration scheme for meshless methods remains an open question. In this paper, the local weak form along with numerical integration over local subdomains is used to derive the discrete equations.

The content of the paper is outlined as follows. In Section 2, formulation of the improved MSLS interpolation is described in detail including the local approximation and support domain with dual definitions. The Kronecker delta property of the interpolation is also proved. In the Section 3, the discretised formulation of the present interpolation is derived using the local Petrov-Galerkin weak form. It is followed by numerical tests demonstrating the convergence characteristic and accuracy of the present interpolation in Section 4. Discussions are given at the end highlighting the features of the present method and suggestions on further studies.

2. Formulation of the MSLS Based on Duo Nodal Supports

In this section, the MSLS based on duo nodal supports is described in detail. We start the description of the formulation using a 2D problem domain of arbitrary shape as

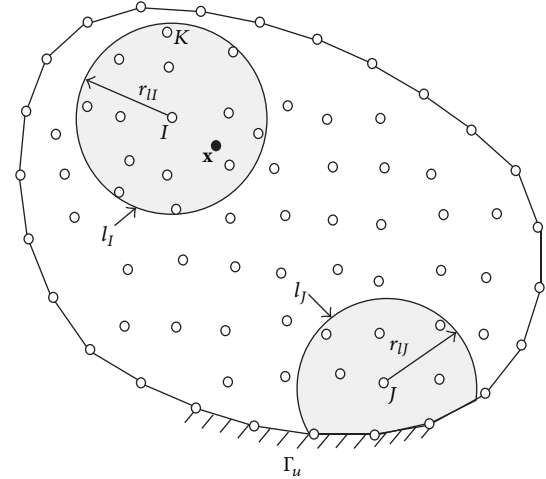


FIGURE 1: The setting of the nodal subdomains in Ω .

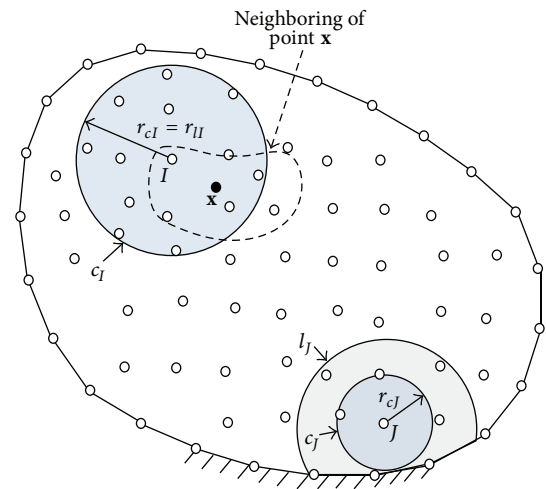


FIGURE 2: Duo support domain of node.

shown in Figure 1. The formulation is described in the context of elastostatics, with the fundamental field variable being a displacement. For an arbitrary node I , its displacement vector in 2D is $\mathbf{u}_I = (u_I, v_I)^T$, where u_I and v_I are the nodal displacements in the x and y directions, respectively (the following formulation is derived only for u_i in the x direction but an identical process can be used for v_i in the y direction). The interpolation at an arbitrary point \mathbf{x} inside the domain in the x direction is expressed as

$$u(\mathbf{x}) = \sum_{I=1}^n \varphi_I^0(\mathbf{x}) u^I(\mathbf{x}), \quad (1)$$

where $\{\varphi_I^0(\mathbf{x}), I = 1, \dots, n\}$ is a set of shape functions that forms a partition of unity (PU); that is, $\sum_{I=1}^n \varphi_I^0(\mathbf{x}) \equiv 1$, I is the node index, and n is the number of the nodes whose supports c_I include point \mathbf{x} as shown in Figure 2. $u^I(\mathbf{x})$ here is not the nodal displacement in the FEM or the ‘‘fictitious’’

nodal values in the EFGM but the local approximation of node I at \mathbf{x} where the superscript l indicates local. Shepard shape functions used as PU are given by

$$\phi_I^0(\mathbf{x}) = \frac{w_I(\mathbf{x})}{\sum_{j=1}^n w_j(\mathbf{x})}, \quad (2)$$

which is the same as in the original MSLS. The construction of the MSLS interpolation takes the following steps: firstly, construct the local approximation at each node and secondly apply the PU approximation to the local approximation to get the interpolation. The definition of the nodal support domain will be given in detail and the local approximations at a node will be described.

2.1. Local Approximation at a Node. The local approximation $u^{II}(\mathbf{x})$ at an arbitrary node I is given by

$$u^{II}(\mathbf{x}) = \sum_{j=1}^M \bar{\psi}_j^I(\mathbf{x}) u_j, \quad (3)$$

where u_j is the nodal displacement for the J th node in support of node I , M is the total number of nodes in the local cover l_I of node I as shown in Figure 1, and $\bar{\psi}_j^I(\mathbf{x})$ is the modified least square shape function given by

$$\begin{aligned} \bar{\psi}_j^I(\mathbf{x}) &= \psi_j^I(\mathbf{x}) - \psi_j^I(\mathbf{x}_I), \quad \text{for } J \neq I, \\ \bar{\psi}_j^I(\mathbf{x}) &= \psi_j^I(\mathbf{x}) - \psi_j^I(\mathbf{x}_I) + 1, \quad \text{for } J = I, \end{aligned} \quad (4)$$

where $\psi_j^I(\mathbf{x})$ are the modified least square shape functions of node J and are determined by the following equations:

$$\psi^I(\mathbf{x}) = [\psi_1^I(\mathbf{x}) \ \psi_2^I(\mathbf{x}) \ \cdots \ \psi_M^I(\mathbf{x})] = \mathbf{P}^T(\mathbf{x}) \mathbf{A}^{-1} \mathbf{B}, \quad (5)$$

$\mathbf{p}(\mathbf{x}) = [p_1(\mathbf{x}), p_2(\mathbf{x}), \dots, p_m(\mathbf{x})]^T$ is a polynomial basis, and m is the number of monomials in the basis. In the development of the MSLS interpolation, we use a bilinear basis throughout in 2D such that $\mathbf{p}^T(\mathbf{x}) = [1, x, y, xy]$, and

$$\begin{aligned} \mathbf{B} = \mathbf{P}^T &= \begin{bmatrix} 1 & 1 & \cdots & 1 \\ x_1 & x_2 & \cdots & x_M \\ y_1 & y_2 & \cdots & y_M \\ x_1 y_1 & x_2 y_2 & \cdots & x_M y_M \end{bmatrix}, \\ \mathbf{A} &= \mathbf{P}^T \cdot \mathbf{P}. \end{aligned} \quad (6)$$

It can be seen from (4) that $\bar{\psi}_I^I(\mathbf{x}_I) = 1$, $\bar{\psi}_j^I(\mathbf{x}_I) = 0$ ($J \neq I$) for $\mathbf{x} = \mathbf{x}_I$ and $\sum_{j=1}^M \bar{\psi}_j^I(\mathbf{x}) = 1$. Thus

$$u^{II}(\mathbf{x}_I) = u_I. \quad (7)$$

It has been proved in [36, 37] that a singular weight function used as $w_i(\mathbf{x})$ will enforce the interpolation, the equivalent equation (1) here, satisfying the delta property. A similar approach has been used by [45] to produce interpolatory MLS approximation. However, the use of singular weight function will bring some other problems such as the loss of smoothness of interpolation.

2.2. Duo Support Domain of a Node. The support domain of a node is the area where a node exerts influence on the field variable. In this paper it is defined as a circle centered on that node although it may take other shapes such as a rectangle. Here, two support domains are defined at each node, one is used in the construction of local approximation and the other in the PU approximation. In Figure 2, for example, node I has two support domains associated with it, namely, l_I with radius r_{II} and c_I with radius r_{cI} . If a node, for example, node K in Figure 1 falls inside l_I , then node K will be used in constructing the local approximation at node I . Similarly, if a point, point \mathbf{x} in Figure 2, for example, is contained in c_I , then the local approximation $u^{II}(\mathbf{x})$ will contribute to the PU approximation at \mathbf{x} . For an arbitrary node, for example, node I in Figure 1, the size of l_I is defined by

$$r_{II} = a \cdot b \cdot d_I, \quad (8)$$

where a is a scale factor that ranges between 1.0 and 2.0, b is a coefficient such that $b = 2$ for a node lying on the boundary and $b = 1$ for all other nodes, and d_I is the distance between I and the fifth nearest neighbor node to I . If there is a predefined triangular background mesh, d_I can be defined as the maximum distance between I and the nodes of triangles which are connected to the node I .

For a node having its local support domain completely inside the domain, for example, the subdomain l_I of node I in Figure 2, the size of c_I is the same as l_I :

$$r_{cI} = r_{II}. \quad (9)$$

For a node having its local support domain close to or intersecting the boundary, for example, node J shown in Figure 2, the definition of subdomain follows these steps. Firstly, find the nearest boundary node to J among the neighbor nodes which have been used as nodes in defining l_J , and secondly calculate the distance between the nearest boundary node and J , denoted as d_J , and then the size of c_J is set by

$$r_{cJ} = 0.99d_J. \quad (10)$$

If there is an interior node where prescribed values needed to be applied, the procedure described above for setting the support domain of near boundary nodes can be repeated to that node using (10) by assigning this interior node as a boundary node. If we want all nodes to take nodal values at the nodes, the size of the d_J can be taken as the distance between the J and its nearest node for every node J . The following quadratic spline function is used as the weight function over support domain in (2):

$$w_I(\mathbf{x}) = \begin{cases} 1 - 6\left(\frac{r_I}{r_{cI}}\right)^2 + 8\left(\frac{r_I}{r_{cI}}\right)^3 - 3\left(\frac{r_I}{r_{cI}}\right)^4, & r_I \leq r_{cI} \\ 0 & r_I > r_{cI}, \end{cases} \quad (11)$$

where $r_I = \|\mathbf{x} - \mathbf{x}_I\|$ is the distance between the point \mathbf{x} and node I and \mathbf{x}_I is the coordinate of node I . The aim of separately defining local domain and support domain is

to produce MSLS interpolations having the delta property without using a singular weight, so that the difficulties associated with the use of singular weight function can be removed. Indeed this aim is achieved here if the domain for local approximation and domain for PU are defined by the method described above as will be proved later in Section 2.3.

2.3. Delta Property at a Node. Consider a boundary node K to be applied with boundary conditions. If the support domain of the nodes is set according to (9) and (10), then the K will be the only node contained in c_K . Thus the MSLS interpolation equation (1) at \mathbf{x}_K becomes

$$u^h(\mathbf{x}_K) = \sum_{I=1}^n \varphi_I^0(\mathbf{x}_K) u^{II}(\mathbf{x}_K) = \varphi_K^0(\mathbf{x}_K) u^{IK}(\mathbf{x}_K). \quad (12)$$

As there is only one node in the PU, then (2) becomes

$$\varphi_K^0(\mathbf{x}_K) = \frac{w_K(\mathbf{x}_K)}{\sum_{J=1}^n w_J(\mathbf{x}_K)} = \frac{w_K(\mathbf{x}_K)}{w_K(\mathbf{x}_K)} = 1. \quad (13)$$

It is known by (7) that the local approximation $\mathbf{u}^{IK}(\mathbf{x}_K)$ at node K satisfies

$$u^{IK}(\mathbf{x}_K) = u_K. \quad (14)$$

Substituting (13) and (14) into (12) gives

$$u^h(\mathbf{x}_K) = u^{IK}(\mathbf{x}_K) = u_K. \quad (15)$$

Hence, the present MSLS interpolation takes nodal value at boundary nodes and the essential boundary conditions or point load conditions can be directly imposed as in the FEM. Also, the present interpolation preserves the consistency up to the order of the basis function, which is a necessary requirement of accuracy. The proof is the same as has been presented in [36, 37].

3. The Local Petrov-Galerkin Weak Form

Let R be the total number of nodes associated with the given point \mathbf{x} ; then (3) can be rewritten as

$$\begin{aligned} \mathbf{u}(\mathbf{x}) &= \begin{Bmatrix} \varphi_1^0 \\ \varphi_2^0 \\ \vdots \\ \varphi_n^0 \end{Bmatrix}^T \begin{bmatrix} \bar{\psi}_1^1 & \cdots & \bar{\psi}_n^1 & \bar{\psi}_{n+1}^1 & \cdots & \bar{\psi}_R^1 \\ \bar{\psi}_1^2 & \cdots & \bar{\psi}_n^2 & \bar{\psi}_{n+1}^2 & \cdots & \bar{\psi}_R^2 \\ \vdots & \cdots & \vdots & \vdots & \cdots & \vdots \\ \bar{\psi}_1^n & \cdots & \bar{\psi}_n^n & \bar{\psi}_{n+1}^n & \cdots & \bar{\psi}_R^n \end{bmatrix} \begin{Bmatrix} u_1 \\ u_2 \\ \vdots \\ u_R \end{Bmatrix} \\ &= \Phi_{1 \times n}^0 \bar{\Psi}_{n \times R} \mathbf{u}_{R \times 1} = \sum_{k=1}^R \bar{N}_k(\mathbf{x}) u_k, \end{aligned} \quad (16)$$

where Φ^0 is the vector of Shepard shape function, $\bar{\Psi}$ is a matrix comprising the modified least square point interpolation (LSPI) shape functions, and $\bar{N}_k(\mathbf{x})$ is the MSLS shape function.

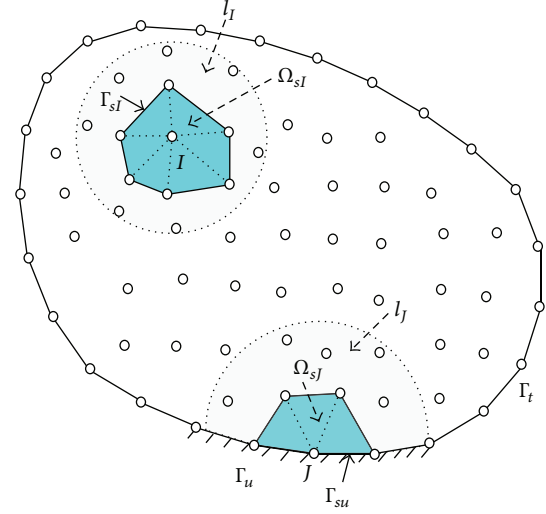


FIGURE 3: The local integration domains.

For domain Ω bounded by Γ (Figure 3), the equilibrium equations and boundary conditions of linear elasticity are given by

$$\begin{aligned} \sigma_{IJ,J} + b_I &= 0 \quad \text{in } \Omega, \\ u_I &= \bar{u}_I \quad \text{at } \Gamma_u, \\ \sigma_{IJ} n_J &= \bar{t}_I \quad \text{at } \Gamma_t, \end{aligned} \quad (17)$$

where σ_{IJ} is the stress tensor, b_I are the body forces, n_J are the unit normal to the domain, and Γ_u and Γ_t are the global boundaries with prescribed displacements and tractions, respectively. Similar to [36], the local polygonal subdomains are constructed for the purpose of simplifying the integration and the discrete equations. For example, based on Delaunay algorithm, a local polygon Ω_{sI} is constructed by using the M nodes in local cover l_I , as shown in Figure 3. A generalized local weak form of the equilibrium equation in (17) is written as

$$\int_{\Omega_{sI}} v_I (\sigma_{IJ,J} + b_I) d\Omega = 0, \quad (18)$$

where Ω_{sI} is the integration domain or subdomain for node I and v_I is the test function. Using the divergence theorem in (18), we obtain the following local weak form:

$$\int_{\partial\Omega_{sI}} v_I \sigma_{IJ} n_J d\Gamma - \int_{\Omega_{sI}} (v_{I,I} \sigma_{IJ} - v_I b_I) d\Omega = 0, \quad (19)$$

where n_J is the outward unit normal to the boundary $\partial\Omega_{sI}$. The boundary $\partial\Omega_{sI}$ for the subdomain Ω_{sI} is usually composed of three parts: the internal boundary Γ_{sl} , the boundary Γ_{su} , and Γ_{st} , over which the essential and natural

boundary conditions are specified. Substituting $\sigma_{IJ}n_J = \bar{t}_I$ in (19), the following is obtained:

$$\int_{\Gamma_{sl}} v_I t_I d\Gamma + \int_{\Gamma_{su}} v_I t_I d\Gamma + \int_{\Gamma_{st}} v_I \bar{t}_I d\Gamma - \int_{\Omega_{sl}} (v_{I,J} \sigma_{IJ} - v_I b_I) d\Omega = 0. \quad (20)$$

In order to simplify (20), we can deliberately select the three-node triangular FEM shape functions N_I , which correspond to the node I of the triangles constructing the polygonal subdomain Ω_{sl} , as test functions v_I , such that they vanish over Γ_{sl} . Substituting shape functions N_I for v_I in (20), we obtain the following local weak form:

$$\int_{\Gamma_{su}} N_I t_I d\Gamma + \int_{\Gamma_{st}} N_I \bar{t}_I d\Gamma - \int_{\Omega_{sl}} (N_{I,J} \sigma_{IJ} - N_I b_I) d\Omega = 0. \quad (21)$$

For a local polygonal subdomain Ω_{sl} located entirely in the global domain Ω , there is no intersection between $\partial\Omega_{sl}$ and the global boundary Γ , and the integrals over Γ_{su} and Γ_{st} in (21) vanish. For a local polygonal subdomain Ω_{sl} near the boundary, the first item of (21) can also be omitted because of the properties of the test functions N_I . Substituting the MSLS approximation in (21) into the above equation leads to the following discretised system of linear equations:

$$\left(\int_{\Omega_{sl}} \mathbf{v}_I^T \mathbf{D} \mathbf{B} d\Omega \right) \cdot \mathbf{U} = \int_{\Gamma_{sl}} N_I \bar{\mathbf{t}} d\Gamma + \int_{\Omega_{sl}} N_I \mathbf{b} d\Omega \quad (22)$$

denoted as

$$\mathbf{K} \mathbf{U} = \mathbf{F}, \quad (23)$$

where \mathbf{D} is the elasticity matrix:

$$\mathbf{v}_I = \begin{bmatrix} N_{I,x} & 0 \\ 0 & N_{I,y} \\ N_{I,y} & N_{I,x} \end{bmatrix}, \quad (24)$$

$$\mathbf{N}_I = \begin{bmatrix} N_I & 0 \\ 0 & N_I \end{bmatrix}, \quad (25)$$

$$\mathbf{B} = \begin{bmatrix} \bar{N}_{1,x} & 0 & \cdots & \bar{N}_{R,x} & 0 \\ 0 & \bar{N}_{1,y} & \cdots & 0 & \bar{N}_{R,y} \\ \bar{N}_{1,y} & \bar{N}_{1,x} & \cdots & \bar{N}_{R,y} & \bar{N}_{R,x} \end{bmatrix}, \quad (26)$$

$$\mathbf{U} = \{u_1 \ v_1 \ \cdots \ u_R \ v_R\}. \quad (27)$$

Equation (23) can be individually integrated over each triangle constructing the local subdomain Ω_{sl} , as shown in Figure 3. In the present work, seven Gaussian points are used in each triangle.

4. Numerical Examples

The proposed MSLSM interpolation has been coded in C++. In this section, we show the performance of the present

interpolation on a range of test problems. The results are compared with the exact solutions, the MLPG solutions, and the linear FEM solutions. The weight functions used in the MLPG for testing purpose are the Gaussian type weight functions given by

$$w_I^c(\mathbf{x}) = \begin{cases} \frac{e^{-(r_I/c_I)^2} - e^{-(r_{II}/c_I)^2}}{1 - e^{-(r_{II}/c_I)^2}}, & \text{if } r_I \leq r_{II} \\ 0, & \text{if } r_I > r_{II}, \end{cases} \quad (28)$$

where r_{II} is defined by (8) and $c_I = 0.3r_{II}$ is used for all test examples. The scale factor a in (8) is set to be 1.5 and the linear bases are used in MLPG and MSLSM. To study the convergence behavior we define the following error norms in displacement and energy, respectively:

$$\|\mathbf{u}\| = \left(\int_{\Omega} \mathbf{u}^T \cdot \mathbf{u} d\Omega \right)^{1/2}, \quad (29)$$

where \mathbf{u} is a vector collecting nodal displacement results $\mathbf{u} = \{u_1, v_1, u_2, v_2, \dots, u_n, v_n\}^T$ and

$$\|\boldsymbol{\varepsilon}\| = \left(\frac{1}{2} \int_{\Omega} \boldsymbol{\varepsilon}^T \cdot \boldsymbol{\sigma} d\Omega \right)^{1/2}, \quad (30)$$

where $\boldsymbol{\varepsilon}$ is the infinitesimal strain tensor and $\boldsymbol{\sigma}$ is the Cauchy stress tensor. The relative displacement error and energy error are calculated by

$$r_u = \frac{\|\mathbf{u}^{\text{num}} - \mathbf{u}^{\text{exact}}\|}{\|\mathbf{u}^{\text{exact}}\|}, \quad (31)$$

$$r_e = \frac{\|\boldsymbol{\varepsilon}^{\text{num}} - \boldsymbol{\varepsilon}^{\text{exact}}\|}{\|\boldsymbol{\varepsilon}^{\text{exact}}\|},$$

where the superscripts num and exact refer to numerical solutions and exact (or reference) solutions, respectively.

4.1. A Constant Strain Patch Test. A constant strain patch test [46] using three distributions of 7, 28, and 126 irregular nodes is shown in Figure 4. Young's modulus and Poisson's ratio of the material are 1000 and 0.25, respectively. The thickness of the plate is taken as a unit following plane stress assumption. Since the exact solution is linear, a linear basis for the MSLS interpolation is able to represent this solution. The computational results in Table 1 show that the present MSLSM passes the patch tests exactly up to the double precision of the computer.

4.2. A Cantilever Beam. A cantilever beam problem with dimensions of $l = 8$ m and $d = 1$ m, as shown in Figure 5, is tested first. The beam is subjected to parabolically distributed downward traction equivalent to a unit load p at the right-hand end and is constrained at the left-hand end as shown in Figure 5. The elastic material properties used are $E = 1 \times 10^5$ Pa and $\nu = 0.25$, and the problem is solved under a plane strain assumption. We refer to the analytical solution of the problem given in [47]. The convergence of the present

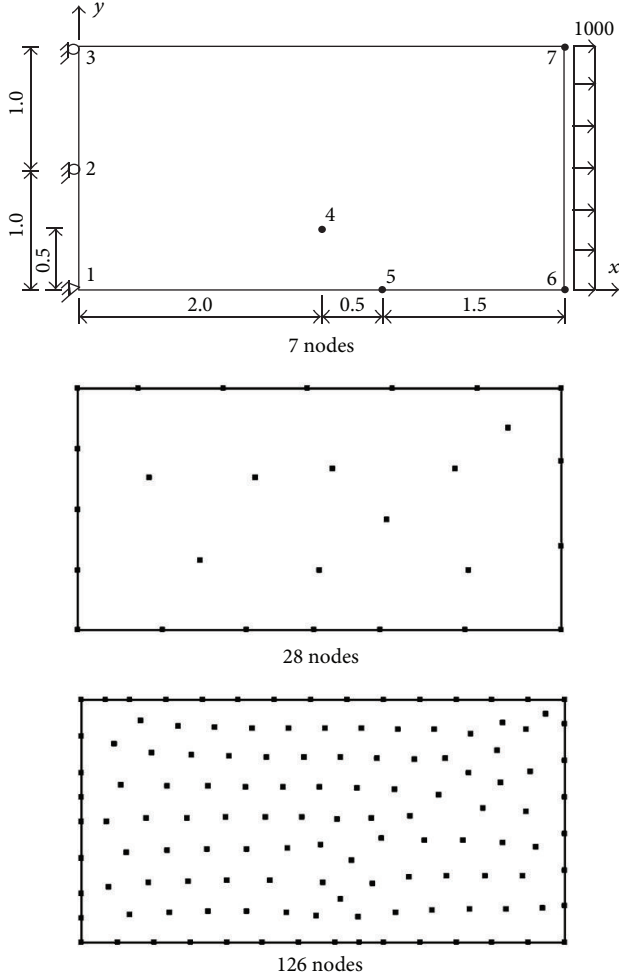


FIGURE 4: Nodal arrangements for the constant strain patch tests.

TABLE I: Results of the constant strain patch test.

Number of nodes	u_4	v_4	u_5	v_5	u_7	v_7
7	2.0	-0.125	2.5	0.0	4.0	-0.5
28	2.0	-0.125	2.5	0.0	4.0	-0.5
126	2.0	-0.125	2.5	0.0	4.0	-0.5
Exact	2.0	-0.125	2.5	0.0	4.0	-0.5

method is studied using four nodal arrangements with 50, 138, 402, and 965 nodes.

The convergence rate is compared among FEM, MLPG, and the present MSLSM in Figures 6 and 7. It can be found that MSLSM shows a good accuracy and convergence rate. Figures 8 and 9 show the vertical displacement v and the normal stress σ_{xx} along the $y = d/2$ indicating accuracy of results using irregular 138 nodes and the proposed formulation.

As has been highlighted in [36, 37], the computational cost in obtaining the shape functions and its derivatives is much lower by the present LS interpolation than by the MLS approximation. This is shown in Table 2. It can also be observed from the table that the difference in computational

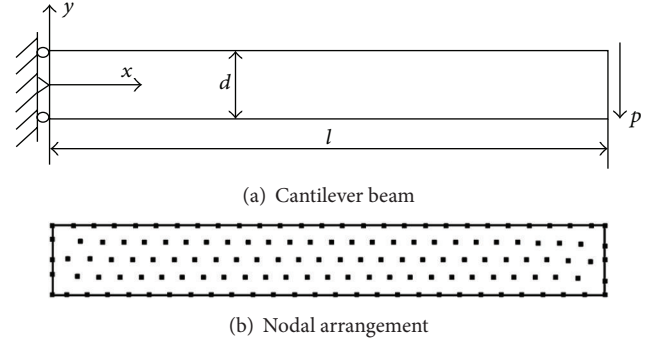


FIGURE 5: Cantilever beam and its nodal arrangement.

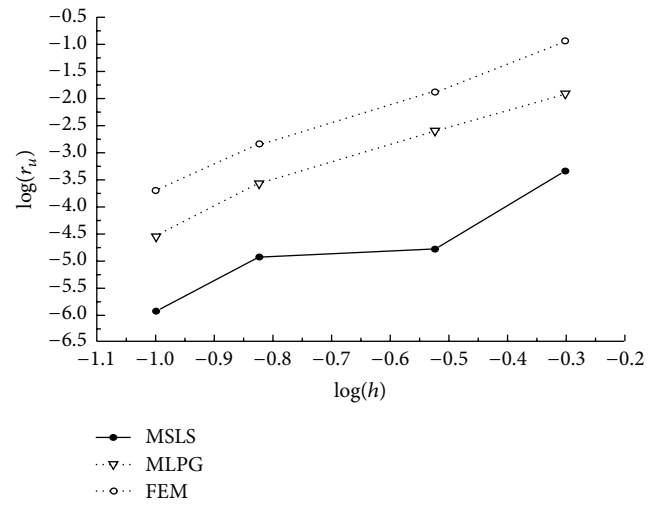


FIGURE 6: Convergence of relative displacement error of the cantilever beam.

efficiency between the two interpolations gets bigger when the number of nodes increases.

4.3. An Infinite Plate with a Circular Hole. The second example is an infinite plate with a circular hole of radius $a = 1$ m. The plate is subjected to a far field traction $\sigma = 1$ Pa in the x direction. A finite portion of the plate is considered for analysis and, due to the symmetry of the problem, only a quarter of the portion requires modeling, as shown in Figure 10. The elastic material properties used are $E = 3.0 \times 10^7$ Pa and $\nu = 0.3$ and plane stress conditions are assumed. The stresses and displacements for this are given in an analytical solution in [47] as

$$\begin{aligned}
 \sigma_{xx} &= 1 - \frac{a^2}{r^2} \left(\frac{3}{2} \cos(2\theta) + \cos(4\theta) \right) + \frac{3a^4}{2r^4} \cos(4\theta), \\
 \sigma_{xy} &= -\frac{a^2}{r^2} \left(\frac{1}{2} \sin(2\theta) + \sin(4\theta) \right) + \frac{3a^4}{2r^4} \sin(4\theta), \\
 \sigma_{yy} &= -\frac{a^2}{r^2} \left(\frac{1}{2} \cos(2\theta) - \cos(4\theta) \right) - \frac{3a^4}{2r^4} \cos(4\theta),
 \end{aligned} \tag{32}$$

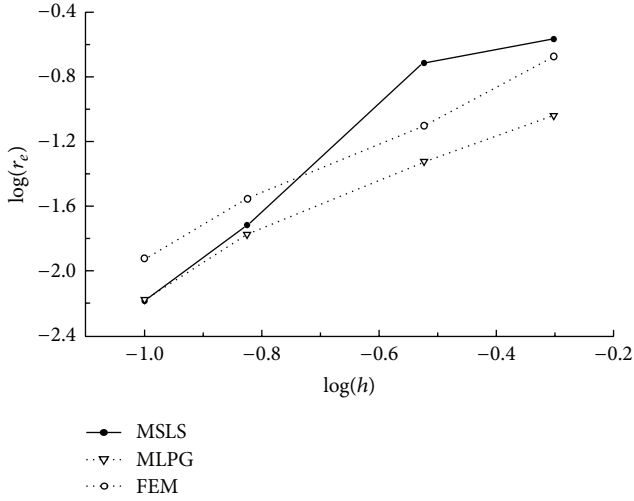


FIGURE 7: Convergence of relative energy error of the cantilever beam.

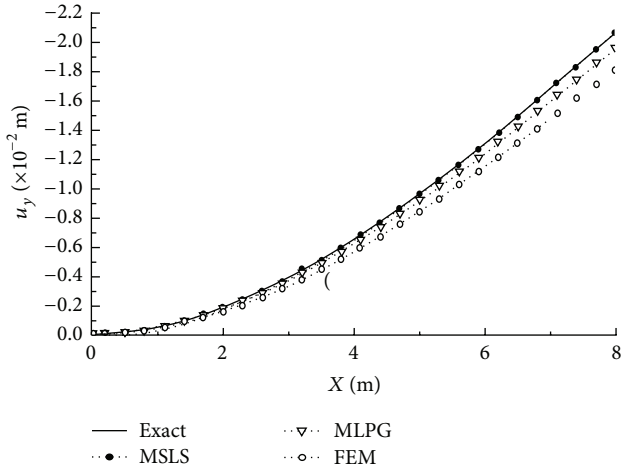


FIGURE 8: Vertical displacement results v along $y = 0$ of the cantilever beam.

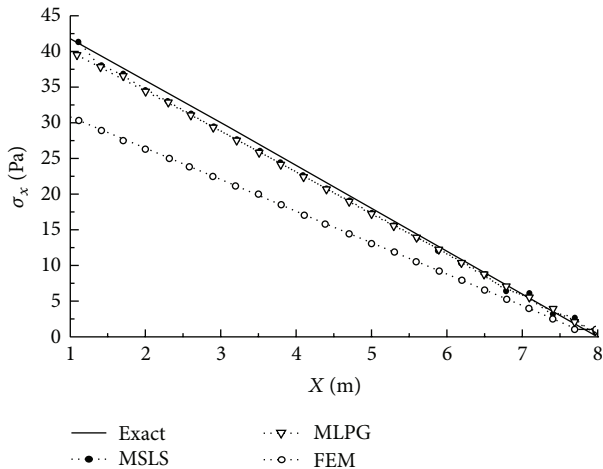
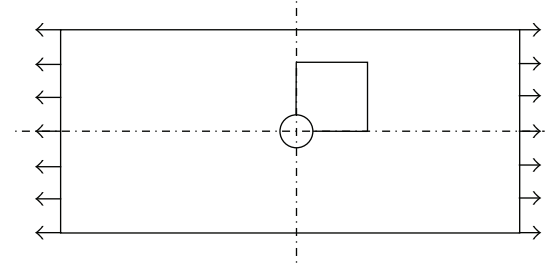


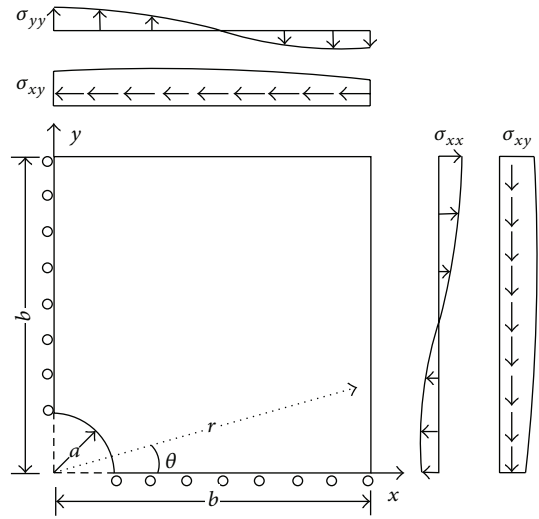
FIGURE 9: σ_{xx} results along $y = 0$ of the cantilever beam.

TABLE 2: Comparison of computational time in obtaining the strain matrix (unit: second).

Number of nodes	50	138	402	965
MLS	0.16	0.59	1.89	4.35
Present MSLS	0.14	0.46	1.15	2.50



(a) A small portion taken for analysis



(b) Boundary conditions applied

FIGURE 10: An infinite plate with a circular hole.

$$\begin{aligned}
 u &= \frac{a}{8G} \left(\frac{r}{a} (\kappa + 1) \cos(\theta) + \frac{2a}{r} [(1 + \kappa) \cos(\theta) + \cos 3(\theta)] \right. \\
 &\quad \left. - \frac{2a^3}{r^3} \cos 3(\theta) \right), \\
 v &= \frac{a}{8G} \left(\frac{r}{a} (\kappa - 3) \sin(\theta) + \frac{2a}{r} [(1 - \kappa) \sin(\theta) + \sin 3(\theta)] \right. \\
 &\quad \left. - \frac{2a^3}{r^3} \sin 3(\theta) \right),
 \end{aligned}
 \tag{33}$$

where G is the shear modulus and κ is the Kolosov constant where $\kappa = (3 - \nu)/(1 - \nu)$ for the plane strain assumption.

Traction-prescribed boundary conditions consistent with the exact solution in (32) are applied at the top and right

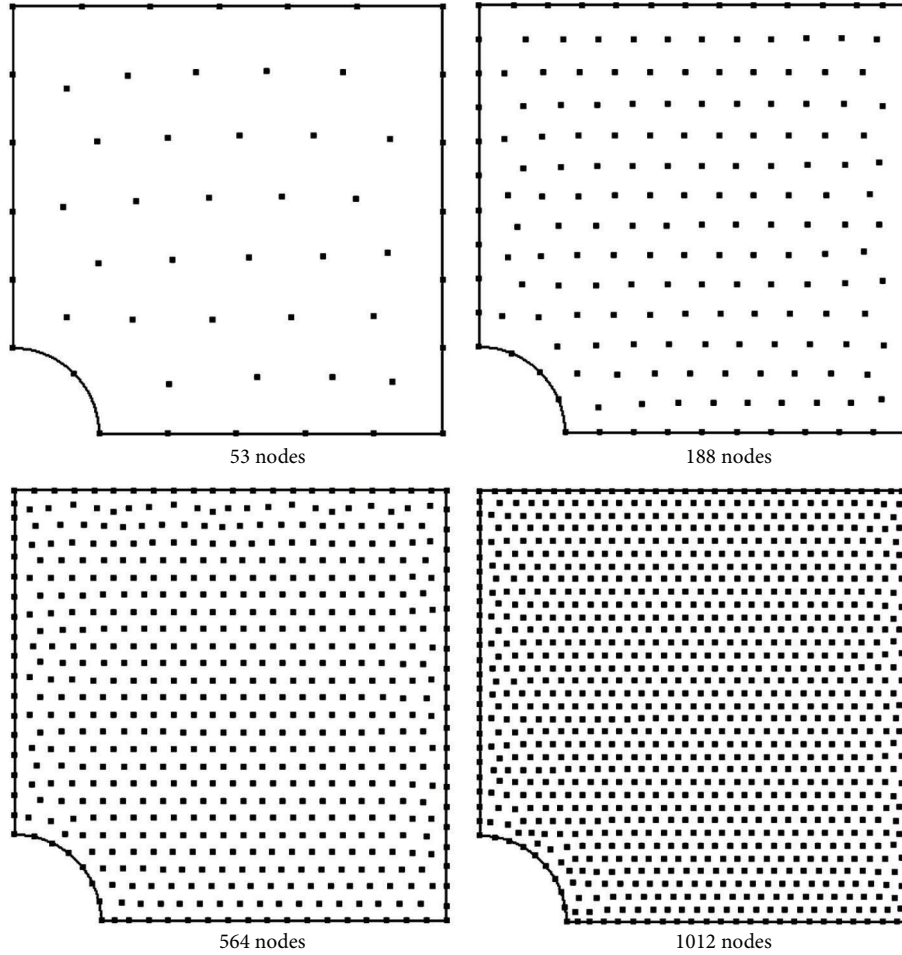


FIGURE 11: Nodal arrangements used for the infinite plate problem.

edges. Four distributions of 53, 188, 564, and 1012 nodes, which are shown in Figure 11, are employed for the convergence studies. Figures 12 and 13 show that the MSLS has a good convergence rate in the displacement and energy norm. The convergence slope of the present method is similar to that of MLPG though the latter is seen to be more accurate. The displacement u_x obtained using MSLS and MLPG is shown in Figure 14. It is seen that the displacement values given by MSLS as well as MLPG are very close to the exact solution.

5. Conclusions

In this paper, we proposed a local weak form meshless Shepard and least-squares interpolation. The interpolation features the use of duo nodal supports for local approximation and global approximation, respectively. The present formulation satisfies the delta property at desired nodes without using singular weight functions. The shape functions constructed conform to the PU property. The local Petrov-Galerkin weak form is used so that there is no need for

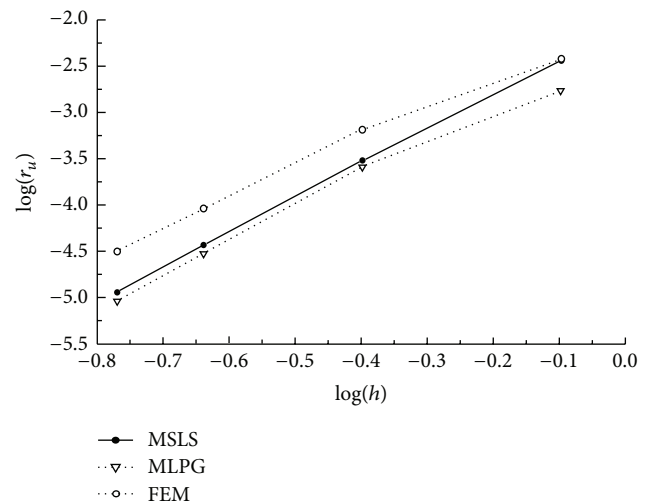


FIGURE 12: Convergence of relative displacement error for the infinite plate problem.

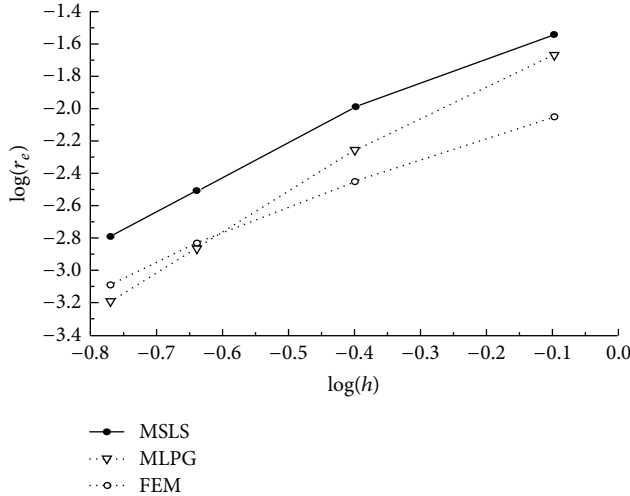


FIGURE 13: Convergence of relative energy error for the infinite plate problem.

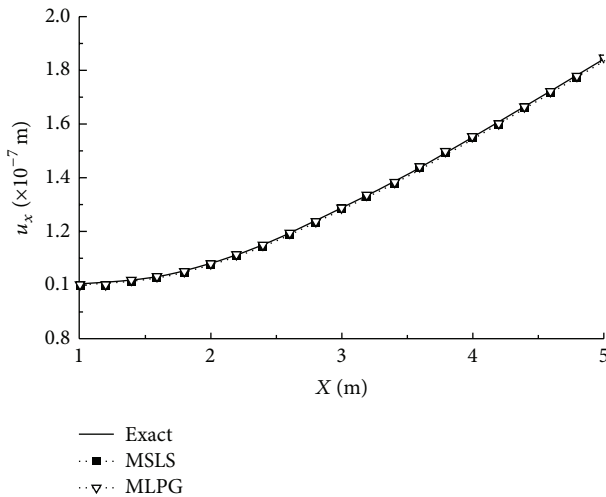


FIGURE 14: Comparison of the horizontal displacement u along $y = 0$ by different methods.

background mesh. It has been tested that the present formulation is more efficient when compared to the currently widely used MLS approximation. For the 2D example of 965 nodes, the computing time of the present MSLS is close to half of the computing time of MLS. The accuracy of the present method is slightly lower than the MLPG but higher than the FEM when the same number of nodes and the same order of basis function, for example, linear or quadratic bases, are used (linear basis corresponding to triangular element in the FEM). The formulation here is derived for 2D analysis but is readily extendable to 3D and the essential ideas are the same. Further development of the present interpolation such as application to problems of changing geometry/moving boundaries, finite deformation, elastoplasticity, and three-dimensional cracking is ongoing.

Conflict of Interests

The authors declare that there is no conflict of interests regarding the publication of this paper.

Acknowledgments

The authors gratefully acknowledge the support of the NSFC Programme (41130751, 51109162), 973 Program (2011CB013800), Shanghai Pujiang Talent Program (12PJ1409100), SRF for ROCS of State Education Ministry, and China Central University Funding.

References

- [1] T. Fries and H. Matthies, Classification and Overview of Meshfree Methods, Technical University Braunschweig, Brunswick, Germany, 2004.
- [2] S. Hao, W. K. Liu, and T. Belytschko, “Moving particle finite element method with global smoothness,” *International Journal for Numerical Methods in Engineering*, vol. 59, no. 7, pp. 1007–1020, 2004.
- [3] V. P. Nguyen, T. Rabczuk, S. Bordas, and M. Duflot, “Meshless methods: a review and computer implementation aspects,” *Mathematics and Computers in Simulation*, vol. 79, no. 3, pp. 763–813, 2008.
- [4] X. Zhuang, C. E. Augarde, and K. M. Mathisen, “Fracture modeling using meshless methods and levels sets in 3D: framework and modeling,” *International Journal for Numerical Methods in Engineering*, vol. 92, no. 11, pp. 969–998, 2012.
- [5] X. Zhuang, C. Augarde, and S. Bordas, “Accurate fracture modelling using meshless methods, the visibility criterion and level sets: formulation and 2D modelling,” *International Journal for Numerical Methods in Engineering*, vol. 86, no. 2, pp. 249–268, 2011.
- [6] T. Rabczuk and T. Belytschko, “Cracking particles: a simplified meshfree method for arbitrary evolving cracks,” *International Journal for Numerical Methods in Engineering*, vol. 61, no. 13, pp. 2316–2343, 2004.
- [7] T. Rabczuk and G. Zi, “A meshfree method based on the local partition of unity for cohesive cracks,” *Computational Mechanics*, vol. 39, no. 6, pp. 743–760, 2007.
- [8] T. Rabczuk, P. M. A. Areias, and T. Belytschko, “A meshfree thin shell method for non-linear dynamic fracture,” *International Journal for Numerical Methods in Engineering*, vol. 72, no. 5, pp. 524–548, 2007.
- [9] T. Jarak and J. Sorić, “Analysis of rectangular square plates by the mixed meshless local Petrov-Galerkin (MLPG) approach,” *Computer Modeling in Engineering & Sciences*, vol. 38, no. 3, pp. 231–261, 2008.
- [10] P. Areias and T. Rabczuk, “Finite strain fracture of plates and shells with configurational forces and edge rotation,” *International Journal For Numerical Methods in Engineering*, vol. 94, pp. 1099–1122, 2013.
- [11] P. Areias, T. Rabczuk, and D. Dias-da-Costa, “Assumed-metric spherically-interpolated quadrilateral shell element,” *Finite Elements in Analysis and Design*, vol. 66, pp. 53–67, 2013.
- [12] C. H. Thai, H. Nguyen-Xuan, N. Nguyen-Thanh, T.-H. Le, T. Nguyen-Thoi, and T. Rabczuk, “Static, free vibration, and buckling analysis of laminated composite Reissner-Mindlin

- plates using NURBS-based isogeometric approach,” *International Journal for Numerical Methods in Engineering*, vol. 91, no. 6, pp. 571–603, 2012.
- [13] T. Chau-Dinh, G. Zi, P. S. Lee, J. H. Song, and T. Rabczuk, “Phantom-node method for shell models with arbitrary cracks,” *Computers and Structures*, vol. 92–93, pp. 242–256, 2012.
- [14] N. Nguyen-Thanh, J. Kiendl, H. Nguyen-Xuan, R. Wüchner, K. U. Bletzinger, and Y. Bazilevs, “Rotation free isogeometric thin shell analysis using PHT-splines,” *Computer Methods in Applied Mechanics and Engineering*, vol. 200, no. 47–48, pp. 3410–3424, 2011.
- [15] N. Nguyen-Thanh, T. Rabczuk, H. Nguyen-Xuan, and S. Bordas, “An alternative alpha finite element method with discrete shear gap technique for analysis of Mindlin-Reissner plates,” *Finite Elements in Analysis and Design*, vol. 47, pp. 519–535, 2011.
- [16] T. Rabczuk and T. Belytschko, “A three-dimensional large deformation meshfree method for arbitrary evolving cracks,” *Computer Methods in Applied Mechanics and Engineering*, vol. 196, no. 29–30, pp. 2777–2799, 2007.
- [17] Z. D. Han and S. N. Atluri, “Meshless local Petrov-Galerkin (MLPG) approaches for solving 3D problems in elasto-statics,” *CMES. Computer Modeling in Engineering & Sciences*, vol. 6, no. 2, pp. 169–188, 2004.
- [18] T. Rabczuk, S. Bordas, and G. Zi, “On three-dimensional modelling of crack growth using partition of unity methods,” *Computers and Structures*, vol. 88, no. 23–24, pp. 1391–1411, 2010.
- [19] T. Rabczuk, R. Gracie, J.-H. Song, and T. Belytschko, “Immersed particle method for fluid-structure interaction,” *International Journal for Numerical Methods in Engineering*, vol. 81, no. 1, pp. 48–71, 2010.
- [20] T. Rabczuk and E. Samaniego, “Discontinuous modelling of shear bands using adaptive meshfree methods,” *Computer Methods in Applied Mechanics and Engineering*, vol. 197, no. 6–8, pp. 641–658, 2008.
- [21] T. Rabczuk, T. Belytschko, and S. P. Xiao, “Stable particle methods based on Lagrangian kernels,” *Computer Methods in Applied Mechanics and Engineering*, vol. 193, no. 12–14, pp. 1035–1063, 2004.
- [22] S. N. Atluri and T. Zhu, “The Meshless Local Petrov-Galerkin(MLPG) approach for solving problems in elasto-statics,” *Computational Mechanics*, vol. 25, pp. 169–179, 2000.
- [23] J. Zheng, S. Long, Y. Xiong, and G. Li, “A finite volume meshless local Petrov-Galerkin method for topology optimization design of the continuum structures,” *Computer Modeling in Engineering & Sciences*, vol. 42, no. 1, pp. 19–34, 2009.
- [24] Y. Cai, X. Zhuang, and C. Augarde, “A new partition of unity finite element free from the linear dependence problem and possessing the delta property,” *Computer Methods in Applied Mechanics and Engineering*, vol. 199, no. 17–20, pp. 1036–1043, 2010.
- [25] Y. Cai, X. Zhuang, and H. Zhu, “A generalized and efficient method for finite cover generation in the numerical manifold method,” *International Journal of Computational Methods*, vol. 10, no. 5, Article ID 1350028, 19 pages, 2013.
- [26] H. Nguyen-Xuan, T. Rabczuk, T. Nguyen-Thoi, T. N. Tran, and N. Nguyen-Thanh, “Computation of limit and shakedown loads using a node-based smoothed finite element method,” *International Journal for Numerical Methods in Engineering*, vol. 90, no. 3, pp. 287–310, 2012.
- [27] C. Thai-Hoang, N. Nguyen-Thanh, H. Nguyen-Xuan, and T. Rabczuk, “An alternative alpha finite element method with discrete shear gap technique for analysis of laminated composite plates,” *Applied Mathematics and Computation*, vol. 217, no. 17, pp. 7324–7348, 2011.
- [28] N. Vu-Bac, H. Nguyen-Xuan, L. Chen et al., “A phantom-node method with edge-based strain smoothing for linear elastic fracture mechanics,” *Journal of Applied Mathematics*, vol. 2013, Article ID 978026, 12 pages, 2013.
- [29] Y. Jia, Y. Zhang, G. Xu, X. Zhuang, and T. Rabczuk, “Reproducing kernel triangular B-spline-based FEM for solving PDEs,” *Computer Methods in Applied Mechanics and Engineering*, vol. 267, pp. 342–358, 2013.
- [30] P. Lancaster and K. Salkauskas, “Surfaces generated by moving least squares methods,” *Mathematics of Computation*, vol. 37, no. 155, pp. 141–158, 1981.
- [31] P. Breitkopf, A. Rassineux, G. Touzot, and P. Villon, “Explicit form and efficient computation of MLS shape functions and their derivatives,” *International Journal for Numerical Methods in Engineering*, vol. 48, no. 3, pp. 451–466, 2000.
- [32] X. Zhuang and C. Augarde, “Aspects of the use of orthogonal basis functions in the element-free Galerkin method,” *International Journal for Numerical Methods in Engineering*, vol. 81, no. 3, pp. 366–380, 2010.
- [33] X. Zhuang, C. Heaney, and C. Augarde, “On error control in the element-free Galerkin method,” *Engineering Analysis with Boundary Elements*, vol. 36, no. 3, pp. 351–360, 2012.
- [34] I. Kaljević and S. Saigal, “An improved element free Galerkin formulation,” *International Journal for Numerical Methods in Engineering*, vol. 40, no. 16, pp. 2953–2974, 1997.
- [35] J.-S. Chen and H.-P. Wang, “New boundary condition treatments in meshfree computation of contact problems,” *Computer Methods in Applied Mechanics and Engineering*, vol. 187, no. 3–4, pp. 441–468, 2000.
- [36] Y. C. Cai and H. H. Zhu, “A local meshless Shepard and least square interpolation method based on local weak form,” *Computer Modeling in Engineering & Sciences*, vol. 34, no. 2, pp. 179–204, 2008.
- [37] X. Zhuang, H. Zhu, and C. Augarde, “An improved meshless Shepard and least squares method possessing the delta property and requiring no singular weight function,” *Computational Mechanics*, 2013.
- [38] G. R. Liu, Y. T. Gu, and K. Y. Dai, “Assessment and applications of point interpolation methods for computational mechanics,” *International Journal for Numerical Methods in Engineering*, vol. 59, pp. 1373–1397, 2004.
- [39] J. Dolbow and T. Belytschko, “Numerical integration of the Galerkin weak form in meshfree methods,” *Computational Mechanics*, vol. 23, no. 3, pp. 219–230, 1999.
- [40] S. Beissel and T. Belytschko, “Nodal integration of the element-free Galerkin method,” *Computer Methods in Applied Mechanics and Engineering*, vol. 139, no. 1–4, pp. 49–74, 1996.
- [41] J. S. Chen, C. T. Wu, S. Yoon, and Y. You, “A stabilized conforming nodal integration for Galerkin meshfree methods,” *International Journal for Numerical Methods in Engineering*, vol. 50, pp. 435–466, 2001.
- [42] M. A. Puso, J. S. Chen, E. Zywickz, and W. Elmer, “Meshfree and finite element nodal integration methods,” *International Journal for Numerical Methods in Engineering*, vol. 74, no. 3, pp. 416–446, 2008.
- [43] S. N. Atluri, *The Meshless Local Petrov-Galerkin (MLPG) Method for Domain & Boundary Discretizations*, Tech Science Press, 2004.

- [44] A. Carpinteri, G. Ferro, and G. Ventura, "The partition of unity quadrature in meshless methods," *International Journal for Numerical Methods in Engineering*, vol. 54, no. 7, pp. 987–1006, 2002.
- [45] I. Kaljević and A. S. Saigal, "An improved element free Galerkin formulation," *International Journal for Numerical Methods in Engineering*, vol. 40, no. 16, pp. 2953–2974, 1997.
- [46] S. Rajendran and B. R. Zhang, "A "FE-meshfree" QUAD4 element based on partition of unity," *Computer Methods in Applied Mechanics and Engineering*, vol. 197, no. 1–4, pp. 128–147, 2007.
- [47] S. P. Timoshenko and J. N. Goodier, *Theory of Elasticity*, McGraw-Hill, New York, NY, USA, 3rd edition, 1951.

Research Article

A Coupled Thermo-Hydro-Mechanical Model of Jointed Hard Rock for Compressed Air Energy Storage

Xiaoying Zhuang,^{1,2} Runqiu Huang,² Chao Liang,³ and Timon Rabczuk^{4,5}

¹ National Key Laboratory of Disaster Reduction and Protection, Department of Geotechnical Engineering, Tongji University, Shanghai 200092, China

² State Key Laboratory of Geohazard Prevention and Geoenvironment Protection, Chengdu, China

³ Department of Geophysics, School of Earth Sciences, Stanford University, USA

⁴ Institute of Structural Mechanics, Bauhaus-Universität Weimar, Weimar, Germany

⁵ School of Civil, Environmental and Architectural Engineering, Korea University, Republic of Korea

Correspondence should be addressed to Xiaoying Zhuang; xiaoyingzhuang@tongji.edu.cn and Timon Rabczuk; timon.rabczuk@uni-weimar.de

Received 8 September 2013; Accepted 7 November 2013; Published 19 January 2014

Academic Editor: Goangseup Zi

Copyright © 2014 Xiaoying Zhuang et al. This is an open access article distributed under the Creative Commons Attribution License, which permits unrestricted use, distribution, and reproduction in any medium, provided the original work is properly cited.

Renewable energy resources such as wind and solar are intermittent, which causes instability when being connected to utility grid of electricity. Compressed air energy storage (CAES) provides an economic and technical viable solution to this problem by utilizing subsurface rock cavern to store the electricity generated by renewable energy in the form of compressed air. Though CAES has been used for over three decades, it is only restricted to salt rock or aquifers for air tightness reason. In this paper, the technical feasibility of utilizing hard rock for CAES is investigated by using a coupled thermo-hydro-mechanical (THM) modelling of nonisothermal gas flow. Governing equations are derived from the rules of energy balance, mass balance, and static equilibrium. Cyclic volumetric mass source and heat source models are applied to simulate the gas injection and production. Evaluation is carried out for intact rock and rock with discrete crack, respectively. In both cases, the heat and pressure losses using air mass control and supplementary air injection are compared.

1. Introduction

Renewable energy such as wind, solar, tidal, and wave only produces electricity intermittently and with low power and energy density, thus, nondispatchable and difficult to use at large scales as the modern society requires [1]. That is why many renewable energy technologies are lacking the economies of scale, which reduces their competitiveness and delays the transition to a low carbon economy. Therefore, economic solutions to bulk energy storage are urgently needed in order for renewable energy to take a significant share in the total energy mix. A critical issue for renewable energy to be integrated into grids with satisfactory stability is appropriate energy storage to defer electricity demand from peak to off peak times.

Most energy storage systems are expensive, either in terms of Capex and Opex or in terms of energy losses

incurred in storing and retrieving the energy. For example, batteries are costly, fly wheels are suitable for short-duration storage only. The CAES, besides pumped-hydro, is the only conceivable technology able to provide the very large scale energy storage deliverability above 100 MW in single unit sizes while free from adverse environmental effects of pumped-hydro. Hence, CAES has recently received lots of attention [2, 3] and it has been recently proposed that large-scale solar-CAES and wind-CAES deployment can enable renewable energy to compete against coal-fired electricity generation [4, 5]. In CAES, a source energy is stored in the form of highly pressurized air in underground rock caverns and the compressed air is released through turbines to generate electricity when needed [6] as shown in Figure 1. Underground rock caverns are the mostly chosen type of reservoirs in the CAES which provide initial ground stress against air pressure, strengths to withstand cyclic loadings,

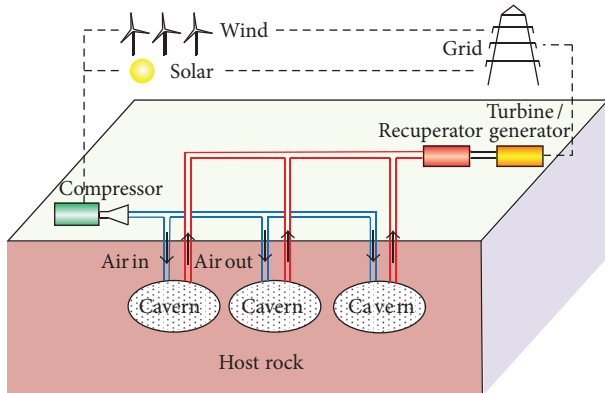


FIGURE 1: Compressed air energy storage plant using hard rock caverns.

and large volumes of storage space and therefore are more economical than other types of storage such as steel tanks [7].

Existing and planning CAES facilities for utility purpose are mainly in salt rock formation where vacuums are formed by pumping pressurized water to dissolve the rock medium. The only existing CAES built in hard rock, however, for experimental purpose, is a 1600 m³ cave constructed in deplete mine in Hokkaido, Japan. The air pressure during cyclic charging and discharging is between 4 and 8 MPa and rubber lining is used for air tightness. Another small scale CAES using water sealing in hard rock is now under plan in Switzerland and air pressure will be around 3.3 MPa. Though the CAES technology has come into existence for over 30 years [8], the exploration of utilizing hard rock is important for wider application of this technique since the requirement of salt rock is too restrictive geological constraint in many areas. In this paper, we carried out the investigation of utilizing hard rock cavern for CAES through a coupled thermal-hydro-mechanical modelling for physical quantities.

2. Geological Conditions for CAES

To date, there have been only two CAES plants in operation at utility scales. The first is the 290 MW Huntorf plant in Germany with a total storage volume of 310,000 m³, operational since 1978 [9, 10]. And the second of 110 MW-scale with a storage space of 500,000 m³ was built in McIntosh, AL, in 1991 [6]. While energy conversion equipment including compressors, recuperators, and gas turbines is well established technology and procurable from the market, present challenges of CAES lie in finding geo-storage spaces such as rock caverns that are competent for cost effective and reliable performance during long-term plant operation. Though using subsurface rock as oil/gas storage started from the 1900s, new issues arise for CAES including the cyclic actions of high air pressure and thermalfluidics. Other types of storage such as above ground gas tanks, though technically available, are too expensive, about 5 times the cost of caverns [11]. Moreover, the security of the storage is also a major concern for highly pressurized tanks above ground. Hence, the implementation of CAES

technology waits for the exploring and characterizing sites suitable for storage.

To the best of the authors' knowledge, the CAES projects declared over the world are listed in Table 1. From the successful experiences of the existing facilities, the caverns are ideally constructed in salt rock formations due to their good air tightness. However, the requirements of salt rocks are too restrictive and not available in many areas. Recently, research interests in exploring the potential of using bedrocks other than salt rock have been motivated such as crystalline rock [12], sedimentary porous rock [13], aquifer, depleted oil/gas wells [14], and limestone [15]. More CAES plants built on various types of rock are under plan around the world such as the 300 MW plant by Pacific Gas & Electric in CA, USA [15], 300 MW plant in China [11], and other pilot plants in Korea [12] and Israel [13]. In Australia, sandstones are typical hard rock from depleted copper, gold, and silver mines. Sandstones are normally porous enough to store large quantities and can be used as valuable aquifers for reservoirs. Such CAES can provide sufficient strengths to sustain the stress induced by the rise and drop of air pressure and temperatures. The depleted reservoir formation is economically attractive because it allows the reuse, with suitable modification, which reduces the start-up costs.

The most significant challenge in CAES is to ensure the air tightness and prevent the air leak-off that may occur due to crack propagation under long-term cyclic actions resulting in pressure and heat losses. On the other hand, rock is natural mineral aggregate with distributed discontinuities such as joints, cracks, or inclusions. The CAES operation exerts complex and cyclic mechanical, thermal, and wet-dry cycles. These excitations may cause monotonic failure and require close examination useful for engineering design of cavern. The stagnation of the 2700 MW CAES plant in Huston, the US, is an example [15]. The construction of the plant was launched in 2001 and stalled later due to the air leakage problem in the limestone caverns occurred [11, 14]. The understanding of the air leak-off requires both understanding on the mechanisms, geological conditions, the development of physical model, and advanced numerical simulation for engineering design [16]. In the past two decades, there have been significant advancements in fracture simulation methods such as the Extended Finite Element Method (XFEM) or extended meshfree methods [17–36] to allow for the application of discrete crack modelling techniques to THM simulations [37, 38] as well as fluid structure interaction-induced cracks [39]. In this paper, we aim to find out the relation between cavern characteristics, energy efficiency, and heat and pressure losses and stresses of rock induced by hydraulic and thermal changes and the existence of crack.

3. Governing Equations of the THM Modelling

In this paper, three fields, namely, mechanical, thermal, and hydro fields, are considered and coupled. The hydro or seepage field represents the gas flow behaviour, which changes the temperature distribution by the thermalfluidic flow through the porous media. The thermal field in turn will change the density and pressure of the fluid and hence the velocity of

TABLE 1: CAES projects over the world (data collected from various sources).

Project name	Location	Power capacity (MW)	Geological formation	Type	Cavern volume (m ³)	Embedded depth	Max. pressure (MPa)	Status
Huntorf	Breman, Germany	290	Salt Rock	Diabetic	310,000	600	4.3–7.0	Operation
Norton	Norton, USA	2700	Hard rock (limestone)	Diabetic	9,600,000	670	5.5–11	Construction
Iowa Energy Park	Iowa, USA	270	Porous sand stone	Diabetic	—	914	—	Construction
ADELE	Germany	300	Salt Rock	Adiabatic	—	—	~10	Planning
Matagorga	Texas, USA	540	Salt Rock	Diabetic	—	—	—	Planning
Seneca	New York, USA	150–270	Salt Rock	Diabetic	150,000	760	8–11	Planning
PG&E	California, USA	300	Porous aquifer	Diabetic	—	—	—	Planning
Datang CAES	Inner Mongolia, China	300	Sand stone	Diabetic	900,000	500 m	5–8	Planning

the fluid. The thermal strain will result in the internal stress of the mechanical field, which influences the seepage field through volumetric strain. The seepage will change the pore pressure of the fluid with the porous media. The complete coupling of the three fields can involve a large quantity of field variables and material properties associated with each other in the three fields, which is computationally expensive and unnecessary from an engineering perspective. For example, the viscosity of the fluid is temperature dependent and can add another relation between seepage and thermal field. Therefore, we introduce some assumptions in the present THM modelling framework as follows.

- (1) The rock is treated as isotropic elastic porous media and the mechanical parameters of the rock are not changing with respect to the temperature.
- (2) The seepage of the air through the rock follows Darcy's law where the inertia and gravity of the air are not considered.
- (3) The physical state of compressed air conforms with the ideal gas law.
- (4) There is no ground water considered in the model and it is a single phase fluid flow problem, that is, air. The rock pore is saturated by air.
- (5) The heat mass is transferred between the solid and fluid through both convection and conduction. The heat capacity and conductivity coefficients of all the media are not changing with respect to the temperature and pressure. The volumetric strain energy of the solid and the work produced by the fluid from the air compression are taken into account for the energy balance.
- (6) The volume change of the porous media is mainly due to the deformation of the pores.

The above assumptions are used both in the derivation of the governing equations in the following, and the model settings of the numerical studies in Section 4.

3.1. Fluid Field: Mass Conservation. The seepage of the air in rock satisfies the continuity equation described by

$$\frac{\partial(\rho_{\text{gas}}\phi)}{\partial t} + \nabla \cdot (\rho_{\text{gas}}\mathbf{q}) = Q_m, \quad (1)$$

where ρ_{gas} is the density of the air, ϕ is the pore ratio of rock, \mathbf{q} is the seepage velocity vector of the fluid, Q_m is the source of mass (positive for inputting fluid and negative for outputting). The first term on the LHS of (1) can be further calculated by

$$\frac{\partial(\rho_{\text{gas}}\phi)}{\partial t} = \phi \frac{\partial \rho_{\text{gas}}}{\partial t} + \rho_{\text{gas}} \frac{\partial \phi}{\partial t} = \phi \frac{\partial \rho_{\text{gas}}}{\partial t} + b \cdot \rho_{\text{gas}} \frac{\partial \varepsilon_V}{\partial t}, \quad (2)$$

where ε_V is the volumetric strain and b is Biot's consolidation coefficient. The last term on the RHS of (2) shows the direction relation between the volumetric change of the porous media and the porosity ratio. The density of the air is changing with the temperature T and pressure P which is described by the ideal gas law

$$\rho_{\text{gas}} = \frac{PM}{RT}, \quad (3)$$

where P is the pore pressure, M is Molar mass of air that $M = 29$ g/mol, R is ideal gas constant that $R = 8.314$ J/(mol · K), T is absolute (thermodynamic) temperature and P is the pore pressure. The momentum of air seepage conforms to Darcy's law. If the inertia, gravity, and adhesion of air is not considered, the seepage equation of air is expressed by

$$\mathbf{q} = -\frac{k}{\eta} \nabla P, \quad (4)$$

where k is the permeability coefficient of rock and η is the coefficient of viscosity.

By substituting (3) and (4) into (2), the governing equations of seepage field can be obtained by

$$b \cdot \rho_{\text{gas}} \frac{\partial \varepsilon_V}{\partial t} + \frac{\phi M}{RT} \frac{\partial P}{\partial t} - \frac{\phi MP}{RT^2} \frac{\partial T}{\partial t} - \nabla \cdot \left(\frac{PM}{RT} \frac{k}{\eta} \nabla P \right) = Q_m. \quad (5)$$

The changing density is the main difference between the governing equations of air seepage and incompressible fluid seepage. The density of air changes with the temperature, and therefore the thermal field is associated with the fluid field. It can be seen from (5) that the temperature T appears in the coefficient term $\phi M/RT$ for the pressure temporal derivatives $\partial P/\partial t$ and also adjoins with the spatial gradient of pressure term ∇P . This results in the high nonlinearity of the governing equation which brings numerical convergence and stability problem. It can also be seen from the first term on LHS that volumetric strain of the solid also couples the stress field with fluid field.

3.2. Thermal Field: Energy Conservation. According to the first law of thermodynamics, the heat added to a system should be equal to the change of the internal energy of the system and the work done in the system. By considering the energy conservation of the skeleton of the rock as porous media, we can get

$$\rho_s C_{p,s} \frac{\partial T}{\partial t} + TK_s \beta \frac{\partial \varepsilon_V}{\partial t} = \nabla \cdot (\alpha_s \nabla T) + Q_s, \quad (6)$$

where ρ_s , $C_{p,s}$, α_s , Q_s , K_s , and β are the density, specific heat, thermal conductivity, heat source, volumetric modulus, and thermal expansion coefficient of the porous media. It can be seen that the energy transportation in the solid is through the thermal conduction as the first term on RHS. The volumetric work induced by the temperature as the second term on LHS also results in the dissipation of energy. From the energy conservation of fluid, we can get

$$\begin{aligned} & \rho_{\text{gas}} C_{p,\text{gas}} \frac{\partial T}{\partial t} + \rho_{\text{gas}} C_{p,\text{gas}} \mathbf{q} \cdot \nabla T + P (\nabla \cdot \mathbf{q}) \\ & = \nabla \cdot (\alpha_{\text{gas}} \nabla T) + Q_{\text{gas}}, \end{aligned} \quad (7)$$

where ρ_{gas} , $C_{p,\text{gas}}$, α_{gas} , and Q_{gas} are the density of air, heat specific of air, thermal conductivity, and heat source of the fluid. The energy transportation of air includes the heat conduction as the first term on RHS, convection as the second term on LHS, and external work of air as the third term on LHS. For a single phase flow, we assume that the solid and air are in thermal steady state, that is, the temperature of the fluid and solid are equal at the interface. The heat exchange along

the interface of two phases is not considered. By combining (6) with (7), we can get the following:

$$\begin{aligned} & (\rho C_p)_{\text{eq}} \frac{\partial T}{\partial t} + \rho_{\text{gas}} C_{p,\text{gas}} \mathbf{q} \cdot \nabla T \\ & + (1 - \phi) TK_s \beta \frac{\partial \varepsilon_V}{\partial t} + P (\nabla \cdot \mathbf{q}) \\ & = \nabla \cdot (\alpha_{\text{eq}} \nabla T) + Q, \end{aligned} \quad (8)$$

$$(\rho C_p)_{\text{eq}} = \phi \cdot \rho_{\text{gas}} C_{p,\text{gas}} + (1 - \phi) \cdot \rho_s C_{p,s}, \quad (9)$$

$$\alpha_{\text{eq}} = \phi \cdot \alpha_{\text{gas}} + (1 - \phi) \cdot \alpha_s, \quad (10)$$

$$Q = \phi \cdot Q_{\text{gas}} + (1 - \phi) \cdot Q_s, \quad (11)$$

where in (8) $(\rho C_p)_{\text{eq}}$ is the equivalent specific heat capacity of rock as a porous media saturated with air, α_{eq} is the equivalent heat conduction coefficient, and Q is the equivalent heat source of saturated porous media. Equations (8)–(11) describe the governing equations of porous media and the fluid as the thermal field governing equations.

3.3. Mechanical Field: Equilibrium Condition. Since the rock is assumed to be saturated with air, the constitutive model of thermal porous media should consider the contribution of the pore pressure and temperature of the air as follows:

$$\boldsymbol{\sigma} = (\lambda + \mu) (\nabla \cdot \mathbf{u}) + \mu \nabla \mathbf{u} - b P \mathbf{I} - (3\lambda + 2\mu) \beta (T - T_0) \mathbf{I}, \quad (12)$$

where $\boldsymbol{\sigma}$ is the Cauchy stress tensor, λ and μ are Lamé coefficients of rock, \mathbf{u} is the displacement vector, \mathbf{I} is a second-order identity tensor, β is linear thermal expansion coefficient of rock, and b is Biot's consolidation coefficient. The relation between E and ν with respect to λ and μ is well known as

$$\begin{aligned} \lambda &= \frac{E\nu}{(1 + \nu)(1 - 2\nu)}, \\ \mu &= \frac{E}{2(1 + \nu)}. \end{aligned} \quad (13)$$

The equilibrium of porous media is expressed as

$$\nabla \boldsymbol{\sigma} + \mathbf{f} = 0, \quad (14)$$

where \mathbf{f} is the body force vector. Substituting (12) into (14) leads to the governing equation of the stress field as

$$(\lambda + \mu) \nabla (\nabla \cdot \mathbf{u}) + \mu \nabla^2 \mathbf{u} - b \cdot \nabla P - (3\lambda + 2\mu) \beta \cdot \nabla T + \mathbf{f} = 0. \quad (15)$$

3.4. The Governing Equation of Fluid Flow along Single Discrete Crack (Joint). The existence of crack will have influence on all the three fields, especially the mechanics field and stress field. The thermal field will also change due to the crack; however, it will be relatively minor compared to stress and fluid field.

Due to the existence of the crack in rock, the distribution of the air is changing in the rock and consequently results in the change of effective stress and thermal field. In the analysis, the joint is modeled as a channel, that is, internal boundaries in rock. We have not considered the influence of crack over the distribution of thermal and mechanical fields. Therefore, the stress field and thermal field over the crack are continuous. The coupling of the three fields for discontinuities is an interesting and challenging topic for the future. It is generally recognized that a continuum based equivalent elastic porous media, such as Barentblatt and Gil'man [40] nonequilibrium two-phase immiscible flow mode, is not capable of capturing the discontinuity or jump in the thermalfuidic and mechanical field. In this type of approach, the mass and energy is transferred with higher gradient compared to base rock by modifying the material parameters. The crack is modeled as equivalent porous media and there exists numerical instability of extra refined mesh near the crack. In the present paper, the discrete crack model is adopted for a single joint. The upper and lower surfaces of the crack are modeled as internal boundaries inside the domain and the fluid is allowed to flow between the boundaries. Darcy's law for tangential flow along crack is defined as

$$\mathbf{q}_f = -\frac{k_f}{\eta} d_f (\nabla_T P), \quad (16)$$

where \mathbf{q}_f is the flow rate along the unit length of a crack, k_f is the permeability coefficient, d_f is the width of the crack opening, and $\nabla_T P$ is the pressure gradient along the length of the crack. The continuity of the fluid, that is, the mass conservation, between the two surfaces of a single joint is described by

$$d_f \frac{\partial (\rho_{\text{gas}} \phi_f)}{\partial t} + \nabla_T \cdot (\rho_{\text{gas}} \mathbf{q}_f) = d_f Q_m. \quad (17)$$

It can be seen that the same variable of air pressure, namely, P , appears in the governing variable in both the governing equation of the fluid flow along the fracture (joint) and the rock as the porous media.

4. Numerical Modelling of the CAES System in Hard Rock

The governing equations described in Section 3 for mass balance, energy conservation, and equilibrium are discretised by the finite element method and coded to study the hard rock cavern performance for CAES. In this section, a hard rock cavern under the designed operational conditions of CAES without considering the existence of ground water is modeled. The aim of the numerical modelling is to investigate the heat loss, pressure distribution, and seepage of air near the vicinity of cavern.

A rock cavern with a diameter of 5 m and embedded with 100 m depth is modeled as shown in Figure 2(a). Initial ground stress for the equivalent stress state is modeled and excavation step is modeled and the rock near the cavern is regarded as excavation disturbed zone. Standard atmospheric pressure and ground temperature of 286.15 K (13°C) are

TABLE 2: Material parameters and boundary conditions used in the example.

Parameters	
Young's modulus E of rock (GPa)	35
Poisson's ration of rock ν	0.3
Density of rock ρ_s (kg/m ³)	2800
Pore ratio ϕ	1.0
Permeability coefficient k (m ²)	1×10^{-9}
Permeability coefficient along crack k_f (m ²)	—
Crack width d_f (m)	—
Viscosity of air η (Pa·s)	1.86×10^{-5}
Biot's consolidation coefficient b	0.95
Heat conduction of rock α_s (W/m·K)	3
Heat conduction of air α_s (W/m·K)	1000
Heat specific of air under constant pressure $C_{p,\text{gas}}$ (J/kg·K)	1000
Heat specific of rock $C_{p,s}$ (J/kg·K)	900
Expansion coefficient β (1/K)	1.0×10^{-5}
Initial pressure P_0 (atm)	1
Initial temperature T_0 (K)	286.15
Air injection temperature T_{in} (K)	296.65

applied to the four edges of boundaries. Six points of interest marked P1–P6 are sampled in the simulation results as shown in Figure 2(b). The operational cycle of the cavern is 24 hours. In the initial condition of the cavern, the air is injected into the design value of 5.5 MPa after 16 hours injection and followed by 8 hours storage. After that, the air injection and release follows a cycle of 8 hours storage, 4 hours storage, 4 hours release, and another 8 hours storage. In air compression stage, the air is injected at the rate of 1.12×10^{-3} kg/(s · m³) to the cavern at the temperate of 296.65 K (23.5°C). In the energy recuperation stage, the air is released at the rate of 2.24×10^{-3} kg/(s · m³). The time length of the present example is 80 operational days. The material parameters used in this case study are listed in Table 2.

The pressure drop along the cavern ceiling with respect to the time is shown in Figure 3. Due to the seepage of air through the pores of rock, pressure drop is observed in the consecutive days of operation. With the mass conservation control, that is, same injection and production of air in terms of mass, a substantial drop of pressure can be observed after 60 days of operation. At day 60, the minimum pressure inside the cavern is about 5 MPa lower than the desired operational pressure. This is different from the observation of CAES cavern in aquifer by Kim et al. [41]. It means that for hard rock cavern without water concealing, supplementary air injection is necessary to maintain operational pressure due to air seepage.

It was also found that the influence of pressure fluctuation over the rock diminishes at about 2.1 m distant to the internal boundary of cavern (at P3 in Figure 2). It can also be seen that the air seepage through the rock gradually converges as shown in Figure 4. On day 1, the pressure drop along the

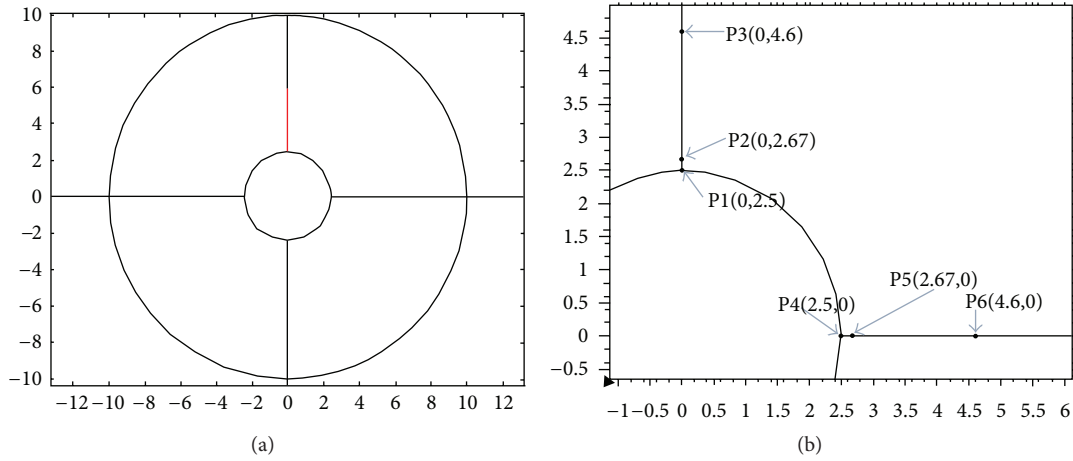


FIGURE 2: Model setting of the hard rock cavern. (a) Geometry and profile of cavern. (b) Points of interest near the cavern.

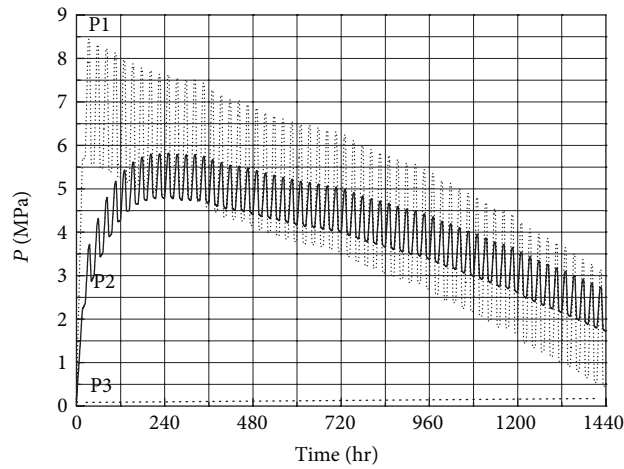


FIGURE 3: Pressure drop of air after 60 operational days.

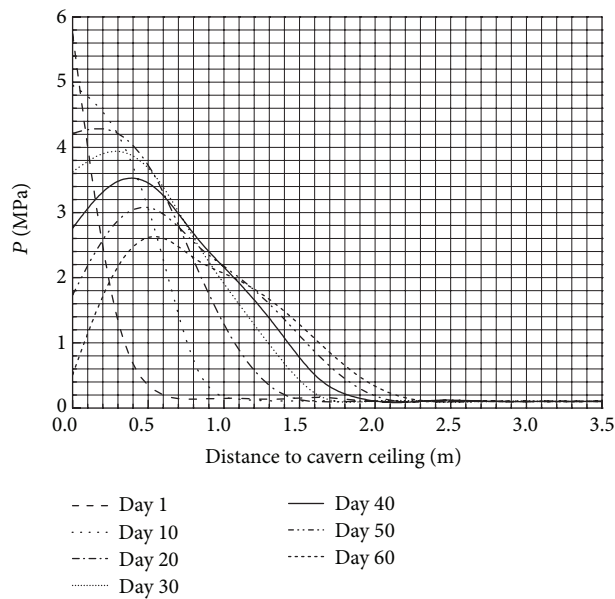


FIGURE 4: Pressure variation along the cavern ceiling from Day 1 to 60.

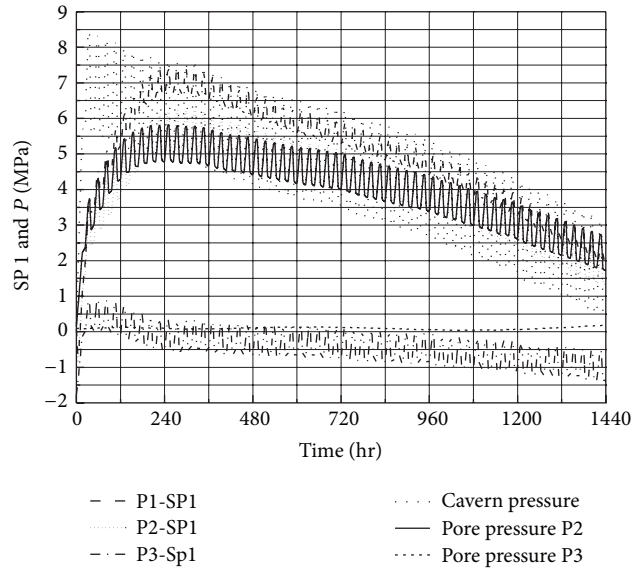


FIGURE 5: The maximum principle stress and pore pressure with respect to time.

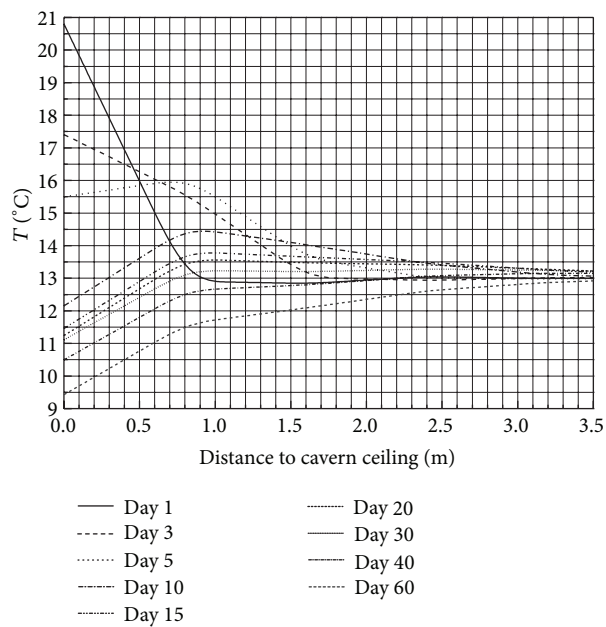


FIGURE 6: The temperature along cavern ceiling with respect to the time from Day 1 to 60.

distance to the cavern is steep. The maximum pressure occurs at the interface of air and rock. At day 20, the maximum pressure is observed at about 0.2 m distant to the cavern boundary. After 60 days of operation, the maximum pressure point is shifted to about 0.5 m to the cavern boundary. The indication of the result to cavern design is that the validation of rock strength should be conducted for certain range to the cavern boundary. The change of pressure and pore pressure at different distances to the cavern with respect to the time is plotted in Figure 5. It can be seen that there is slight lagging behind for the development of stress in rock with respect to the pore pressure. This conforms to common phenomenon

of the fluid seepage and saturation in porous media, and shows the validity of the present THM models. It can also be seen that at P3 which is 2.1 m distant to the inner boundary of cavern, the pore pressure vanishes showing the vanishing influence from cavern.

For the thermal field, the temperature gradually converges to the ground temperature of 13 °C when it is distant from the cavern as shown in Figure 6. The temperature on Day 1 at steady state is about 3 degrees than the injection temperature due the thermal conduction. It can be seen that the temperature decreases since the expansion of air is a heat consumption process.

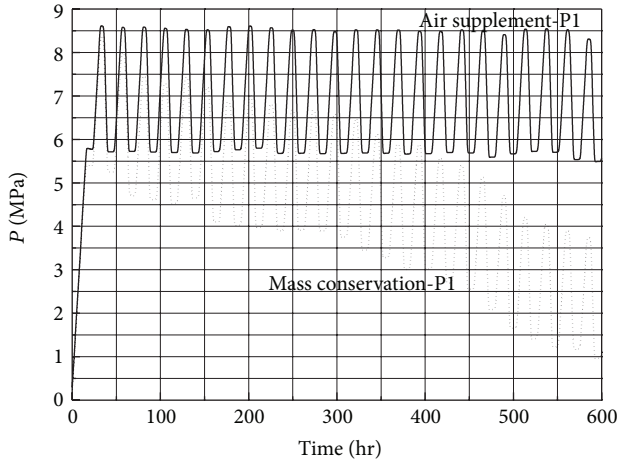


FIGURE 7: The pressure difference with and without considering the volumetric strain induced by thermal field.

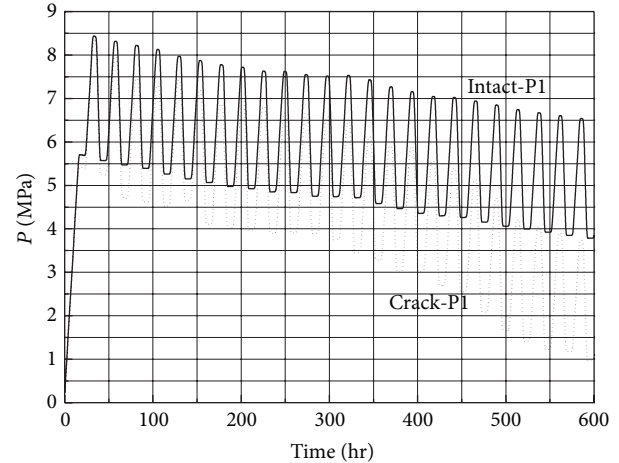


FIGURE 9: Comparison of pressure loss between intact and jointed rock cavern.

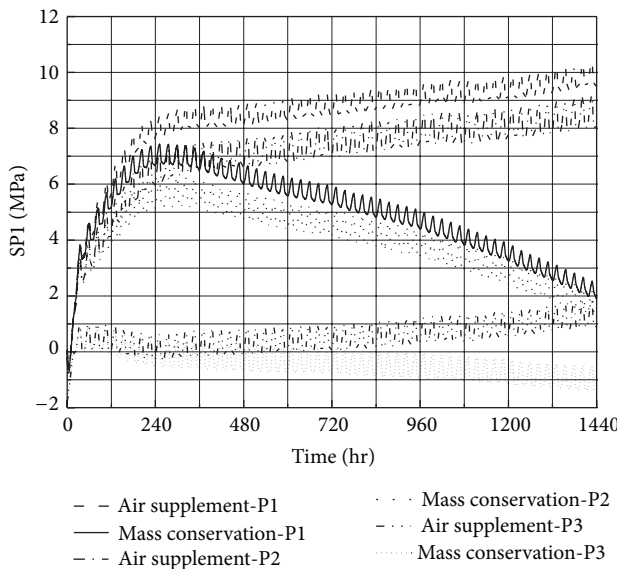


FIGURE 8: The comparison of the maximum principal stress in rock between air supplement control and mass control during CAES operation.

To study the pressure control strategy of the system, supplementary air condition is also modeled. By comparing the results of air density at day 60 with respect to day 1, the average density loss can be calculated which is about 1.048 kg/m^3 daily. Therefore, in the model, supplementary air mass of 3.252% is injected. The results of cavern pressure with and without supplementary injection are compared in Figure 7. It can be seen that with supplementary air injection, the air pressure can be maintained between 5.5 and 8.5 MPa, which is ideal for the operational requirement. The maximum principle stresses at different points in rock are compared between mass conservation and air supplement conditions in Figure 8. The air supplement on one hand results in

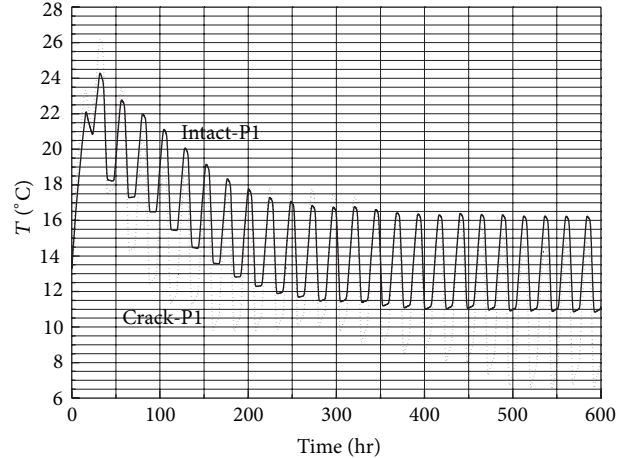


FIGURE 10: Comparison of heat loss between intact and jointed rock cavern.

more stable air pressure inside cavern but also induces the increased stress in rock.

The difference of pressure between intact rock cavern and a cavern with a single joint at the rock ceiling is compared as shown in Figure 9. It can be seen that a single fracture with settings in Table 2 results in the pressure loss of about 4 MPa after 600 hours operation. For the energy loss, the cracked rock cavern has lost about 5 degrees of temperature as shown in Figure 10. It can also be seen that, cracked rock cavern will have larger fluctuation compared to intact rock in each operational cycle. The pores pressure distribution shows the seepage of air through the joint after 25 days of operation where the concentration takes place near the joint as shown in Figure 11. The internal pressure of air through dissipation into rock induces the pore pressure where the maximum value takes place near the joint of 2.5 MPa. In the present study, the discontinuous stress field and seepage field are not considered here.

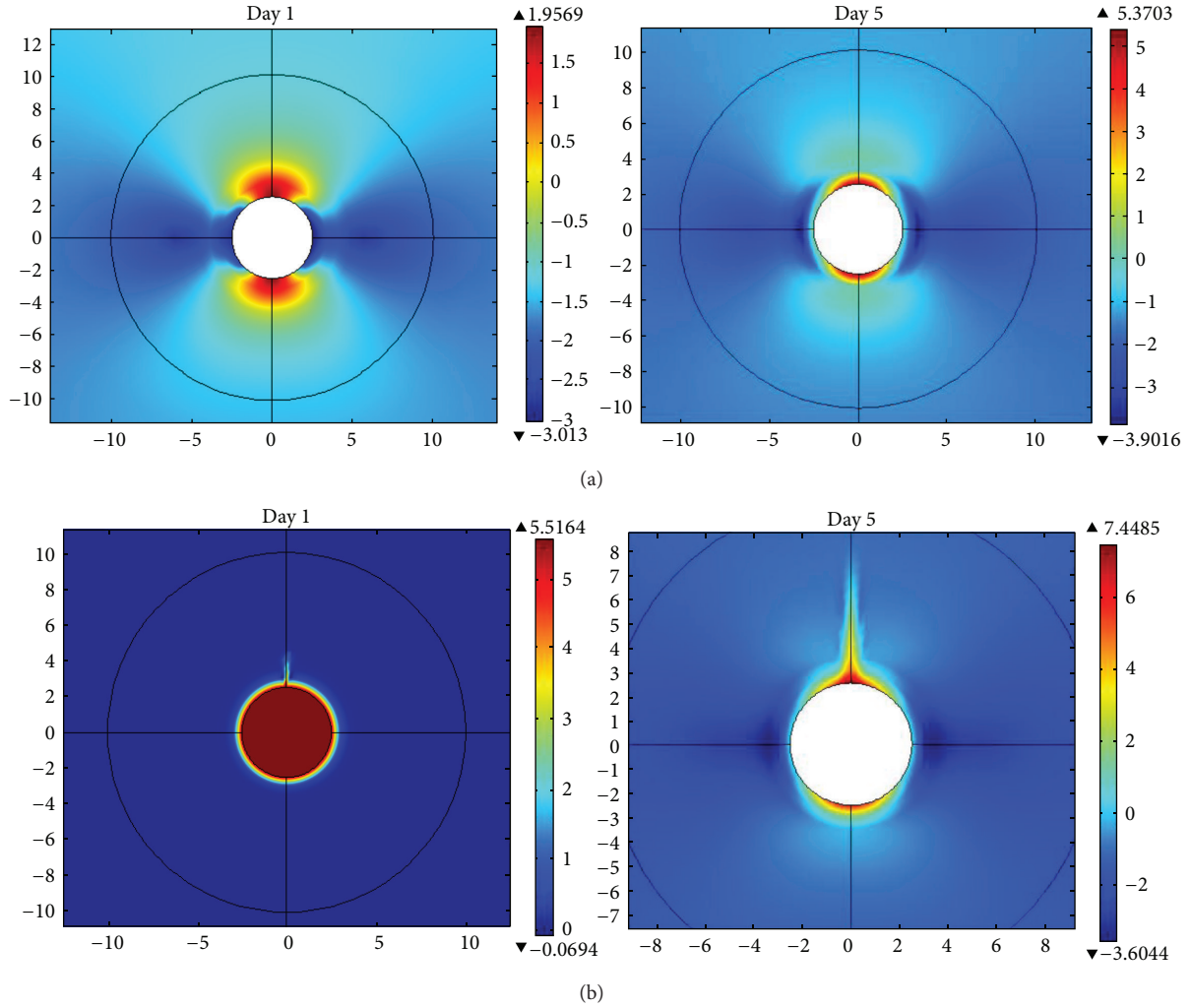


FIGURE 11: Comparison of the maximum principle stress in the rock cavern with and without joint on the ceiling. (a) Intact rock and (b) with single joint on the ceiling.

5. Discussions

In this paper, we investigate the feasibility of utilizing hard rock for compressed air energy storage by a coupled THM model. The energy loss, stress distribution, and pore pressure distribution during cyclic operational condition are studied. It was found that mass control based CAES operation results in energy loss and is not feasible in substantial hard rock cavern. Supplementary air injection is needed to maintain the required pressure level. For rock cavern with single joint, higher fluctuation of pressure and temperatures are found which is unfavorable for CAES system stability. The energy loss is significantly increased due to the crack and the principle. In the air injection modelling, the injection rate is based on the density loss of mass control condition after 60 days of operational condition. A constant air supplement of 3.25% is adopted. However, it is only an average means of injection while in the real seepage field and the supplementary injection should be dynamical to maintain designed pressure value. Only a single static crack is studied

in the present work. The crack propagation due to cyclic THM actions is not considered. These two problems can be the topics for further study.

Conflict of Interests

The authors declare that there is no conflict of interests regarding the publication of this paper.

Acknowledgments

The authors acknowledge the support of the Natural Science Foundation of China (NSFC 41130751 and 51278378), the National Basic Research Program of China (973 program: 2011CB013800), the Opening fund of State Key Laboratory of Geohazard Prevention and Geoenvironment Protection (Chengdu University of Technology) SKLGP2011K044, the National 863 programme (SS2012AA052501) the Shanghai Chenguang Talent program (12CG20), and program for

Changjiang Scholars and Innovative Research Team in University (PCSIRT, IRT1029). Thanks to Mr Haiyang Wen for his help with the postprocessing of the numerical results.

References

- [1] M. Dopita and R. Williamson, "Clean energy Australia 2010," Tech. Rep., Clean Energy Council, Australian Academy of Sciences, 2010.
- [2] I. Hadjipaschalis, A. Poullikkas, and V. Efthimiou, "Overview of current and future energy storage technologies for electric power applications," *Renewable and Sustainable Energy Reviews*, vol. 13, no. 6-7, pp. 1513–1522, 2009.
- [3] H. Ibrahim, R. Younès, A. Ilinca, M. Dimitrova, and J. Perron, "Study and design of a hybrid wind-diesel-compressed air energy storage system for remote areas," *Applied Energy*, vol. 87, no. 5, pp. 1749–1762, 2010.
- [4] V. Vongmanee, "The renewable energy applications for uninterruptible power supply based on compressed air energy storage system," in *Proceedings of the IEEE Symposium on Industrial Electronics and Applications (ISIEA '09)*, pp. 827–830, Kuala Lumpur, Malaysia, October 2009.
- [5] Y. Makarov, B. Yang, J. DeSteele et al., "Wide-area energy storage and management system to balance intermittent resources in the Booneville power administration and California ISO control areas," Tech. Rep., Pacific Northwest National Laboratory, 2008.
- [6] V. de Biasi, "New solutions for energy storage and smart grid load management," *Gas Turbine World*, vol. 39, no. 2, pp. 22–26, 2009.
- [7] "Australian mines and mineral deposits," Geoscience Australia, 2012.
- [8] I. Glendenning, "Long-term prospects for compressed air storage," *Applied Energy*, vol. 2, no. 1, pp. 39–56, 1976.
- [9] F. Crotogino, K. U. Mohmeyer, and R. Scharf, "Huntorf CAES: more than 20 years of successful operation," in *Proceedings of the Spring 2001 Meeting*, Orlando, Fla, USA, April 2001.
- [10] M. Raju and S. Kumar Khaitan, "Modeling and simulation of compressed air storage in caverns: a case study of the Huntorf plant," *Applied Energy*, vol. 89, no. 1, pp. 474–481, 2012.
- [11] N. Michael, "Report on status of compressed air energy storage technology," in *Proceedings of the Internal Meeting on CAES Project of National 863 Program in Inner Mongolia*, Beijing, China, November 2011.
- [12] W. K. Song, D. W. Ryu, and Y. K. Lee, "Stability analysis of concrete plugs in a pilot cavern for compressed air energy storage," in *Proceedings of the 12th International Congress on Rock Mechanics of the International Society for Rock Mechanics (ISRM '11)*, pp. 1813–1816, Beijing, China, October 2011.
- [13] A. Dayan, J. Flesh, and C. Saltiel, "Drying of a porous spherical rock for compressed air energy storage," *International Journal of Heat and Mass Transfer*, vol. 47, no. 19-20, pp. 4459–4468, 2004.
- [14] J. Levine, G. Martin, R. Moutoux, and F. Barnes, "large scale electrical energy storage in Colorado," Tech. Rep., Colorado Energy Research Institute, 2007.
- [15] S. Miller, "Mining megawatts from compressed air," *IEEE Spectrum*, vol. 38, no. 8, pp. 27–28, 2001.
- [16] S. J. Bauer, "Underground aspects of underground compressed air energy storage," in *Proceedings of the Compressed Air Energy Storage Scoping Workshop (CAES '08)*, Columbia University, 2008.
- [17] X. Zhuang, C. E. Augarde, and K. M. Mathisen, "Fracture modeling using meshless methods and levels sets in 3D: framework and modeling," *International Journal for Numerical Methods in Engineering*, vol. 92, no. 11, pp. 969–998, 2012.
- [18] X. Zhuang, C. Augarde, and S. Bordas, "Accurate fracture modelling using meshless methods, the visibility criterion and level sets: Formulation and 2D modelling," *International Journal for Numerical Methods in Engineering*, vol. 86, no. 2, pp. 249–268, 2011.
- [19] N. Nguyen-Thanh, J. Muthu, X. Zhuang, and T. Rabczuk, "An adaptive three-dimensional RHT-splines formulation in linear elasto-statics and elasto-dynamics," *Computational Mechanics*, 2013.
- [20] X. Zhuang, R. Huang, H. Zhu, H. Askes, and K. Mathisen, "A new and simple locking-free triangular thick plate element using independent shear degrees of freedom," *Finite Elements in Analysis and Design*, vol. 75, pp. 1–7, 2013.
- [21] Y. Cai, X. Zhuang, and H. Zhu, "A generalized and efficient method for finite cover generation in the numerical manifold method," *International Journal of Computational Methods*, vol. 10, no. 5, Article ID 1350028, 19 pages, 2013.
- [22] X. Zhuang, H. Zhu, and C. Augarde, "An improved meshless Shepard and least square method possessing the delta property and requiring no singular weight function," *Computational Mechanics*, 2013.
- [23] N. Vu-Bac, H. Nguyen-Xuan, L. Chen et al., "A Phantom-node method with edge-based strain smoothing for linear elastic fracture mechanics," *Journal of Applied Mathematics*, vol. 2013, Article ID 978026, 12 pages, 2013.
- [24] Y. Jia, Y. Zhang, G. Xu, X. Zhuang, and T. Rabczuk, "Reproducing kernel triangular B-spline-based FEM for solving PDEs," *Computer Methods in Applied Mechanics and Engineering*, vol. 267, pp. 342–358, 2013.
- [25] H. H. Zhu, X. Zhuang, Y. C. Cai, and G. Ma, "High rock slope stability analysis using the enriched meshless shepard and least squares method," *International Journal of Computational Methods*, vol. 8, no. 2, pp. 209–228, 2011.
- [26] Y. C. Cai, X. Zhuang, and C. Augarde, "A new partition of unity finite element free from the linear dependence problem and possessing the delta property," *Computer Methods in Applied Mechanics and Engineering*, vol. 199, no. 17–20, pp. 1036–1043, 2010.
- [27] X. Zhuang, C. Heaney, and C. Augarde, "On error control in the element-free Galerkin method," *Engineering Analysis with Boundary Elements*, vol. 36, no. 3, pp. 351–360, 2012.
- [28] X. Zhuang and C. Augarde, "Aspects of the use of orthogonal basis functions in the element-free Galerkin method," *International Journal for Numerical Methods in Engineering*, vol. 81, no. 3, pp. 366–380, 2010.
- [29] T. Rabczuk and T. Belytschko, "Cracking particles: a simplified meshfree method for arbitrary evolving cracks," *International Journal for Numerical Methods in Engineering*, vol. 61, no. 13, pp. 2316–2343, 2004.
- [30] T. Rabczuk, T. Belytschko, and S. P. Xiao, "Stable particle methods based on Lagrangian kernels," *Computer Methods in Applied Mechanics and Engineering*, vol. 193, no. 12–14, pp. 1035–1063, 2004.
- [31] T. Rabczuk and G. Zi, "A meshfree method based on the local partition of unity for cohesive cracks," *Computational Mechanics*, vol. 39, no. 6, pp. 743–760, 2007.
- [32] T. Rabczuk and T. Belytschko, "A three-dimensional large deformation meshfree method for arbitrary evolving cracks,"

- Computer Methods in Applied Mechanics and Engineering*, vol. 196, no. 29-30, pp. 2777–2799, 2007.
- [33] T. Rabczuk, S. Bordas, and G. Zi, “On three-dimensional modelling of crack growth using partition of unity methods,” *Computers and Structures*, vol. 88, no. 23-24, pp. 1391–1411, 2010.
- [34] T. Chau-Dinh, G. Zi, P. S. Lee, T. Rabczuk, and J. H. Song, “Phantom-node method for shell models with arbitrary cracks,” *Computers and Structures*, vol. 92-93, pp. 242–246, 2012.
- [35] H. Talebi, C. Samaniego, E. Samaniego, and T. Rabczuk, “On the numerical stability and mass-lumping schemes for explicit enriched meshfree methods,” *International Journal for Numerical Methods in Engineering*, vol. 89, no. 8, pp. 1009–1027, 2012.
- [36] T. Rabczuk and E. Samaniego, “Discontinuous modelling of shear bands using adaptive meshfree methods,” *Computer Methods in Applied Mechanics and Engineering*, vol. 197, no. 6–8, pp. 641–658, 2008.
- [37] F. Tong, L. Jing, and R. W. Zimmerman, “A fully coupled thermo-hydro-mechanical model for simulating multiphase flow, deformation and heat transfer in buffer material and rock masses,” *International Journal of Rock Mechanics and Mining Sciences*, vol. 47, no. 2, pp. 205–217, 2010.
- [38] J. G. Wang, Y. Zhang, J. S. Liu, and B. Y. Zhang, “Numerical simulation of geofluid focusing and penetration due to hydraulic fracture,” *Journal of Geochemical Exploration*, vol. 106, no. 1–3, pp. 211–218, 2010.
- [39] T. Rabczuk, R. Gracie, J. H. Song, and T. Belytschko, “Immersed particle method for fluid-structure interaction,” *International Journal for Numerical Methods in Engineering*, vol. 81, no. 1, pp. 48–71, 2010.
- [40] G. I. Barenblatt and A. A. Gilman, “Nonequilibrium counterflow capillary impregnation,” *Journal of Engineering Physics and Thermophysics*, vol. 52, no. 3, pp. 335–339, 1987.
- [41] H. M. Kim, J. Rutqvist, D. W. Ryu, B. H. Choi, C. Sunwoo, and W. K. Song, “Exploring the concept of compressed air energy storage (CAES) in lined rock caverns at shallow depth: a modeling study of air tightness and energy balance,” *Applied Energy*, vol. 92, pp. 653–667, 2012.

Research Article

Dynamic Fracture in Thin Shells Using Meshfree Method

Y. Shie

Harbin Engineering University, College of Mechanical Engineering, Harbin, China

Correspondence should be addressed to Y. Shie; yshie@ymail.com

Received 14 September 2013; Accepted 11 November 2013; Published 16 January 2014

Academic Editor: Timon Rabczuk

Copyright © 2014 Y. Shie. This is an open access article distributed under the Creative Commons Attribution License, which permits unrestricted use, distribution, and reproduction in any medium, provided the original work is properly cited.

We present a meshfree approach to model dynamic fracture in thin structures. Material failure is modeled based on a stress-based criterion and viscoplastic is used to describe the material behavior in the bulk material. Material fracture is simply modeled by breaking bonds between neighboring particles. The method is applied to fracture of cylindrical thin structures under explosive loading. The loading is modelled by a pressure-time history. Comparisons between the computational results and experimental data illustrate the validity and robustness of the proposed method.

1. Introduction

Modeling dynamic fracture of thin-walled structures remains a challenging task in computational mechanics. Such applications are of major importance in civil engineering, aeronautical engineering, aerospace engineering, and mechanical engineering. Thin structures are often modelled by shell theory. When shear effects can be neglected, the Kirchhoff-Love (KL) condition requires C^1 continuity of the underlying discretization. Effective formulations exploiting the higher order continuity of the meshfree methods have been exploited by [1, 2] for the first time; see also the contribution by [3–5] in the context of Isogeometric Analysis. The contribution in [1, 2] includes also fracture of the thin structure under dynamic loading. In [6], a fully coupled fluid-structure interaction method for fracturing thin structure has been proposed. On the other hand, there are many applications where shear effects need to be accounted for. There are numerous finite element formulations based on Mindlin-Reissner theory; see, for example, the manuscripts by [7–21]. On the other hand, thin-walled structures can also be modelled by three-dimensional continuum modeling.

Meshfree methods [22–34] are promising alternatives to finite element methods for applications involving large deformations, fracture and fluid-structure interaction. Meshfree method commonly exploits Lagrangian formulation [35–43] for both fluid and structure but does not suffer drawbacks of

Lagrangian based finite element methods. They can handle large deformation and also fracture in a natural manner [44–51]. An excellent review of meshfree methods is given in [52, 53].

While there are many meshfree formulations for continua, there exist far less meshfree formulations for structures. A meshfree thin shell formulation based on KL theory has been presented by [54]. They employed the element-free Galerkin (EFG) method. Krysl et al. did not consider fracture. The first meshfree thin shell method for fracture was proposed by Rabczuk et al. [2]. This method was developed for linear and nonlinear materials and applied to static and dynamic problems. Moreover, it was developed for a finite-strain framework. The crack was modelled by partition-of-unity enrichment. Subsequently, [55–57] have simplified the treatment of cracks in thin shell and exploited an extrinsic basis [1]. However, the ill-posedness due to the enrichment scheme has not been addressed. Donning and Liu [58] used the reproducing kernel particle method (RKPM) [23] to model beam and plate elements. This approach has later been extended by [59]. Membranes and shells based on higher order approximations have been implemented by [60]. They report the higher order functions that are necessary to avoid locking. Wang and Chen [61] presented a locking-free meshfree formulation and showed that the Kirchhoff mode in the Mindlin plate can be reproduced by second-order approximations. Yagawa and Miyamura [62] combined a mixed

approach within a free mesh framework. They used discrete Kirchhoff theory. Other approaches for thin structures based on 3D continuum approaches have been developed, for example, by the group of Li et al. [63].

As we want to keep the methodology applicable for thin structures with and without shear deformations, we will use a 3D continuum formulation that can be used also for real 3D simulations. The method will be applied to fracturing cylindrical structures under explosive loading. As the interaction between the solid and the fluid is highly complex [64–66], we will use a pressure-time history for the loading. The loading will be estimated by explosion simulations in rigid cylinders. Material failure of the solid is realized by simply breaking bonds between neighboring particles once a certain threshold is exceeded.

The paper is structured as follows. We first present the meshfree method, then briefly the constitutive model, and finally the fracture criterion. Then, we apply the method to fracturing thin cylinders. The numerical simulations will be compared to experimental data. The paper will be summarized in the last section.

2. Weak Form and Meshfree Discretization

Let us consider the linear momentum equation in the weak form. It is given in a total Lagrangian description of motion by finding the displacement field \mathbf{u} for all $\delta\mathbf{u}$ such that the variation in the energy is zero as

$$\delta W = \delta W_{\text{int}} - \delta W_{\text{ext}} + \delta W_{\text{kin}} = 0 \quad (1)$$

with

$$\begin{aligned} \delta W_{\text{int}} &= \int_{\Omega_0} \nabla_X \delta \mathbf{u} : \mathbf{P} \, d\Omega_0 \\ \delta W_{\text{ext}} &= \int_{\Gamma_{0t}} \delta \mathbf{u} \cdot \bar{\mathbf{t}}_0 \, d\Gamma_0 + \int_{\Omega_0} \varrho_0 \delta \mathbf{u} \cdot \mathbf{b} \, d\Omega_0 \\ \delta W_{\text{kin}} &= \int_{\Omega_0} \varrho_0 \delta \mathbf{u} \cdot \dot{\mathbf{u}} \, d\Omega_0, \end{aligned} \quad (2)$$

where W_{int} and W_{ext} are the internal and external energy, respectively, W_{kin} denotes the kinetic energy, \mathbf{X} are the material coordinates, Ω_0 is the domain in the initial configuration and Γ_0 is the boundary in the initial configuration, \mathbf{b} denotes the body force, ϱ_0 is initial density, \mathbf{u} is displacement, \mathbf{P} is the first Piola-Kirchhoff stress tensor, $\bar{\mathbf{t}}_0$ is the applied traction, ∇_X denotes spatial derivatives with respect to material coordinate, and superimposed dots denote material time derivatives.

The boundary conditions are given by

$$\begin{aligned} \mathbf{u} &= \bar{\mathbf{u}}, \quad \mathbf{X} \in \Gamma_{0u} \\ \mathbf{n} \cdot \mathbf{P} &= \mathbf{t}_0 = \bar{\mathbf{t}}_0, \quad \mathbf{X} \in \Gamma_{0t} \end{aligned} \quad (3)$$

with boundaries $\Gamma_{0u} \cup \Gamma_{0t} = \Gamma_0$ and $\Gamma_{0u} \cap \Gamma_{0t} = \emptyset$, the index t referring to traction boundaries and the index u to displacement boundaries; \mathbf{n} is the normal vector to the traction boundary.

The discretization of the displacement field in the mesh-free approximation is given by

$$\mathbf{u}^h(\mathbf{X}) = \sum_{J=1}^n N_J(\mathbf{X}) \mathbf{u}_J = \mathbf{N}\mathbf{u}, \quad (4)$$

where $N_J(\mathbf{X})$ denotes the meshfree shape functions and n denotes the number of particles. The EFG method [22] is based on a moving least squares approximation. It can be shown that the shape functions are expressed by

$$\mathbf{N}^T(\mathbf{X}) = \mathbf{p}^T(\mathbf{X}) \mathbf{A}^{-1}(\mathbf{X}) \mathbf{P}\mathbf{W}(\mathbf{X}) \quad (5)$$

with the moment matrix

$$\mathbf{A}(\mathbf{X}) = \mathbf{P}(\mathbf{Y}) \mathbf{W}(\mathbf{X}) \mathbf{P}^T(\mathbf{Y}), \quad (6)$$

where the matrix $\mathbf{P}^T(\mathbf{Y})$ contains the polynomial basis \mathbf{p} . We employ linear basis polynomials to ensure that the method fulfills the patch test. The matrix

$$\mathbf{W}(\mathbf{X}) = \text{diag} \{W_I(\mathbf{X} - \mathbf{X}_I, h) V_I\}, \quad I = 1, \dots, n, \quad (7)$$

contains usually rational weighting functions $W_I(\mathbf{X} - \mathbf{X}_I, h)$. For computational efficiency, usually weighting functions with compact support are chosen; h is the dilation parameter determining the size of the domain of influence of a central particle. We use the quartic B-spline function:

$$\begin{aligned} W(\mathbf{X} - \mathbf{X}_I, h) &= w(s) \\ &= \begin{cases} 1 - 6s^2 + 8s^3 - 3s^4 & s \leq 1 \\ 0 & s > 1 \end{cases} \end{aligned} \quad (8)$$

with $s = (\mathbf{X} - \mathbf{X}_I)/2h$.

The test and trial functions have the structure of (4). Substituting them into the weak formulation leads to the following equation:

$$\begin{aligned} \sum_{I=1}^n \delta \mathbf{u}_I \left\{ \sum_{J=1}^n - \int_{\Omega_0} \nabla_X N_I(\mathbf{X}) \mathbf{P} \, d\Omega_0 + \int_{\Omega_0} N_I(\mathbf{X}) \mathbf{b} \, d\Omega_0 \right. \\ \left. + \int_{\Gamma_{0t}} N_I(\mathbf{X}) \bar{\mathbf{t}}_0 \, d\Gamma_0 + \int_{\Omega_0} \varrho_0 N_I(\mathbf{X}) N_J(\mathbf{X}) \mathbf{u} \, d\Omega_0 \right\} \\ = 0. \end{aligned} \quad (9)$$

After some algebraic operations, the well-known equation of motion is obtained as

$$\mathbf{M}_{IJ} \ddot{\mathbf{u}}_J = -\mathbf{f}_I^{\text{ext}} + \mathbf{f}_I^{\text{int}} \quad (10)$$

with

$$\begin{aligned} \mathbf{M}_{IJ} &= \int_{\Omega_0} \varrho N_I(\mathbf{X}) \mathbf{N}_J^T(\mathbf{X}) \, d\Omega_0 \\ \mathbf{f}_I^{\text{ext}} &= \int_{\Gamma_{0t}} \mathbf{N}_I^T(\mathbf{X}) \bar{\mathbf{t}}_0 \, d\Gamma_0 + \int_{\Omega_0} \mathbf{N}_I^T(\mathbf{X}) \mathbf{b} \, d\Omega_0 \\ \mathbf{f}_I^{\text{int}} &= \int_{\Omega_0} \nabla_X \mathbf{N}_I^T(\mathbf{X}) \mathbf{P} \, d\Omega_0. \end{aligned} \quad (11)$$

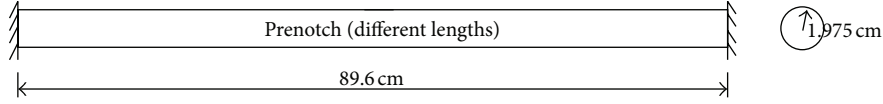


FIGURE 1: Implosively loaded tube with different notch length: 1.1 inches, 2.2 inches, and 3.3 inches; notch depth is 0.6 mm.

3. Material Model

A viscoplastic constitutive model from Zhou et al. [67] is used to describe the material behavior in the bulk. The material model in the bulk is of utmost importance for reliable predictions of material and structural behavior. Thermal effects are incorporated into the constitutive model as they are crucial in dynamic fracture simulations of thin structures as presented in this paper. The rate equations can be expressed in terms of the Jaumann rate of the Kirchhoff stress by

$$\boldsymbol{\tau}^{\nabla} = \mathbf{C} : (\mathbf{D} - \mathbf{D}^{vp} - \alpha \dot{\mathbf{T}}\mathbf{I}), \quad (12)$$

where \mathbf{C} is the fourth order elasticity tensor, \mathbf{D} is the symmetric part of the velocity gradient \mathbf{L} , $\boldsymbol{\tau}^{\nabla} = \dot{\boldsymbol{\tau}} - \mathbf{W} \cdot \boldsymbol{\tau} - \boldsymbol{\tau} \cdot \mathbf{W}$ is the Jaumann rate of the Kirchhoff stress, with \mathbf{W} being the anti-symmetric part of the velocity gradient, α is the thermal expansion coefficient, and \mathbf{I} is the second-order identity matrix. The viscoplastic overstress model here is based on von Mises as

$$\mathbf{D}^{vp} = \left(\frac{3\bar{\dot{\epsilon}}}{2\bar{\sigma}} \right) \bar{\mathbf{s}} \quad (13)$$

with

$$\bar{\mathbf{s}} = \mathbf{s} - \mathbf{a} \quad \text{with } \mathbf{s} = \frac{\boldsymbol{\tau} - 1}{3 \text{tr}(\boldsymbol{\tau})} \mathbf{I}, \quad \bar{\sigma} = \frac{3}{2\bar{\mathbf{s}}} : \bar{\mathbf{s}}, \quad (14)$$

with \mathbf{a} being the back stress which is assumed to be zero here. A power law governs the thermal viscoplastic flow by

$$\bar{\dot{\epsilon}} = \dot{\epsilon}_0 \left(\frac{\bar{\sigma}}{g(\bar{\epsilon}, T)} \right)^m \quad (15)$$

with

$$g(\bar{\epsilon}, T) = \bar{\sigma} \left(1 + \frac{\bar{\epsilon}}{\epsilon_0} \right)^n \left(1 - \delta \left[\exp \left(\frac{T - T_0}{\kappa} \right) - 1 \right] \right). \quad (16)$$

In (15) and (16), $\dot{\epsilon}_0$ is a reference strain rate, m is the rate sensitivity parameter, σ_0 is the yield stress, $\epsilon_0 = \sigma_0/E$ is the corresponding reference strain and E is Young's modulus, n is the strain hardening exponent, T_0 is a reference temperature, and δ and κ are thermal softening parameters. The function $g(\bar{\epsilon}, T)$ is the stress-strain relation measured at quasistatic strain rate of $\dot{\epsilon}$ at temperature T . The equivalent plastic strain $\bar{\epsilon}$ is defined as

$$\bar{\epsilon} = \int_0^t \bar{\dot{\epsilon}} dt = \int_0^t \sqrt{\frac{2}{3} \mathbf{D}^{vp} : \mathbf{D}^{vp}} dt. \quad (17)$$

Softening in material due to temperature is accounted for by varying material parameters

$$\begin{aligned} E(T) &= E_0 - 1.6 \times 10^6 (T - T_0) - 10^5 (T - T_0)^2 \quad [\text{Pa}] \\ \nu &= \nu_0 + 5 \times 10^{-5} (T - T_0) \\ \sigma_0(T) &= \sigma_0 - 1.5 \times 10^3 (T - T_0)^2 \quad [\text{Pa}] \\ \alpha(T) &= (2.2 + 0.0016 [T - T_0]) \times 10^{-5} \quad [\text{K}^{-1}], \end{aligned} \quad (18)$$

where E and ν are Young's modulus and the Poisson ratio at temperature T .

We employ the tangent modulus approach to update the thermal viscoplastic constitutive model. The details of the scheme can be found in the excellent manuscript by [68].

A stress-based criterion is employed to model fracture. Connectivities between neighboring nodes are broken when the maximum principal tensile strength is three times the strength σ_0 . More sophisticated models based, for example, on loss of material stability might be used in future research.

4. Results

We validate our computational approach by comparison with experimental results. Therefore, we compare our numerical results to the fracture experiments by [69] who studied the failure mechanism of thin aluminum cylinders under detonation loading. They found that the failure mechanism changes with the length of the longitudinal precracks. Classical test set-up of their experiments is illustrated in Figure 1. The length of the initial cracks varies from 1'' to 3'':

- (i) 1'' (short notch),
- (ii) 2'' (medium-length notch),
- (iii) 3'' (long notch).

In the experiments, the cylinder is filled with a combustible gas consisting of oxygen and ethylene. The pressure after ignition varies between 80 kPa and 180 kPa. After the gas is ignited at the left end, a detonation wave travels through the cylinder. In the thin aluminum specimen, pressures close to the Chapman-Jouguet (CJ) limit were measured. Its velocity is between 2300 m/s and 2400 m/s and the pressure values in the fully recreated CJ state range from 2.6 MPa to 6.1 MPa (depending on the initial pressure).

As it is computationally expensive to carry out a fully coupled FSI simulation as, for example, done in [6], we first study the pure detonation in a rigid tube needed to estimate the pressure-time history conditions in the aluminum cylinder. Those simulations are also based on meshfree simulations where the fluid is modelled with the element-free Galerkin

method. A single exothermic chemical reaction $A \rightarrow B$ with a progress variable Y corresponding to the mass fraction ratio between the partial density of the reactant A and the total density ρ , that is, $Y = \rho_A/\rho$, governs the detonation by a modified Euler equation that contains additional inhomogeneous conservation laws:

$$(\dot{Y}\rho) + \nabla \cdot (Y\rho\mathbf{u}) = \Psi. \quad (19)$$

The chemical reaction follows the Arrhenius law [70]

$$\Psi = -kY\rho \exp\left(\frac{-E_A\rho}{p}\right), \quad (20)$$

with p being obtained from the following equation of state:

$$p = (\gamma - 1)(\rho e - \rho Yq), \quad (21)$$

where the parameter q denotes the heat release due to the chemical reaction per unit mass [70]. The volume burn model according to [71] is exploited in order to guarantee the correct propagation speed and state in chemical equilibrium at all points in the discretization. Figure 2 illustrates the pressure-time history exemplarily for one point close to the precrack. The pressure at the entire interior surface is monitored during the course of the simulation and subsequently applied as pressure-time history to study the fracture behavior of thin aluminum cylinders. We are aware that effects due to the changing structure after deformation are not included in our model. These effects might have a significant influence in particular on fatal failure as the results below indicate. As stated previously, a fully coupled FSI model might be inevitable in this case.

For the fracture simulations, we employ discretizations of different refinements ranging from 140,000 particles to 280,000 particles. The following material parameters are used for all simulations: $E = 69$ GPa, $\rho = 2719$ kg/m³, $\nu = 0.33$, $\sigma_0 = 275$ GPa, $\epsilon_0^p = 0.001$, $1/n = 0.07$, and $1/m = 0.01$.

4.1. Short Notch. Figure 3 shows the deformed cylinder for a short notch. The crack grows straight in longitudinal direction. At a certain point, it curves in a 45-degree angle and continues to propagate in circumferential direction before it is arrested. At the end of the simulation, the fracture encompasses approximately 75% of the circumference. Similar results were obtained in the experiments from Chao [69] suggesting that effects due to fluid-structure interaction are not relevant.

5. Medium-Length Notch

Different failure pattern is observed for the medium-length notched cylinder. In the experiments, the fracture farther from the detonation wave propagated first. After initial straight crack propagation, the fracture branched in 2 circumferential cracks separating the specimen in 2 pieces; see Figure 4.

Our computational results also predict severe failure though we are not capable of capturing the complete separation of the cylinder into two pieces. The fractures grow in two

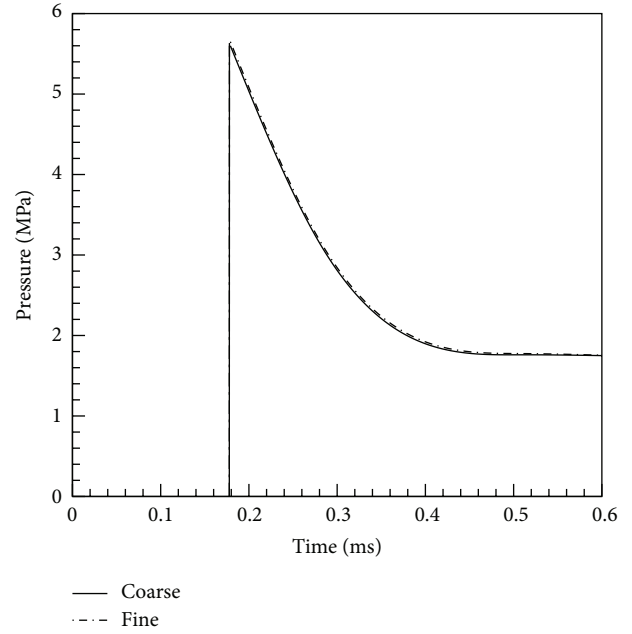


FIGURE 2: Pressure over the time of a particle close to the notch from a pure fluid simulation of gas detonation in rigid specimen; fine refers to a discretization with around 1,900,000 particles while the coarse discretization refers to a discretization with around 600,000 particles.

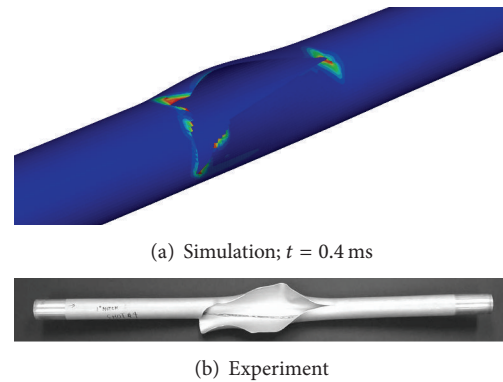


FIGURE 3: Displaced configuration and effective stress of the detonation-driven fracture of cylinder; notch length is 1".

directions simultaneously and quickly turn into radial directions. The crack opening is more pronounced as for the short notch though. However, the fracture does not encompass the circumference. We believe that FSI simulations might be able to capture the failure mechanism better.

6. Long Notch

When the notch length is increased to 3", the specimen was broken into three pieces (in the experiments). This behavior is indeed captured well by our numerical simulations. Fractures grow first in longitudinal direction again. Several branches evolve leading finally to the failure illustrated in Figures 5 and 6.

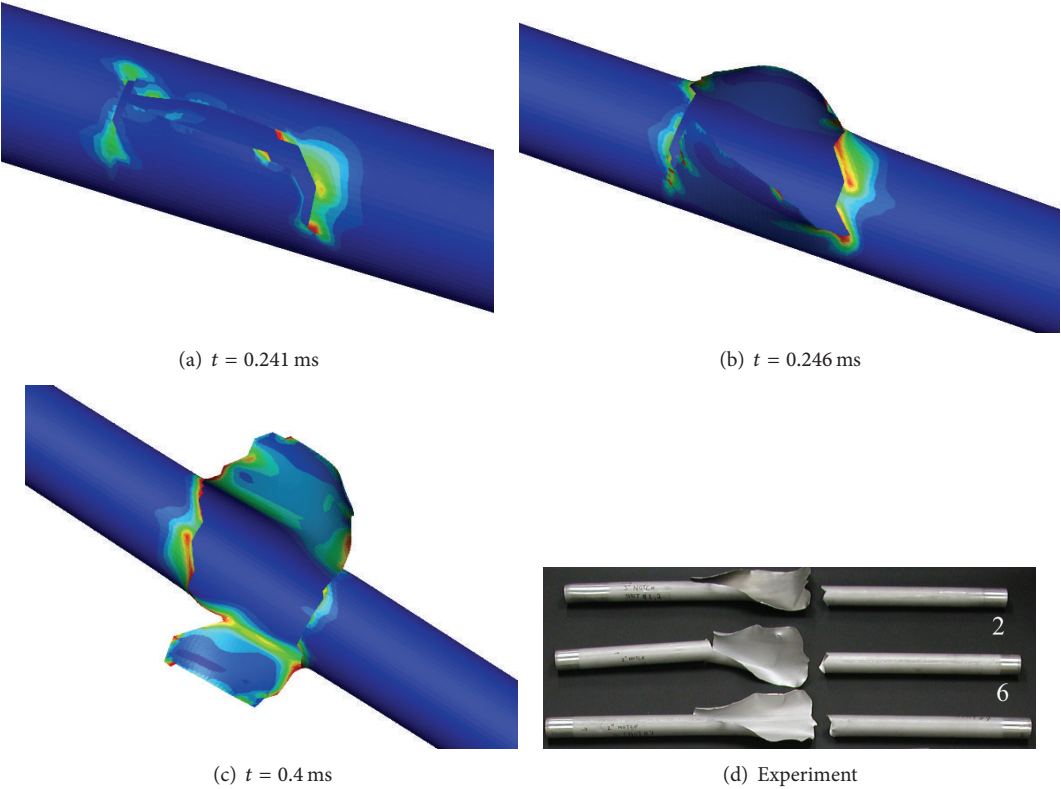


FIGURE 4: Displaced configuration and effective stress of the detonation-driven fracture of cylinder at different times; notch length is 2".

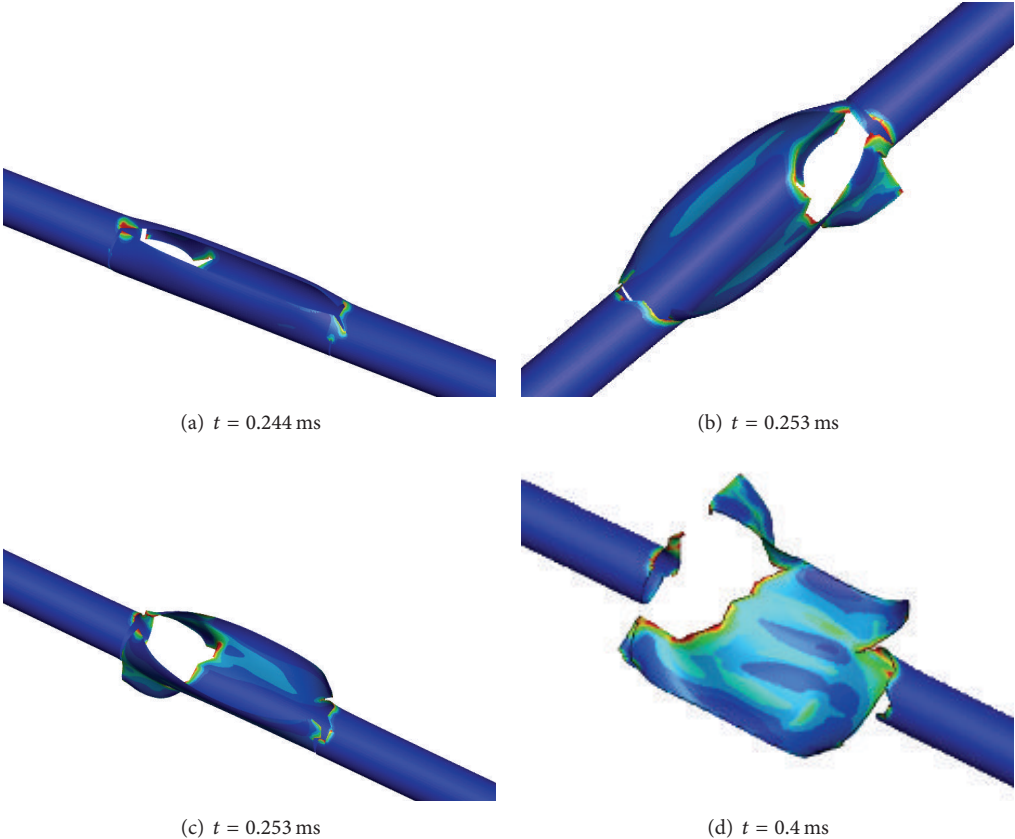


FIGURE 5: Displaced configuration and effective stress of the detonation-driven fracture of cylinder at different times; notch length is 3".

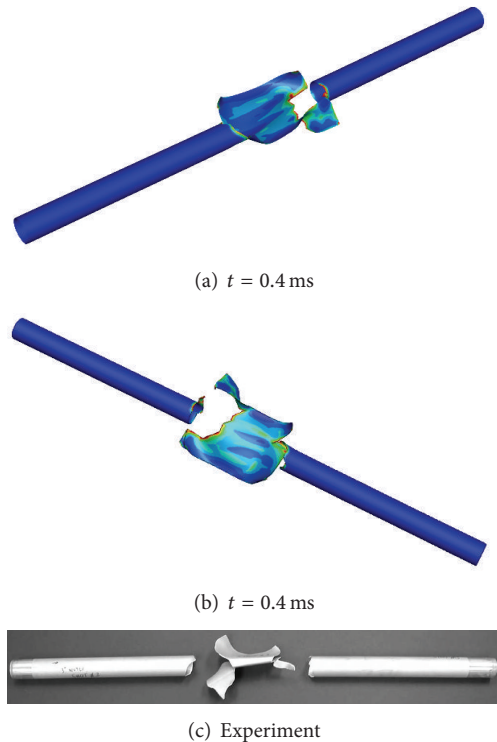


FIGURE 6: Displaced configuration and effective stress of the detonation-driven fracture of cylinder; notch length is 3".

7. Conclusions

In conclusion, we presented a simple and robust meshfree method for dynamic fracture in thin structures. The method is based on a 3D continuum approach and a simple fracture criterion is used to nucleate or propagate a crack. A viscoplastic model is employed in the bulk.

The method was applied to dynamic fracture in thin aluminum cylinders. The experiments from [69] were exploited to validate our method. In those experiments, a shock wave initiated by an explosive mixture was propagating through the aluminum cylinders. Different notch lengths were studied in their experiments, ranging from 1" to 3". As it is computationally and extremely challenging to model the entire process, we first performed simulations of the explosion in rigid tubes. The pressures in the rigid tubes were monitored during the course of the simulation and in a second step applied as boundary conditions to the thin aluminum cylinder, the specimen of interest. In other words: our simulations neglect effects due to fluid-structure interaction. Nevertheless, for the 1" and 3" notched specimen, our numerical simulations were able to capture the appropriate failure mechanisms while for the 2", we observed discrepancies to the experimental results.

Future studies will therefore focus on the extension of our model to fluid-structure interaction. Moreover, we intend to incorporate more advanced fracture models as proposed, for example, by [39, 72–75].

Conflict of Interests

The author declares that there is no conflict of interests regarding the publication of this article.

References

- [1] T. Rabczuk and P. Areias, "A meshfree thin shell for arbitrary evolving cracks based on an extrinsic basis," *Computer Modeling in Engineering and Sciences*, vol. 16, no. 2, pp. 115–130, 2006.
- [2] T. Rabczuk, P. M. A. Areias, and T. Belytschko, "A meshfree thin shell method for non-linear dynamic fracture," *International Journal for Numerical Methods in Engineering*, vol. 72, no. 5, pp. 524–548, 2007.
- [3] N. Nguyen-Thanh, J. Kiendl, H. Nguyen-Xuan, R. Wüchner, K. U. Bletzinger, and Y. Bazilevs, "Rotation free isogeometric thin shell analysis using PHT-splines," *Computer Methods in Applied Mechanics and Engineering*, vol. 200, no. 47–48, pp. 3410–3424, 2011.
- [4] D. J. Benson, Y. Bazilevs, M.-C. Hsu, and T. J. R. Hughes, "A large deformation, rotation-free, isogeometric shell," *Computer Methods in Applied Mechanics and Engineering*, vol. 200, no. 13–16, pp. 1367–1378, 2011.
- [5] N. Nguyen-Thanh, H. Nguyen-Xuan, S. P. A. Bordas, and T. Rabczuk, "Isogeometric analysis using polynomial splines over hierarchical T-meshes for two-dimensional elastic solids," *Computer Methods in Applied Mechanics and Engineering*, vol. 200, no. 21–22, pp. 1892–1908, 2011.
- [6] T. Rabczuk, R. Gracie, J.-H. Song, and T. Belytschko, "Immersed particle method for fluid-structure interaction," *International Journal for Numerical Methods in Engineering*, vol. 81, no. 1, pp. 48–71, 2010.
- [7] H. Nguyen-Xuan, T. Rabczuk, N. Nguyen-Thanh, T. Nguyen-Thoi, and S. Bordas, "A node-based smoothed finite element method with stabilized discrete shear gap technique for analysis of Reissner-Mindlin plates," *Computational Mechanics*, vol. 46, no. 12, pp. 679–701, 2010.
- [8] N. Nguyen-Thanh, T. Rabczuk, H. Nguyen-Xuan, and S. Bordas, "An alternative alpha finite element method with discrete shear gap technique for analysis of isotropic Mindlin-Reissner plates," *Finite Elements in Analysis and Design*, vol. 47, no. 5, pp. 519–535, 2011.
- [9] N. Valizadeh, S. Natarajan, O. A. Gonzalez-Estrada, T. Rabczuk, T. Quoc Bui, and S. Bordas, "Nurbs-based finite element analysis of functionally graded plates: static bending, vibration, buckling and flutter," *Composite Structures*, vol. 99, pp. 309–326, 2013.
- [10] C. H. Thai, H. Nguyen-Xuan, N. Nguyen-Thanh, T.-H. Le, T. Nguyen-Thoi, and T. Rabczuk, "Static, free vibration, and buckling analysis of laminated composite Reissner-Mindlin plates using NURBS-based isogeometric approach," *International Journal for Numerical Methods in Engineering*, vol. 91, no. 6, pp. 571–603, 2012.
- [11] T. Nguyen-Thoi, P. Phung-Van, T. Rabczuk, H. Nguyen-Xuan, and C. Le-Van, "Free and forced vibration analysis using the n-sided polygonal cell-based smoothed finite element method (ncs-fem)," *International Journal of Computational Methods*, vol. 10, no. 1, Article ID 13400082, 2013.
- [12] P. Areias, T. Rabczuk, D. Dias-da-Costa, and E. B. Pires, "Implicit solutions with consistent additive and multiplicative components," *Finite Elements in Analysis and Design*, vol. 57, pp. 15–31, 2012.

- [13] P. Areias and T. Rabczuk, "Finite strain fracture of plates and shells with configurational forces and edge rotation," *International Journal For Numerical Methods in Engineering*, vol. 94, pp. 1099–1122, 2013.
- [14] P. Areias, T. Rabczuk, and D. Dias da Costa, "Assumed-metric spherically-interpolated quadrilateral shell element," *Finite Elements in Analysis and Design*, vol. 66, pp. 53–67, 2013.
- [15] H. Nguyen-Xuan, T. Rabczuk, S. Bordas, and J. F. Debongnie, "A smoothed finite element method for plate analysis," *Computer Methods in Applied Mechanics and Engineering*, vol. 197, no. 13–16, pp. 1184–1203, 2008.
- [16] H. Nguyen-Xuan, T. Rabczuk, T. Nguyen-Thoi, T. N. Tran, and N. Nguyen-Thanh, "Computation of limit and shakedown loads using a node-based smoothed finite element method," *International Journal for Numerical Methods in Engineering*, vol. 90, no. 3, pp. 287–310, 2012.
- [17] H. H. Phan-Do, H. Nguyen-Xuan, C. Thai-Hoang, T. Nguyen-Thoi, and T. Rabczuk, "An edge-based smoothed finite element method for analysis of laminated composite plates," *International Journal of Computational Methods*, vol. 10, no. 1, Article ID 13400057, 2013.
- [18] C. Thai-Hoang, N. Nguyen-Thanh, H. Nguyen-Xuan, and T. Rabczuk, "An alternative alpha finite element method with discrete shear gap technique for analysis of laminated composite plates," *Applied Mathematics and Computation*, vol. 217, no. 17, pp. 7324–7348, 2011.
- [19] N. Nguyen-Thanh, T. Rabczuk, H. Nguyen-Xuan, and S. P. A. Bordas, "A smoothed finite element method for shell analysis," *Computer Methods in Applied Mechanics and Engineering*, vol. 198, no. 2, pp. 165–177, 2008.
- [20] T. Chau-Dinh, G. Zi, P.-S. Lee, T. Rabczuk, and J.-H. Song, "Phantom-node method for shell models with arbitrary cracks," *Computers and Structures*, vol. 92–93, pp. 242–246, 2012.
- [21] P. Baiz, S. Natarajan, S. Bordas, P. Kerfriden, and T. Rabczuk, "Linear buckling analysis of cracked plates by sfem and xfem (smxfem)," *Journal of Mechanics of Materials and Structures*, vol. 6, no. 9–10, pp. 1213–1238, 2011.
- [22] T. Belytschko, Y. Y. Lu, and L. Gu, "Element-free Galerkin methods," *International Journal for Numerical Methods in Engineering*, vol. 37, no. 2, pp. 229–256, 1994.
- [23] W. K. Liu, S. Jun, and Y. F. Zhang, "Reproducing kernel particle methods," *International Journal for Numerical Methods in Engineering*, vol. 20, pp. 1081–1106, 1995.
- [24] T. Rabczuk and E. Samaniego, "Discontinuous modelling of shear bands using adaptive meshfree methods," *Computer Methods in Applied Mechanics and Engineering*, vol. 197, no. 6–8, pp. 641–658, 2008.
- [25] T. Rabczuk and P. M. A. Areias, "A new approach for modelling slip lines in geological materials with cohesive models," *International Journal for Numerical and Analytical Methods in Geomechanics*, vol. 30, no. 11, pp. 1159–1172, 2006.
- [26] W. K. Liu, S. Hao, T. Belytschko, S. Li, and C. T. Chang, "Multiple scale meshfree methods for damage fracture and localization," *Computational Materials Science*, vol. 16, no. 1–4, pp. 197–205, 1999.
- [27] M. R. Moosavi, F. Delfanian, A. Khelil, and T. Rabczuk, "Orthogonal meshless finite volume method in elastodynamics," *Thin-Walled Structures*, vol. 49, no. 9, pp. 1171–1177, 2011.
- [28] P. B. H. Le, T. Rabczuk, N. Mai-Duy, and T. Tran-Cong, "A moving IRBFN-based Galerkin meshless method," *Computer Modeling in Engineering & Sciences*, vol. 66, no. 1, pp. 25–52, 2010.
- [29] P. B. H. Le, T. Rabczuk, N. Mai-Duy, and T. Tran-Cong, "A moving IRBFN-based integration-free meshless method," *Computer Modeling in Engineering & Sciences*, vol. 61, no. 1, pp. 63–109, 2010.
- [30] H. Talebi, C. Samaniego, E. Samaniego, and T. Rabczuk, "On the numerical stability and mass-lumping schemes for explicit enriched meshfree methods," *International Journal for Numerical Methods in Engineering*, vol. 89, no. 8, pp. 1009–1027, 2012.
- [31] Y. Cai, X. Zhuang, and H. Zhu, "A generalized and efficient method for finite cover generation in the numerical manifold method," *International Journal of Computational Methods*, vol. 10, no. 5, Article ID 1350028, 19 pages, 2013.
- [32] X. Zhuang, C. Augarde, and K. Mathisen, "Fracture modelling using meshless methods and level sets in 3D: framework and modelling," *International Journal For Numerical Methods in Engineering*, vol. 92, pp. 969–998, 2012.
- [33] H. Zhu, X. Zhuang, and Y. Cai, "High rock slope stability analysis using the enriched meshless Shepard and least squares method," *International Journal of Computational Methods*, vol. 8, pp. 209–228, 2011.
- [34] W. Zheng, X. Zhuang, and Y. Cai, "A new method for seismic stability analysis of anchored rock slope and its application in anchor optimization," *Frontiers of Structural and Civil Engineering*, vol. 6, pp. 111–120, 2012.
- [35] T. Rabczuk and J. Eibl, "Simulation of high velocity concrete fragmentation using SPH/MLSPH," *International Journal for Numerical Methods in Engineering*, vol. 56, no. 10, pp. 1421–1444, 2003.
- [36] S. R. Idelsohn, E. Oñate, and F. Del Pin, "The particle finite element method: a powerful tool to solve incompressible flows with free-surfaces and breaking waves," *International Journal for Numerical Methods in Engineering*, vol. 61, no. 7, pp. 964–989, 2004.
- [37] S. Hao, W. K. Liu, and D. Qian, "Localization-induced band and cohesive model," *Journal of Applied Mechanics*, vol. 67, no. 4, pp. 803–812, 2000.
- [38] T. Rabczuk and T. Belytschko, "Adaptivity for structured mesh-free particle methods in 2D and 3D," *International Journal for Numerical Methods in Engineering*, vol. 63, no. 11, pp. 1559–1582, 2005.
- [39] T. Rabczuk, T. Belytschko, and S. P. Xiao, "Stable particle methods based on Lagrangian kernels," *Computer Methods in Applied Mechanics and Engineering*, vol. 193, no. 12–14, pp. 1035–1063, 2004.
- [40] T. Rabczuk, P. M. A. Areias, and T. Belytschko, "A simplified mesh-free method for shear bands with cohesive surfaces," *International Journal for Numerical Methods in Engineering*, vol. 69, no. 5, pp. 993–1021, 2007.
- [41] S. Hao, W. K. Liu, P. A. Klein, and A. J. Rosakis, "Modeling and simulation of intersonic crack growth," *International Journal of Solids and Structures*, vol. 41, no. 7, pp. 1773–1799, 2004.
- [42] S. Hao and W. K. Liu, "Moving particle finite element method with superconvergence: nodal integration formulation and applications," *Computer Methods in Applied Mechanics and Engineering*, vol. 195, no. 44–47, pp. 6059–6072, 2006.
- [43] T. Rabczuk, S. P. Xiao, and M. Sauer, "Coupling of mesh-free methods with finite elements: basic concepts and test results," *Communications in Numerical Methods in Engineering with Biomedical Applications*, vol. 22, no. 10, pp. 1031–1065, 2006.
- [44] F. Del Pin, S. Idelsohn, E. Oñate, and R. Aubry, "The ALE/Lagrangian particle finite element method: a new

- approach to computation of free-surface flows and fluid-object interactions," *Computers and Fluids*, vol. 36, no. 1, pp. 27–38, 2007.
- [45] S. R. Idelsohn, J. Marti, A. Limache, and E. Oñate, "Unified Lagrangian formulation for elastic solids and incompressible fluids: application to fluid-structure interaction problems via the PFEM original," *Computer Methods in Applied Mechanics and Engineering*, vol. 197, no. 19–20, pp. 1762–1776, 2008.
- [46] S. R. Idelsohn, E. Oñate, F. Del Pin, and N. Calvo, "Fluid-structure interaction using the particle finite element method," *Computer Methods in Applied Mechanics and Engineering*, vol. 195, no. 17–18, pp. 2100–2123, 2006.
- [47] S. Idelsohn, M. Mier-Torrecilla, and E. Oñate, "Multi-fluid flows with the particle finite element method," *Computer Methods in Applied Mechanics and Engineering*, vol. 198, no. 33–36, pp. 2750–2767, 2009.
- [48] T. Rabczuk, J. Eibl, and L. Stempniewski, "Numerical analysis of high speed concrete fragmentation using a meshfree Lagrangian method," *Engineering Fracture Mechanics*, vol. 71, pp. 547–556, 2004.
- [49] T. Rabczuk and J. Eibl, "Numerical analysis of prestressed concrete beams using a coupled element free Galerkin/finite element method," *International Journal of Solids and Structures*, vol. 41, no. 3–4, pp. 1061–1080, 2004.
- [50] E. Oñate, S. Idelsohn, O. C. Zienkiewicz, R. L. Taylor, and C. Sacco, "A stabilized finite point method for analysis of fluid mechanics problems," *Computer Methods in Applied Mechanics and Engineering*, vol. 139, no. 1–4, pp. 315–346, 1996.
- [51] T. Nguyen-Thoi, H. C. Vu-Do, T. Rabczuk, and H. Nguyen-Xuan, "A node-based smoothed finite element method (NS-FEM) for upper bound solution to visco-elastoplastic analysis of solids using triangular and tetrahedral meshes," *Computer Methods in Applied Mechanics and Engineering*, vol. 199, no. 45–48, pp. 3005–3027, 2010.
- [52] V. P. Nguyen, T. Rabczuk, S. Bordas, and M. Duflot, "Meshless methods: a review and computer implementation aspects," *Mathematics and Computers in Simulation*, vol. 79, no. 3, pp. 763–813, 2008.
- [53] S. R. Idelsohn and E. Oñate, "To mesh or not to mesh. That is the question..." *Computer Methods in Applied Mechanics and Engineering*, vol. 195, no. 37–40, pp. 4681–4696, 2006.
- [54] P. Krysl and T. Belytschko, "Analysis of thin shells by the element-free Galerkin method," *International Journal for Numerical Methods in Engineering*, vol. 33, no. 20–22, pp. 3057–3078, 1996.
- [55] T. Rabczuk and T. Belytschko, "Cracking particles: a simplified meshfree method for arbitrary evolving cracks," *International Journal for Numerical Methods in Engineering*, vol. 61, no. 13, pp. 2316–2343, 2004.
- [56] T. Rabczuk, J.-H. Song, and T. Belytschko, "Simulations of instability in dynamic fracture by the cracking particles method," *Engineering Fracture Mechanics*, vol. 76, no. 6, pp. 730–741, 2009.
- [57] T. Rabczuk, G. Zi, A. Gerstenberger, and W. A. Wall, "A new crack tip element for the phantom-node method with arbitrary cohesive cracks," *International Journal for Numerical Methods in Engineering*, vol. 75, no. 5, pp. 577–599, 2008.
- [58] B. M. Donning and W. K. Liu, "Meshless methods for shear-deformable beams and plates," *Computer Methods in Applied Mechanics and Engineering*, vol. 152, no. 1–2, pp. 47–71, 1998.
- [59] W. Kanok-Nukulchai, W. Barry, K. Saran-Yasoontorn, and P. H. Bouillard, "On elimination of shear locking in the element-free Galerkin method," *International Journal for Numerical Methods in Engineering*, vol. 52, no. 7, pp. 705–725, 2001.
- [60] H. Noguchi, T. Kawashima, and T. Miyamura, "Element free analyses of shell and spatial structures," *International Journal for Numerical Methods in Engineering*, vol. 47, no. 6, pp. 1215–1240, 2000.
- [61] D. Wang and J.-S. Chen, "A locking-free meshfree curved beam formulation with the stabilized conforming nodal integration," *Computational Mechanics*, vol. 39, no. 1, pp. 83–90, 2006.
- [62] G. Yagawa and T. Miyamura, "Three-node triangular shell element using mixed formulation and its implementation by free mesh method," *Computers and Structures*, vol. 83, no. 25–26, pp. 2066–2076, 2005.
- [63] S. Li, W. Hao, and W. K. Liu, "Numerical simulations of large deformation of thin shell structures using meshfree methods," *Computational Mechanics*, vol. 25, no. 2, pp. 102–116, 2000.
- [64] T. Rabczuk, J. Y. Kim, E. Samaniego, and T. Belytschko, "Homogenization of sandwich structures," *International Journal for Numerical Methods in Engineering*, vol. 61, no. 7, pp. 1009–1027, 2004.
- [65] T. Rabczuk, E. Samaniego, and T. Belytschko, "Simplified model for predicting impulsive loads on submerged structures to account for fluid-structure interaction," *International Journal of Impact Engineering*, vol. 34, no. 2, pp. 163–177, 2007.
- [66] T. Rabczuk and J. Eibl, "Modelling dynamic failure of concrete with meshfree methods," *International Journal of Impact Engineering*, vol. 32, no. 11, pp. 1878–1897, 2006.
- [67] M. Zhou, G. Ravichandran, and A. J. Rosakis, "Dynamically propagating shear bands in impact-loaded prenotched plates. II: numerical simulations," *Journal of the Mechanics and Physics of Solids*, vol. 44, no. 6, pp. 1007–1032, 1996.
- [68] D. Peirce, C. F. Shih, and A. Needleman, "A tangent modulus method for rate dependent solids," *Computers and Structures*, vol. 18, no. 5, pp. 875–887, 1984.
- [69] T. W. Chao, *Gaseous detonation-driven fracture of tubes [Ph.D. thesis]*, California Institute of Technology, 2004.
- [70] W. Fickett and W. C. Davis, *Detonation*, University of California Press, Berkeley, Calif, USA, 1979.
- [71] C. L. Mader, *Numerical Modeling of Detonations*, University of California Press, Berkeley, Calif, USA, 1979.
- [72] G. Zi, T. Rabczuk, and W. Wall, "Extended meshfree methods without branch enrichment for cohesive cracks," *Computational Mechanics*, vol. 40, no. 2, pp. 367–382, 2007.
- [73] T. Rabczuk and T. Belytschko, "Application of particle methods to static fracture of reinforced concrete structures," *International Journal of Fracture*, vol. 137, no. 1–4, pp. 19–49, 2006.
- [74] T. Rabczuk and T. Belytschko, "A three-dimensional large deformation meshfree method for arbitrary evolving cracks," *Computer Methods in Applied Mechanics and Engineering*, vol. 196, no. 29–30, pp. 2777–2799, 2007.
- [75] T. Rabczuk and G. Zi, "A meshfree method based on the local partition of unity for cohesive cracks," *Computational Mechanics*, vol. 39, no. 6, pp. 743–760, 2007.

Research Article

Evaluating the Applicability of Fracture Criteria to Predict the Crack Evolution Path of Dolomite Based on SCB Experiments and FEM

Cunbao Li,^{1,2} Lingzhi Xie,^{1,2} Li Ren,^{1,2} Heping Xie,^{1,2} and Jun Wang^{1,2}

¹ Key Laboratory of Energy Engineering Safety and Disaster Mechanics of Ministry of Education, Sichuan University, Chengdu 610065, China

² School of Architecture and Environment, Sichuan University, Chengdu 610065, China

Correspondence should be addressed to Lingzhi Xie; xielingzhi@scu.edu.cn

Received 2 October 2013; Revised 17 November 2013; Accepted 18 November 2013

Academic Editor: Goangseup Zi

Copyright © 2013 Cunbao Li et al. This is an open access article distributed under the Creative Commons Attribution License, which permits unrestricted use, distribution, and reproduction in any medium, provided the original work is properly cited.

Mixed mode fracture tests are conducted under various initial loading combinations of mode I and mode II (from pure mode I to pure mode II) on semicircular bend (SCB) specimens of dolomite rock. Damage zones are observed behind the fracture surfaces of the broken samples. Scanning electron microscope images of the fracture surfaces are used to study the failure manner. Using the conventional remesh method based on the finite element method (FEM), several widely accepted fracture criteria are employed to theoretically predict the fracture paths. These criteria include the maximum tangential stress criterion, minimum strain energy density criterion, maximum energy release rate criterion, maximum dilatational strain energy density criterion, and the distortional strain energy density criterion. The applicability of the five fracture criteria is examined. The results show that none of the criteria are successful in predicting the crack trajectories of the predominately mode II cracks; the differences among the predicted results of the crack growth paths are negligible for each crack inclined angle. The effect of Poisson's ratio on the fracture criteria is also investigated and the results show that the predicted crack trajectories are not sensitive to Poisson's ratio.

1. Introduction

Extensive development in rock fracture mechanics research has covered many diverse areas including blasting, hydraulic fracturing and *in situ* stress determination, mechanical fragmentation, rock slope analysis, earthquake mechanics, earthquake prediction, plate tectonics, magmatic intrusions, hot dry rock geothermal energy extraction, fluid transport properties of fracturing rock masses, propagating oceanic rifts, crevasse penetration, and other glaciological problems [1]. As a result of complicated geological processes, numerous flaws, cracks, and faults exist in rock masses. Fracture mechanics is a useful technique for investigating the initiation and propagation of an individual crack or cracks in geological materials. Due to the complexity of *in situ* stresses, most fractures in these applications occur under a combination of opening and sliding deformation (I/II mixed mode). Under mixed mode loading, a fracture usually propagates along a curvilinear path

[2]. However, it is quite difficult to predict the curvilinear fracture path theoretically because the crack growth direction has to be determined by the present mixed-mode loading condition which corresponds to a specified position on the curvilinear path. Further investigations into fracture initiation angle and fracture propagation path under mixed-mode loading will improve the understanding of mixed mode fracture behavior.

Many researches have been conducted to describe crack initiation and crack propagation under mixed-mode loading. For example, Jia et al. [3] conducted a series of mixed-mode fracture experiments using center cracked circular disc (CCCD) specimens to observe the fracture path of concrete under mixed mode I/II loading; Xeidakis et al. [4] investigated the trajectory of crack growth for marble using antisymmetric three-point bend specimens under different mixed mode loading conditions; Bobet and Einstein [5] studied the fracture initiation, propagation, and, ultimately,

coalescence (which plays an important role in the behavior of brittle materials) by loading prefractured specimens of gypsum, used as the rock model material, in uniaxial and biaxial compression; Chen et al. [6] conducted a set of fracture experiments on anisotropic shale by using CCCD specimens under different mixed mode loading conditions for studying the fracture initiation path and also employed the numerical technique of boundary element method to simulate the observed fracture paths. Vászrhelyi and Bobet [7] investigated the crack initiation stress, direction, and propagation of newly generated cracks for both open and closed fractures; Wong et al. [8] numerically investigated the crack initiation, propagation, and coalescence of rock specimens containing preexisting crack-like flaws under compression by using Rock Failure Process Analysis (RFPA^{2D}); Al-shayea [9] studied the crack initiation angle and subsequent crack propagation path experimentally for notched Brazilian disk specimens of limestone; Liu et al. [10] used a numerical method for modeling the mixed mode fracture process of heterogeneous rocks using different test samples including CCCD specimens. More recently, Aliha et al. [11] investigated the mixed mode I/II fracture initiation angle and the crack growth trajectory of soft rock (Guiting Limestone) by using both CCCD and edge cracked SCB specimens of various sizes.

In order to theoretically estimate the crack initiation angle, several widely accepted fracture criteria have been proposed, for example, the maximum tangential stress criterion (σ_θ -criterion) [12], minimum strain energy density criterion (S_{\min} -criterion) [13], maximum energy release rate criterion (G_{\max} -criterion) [14–18], maximum dilatational strain energy density criterion (NT -criterion) [19], and distortional strain energy density criterion (Y -criterion) [20]. From a material mechanics view, it is reasonable to suggest that mixed mode brittle fracture occurs on reaching a certain level of critical energy, tensile stress, tensile strain, shear stress, shear strain, or another physical variable near the crack tip. However, it seems that none of these variables can predict the fracture strengths of predominately mode II fractures accurately because each criterion will predict a corresponding invariant fracture toughness ratio K_{Ic}/K_{IIc} [2] which cannot be applied to a wide range of engineering materials. In fracture mechanics, it is also important to predict where the crack will go, that is, the initiation angle and the growth path of the crack. Therefore, the applicability of these fracture criteria on the crack growth direction and crack evolution path should be discussed.

In this study, a series of mixed-mode fracture tests are conducted on dolomite rock using SCB specimens. Additionally, scanning electron microscope (SEM) images are used to study the failure manner. Moreover, using the conventional remesh method based on the FEM, the crack growth trajectories for various mixed mode loading conditions (from pure mode I to mode II) are theoretically (by the σ_θ -criterion, S_{\min} -criterion, G_{\max} -criterion, NT -criterion, and Y -criterion) and numerically predicted. A detailed investigation on the applicability of the five fracture criteria to the prediction of crack evolution paths under mixed mode loading conditions has been presented. Finally, the effect of Poisson's ratio on the fracture criteria is also investigated.

2. Crack Propagation Criteria

Most theoretical fracture criteria consider that when an appropriate characteristic quantity like stress, strain, and energy density energy release rate, in front of the crack tip reaches its critical value which is deemed to a material constant, then the crack begins propagating. For plane problem, the singular stresses around a crack tip in polar coordinate can be expressed as

$$\begin{aligned}\sigma_{rr} &= \frac{1}{\sqrt{2\pi r}} \left[\frac{K_I}{2} \cos \frac{\theta}{2} (3 - \cos \theta) - \frac{K_{II}}{2} \sin \frac{\theta}{2} (1 - 3 \cos \theta) \right], \\ \sigma_{\theta\theta} &= \frac{1}{\sqrt{2\pi r}} \left[\frac{K_I}{2} \cos \frac{\theta}{2} (1 + \cos \theta) - \frac{3K_{II}}{2} \sin \frac{\theta}{2} (1 + \cos \theta) \right], \\ \sigma_{r\theta} &= \frac{1}{\sqrt{2\pi r}} \left[\frac{K_I}{2} \sin \frac{\theta}{2} (1 + \cos \theta) - \frac{K_{II}}{2} \cos \frac{\theta}{2} (1 - 3 \cos \theta) \right],\end{aligned}\quad (1)$$

where r and θ are the polar coordinates with the origin at the crack tip and K_I and K_{II} are mode I and mode II stress intensity factors, respectively. And the stress field in Cartesian coordinates is defined as

$$\begin{aligned}\sigma_{xx} &= \frac{1}{\sqrt{2\pi r}} \left[K_I \cos \frac{\theta}{2} \left(1 - \sin \frac{\theta}{2} \sin \frac{3\theta}{2} \right) \right. \\ &\quad \left. - K_{II} \sin \frac{\theta}{2} \left(2 + \cos \frac{\theta}{2} \cos \frac{3\theta}{2} \right) \right], \\ \sigma_{yy} &= \frac{1}{\sqrt{2\pi r}} \left[K_I \cos \frac{\theta}{2} \left(1 + \sin \frac{\theta}{2} \sin \frac{3\theta}{2} \right) \right. \\ &\quad \left. + K_{II} \sin \frac{\theta}{2} \cos \frac{\theta}{2} \cos \frac{3\theta}{2} \right], \\ \sigma_{xy} &= \frac{1}{\sqrt{2\pi r}} \left[K_I \cos \frac{\theta}{2} \sin \frac{\theta}{2} \sin \frac{3\theta}{2} \right. \\ &\quad \left. + K_{II} \cos \frac{\theta}{2} \left(1 - \sin \frac{\theta}{2} \sin \frac{3\theta}{2} \right) \right], \\ \sigma_{zz} &= 0, \text{ for plane stress,} \\ \sigma_{zz} &= \nu (\sigma_{xx} + \sigma_{yy}), \text{ for plane strain,}\end{aligned}\quad (2)$$

where ν is Poisson's ratio.

2.1. σ_θ -Criterion. Erdogan and Sih [12] propose the maximum tangential stress criterion, which considers that a crack would grow in the direction in which the $\sigma_{\theta\theta}$ is the maximum; the direction should meet the following conditions:

$$\frac{\partial \sigma_{\theta\theta}}{\partial \theta} = 0, \quad \frac{\partial^2 \sigma_{\theta\theta}}{\partial \theta^2} < 0. \quad (3)$$

2.2. S_{\min} -Criterion. Sih [13] formulates the specific strain energy density factor S at the radius r_0 in term of the energy as follows:

$$S = a_{11}K_I^2 + 2a_{12}K_IK_{II} + a_{22}K_{II}^2, \quad (4)$$

where

$$a_{11} = \frac{1}{16\pi\mu} (1 + \cos\theta) (\kappa - \cos\theta),$$

$$a_{12} = \frac{1}{16\pi\mu} \sin\theta (2 \cos\theta - \kappa + 1),$$

$$a_{22} = \frac{1}{16\pi\mu} [(\kappa + 1)(1 - \cos\theta) + (1 + \cos\theta)(3 \cos\theta - 1)], \quad (5)$$

where μ is the shear modulus, $\kappa = 3 - 4\nu$ for the plane strain problem, and $\kappa = (3 - 4\nu)/(1 + \nu)$ for the plane stress problem. The S_{\min} -criterion postulates that the crack initiates in the direction of minimum strain energy density along a constant radius around the crack tip when S reaches a critical value; that is,

$$\frac{\partial S}{\partial \theta} = 0, \quad \frac{\partial^2 S}{\partial \theta^2} > 0. \quad (6)$$

2.3. G_{\max} -Criterion. Several forms [15–18] of G_{\max} -criterion have been formulated and only the expressions presented by Hussain et al. [15] will be reviewed here. The energy release rate is given as

$$G = \frac{4}{E} \left(\frac{1}{3 + \cos^2\theta} \right)^2 \left(\frac{\pi + \theta}{\pi - \theta} \right)^{-\theta/\pi} \times \left[(1 + 3\cos^2\theta) K_I^2 - 4 \sin(2\theta) K_I K_{II} + (9 - 5\cos^2\theta) K_{II}^2 \right], \quad (7)$$

where E is Young's modulus. According to the assumptions made by Palaniswamy and Knauss [14], the direction of crack propagation is the orientation in which the maximum rate of elastic energy release rate once exceeds a critical value; that is,

$$\frac{\partial G}{\partial \theta} = 0, \quad \frac{\partial^2 G}{\partial \theta^2} < 0. \quad (8)$$

2.4. NT -Criterion. In NT -criterion [19] the total strain energy density N (equivalent to S in (4)) is split into the distortional strain energy density N_d and dilatational strain energy density N_v ; that is,

$$N = N_d + N_v, \quad (9)$$

where

$$N_d = \frac{1}{6\mu} \times \left(\sigma_{xx}^2 + \sigma_{yy}^2 + \sigma_{zz}^2 - \sigma_{xx}\sigma_{yy} - \sigma_{yy}\sigma_{zz} - \sigma_{zz}\sigma_{xx} + 3\sigma_{xy}^2 \right),$$

$$N_v = \frac{1}{18K} \left(\sigma_{xx} + \sigma_{yy} + \sigma_{zz} \right)^2, \quad K = \frac{E}{3(1 - 2\nu)}. \quad (10)$$

The elastic-plastic boundary then can be obtained by employing a suitable yield condition, and in NT -criterion, the Von Mises yield function is adopted. Then, one can have

$$N_{d,0} = \frac{\sigma_y^2}{6\mu}, \quad (11)$$

where σ_y is the critical material yield strength. NT -criterion postulates that a crack propagates in the direction of maximum dilatational strain energy $N_{v,\max}$ along the contour of constant distortional strain energy $N_{d,0}$ when the distance from crack tip to the elastic-plastic boundary r_p in the growth direction reached a critical value r_{pcr} ; that is,

$$\frac{\partial N_{v|r_p}}{\partial \theta} = 0, \quad \frac{\partial^2 N_{v|r_p}}{\partial \theta^2} < 0, \quad (12)$$

where $r_{pcr} = (1 - 2\nu)^2 K_{Ic}^2 / (2\pi\sigma_y^2)$ for plane strain and $r_{pcr} = K_{Ic}^2 / (2\pi\sigma_y^2)$ for plane stress case.

2.5. Y -Criterion. Y -criterion [20] also divides the total energy density into two components, the dilatational strain energy density Y_v and the distortional strain energy density Y_d , as

$$Y_d = N_d, \quad Y_v = N_v. \quad (13)$$

Y -criterion presumes that a crack growth occurs in the direction of minimum distortional strain energy density along the constant core region boundary r_0 when the minimum distortional strain energy density Y_{d,θ_0} reached a critical value $Y_{d,0}$, and it can expressed as

$$\frac{\partial Y_{d|r_0}}{\partial \theta} = 0, \quad \frac{\partial^2 Y_{d|r_0}}{\partial \theta^2} > 0. \quad (14)$$

3. Mixed Mode Fracture Tests on Dolomite Rock

3.1. Rock Properties. The experimental material, dolomite rock, was taken from a quarry in Fangshan County, Beijing. Visual inspections indicated that the rock was isotropic, homogenous, and white in color. Its structure was continuous and very tight. The X-ray diffraction (XRD) analysis (Figure 1) showed that the rock was composed of dolomite ($\text{CaMg}(\text{CO}_3)_2$) and quartz (SiO_2). No pores or microcracks were visible using SEM with $\times 50$ magnification (Figure 2), therefore, the porosity of this rock can be neglected. SEM images also identified the material as a microcrystalline-textured, fine grained rock. Its dry density was about 2.59 g/mm^3 . In order to get the mechanical properties of dolomite rock, 4 groups of uniaxial compression tests and 4 groups of Brazilian tests were conducted. The mechanical properties of the rock included a uniaxial unconfined compressive strength of 135 MPa, a tensile strength of 3.0 MPa, Young's modulus of elasticity of 50 GPa, and Poisson's ratio of 0.25.

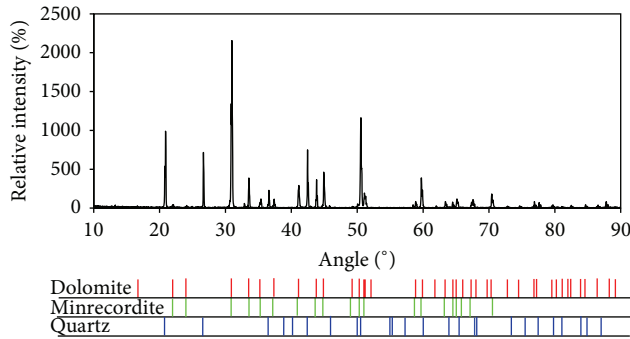
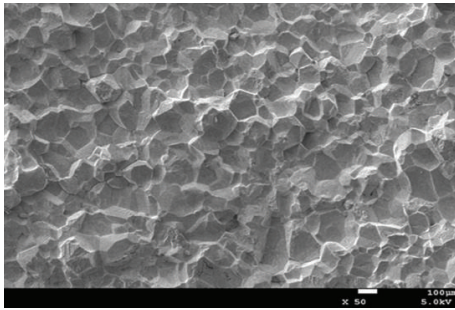


FIGURE 1: XRD results for dolomite rock.

FIGURE 2: SEM image for dolomite rock with $\times 50$ magnifications.

3.2. Sample Preparation. The SCB specimens [21] were selected for mixed mode fracture tests on dolomite rock. Figure 3 shows the geometry of the SCB specimen and the loading setup of the experiments. SCB specimen was a half disc of radius R and thickness t . The edge crack was of length a and angle α relative to the loading direction. The specimen was loaded by a vertical load P under three-point bending and the distance between the bottom supports was $2s$. When α was zero, the specimen was subjected to pure mode I (opening mode) independent of a/R and s/R [22]. By increasing the angle α , the contribution of mode II (or sliding mode) to the crack deformation increased. Pure mode II took place at a specific angle α depending on a/R and s/R [22].

To avoid any possible boundary effects, the specimens were taken from the center of the rocks. The SCB specimens had a radius of 25 mm and were 15 mm in thickness. Values of $a/R = 0.4$ and $s/R = 0.4$ were selected for all the specimens. The cracks were created using a 0.2 mm thick diamond impregnated wire saw and the crack length a was 10 mm. According to [22] and numerical analysis, for the selected specimen configuration and loading condition, at an inclination angle of 34.8° the crack was pure mode II crack. Therefore, the crack inclination angles of $\alpha = 0^\circ$ (pure mode I), 10° , 20° , 30° , 34.8° (pure mode II), and 40° (compression-shear mode) were selected. For each crack angle, four samples were prepared.

3.3. Fracture Tests. Each SCB specimen was located inside a three-point bending fixture (Figure 3) and then loaded by

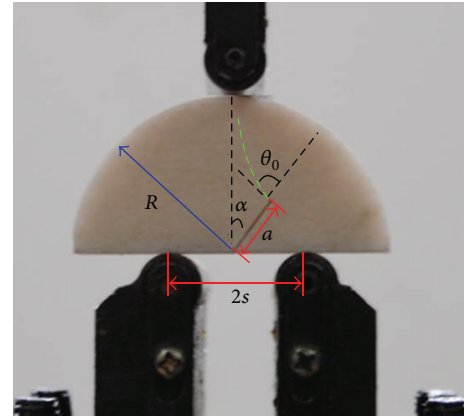


FIGURE 3: Geometrical characteristics of specimens and loading setup.

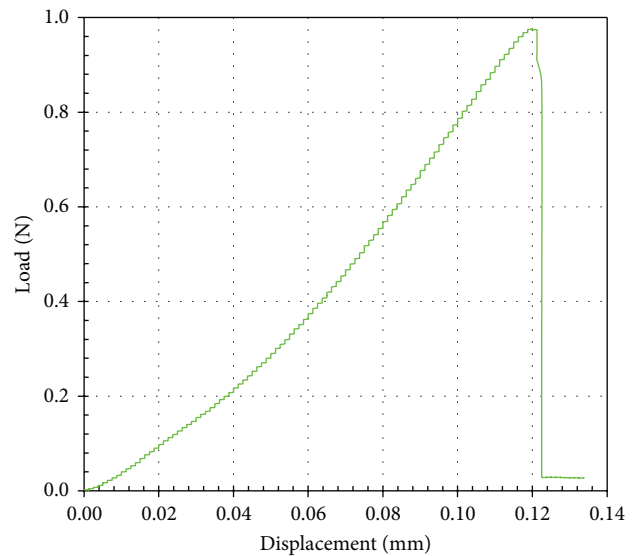


FIGURE 4: Typical plot of the applied load against the load-point displacement.

a test machine with a capacity of 10 kN. The loading rate was set to 0.1 mm/min for all the experiments. Figure 4 represents a typical plot of the applied load against load-point displacement. It can be seen that after a nonlinear stage the load-displacement curve gives a linear relationship up to the maximum load. The dolomite specimens, including the crack, remain stable without any visible changes during the loading process until the load reaches a critical value. At that point the load-displacement curve drops suddenly, which is the characteristic of brittle fracture; the original crack propagates rapidly toward to the point where the load is applied. When the crack reaches the edge of the specimen, the specimen breaks into two pieces (Figure 5). The fracture surfaces can reveal some useful information about the failure mechanism. Therefore, SEM was used to conduct a microscale investigation on the typical fracture surfaces.

TABLE 1: Failure loads P_{cr} obtained from mixed mode fracture tests.

Specimen code	Crack inclined angle α ($^{\circ}$)	Failure load (N)
D-1 (pure mode I)	0	832
D-2 (pure mode I)	0	857
D-3 (pure mode I)	0	846
D-4 (pure mode I)	0	836
D-5	10	925
D-6	10	910
D-7	10	892
D-8	10	945
D-9	20	960
D-10	20	810
D-11	20	929
D-12	20	901
D-13	30	1002
D-14	30	936
D-15	30	997
D-16	30	993
D-17 (pure mode II)	34.8	1001
D-18 (pure mode II)	34.8	1035
D-19 (pure mode II)	34.8	1210
D-20 (pure mode II)	34.8	890
D-21	40	956
D-22	40	1256
D-23	40	1254
D-24	40	1042

3.4. Test Results and Analysis. The failure loads P_{cr} obtained from the mixed mode fracture tests are listed in Table 1. The average values of P_{cr} for $\alpha = 0^{\circ}, 10^{\circ}, 20^{\circ}, 30^{\circ}, 34.8^{\circ}$, and 40° are 840 N, 918 N, 930 N, 982 N, 1034 N, and 1127 N, respectively. The failure load increases gradually as the proportion of mode II deformation increases.

Crack initiation includes two components: the crack initiation angle and the crack initiation point. According to linear elastic fracture mechanics (LEFM), the crack initiation point is usually expected to be the crack tip of the original crack. However, for specimens with $\alpha = 30^{\circ}$ and 34.8° (pure mode II), the crack initiation point is not from the crack tip, as shown in Figure 5. Generally, only when the crack inclination angle α is very large, usually bigger than the values of pure mode II or when the crack tip is obtuse seriously, the crack initiation point may not originate from the crack tip. However, the two cases in the tests do not fall into either of these two categories. In order to better explain such phenomenon, the fracture surface near the crack tip has been observed with SEM. It is found that the mineral grain near the crack tip is much larger than that in the surrounding area (Figure 6), which may lead to this unexpected failure behavior. The other reason may be that the specimen contains quartz, which possesses a much higher strength than dolomite. It is difficult to evaluate the influence of the size of the particles

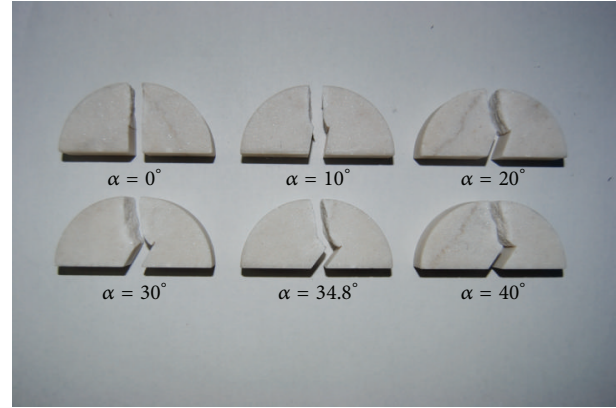
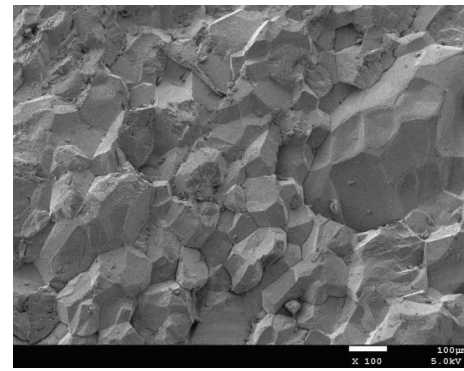


FIGURE 5: SCB specimens after failure.

FIGURE 6: Size of particles around the crack tip ($\alpha = 30^{\circ}$).

and the mineral composition on the crack initiation, either qualitatively or quantitatively.

Dolomite is a brittle rock with a relatively low hardness. After the failure of specimens, an obvious damaged zone can be found for each specimen, as illustrated in Figure 7. The damage zone is narrow relative to the specimen. The color of the damaged zone is different from the surrounding area; its color is much whiter obviously. Regardless of the position of crack tip, a high stress zone must exist around the crack tip and lead to damage. Fonseka et al. [23] has confirmed this view using the technology of SEM and acoustic emission (AE). But this is a macroscopic experiment that may demonstrate directly that the emergence of a macroscopic crack is the result of damage that develops from microcracks and microvoids.

SEM image was used to examine the failure manner to better understand the fracture mechanism and the evolution of the damage in dolomite rock. The fracture faces near the original crack tip for the cases of $\alpha = 0^{\circ}, 10^{\circ}, 20^{\circ}, 30^{\circ}, 34.8^{\circ}$, and 40° were observed by SEM; the fracture faces produced by the Brazilian test were also studied for comparison. Figure 8 shows SEM images of crack surface of the dolomite SCB specimens and Brazilian test with $\times 100$ magnification.

In the case of $\alpha = 0^{\circ}$ (Figure 8(a)), the cracked surface is coarse which was mainly caused by intergranular failure. Compared with the fracture surface of the broken sample

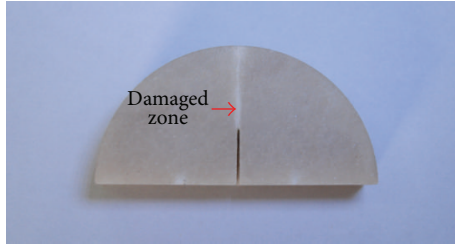


FIGURE 7: Visible damaged zone of a specimen.

from a Brazilian test (Figure 8(g)), the two faces are very similar, indicating that the specimen is destroyed by splitting and stretching. The SEM image for $\alpha = 10^\circ$ (Figure 8(b)) shows that the cracked surface is also produced primarily by splitting, tensile stress is the main factor, and only few of the crystalline particles are sheared off. There is no evidence of crushing or friction. The micrograph for the case of $\alpha = 20^\circ$ illustrates that the fractured surface is similar to that of $\alpha = 10^\circ$ image. The notable difference is the increment of transgranular damage, revealing that the impact of shear stress is increasing, although it is still small relative to the effect of splitting. There is still no evidence of crushing in the specimen of $\alpha = 20^\circ$. In the SEM image for $\alpha = 30^\circ$ the transgranular damage becomes more apparent; the fractured surface is produced by a combination of splitting and sliding shear. When the angles are $\alpha = 34.8^\circ$, and 40° , the SEM images show obvious crushing between the boundary of the crystals. For $\alpha = 34.8^\circ$, the failure is due to shear stress that is consistent with LEFM. For the specimens of $\alpha = 40^\circ$, crushing is more serious. The analysis indicates that when the angle increases from pure mode I to pure mode II, the effect of the shear stress grows, but there is no crushing or abrasion on the cracked surface, which is different from the results proposed in previous studies [9]. Moreover, when the angle reaches pure mode II or continues to increase (compression-shear mode), the signs of crushing become apparent, with many rock fragments observed on the fractured surface.

4. Numerical Analysis and Comparison

Based on (1)–(14), the crack initiation direction and growth path can be derived. Equations (1)–(14) are functions of the stress intensity factors and various material constants. By using the conventional remesh method based on FEM, (1)–(14) were employed to theoretically predict the fracture paths. No dynamic effects were considered in the crack propagation process. The finite element code ABAQUS and the mathematical software MATLAB were combined to evaluate the direction of crack growth. Stress intensity factors calculated by ABAQUS would output to a specified file, and fracture criterion was written as a program by MATLAB. The program would read stress intensity factors from the specified file and calculate the angle in which the crack would propagate. In each step, the simulation model was remodeled with a small crack extension of 0.5–1 mm. In the initial steps, the extension was relatively small. As the crack tip gradually approached

the loading point, the crack extension of each step became larger. Generally, simulating each model required at least 21 steps. The following procedure gave more details for predicting the crack evolution path using the five fracture criteria:

- (1) calculating K_I and K_{II} for the existing crack,
- (2) using each criterion to evaluate the corresponding crack growth direction,
- (3) remodeling the crack with a small extension along the direction which was calculated in step 2,
- (4) repeating steps 1–3 for the new crack growth.

The loading conditions were considered similar to those of the fracture tests; for $\alpha = 0^\circ, 10^\circ, 20^\circ, 30^\circ, 34.8^\circ$, and 40° , the loads were 840 N, 918 N, 930 N, 982 N, 1034 N, and 1127 N, respectively. ABAQUS provides a domain integral method to compute the stress intensity factors directly for a crack under mixed-mode loading. To produce the square root singular of the stress/strain field, the singular elements were considered in the first ring of elements surrounding the crack tip. In order to ensure a smooth curve which was the boundary of domain integral used to calculate stress intensity factors, 8 rings of quadratic quadrilateral elements surrounding the singular elements were meshed by the meshing technique of sweep. Other regions of the numerical model were meshed by the meshing methods of sweep or free, and the element type was also quadratic quadrilateral elements. A total of about 5000 eight-node plane strain elements (CPE8) were used for each model. Figure 9 represents a typical finite element mesh used for numerical analysis. The alterations of K_I and K_{II} with the mesh density are shown in Figure 10. It is observed that the values of K_I and K_{II} are not sensitive to mesh density. The mesh density adopted in this research is reasonable. Using the method described above, the crack initiation angle and crack propagation path for different crack inclined angles were analyzed. The experimental and numerical results were compared to evaluate the applicability of the fracture criteria to predict the crack evolution path of dolomite rock.

The impact of Poisson's ratio on the crack initial direction and crack propagation path was also considered. Poisson's ratio of the experimental dolomite SCB specimens was 0.25. Thus numerical models with Poisson's ratio of 0.1, 0.25, and 0.4 were simulated.

4.1. Crack Initiation Angle. The crack initiation angle θ_0 is the direction in which the crack propagates from the original crack (Figure 3). For different α , the value of θ_0 is calculated by each fracture criteria introduced in Section 2. Table 2 summarizes the crack initiation angle from simulated results.

Generally, the point possesses maximum stress, and maximum energy is at different locations and in a different direction, so the crack initiation angle predicted by different fracture criteria should be different. When mode I deformation is dominant ($\alpha < 10^\circ$), the difference in crack initiation angle is very small. The maximum difference between the predicted angles is 3.8° (between the S_{\min} -criterion and G_{\max} -criterion), and there is little difference between the σ_θ -criterion and

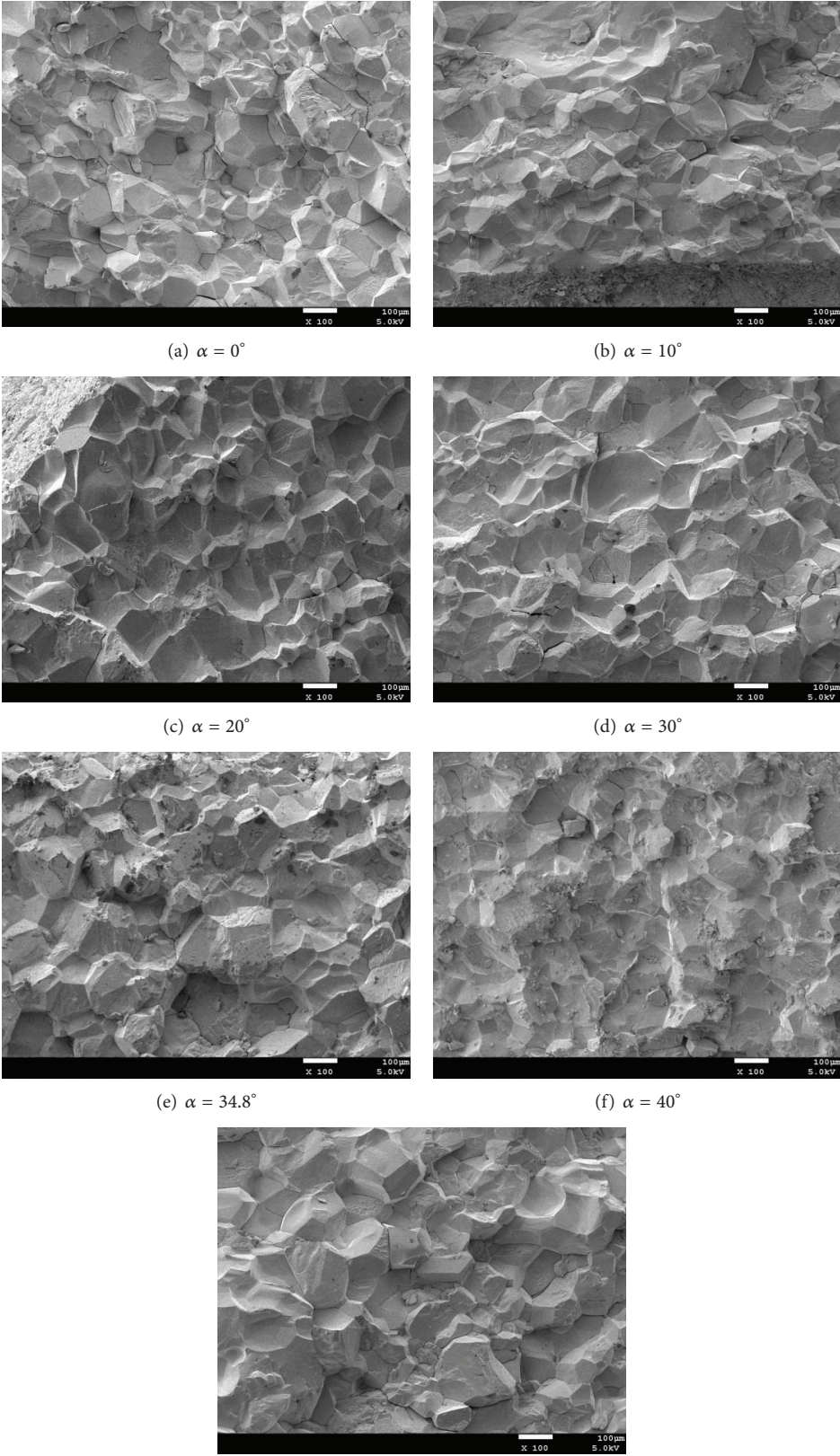


FIGURE 8: SEM images of fractured surfaces of SCB and Brazilian test specimens with $\times 100$ magnification.

TABLE 2: Summary of the crack initiation angle θ_0 of simulation for different crack inclination angle α ($^\circ$).

α	σ_θ -criterion	S_{\min} -criterion	G_{\max} -criterion	NT -criterion	Y -criterion
0	0	0	0	0	0
10	29.1	26.0	29.8	29.3	29.0
20	48.8	44.7	51.6	52.8	51.1
30	63.7	66.5	68.5	81.3	74.8
34.8	70.5	80.4	75.2	98.9	88.4
40	70.5	80.4	75.2	98.9	88.4

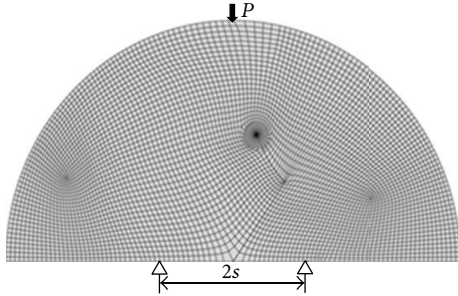
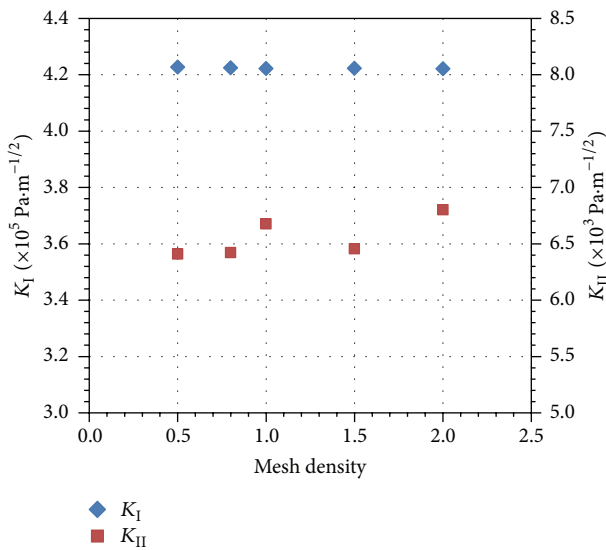


FIGURE 9: Typical finite element mesh used for numerical analysis.

FIGURE 10: Alterations of K_I and K_{II} with mesh density (the mesh density adopted (Figure 9 in the paper) for numerical simulation in this research is assumed to be 1; the mesh density of other numerical models is 0.5, 0.75, 1.5, and 2 times as dense as Figure 9).

Y -criterion. Hence, when the angle α is small, that is, the proportion of the mode II deformation is relatively small, the difference of the simulated results by the five fracture criteria is negligible. As α increases, the difference in initiation angle between the various fracture criteria becomes apparent. When $\alpha = 20^\circ$, the difference between different criteria becomes larger. The predicted angle for the G_{\max} -criterion is 51.6° and for the S_{\min} -criterion is 44.7° . The difference is about 7° . For $\alpha = 30^\circ$, the biggest difference between different criteria is nearly 18° . When $\alpha = 34.8^\circ$, the predicted value

changes from 70.5 to 98.9° , a difference of almost 30° . The proportion of the mode II deformation plays an important role in the predicted results of different fracture criteria. When $\alpha = 40^\circ$, the crack belongs to compression crack. From the perspective of physics, the materials on both sides of the closed crack surface cannot penetrate into each other, and therefore, such cracks are pure mode II cracks according to the LEFM. Thus, the initiation angle for the specimen of $\alpha = 40^\circ$ would be the same as the case of $\alpha = 34.8^\circ$, as shown in the last two rows of Table 2. However, this is inconsistent with the experimental results. For α being larger than the angle of pure mode II, the fracture criteria are not applicable.

4.2. Crack Propagation Path. The dolomite specimens' failure paths under various combination loadings of mode I and mode II are plotted in Figure 11. When the sample is subjected to pure mode I, the crack propagates straight along the line of the original crack. As the effect of mode II deformation increases, the crack evolution path becomes curved. When $\alpha = 40^\circ$, the crack path is the most curving. Figure 12 shows the simulation results of crack trajectories for each inclined angle specimens using the five fracture criteria.

When $\alpha = 0^\circ$, the crack extension angle is 0° for each fracture criterion (Figure 12(a)). As α increases from 10° to 40° , the simulated crack trajectories are very similar for all the fracture criteria. To further examine the crack growth paths calculated by different criteria, the plots of the crack trajectories near the original crack tip are enlarged. At the initial part of crack growth path, the difference between the various fracture criteria is relatively large. This is due to the initial angle of the crack varies between different fracture criteria, but after a few steps of crack growth, the difference between the predicted crack trajectories of the various fracture criteria become smaller and can be neglected. Therefore, any one of the five simulated results can be used for comparison with the experimental results.

After the initial stage of crack propagating, mode I deformation becomes dominant. Taking $\alpha = 34.8^\circ$ (pure mode II) as an example, after four steps of simulation, the stress intensity factors K_I and K_{II} calculated by the S_{\min} -criterion are 422200 and $6676 \text{ Pa}\cdot\text{m}^{-1/2}$, respectively; for the NT -criterion, Y -criterion, G_{\max} -criterion, and σ_θ -criterion, the values of K_I and K_{II} are 437400 and $10280 \text{ Pa}\cdot\text{m}^{-1/2}$, $430400 \text{ Pa}\cdot\text{m}^{-1/2}$ and $8607 \text{ Pa}\cdot\text{m}^{-1/2}$, 427500 and $3186 \text{ Pa}\cdot\text{m}^{-1/2}$, and 429500 and $5892 \text{ Pa}\cdot\text{m}^{-1/2}$, respectively. It is obvious that the proportion of mode II deformation is relatively small compared with that of mode I. Based on the discussion in Section 4.1,

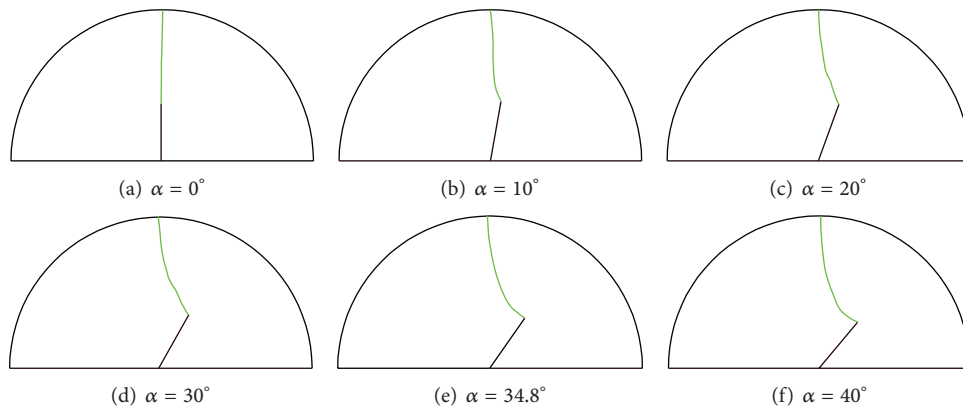


FIGURE 11: Crack path of fractured SCB specimens with different crack inclination angle α .

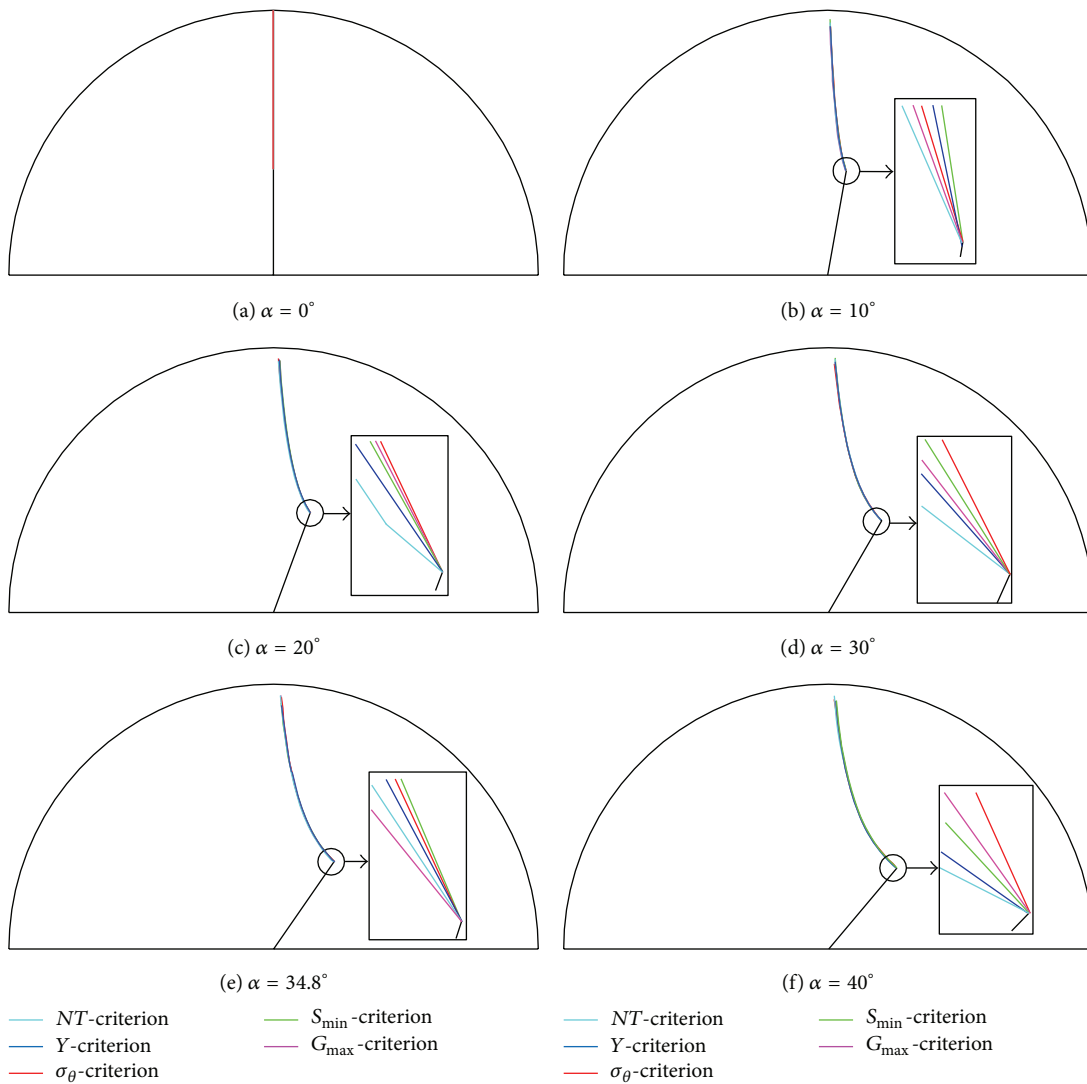
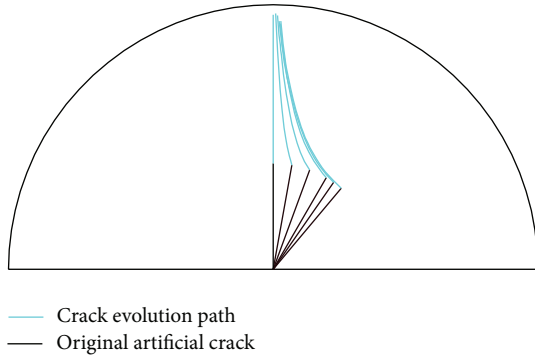


FIGURE 12: Simulated results of crack trajectories. The red, green, blue, magenta, and cyan lines represent the paths predicted by the σ_θ -criterion, S_{\min} -criterion, Y-criterion, G_{\max} -criterion, and NT-criterion, respectively.

TABLE 3: Summary of the crack initiation angles θ_0 for different Poisson's ratio (ν).

α	S_{\min} -criterion			NT -criterion			Y -criterion		
	$\nu = 0.1$	$\nu = 0.25$	$\nu = 0.4$	$\nu = 0.1$	$\nu = 0.25$	$\nu = 0.4$	$\nu = 0.1$	$\nu = 0.25$	$\nu = 0.4$
0	0	0	0	0	0	0	0	0	0
10	22.6	26.0	28.6	29.3	29.3	29.3	28.6	29.0	29.3
20	37.4	44.7	49.6	52.8	52.8	52.8	49.4	51.1	51.9
30	59.5	66.5	72.6	81.3	81.3	81.3	72.4	74.8	76.1
34.8	74.5	80.4	86.2	98.9	98.9	98.9	85.9	88.4	89.8
40	74.5	80.4	86.2	98.9	98.9	98.9	85.9	88.4	89.8

FIGURE 13: Crack trajectories for the different angles of inclination predicted by one fracture criterion (take NT -criterion as an example).

when the proportion of mode I deformation is dominant, the estimated crack initiation angles of all five criteria are similar, which leads to the simulated crack trajectories of the various fracture criteria are similar when the new crack tip moves slightly away from the original crack tip. Examining the predicted crack trajectories for the different angles of inclination using one fracture criterion, and NT -criterion is taken as an example (Figure 13); it is found that when the crack extends to the loading point, the crack paths gradually move close to each other; the same reasons mentioned above can explain this phenomenon.

4.3. Comparison between the Experimental and Simulated Results. The crack trajectories predicted based on the five fracture criteria are very similar. Therefore, for simplification, only the simulated crack evolution paths of the S_{\min} -criterion were selected to compare with the experimental results. Figure 14 describes the experimental results (crack evolution paths and damaged zones) and the calculated trajectories based on the S_{\min} -criterion.

For cracks of pure mode I, the test result coincides with the simulation result of the fracture criteria. When $\alpha = 10^\circ$, the simulation paths are also in good agreement with the experimental results. For $\alpha = 20^\circ$, the difference between the experimental result and the simulation result becomes larger but still acceptable. It is interesting that all the predicted crack trajectories of $\alpha = 0^\circ, 10^\circ$, and 20° are in the damaged zone. That is, the appearance of crack is the consequence of damage evolution and the crack propagation path should locate in

the damaged zone. Therefore, when mode I deformation is predominant, the results predicted by the five fracture criteria are reliable. In current work, for predominately mode II cracks ($\alpha = 30^\circ, 34.8^\circ$, and 40° (Figures 14(d)–14(f))), the predicted crack paths locate outside the damaged zones and are not consistent with the experimental results. For a predominately mode II deformation, all the fracture criteria fail to predict the crack path.

4.4. Influence of Poisson's Ratio. Equations (6), (12), and (14) indicate that Poisson's ratio ν has an influence on the numerical analysis results. To assess the effect of ν quantitatively, three different values ($\nu = 0.1, 0.25$, and 0.4) were selected for the numerical analysis. Table 3 summarizes the crack initiation angles θ_0 for different Poisson's ratio calculated by the S_{\min} -criterion, NT -criterion, and Y -criterion. The last two rows of Table 3 are the same and the reasons have been explained in Section 4.1. For the NT -criterion, the crack initiation angles do not change with Poisson's ratio, indicating that Poisson's ratio has no effect on the NT -criterion prediction of the crack initiation angle. For the S_{\min} -criterion, as Poisson's ratio increases, the predicted crack initiation angle becomes larger. When $\alpha < 10^\circ$, the difference is relatively small; the maximum difference is less than 7° . For $\alpha > 10^\circ$, the difference between the results of $\nu = 0.1$ and $\nu = 0.4$ is more than 11° . Poisson's ratio plays an important role in the predicted angle of the S_{\min} -criterion. The effect of Poisson's ratio on the Y -criterion is similar to that of the S_{\min} -criterion, but the effect is much smaller. For $\nu = 0.1$ and $\nu = 0.4$, the biggest difference for the Y -criterion is less than 5° . Poisson's ratio has the greatest influence on the S_{\min} -criterion, followed by the Y -criterion, and no effect on the NT -criterion. Furthermore, the crack trajectories are not sensitive to Poisson's ratio for the three fracture criteria. The simulated results of the crack evolution path are similar to those of Figures 12(a)–12(e).

5. Conclusions

Using SCB specimens of dolomite rock, mixed mode brittle fracture was studied by experiments. In order to explain the observed failure behavior, the SEM technique was used to study the microfailure mechanism. Furthermore, by using the conventional remesh method based on FEM, the crack growth trajectories for various mixed mode loading conditions, from pure mode I to mode II, were theoretically

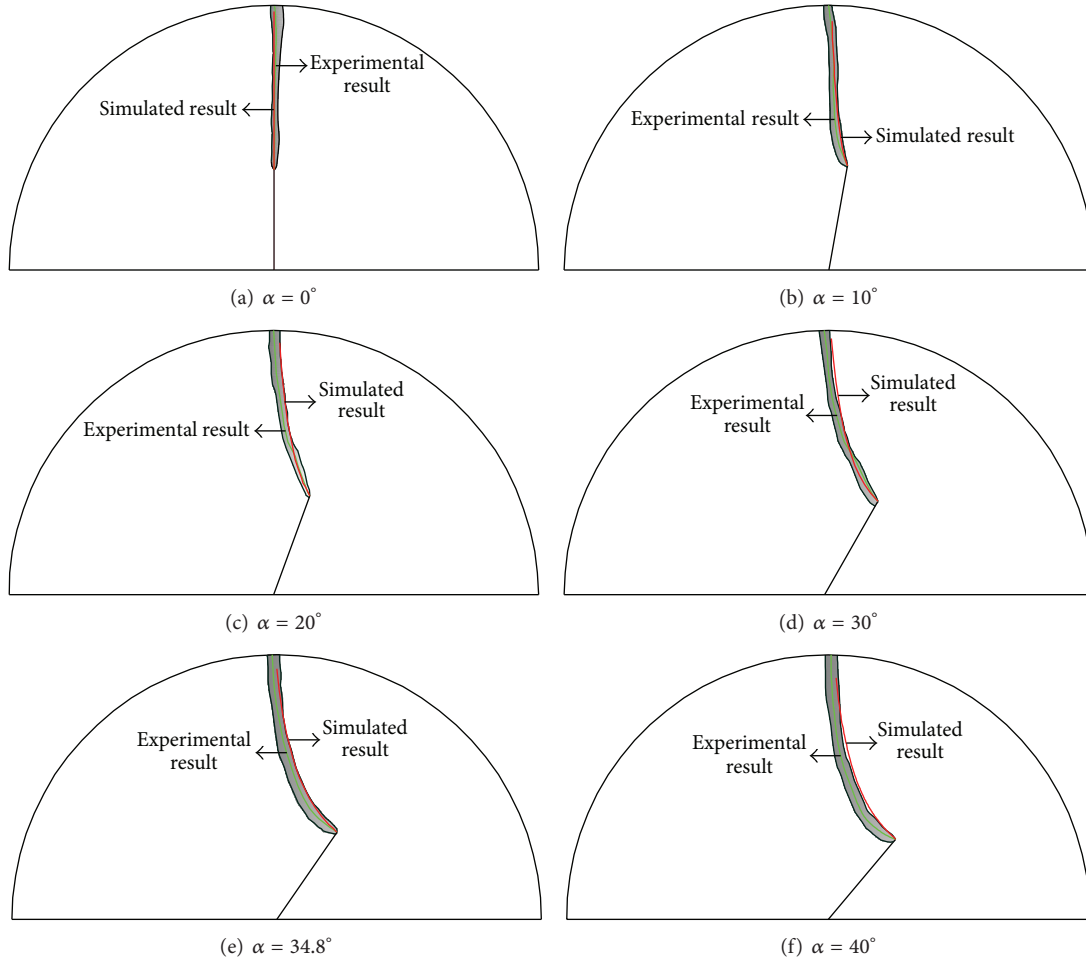


FIGURE 14: Experimental crack propagated paths, damaged zones, and crack trajectories calculated by S_{\min} -criterion (the gray zone, red line, and green line represent the damaged zone, numerical result, and experimental result, resp.).

(by the σ_{θ} -criterion, S_{\min} -criterion, G_{\max} -criterion, NT -criterion, and Y -criterion) and numerically predicted. The applicability of the five criteria was examined. Finally, an investigation on the effect of Poisson's ratio on fracture criteria was also presented. Based on the current work, the following conclusions can be obtained.

- (1) The dolomite specimens fracture in a brittle manner: as the proportion of mode II deformation increased, the average failure load increased.
- (2) Damaged zones were observed on both sides of the crack. It was a macroscopic experiment that could demonstrate that the emergence of macroscopic cracks was the result of the evolution of damage.
- (3) When the crack inclination angle increased, the effect of the shear stress increased but no crushing or abrasion was observed on the cracked surface. When the crack inclined angle was 34.8° or 40° , evidences of crushing between the cracked faces began to appear.
- (4) When mode I deformation was dominant, the difference between the crack initiation angles predicted by

the five fracture criteria was small. As the proportion of mode II deformation increased, the difference became larger. Mode II deformation had a considerable impact on the crack initiation angle.

- (5) The crack trajectories predicted by the five fracture criteria were very similar and the differences among the prediction paths were negligible.
- (6) The predicted crack trajectories were located in the damaged zones for predominately mode I cracks and in such cases, the fracture criteria were suitable; when mode II deformation was predominant, all five fracture criteria failed to predict the crack trajectories.
- (7) The crack initiation angle predicted by the Y -criterion and S_{\min} -criterion was sensitive to Poisson' ratio, particularly the S_{\min} -criterion; however, the crack trajectories were not sensitive to Poisson's ratio for these two fracture criteria. For the NT -criterion, the crack initiation angle and the crack trajectories were independent of Poisson's ratio.

Nomenclature

AE:	Acoustic emission
a :	Crack length
a/R :	Crack length ratio
a_{11}, a_{12}, a_{22} :	Parameters defining the stain energy density factor
E :	Young's modulus
FEM:	Finite element method
G :	Energy release rate
G_{\max} -criterion:	Maximum energy release rate criterion
K :	Bulk modulus
K_I :	Mode I stress intensity factor
K_{Ic} :	Fracture toughness of pure mode I crack
K_{II} :	Mode II stress intensity factor
K_{III} :	Mode III stress intensity factor
N :	Total strain energy density
N_d :	Distortional stain energy density in NT -criterion
$N_{d,0}$:	A constant distortional stain energy density in NT -criterion
NT -criterion:	Maximum dilatational strain energy density criterion
N_v :	Dilatational stain energy density in NT -criterion
$N_{v,\max}$:	Maximum dilatational stain energy density in NT -criterion
P :	Applied load
P_{cr} :	Failure load
R :	Radius of SCB specimens
$r\theta$:	Crack tip coordinates
r_o :	A constant radius
r_p :	Elastic-plastic boundary
r_{pcr} :	Critical radius in NT -criterion
S :	Stain energy density factor
S_{\min} -criterion:	Minimum stain energy density criterion
SCB:	Semicircular bend
SEM:	Scanning electron microscope
$2s$:	Loading span in the SCB test
s/R :	Loading point span ratio in SCB specimen
t :	Thickness of specimens
Y -criterion:	Distortional strain energy density criterion
Y_d :	Distortional stain energy density in Y -criterion
$Y_{d,0}$:	Critical value distortional stain energy density
Y_{d,θ_0} :	Minimum of distortional stain energy density
Y_v :	Dilatational stain energy density in Y -criterion
XRD:	X-ray diffraction
μ :	Shear modulus
$\sigma_{rr}, \sigma_{\theta\theta}, \sigma_{r\theta}$:	Stress components near the crack tip in polar coordinates
$\sigma_{xx}, \sigma_{yy}, \sigma_{xy}$:	Stress components near the crack tip in Cartesian coordinates
σ_y :	Critical material yield strength

σ_θ -criterion: Maximum tangential stress criterion
 α : Crack inclination angle
 θ_0 : Crack initiation angle.

Acknowledgments

This work was financially supported by the Provincial Science and Technology Support Project (2012FZ0124), Major State Basic Research Project (2011CB201201), and the International Science & Technology Cooperation Program of China (2012DFA60760).

References

- [1] S.-H. Chang, C.-I. Lee, and S. Jeon, "Measurement of rock fracture toughness under modes I and II and mixed-mode conditions by using disc-type specimens," *Engineering Geology*, vol. 66, no. 1-2, pp. 79–97, 2002.
- [2] I. L. Lim, I. W. Johnston, S. K. Choi, and J. N. Boland, "Fracture testing of a soft rock with semi-circular specimens under three-point bending. Part 2-mixed-mode," *International Journal of Rock Mechanics and Mining Sciences*, vol. 31, no. 3, pp. 199–212, 1994.
- [3] Z. Jia, A. Castro-Montero, and S. P. Shah, "Observation of mixed mode fracture with center notched disk specimens," *Cement and Concrete Research*, vol. 26, no. 1, pp. 125–137, 1996.
- [4] G. S. Xeidakis, I. S. Samaras, D. A. Zacharopoulos, and G. E. Papakaliatakis, "Trajectories of unstably growing cracks in mixed mode I-II loading of marble beams," *Rock Mechanics and Rock Engineering*, vol. 30, no. 1, pp. 19–33, 1997.
- [5] A. Bobet and H. H. Einstein, "Fracture coalescence in rock-type materials under uniaxial and biaxial compression," *International Journal of Rock Mechanics and Mining Sciences*, vol. 35, no. 7, pp. 863–888, 1998.
- [6] C.-S. Chen, E. Pan, and B. Amadei, "Fracture mechanics analysis of cracked discs of anisotropic rock using the boundary element method," *International Journal of Rock Mechanics and Mining Sciences*, vol. 35, no. 2, pp. 195–218, 1998.
- [7] B. Vásárhelyi and A. Bobet, "Modeling of crack initiation, propagation and coalescence in uniaxial compression," *Rock Mechanics and Rock Engineering*, vol. 33, no. 2, pp. 119–139, 2000.
- [8] R. H. C. Wong, C. A. Tang, K. T. Chau, and P. Lin, "Splitting failure in brittle rocks containing pre-existing flaws under uniaxial compression," *Engineering Fracture Mechanics*, vol. 69, no. 17, pp. 1853–1871, 2002.
- [9] N. A. Al-Shayea, "Crack propagation trajectories for rocks under mixed mode I-II fracture," *Engineering Geology*, vol. 81, no. 1, pp. 84–97, 2005.
- [10] H. Y. Liu, S. Q. Kou, P.-A. Lindqvist, and C. A. Tang, "Numerical modelling of the heterogeneous rock fracture process using various test techniques," *Rock Mechanics and Rock Engineering*, vol. 40, no. 2, pp. 107–144, 2007.
- [11] M. R. M. Aliha, M. R. Ayatollah, D. J. Smith, and M. J. Pavier, "Geometry and size effects on fracture trajectory in a limestone rock under mixed mode loading," *Engineering Fracture Mechanics*, vol. 77, no. 11, pp. 2200–2212, 2010.
- [12] F. Erdogan and G. C. Sih, "On the crack extension in plates under plane loading and transverse shear," *Journal of Basic Engineering*, vol. 85, no. 4, pp. 519–527, 1963.

- [13] G. C. Sih, "Strain-energy-density factor applied to mixed mode crack problems," *International Journal of Fracture*, vol. 10, no. 3, pp. 305–321, 1974.
- [14] K. Palaniswamy and W. G. Knauss, "Propagation of a crack under general, in-plane tension," *International Journal of Fracture Mechanics*, vol. 8, no. 1, pp. 114–117, 1972.
- [15] M. A. Hussain, S. L. Pu, and J. Underwood, "Strain energy release rate for a crack under combined Mode I and Mode II," Fracture Analysis STP 560, ASTM, 1974.
- [16] R. J. Nuismer, "An energy release rate criterion for mixed mode fracture," *International Journal of Fracture*, vol. 11, no. 2, pp. 245–250, 1975.
- [17] C. H. Wu, "Fracture under combined loads by maximum-energy-release-rate criterion," *Journal of Applied Mechanics—Transactions ASME*, vol. 45, no. 3, pp. 553–558, 1978.
- [18] A. P. Kfoury and M. W. Brown, "Fracture criterion for cracks under mixed-mode loading," *Fatigue & Fracture of Engineering Materials and Structures*, vol. 18, no. 9, pp. 959–969, 1995.
- [19] N. A. B. Yehia and M. S. Shephard, "The nt-criterion for predicting crack growth increments," *Engineering Fracture Mechanics*, vol. 26, no. 3, pp. 371–382, 1987.
- [20] N. A. B. Yehia, "Distortional strain energy density criterion: the Y-Criterion," *Engineering Fracture Mechanics*, vol. 39, no. 3, pp. 477–485, 1991.
- [21] K. P. Chong and M. D. Kuruppu, "New specimen for fracture toughness determination for rock and other materials," *International Journal of Fracture*, vol. 26, no. 2, pp. R59–R62, 1984.
- [22] M. R. Ayatollahi and M. R. M. Aliha, "Wide range data for crack tip parameters in two disc-type specimens under mixed mode loading," *Computational Materials Science*, vol. 38, no. 4, pp. 660–670, 2007.
- [23] G. M. Fonseka, S. A. F. Murrell, and P. Barnes, "Scanning electron microscope and acoustic emission studies of crack development in rocks," *International Journal of Rock Mechanics and Mining Sciences and Geomechanics Abstracts*, vol. 22, no. 5, pp. 273–289, 1985.

Research Article

POD for Real-Time Simulation of Hyperelastic Soft Biological Tissue Using the Point Collocation Method of Finite Spheres

Suleiman Banihani,¹ Timon Rabczuk,^{2,3} and Thakir Almomani⁴

¹ Department of Mechatronics Engineering, Hashemite University, Zarqa 13115, Jordan

² Institute of Structural Mechanics, Bauhaus University, Weimar, Marienstraße 15, 99423 Weimar, Germany

³ School of Civil, Environmental and Architectural Engineering, Korea University, Seoul 136-701, Republic of Korea

⁴ Department of Biomedical Engineering, Hashemite University, Zarqa 13115, Jordan

Correspondence should be addressed to Timon Rabczuk; timon.rabczuk@uni-weimar.de

Received 25 August 2013; Accepted 28 October 2013

Academic Editor: Goangseup Zi

Copyright © 2013 Suleiman Banihani et al. This is an open access article distributed under the Creative Commons Attribution License, which permits unrestricted use, distribution, and reproduction in any medium, provided the original work is properly cited.

The point collocation method of finite spheres (PCMFS) is used to model the hyperelastic response of soft biological tissue in real time within the framework of virtual surgery simulation. The proper orthogonal decomposition (POD) model order reduction (MOR) technique was used to achieve reduced-order model of the problem, minimizing computational cost. The PCMFS is a physics-based meshfree numerical technique for real-time simulation of surgical procedures where the approximation functions are applied directly on the strong form of the boundary value problem without the need for integration, increasing computational efficiency. Since computational speed has a significant role in simulation of surgical procedures, the proposed technique was able to model realistic nonlinear behavior of organs in real time. Numerical results are shown to demonstrate the effectiveness of the new methodology through a comparison between full and reduced analyses for several nonlinear problems. It is shown that the proposed technique was able to achieve good agreement with the full model; moreover, the computational and data storage costs were significantly reduced.

1. Introduction

Minimally invasive surgery (MIS) is becoming the method of choice for most surgical procedures with its many advantages of reduced postoperative pain, shorter hospital stays, quicker recoveries, less scarring, and better cosmetic results [1]. However, MIS is very demanding in terms of the skill of the surgeon together with poor depth perception, limited field of view, unnatural hand-eye coordination, and poor tactile perception. Moreover, the learning curve to master such techniques is long and tedious [2].

The success of flight simulators to train pilots has fuelled the enthusiasm for computer-based training systems for surgeons. The goal of surgical simulation is to produce a realistic virtual environment where a trainee can explore in real time a medical procedure of a three-dimensional organ model using his or her sense of vision and touch through specialized haptic interface devices [3]. Computational speed

is a major driving factor in such simulations [3–5]. The demand for accuracy is not as high as in engineering-based simulations; it is dictated by the just noticeable difference (JND) of the human sensory system [4]. Hence, novel computational algorithms are necessary which can deliver the high computational speeds at reasonable accuracy. Over the last decade, much research has witnessed an explosion of the number of tools available to enhance medical education, such as virtual reality—(VR) based medical training systems.

Several methods have been proposed for fast computation of mechanical deformation of soft tissues. Early attempts were based on a nonphysical approach, focusing on the visualization aspect of deformation and operation. In [6] a linked volume representation was used to model objects interactions. In [7], a physical model based on elasticity was introduced to describe deformable objects.

Mass-spring model is one of the most widely used physical methods in which the material is represented by

an array of nodes connected by elastic springs [8–11]. This model has been applied for a variety of objects including human tissues, muscles, and blood vessels [12–14]. A mass-spring-damper system was used as well in [15] to attain a more realistic representation.

However, both models inaccurately simplify the governing equations and offer a very unrealistic behavior [16]. An alternative is to use the finite-element method (FEM) [17–19] which is based on the principles of continuum mechanics. Due to the viability and potential of FEM, it is increasingly becoming the method of choice in most surgery simulators. In [17, 18], the FEM was used for surgery simulations in real time using an elastic quasi-static formulation. Later in [19], a dynamic formulation was used based on the tensor-mass method, where a long preprocessing step is required, which is not suitable for applications such as real-time planning for surgical procedures. In [20], the boundary element method (BEM) with a surface mesh was used to build a real-time model. However, this approach is not suitable especially if the inside of the organ is involved or for nonhomogenous materials.

Linear elastic models are only applicable for small deformations; experimental characterization of soft biological tissue indicates that the behavior of tissues is rather nonlinear. Therefore, a viscoelastic constitutive model is more evocative [21–25]. In [26], a nonlinear hyperelastic St. Venant Kirchhoff material was used for modeling soft tissue in real time, which is restricted to a linear stress-strain relation.

The finite volume method was used in [27] to simulate soft tissue deformation through an explicit integration scheme. A total Lagrangian explicit dynamic (TLED) algorithm was proposed in [28] where the calculations are based on the reference configuration of the material. In [29], a graphics processing unit (GPU) was utilized in applying this approach combined with Prony series to model viscoelasticity, reaching real-time speed. However, explicit time integration simplifies the update at each time step, but it requires small time steps to guarantee computational stability especially for stiff materials. Furthermore, with explicit schemes, it is necessary to iterate multiple times to propagate applied forces from a node to the whole mesh.

Although computerized skill trainers and VR training systems have been developed, none of them has been integrated officially into a medical curriculum or any other official training program or course, and the current technology is inadequate to address the issues of realistic simulation and rendering in such simulators.

Meshfree collocation-based methods [30, 31] offer a huge advantage in terms of time saving, in which the essential boundary conditions are applied directly on the boundary nodes with no additional treatment; moreover, there is no time-consuming numerical integration of the weak form as the approximation functions are applied directly on the strong form of the problem. In [32], it was shown that the accuracy of the solution in the meshfree point collocation method for elasticity and crack problems is excellent and the error is less than that in the element-free Galerkin (EFG) method with linear basis. Nodally integrated meshfree

methods allow for much larger critical time steps in explicit dynamics. Reference [33] showed an increase by factors up to 100.

The goal of this research is the development of physics-based simulation techniques for the modeling of surgical tool-soft tissue interactions, such as deformation, incision, and cutting as well as the reaction forces on the surgical tools, in real time. In [30], we presented a novel meshfree computational approach, that is, the point collocation method of finite spheres for realizing a viscoelastic tissue model.

Different model order reduction techniques were applied to reduce the computational time. The results were promising, but more investigations need to be done. This method has the potential to develop into the de facto standard in future surgical simulators. However, in [30], only modal truncation (MT), Hankel optimal model, and truncated balanced realization (TBR) MOR techniques were investigated for PCMFS. These methods can only apply in certain cases and may result in misleading results for highly nonlinear problems; moreover, they are computationally expensive.

The technology developed in this work is a significant step towards the development of VR-based surgical training systems which will enable medical students and residents to train and practicing surgeons to retrain on complex surgical procedures. The PCMFS is combined with the POD to produce a fast physics-based virtual environment; this will significantly reduce the computational cost which allows for more nonlinear phenomena to be modeled in real time.

The point collocation method of finite spheres is presented in Section 2 as well as the elastodynamic initial value problem. In Section 3, a hyperelastic constitutive model for soft biological tissues is shown, and then proper orthogonal decomposition is utilized to reduce the complexity of the full model and reduce computational cost in Section 4. Finally, numerical examples are presented in Section 5 to demonstrate the effectiveness of the proposed algorithm.

2. The Point Collocation Method of Finite Spheres (PCMFS)

The PCMFS is a computationally efficient technique proposed in [34] where the computational nodes are sprinkled on the computational domain (Figure 1). At every node “ I ” located at \mathbf{X}_I , an approximation function is defined which is compactly supported on the sphere $B_I = B(\mathbf{X}_I, r_I)$ of radius r_I centered at the node. The elastodynamic initial boundary value problem (Section 2.1) is solved using point collocation (Section 2.2). The moving least squares approximation functions, discussed in Section 2.3, are used for discretization, and the discretized set of equations is presented in Section 2.4.

2.1. The Elastodynamic Initial Boundary Value Problem. During surgical simulation, the surgical tool interacts with the portion ∂B_{u_2} of the body B with boundary ∂B . Homogeneous Dirichlet boundary conditions are prescribed on the portion ∂B_{u_1} of the boundary, and tractions are prescribed on ∂B_f

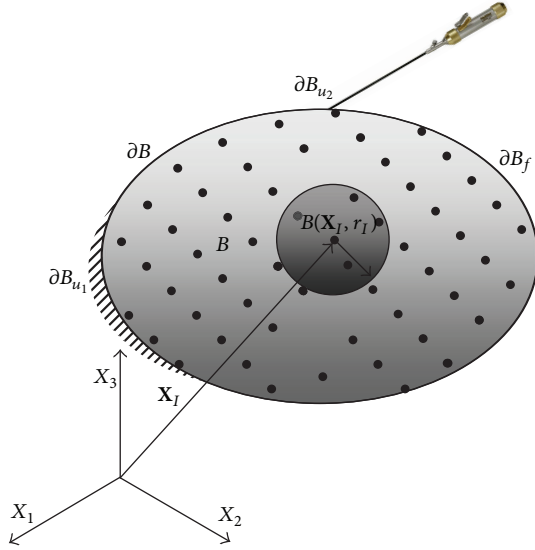


FIGURE 1: Schematic of the PCMFs for dynamic surgery simulation. Discretization of a domain $B \subset \mathfrak{R}^3$ by the PCMFs using a set of nodal points. B_I is the open sphere at node I . Natural boundary conditions are defined on ∂B_f , and the essential boundary conditions are defined on ∂B_u : $\partial B = \partial B_u \cup \partial B_f$, and $\partial B_u \cap \partial B_f = \emptyset$. Note that $\partial B_u = \partial B_{u_1} \cup \partial B_{u_2}$, where $\mathbf{u}(\mathbf{X}) = \mathbf{0}$ for $\mathbf{X} \in \partial B_{u_1}$ and $\mathbf{u} = \mathbf{u}_{\text{tooltip}}$ on $\partial B_{u_2} \times (0, T)$.

(Figure 1). We are interested in solving the specialized strong form of the following initial boundary value problem:

$$\begin{aligned}
 \nabla_0 \cdot \mathbf{P} + \rho_0 \mathbf{f}_b &= \rho_0 \ddot{\mathbf{u}} & \text{on } B \times (0, T), \\
 \mathbf{N} \cdot \mathbf{P} &= \mathbf{f}_s & \text{on } \partial B_f \times (0, T), \\
 \mathbf{u} &= \mathbf{0} & \text{on } \partial B_{u_1} \times (0, T), \\
 \mathbf{u} &= \mathbf{u}_{\text{tooltip}} & \text{on } \partial B_{u_2} \times (0, T), \\
 \mathbf{u}(\mathbf{X}, 0) &= \mathbf{u}_0, & \mathbf{X} \in B, \\
 \dot{\mathbf{u}}(\mathbf{X}, 0) &= \dot{\mathbf{u}}_0, & \mathbf{X} \in B,
 \end{aligned} \tag{1}$$

where \mathbf{P} is the nominal stress, ∇ is the divergence with subscript 0 indicating the reference configuration, $\mathbf{u} = [u \ v \ w]^T$ is the displacement vector, and $\ddot{\mathbf{u}}$ denotes second derivative with respect to time. $\mathbf{u}_0 = [u_0 \ v_0 \ w_0]^T$ and $\dot{\mathbf{u}}_0 = [\dot{u}_0 \ \dot{v}_0 \ \dot{w}_0]^T$ are the initial displacements and velocities, respectively. The surgical tool interacts with the portion ∂B_{u_2} of the boundary and prescribes a displacement field $\mathbf{u}_{\text{tooltip}}$ which is a function of space and time. The displacement on the rest of the Dirichlet boundary (∂B_{u_1}) is assumed to be zero for the entire simulation period (T). $\mathbf{f}_b = [f_{b_x} \ f_{b_y} \ f_{b_z}]^T$ is the body force, and $\mathbf{f}_s = [f_{s_x} \ f_{s_y} \ f_{s_z}]^T$ is the applied traction force. \mathbf{N} is a matrix of direction cosine components (n_x, n_y, n_z) of the unit outward normal to the domain

boundary which, for three-dimensional analysis, have the following representation:

$$\mathbf{N} = \begin{bmatrix} n_x & 0 & 0 & n_y & 0 & n_z \\ 0 & n_y & 0 & n_x & n_z & 0 \\ 0 & 0 & n_z & 0 & n_y & n_x \end{bmatrix}. \tag{2}$$

2.2. Point Collocation. In the point collocation method [35, 36], the displacement solution \mathbf{u} is approximated by \mathbf{u}_h , and the governing partial differential equations are applied at the nodal points. The discrete set of equations is given as follows:

$$[\nabla \cdot \mathbf{P}(\mathbf{u}_h)]_{\mathbf{X}=\mathbf{X}_I} + \rho_0 \mathbf{f}_b(\mathbf{X}_I) = \rho_0 \ddot{\mathbf{u}}(\mathbf{X}_I) \quad \text{on } B \times (0, T), \tag{3}$$

$$[\mathbf{N} \cdot \mathbf{P}(\mathbf{u}_h)]_{\mathbf{X}=\mathbf{X}_I} = \mathbf{f}_s(\mathbf{X}_I) \quad \text{on } \partial B_f \times (0, T), \tag{4}$$

$$\mathbf{u}_h(\mathbf{X}_I, t) = \mathbf{0} \quad \text{on } \partial B_{u_1} \times (0, T), \tag{5}$$

$$\mathbf{u}_h = \mathbf{u}_{\text{tooltip}} \quad \text{on } \partial B_{u_2} \times (0, T), \tag{6}$$

$$\mathbf{u}_h(\mathbf{X}_I, 0) = \mathbf{u}_0(\mathbf{X}_I) \quad \text{on } B, \tag{7}$$

$$\dot{\mathbf{u}}_h(\mathbf{X}_I, t) = \dot{\mathbf{u}}_0(\mathbf{X}_I) \quad \text{on } B. \tag{8}$$

The use of smooth weight functions allows for the higher-order derivatives in (3) to be taken. The point collocation method obviates expensive numerical integration, but it results in a nonsymmetric stiffness matrix.

2.3. The Moving Least Squares Approximation Scheme. In PCMFs, the moving least squares [32] technique is used to generate the approximation functions. In this technique, the approximation $\mathbf{u}_h(\mathbf{X}, t)$ of a variable u , using “ N ” particles, is given as

$$\mathbf{u}(\mathbf{X}, t) \approx \mathbf{u}_h(\mathbf{X}, t) = \sum_{J=1}^N \mathbf{H}_J(\mathbf{X}) \boldsymbol{\alpha}_J(t) = \mathbf{H}(\mathbf{X}) \mathbf{U}(t), \tag{9}$$

where $\boldsymbol{\alpha}_J = [u^J, v^J, w^J]$ is the vector of nodal unknowns corresponding to the X_1, X_2 , and X_3 directions at node “ J ” and $\mathbf{U} = [\boldsymbol{\alpha}_1 \boldsymbol{\alpha}_2 \cdots \boldsymbol{\alpha}_N]^T$. The nodal shape function matrix is given as

$$\mathbf{H}_J(\mathbf{X}) = \begin{bmatrix} h_J(\mathbf{X}) & 0 & 0 \\ 0 & h_J(\mathbf{X}) & 0 \\ 0 & 0 & h_J(\mathbf{X}) \end{bmatrix}, \tag{10}$$

where the shape functions at node “ J ” are generated using a moving least squares procedure and has the form

$$h_I(\mathbf{X}) = W_I(\mathbf{X}) \mathbf{P}^T(\mathbf{X}) \mathbf{A}^{-1}(\mathbf{X}) \mathbf{P}(\mathbf{X}_I), \quad I = 1, \dots, N, \tag{11}$$

with

$$\mathbf{A}(\mathbf{X}) = \sum_{J=1}^N W_J(\mathbf{X}) \mathbf{P}^T(\mathbf{X}_J) \mathbf{P}(\mathbf{X}_J), \tag{12}$$

where $\mathbf{P}(\mathbf{X})$ is a vector of monomials; for example, $\mathbf{P}(\mathbf{x}) = [1, X_1, X_2, X_3]$ ensures first-order accuracy in 3D. We define a positive radial weight function $W_J(\mathbf{X}) = W(s_J) \in C_0^s(B(\mathbf{X}_J, r_J))$, $s \geq 1$ with, $s_J = \|\mathbf{X} - \mathbf{X}_J\|_0 / r_J$ at each node “ J ” which is compactly supported on the sphere at node “ J ”. In our work, we have used a quartic spline weight function of the form

$$W(s) = \begin{cases} 1 - 6s^2 + 8s^3 - 3s^4, & 0 \leq s < 1, \\ 0, & s \geq 1. \end{cases} \quad (13)$$

3. Hyperelastic Constitutive Model

Biological soft tissues are complicated; they are anisotropic, viscoelastic, and inhomogeneous, and they allow large deformation. Therefore, there is no known constitutive model that can capture the exact mechanical and thermodynamical behavior of all tissues. In this work, we are concerned with certain organ, that is, the liver. Liver can be considered to be homogeneous, isotropic, and incompressible because liver tissue is highly consistent with a high water content. A hyperelastic constitutive model for liver is widely used [37].

Most surgical simulations focus on linear elastic models for soft tissue as in [30]. In this paper, we will assume a hyperelastic constitutive model to account for nonlinear behavior of moderate strains. Nevertheless, our development can be easily extended to more complicated material models.

In [38, 39], Ogden proposed a general form of strain energy function as follows:

$$W = \sum_i C_i (\lambda_1^{\alpha_i} + \lambda_2^{\alpha_i} + \lambda_3^{\alpha_i} - 3), \quad (14)$$

where C_i and α_i are material parameters and i is the number of terms included in the summation. λ_1 , λ_2 , and λ_3 are the principal stretch ratios and the eigenvalues of the right Cauchy-Green deformation tensor, $\mathbf{C} = \mathbf{F}^T \mathbf{F}$, where \mathbf{F} is the deformation gradient given by

$$\mathbf{F} = \frac{\partial \mathbf{x}}{\partial \mathbf{X}}, \quad (15)$$

where \mathbf{X} and \mathbf{x} are the coordinates of the material point in the reference and current configuration, respectively.

The Mooney-Rivlin material is a special case of this function where a polynomial form of the strain energy function is used as follows:

$$W = \frac{C_1}{2} (I_1 - 3) + \frac{C_2}{2} (I_2 - 3), \quad (16)$$

where $I_1 = \lambda_1^2 + \lambda_2^2 + \lambda_3^2$ and $I_2 = \lambda_1^2 \lambda_2^2 + \lambda_2^2 \lambda_3^2 + \lambda_3^2 \lambda_1^2$.

Hookean model is the simplest hyperelastic model with C_2 in the Mooney-Rivlin model set to zero, and the strain energy function is given by

$$W = C_1 (I_1 - 3). \quad (17)$$

In order to account for sharp increase in stiffness after toe regions in the stress-strain curve of soft tissue, exponential

or logarithmic functions are introduced in the strain energy function [37] as follows:

$$W = C_1 [\exp(C_2 (\lambda_1^{\alpha_1} + \lambda_2^{\alpha_1} + \lambda_3^{\alpha_1} - 3)) - 1] + C_3 (\lambda_1^{\alpha_2} + \lambda_2^{\alpha_2} + \lambda_3^{\alpha_2} - 3), \quad (18)$$

or

$$W = -C_1 [\ln(1 - C_2 (\lambda_1^{\alpha_1} + \lambda_2^{\alpha_1} + \lambda_3^{\alpha_1} - 3))] + C_3 (\lambda_1^{\alpha_2} + \lambda_2^{\alpha_2} + \lambda_3^{\alpha_2} - 3). \quad (19)$$

For hyperelastic material, the second Piola-Kirchhoff stress, \mathbf{S} , is derived from the strain energy function as follows:

$$\mathbf{S} = 2 \frac{\partial W}{\partial \mathbf{C}}. \quad (20)$$

The nominal stress is related to the second Piola-Kirchhoff stress in the following manner:

$$\mathbf{P} = \mathbf{S} \cdot \mathbf{F}^T. \quad (21)$$

4. Proper Orthogonal Decomposition (POD)

Model order reduction (MOR) methods have been developed for large-scale dynamical systems [40–42] where they are used to approximate the input-output behavior of the system over a certain range of operations using significantly smaller matrices. MOR retains the essential dynamics and physics contained within the full system but at a much lower computational cost. Model order reduction methods offer an excellent route to computing input-output responses by eliminating a large number of degrees of freedom which do not have a significant influence on the output. A useful model order reduction technique [43] has the following properties.

- (i) It reduces the number of variables significantly relative to the full-order model.
- (ii) It is controlled by a limited number of relevant inputs.
- (iii) It is relatively inexpensive to solve and store in computer's memory.

There are three major approaches for generating reduced-order models for linear time-invariant systems:

- (i) Krylov subspace-based methods,
- (ii) Hankel norm and truncated balancing realization (TBR-) based methods,
- (iii) Karhunen-Lóeve expansion or proper orthogonal decomposition (POD) methods.

All of those methods apply the idea of approximating the original high-fidelity system with a relatively lower-dimensional and computationally cheaper model by performing projection of the original space into a lower-dimensional space while maintaining relatively small error. In order to be successful, the reduced-order model (ROM) must be predictive across the design or parameter space of interest.

Krylov subspace-based methods are numerically robust algorithms since they preserve a certain number of moments of the transfer function in the reduced model. Therefore, the reduced system approximates well the original transfer function around a specified frequency or collection of frequency points [44]. However, there are no provable error bounds that guarantee preserving stability or passivity of the original system for the reduced models.

The second group of methods is based on the Hankel norm and truncated balancing realization (TBR). Unlike the Krylov subspace methods, these methods have provable error bounds and guarantee that stability of the original system will be preserved in the reduced-order model [45]. However, these methods are computationally expensive for extracting the reduced model because the solution of Lyapunov equations requires $O(N^3)$ operations.

Karhunen-Lóeve expansion or proper orthogonal decomposition (POD) method offers yet another alternative [46]. It is a powerful and elegant method which obtains projection based on time or frequency domain snapshots [47, 48]. POD has been widely used in a variety of fields including image processing, signal analysis, data compression, process identification, and adaptive control.

4.1. Reduced-Order Models Using Proper Orthogonal Decomposition (POD). Generating a reduced-order model of the high-fidelity original partial differential equation consists of the following two steps.

- (i) The first step is to transform the kinematic information, that is, in our case, the displacement field, to a smaller number of modes.
- (ii) Then, the full-system is reduced to the dynamics implied by the reduced modes.

The result is a set of time-dependent ordinary differential equations (ODEs) in the reduced-order model modes which are able to describe the dynamics of the original PDE with a relatively small error [49].

Let $u(\mathbf{x}, t) \in H(\Omega)$ be our variable of interest in the governing PDE defined over the domain $\Omega \in \mathfrak{R}^n$, where $H(\Omega)$ is a Hilbert space with associated inner product (\cdot, \cdot) , and let $u(\mathbf{x}_i, t_p) = u^p$, $i \in [1, \dots, N]$, $p \in [1, \dots, L]$, be the ensemble set of L instantaneous snapshots in time of this field expressed in a discrete form; that is, it is known typically at the nodes of a spatial mesh and for some time steps of existing numerical solution.

The main idea of POD is to obtain a basis ϕ_k of order $M \ll L$, where $\{\phi_k, k = 1, 2, \dots, M\}$ is the most typical linear basis for describing the original ensemble. Therefore, POD is searching for an M -dimensional subspace spanned by $\phi_k \in H^M(\Omega)$ such that the projection of the difference between the ensemble u^p and its projection onto $H^M(\Omega)$ is minimized on average. That is equivalent to finding the function ϕ_k that solves the following optimization problem:

$$\min_{(\phi_k)_{k=1}^M} \left\langle \|u^p - \Xi_M u^p\|^2 \right\rangle \quad (22)$$

subject to

$$(\phi_i, \phi_j) = \delta_{ij}, \quad 1 \leq i \leq M, \quad 1 \leq j \leq i, \quad (23)$$

where $\langle \cdot \rangle$ is a discrete averaging operator; that is, $\langle \|u^p\|^2 \rangle = (1/L) \sum_{p=1}^L \|u^p\|^2$, and $\Xi_M : H(\Omega) \rightarrow H_M(\Omega)$ is an orthogonal projection operator.

The reduced-order model solution u_M can be represented as a linear combination of ϕ_k , the POD modes, as follows:

$$u_M(\mathbf{x}, t) = \sum_{k=1}^M \phi_k(\mathbf{x}) a_k(t), \quad (24)$$

where $a_k(t)$ are ROM coefficients. The solution of the optimization problem in (22) is reduced to the following eigenvalue problem:

$$C\Phi = \lambda\Phi, \quad (25)$$

where C is self-adjoint positive semidefinite operator defined as

$$C = \langle u^p \otimes u^p \rangle = \frac{1}{L} \sum_{p=1}^L (u^p \otimes u^p). \quad (26)$$

In [49, 50], it was shown that the set of M eigenfunctions, or POD modes, $\{\phi_k, k = 1, 2, \dots, M\}$, corresponds to the M largest eigenvalues of C that is precisely the set that solves (25) and that the minimum value of the objective function in (22) is

$$\begin{aligned} & \left\langle \|u^p - \Xi_M u^p\|^2 \right\rangle \\ &= \frac{1}{L} \sum_{p=1}^L \|u^p - \Xi_M u^p\|^2 = \sum_{j=M+1}^L \lambda_j. \end{aligned} \quad (27)$$

5. Nonlinear Model Reduction for Hyperelastic Material

Using direct simulation of the initial value problem in (3) results in a set of L instantaneous snapshots in time; that is, $u(\mathbf{x}_i, t_p) = u^p$, $i \in [1, \dots, N]$, $p \in [1, \dots, L]$. From the M eigenfunctions, or POD modes, $\{\phi_k(\mathbf{x}_i), k = 1, 2, \dots, M$ and $i = 1, 2, \dots, N\}$ corresponding to the M largest eigenvalues, the matrix \mathbf{Q} can be defined as

$$\mathbf{Q} = \begin{pmatrix} \phi_1(\mathbf{x}_1) & \phi_2(\mathbf{x}_1) & \cdots & \phi_M(\mathbf{x}_1) \\ \phi_1(\mathbf{x}_2) & \phi_2(\mathbf{x}_2) & \cdots & \phi_M(\mathbf{x}_2) \\ \vdots & \vdots & \ddots & \vdots \\ \phi_1(\mathbf{x}_N) & \phi_2(\mathbf{x}_N) & \cdots & \phi_M(\mathbf{x}_N) \end{pmatrix}. \quad (28)$$

The discretization of the partial equation, (3), is given as follows:

$$\mathbf{M}\ddot{\mathbf{U}} + \mathbf{C}\dot{\mathbf{U}} + \mathbf{K}\mathbf{U} = \mathbf{F}, \quad (29)$$

where \mathbf{M} , \mathbf{C} , and \mathbf{K} are the mass, damping, and stiffness matrices, respectively, \mathbf{U} are the nodal unknowns, and \mathbf{F} is the external force vector.

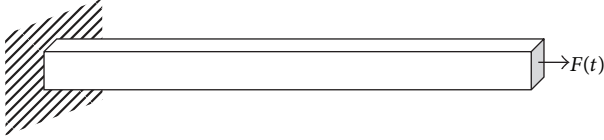


FIGURE 2: Beam under traction: concentrated force is applied to the right side, whereas the other side is fixed.

Using the POD modes equation (24), the nodal unknowns can be expressed as

$$\mathbf{U} = \mathbf{Q}\mathbf{A}, \quad (30)$$

where \mathbf{A} are ROM coefficients, and the dynamic problem in (29), can be approximated as follows:

$$\mathbf{M}\mathbf{Q}\ddot{\mathbf{A}} + \mathbf{C}\mathbf{Q}\dot{\mathbf{A}} + \mathbf{K}\mathbf{Q}\mathbf{A} = \mathbf{F}. \quad (31)$$

Multiplying both sides of (31) by \mathbf{Q}^T gives

$$\mathbf{Q}^T\mathbf{M}\mathbf{Q}\ddot{\mathbf{A}} + \mathbf{Q}^T\mathbf{C}\mathbf{Q}\dot{\mathbf{A}} + \mathbf{Q}^T\mathbf{K}\mathbf{Q}\mathbf{A} = \mathbf{Q}^T\mathbf{F}, \quad (32)$$

which results in a final system of equations of order $M \times M$, with $M \ll L$.

6. Numerical Examples

In order to demonstrate the effectiveness of the proposed technique, we will show 2 examples of hyperelastic models.

6.1. Beam under Traction. In this example, we apply an axial force on the right side of the beam, whereas the left side of the beam is fixed. The beam is 200 mm long with a square cross-sectional area with sides of length 20 mm, as shown in Figure 2.

The force $F(t)$ is given by

$$F(t) = \begin{cases} 200t, & 0 \leq t < 0.5, \\ 200(1-t), & 0.5 \leq t \leq 1. \end{cases} \quad (33)$$

Here, we assumed a Mooney-Rivlin hyperelastic material model with $C_1 = 60 \text{ kPa}$, $C_2 = 1.2 \text{ kPa}$, and density of 1120 kg/m^3 .

Explicit time integration was used in the full model, and the simulation period was 1 sec where a snapshot was taken every 0.01 sec.

Figure 3 shows the average relative error in the displacement field solution as the number of POD basis modes increases, and the average error is defined relative to the solution of the full model as follows:

$$\text{error} = \frac{\sum_{I=1}^N |u_{\text{Full}}(x_I) - u_{\text{POD}}(x_I)|}{|u_{\text{Full}}(x_I)|}, \quad (34)$$

where u_{Full} and u_{POD} refer to the displacement solution for the full- and reduced-order models, respectively, and the error is averaged over time as well.

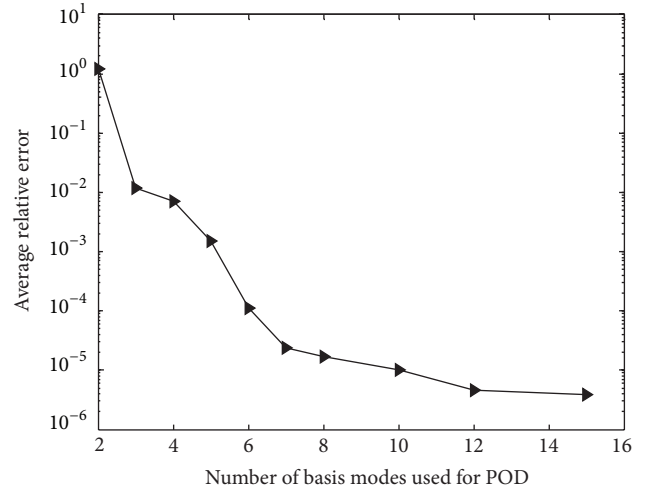


FIGURE 3: Average relative error in the solution of the displacement of the beam as the number of basis modes in the POD increases.

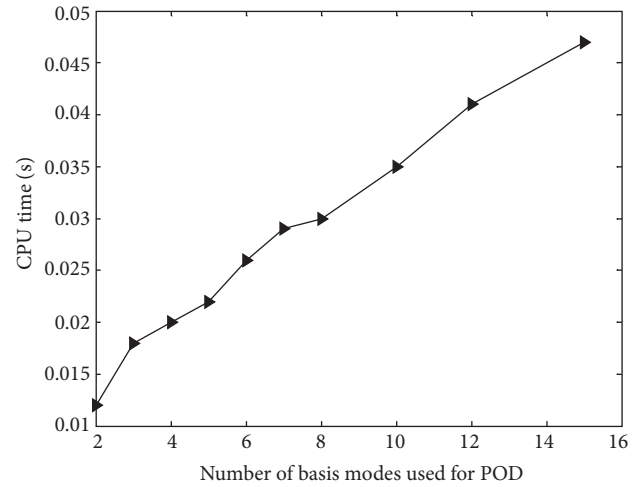


FIGURE 4: CPU time used in seconds for the solution of the beam problem using the PCMF5 with POD model order reduction method.

It is shown from Figure 3 that the relative error decreases steeply with increasing the number of POD modes used; for example, the relative error with only 6 basis modes is less than 3% of the full-order model. However, after 8 basis modes the decrease in the relative error is slight.

Figure 4 shows the CPU time consumed in seconds for the solution of the beam problem using the PCMF5 with POD as the number of basis functions increases in the reduced-order model.

As shown in the figure, it is noticed that the time scales almost linearly with increasing the number of basis modes for the beam problem.

Figure 5 shows the time used to solve the reduced-order model problem relative to the full-order model as the number of POD basis modes increases. The time used for POD with only 2 basis functions was almost 1% of the time needed for the full-order model, whereas for 8 basis functions the time

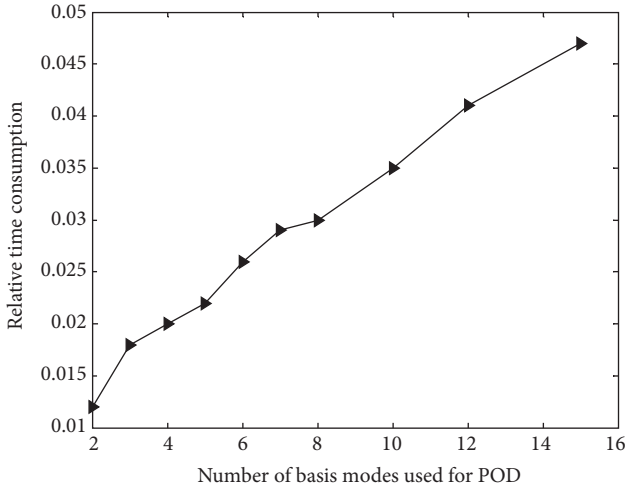


FIGURE 5: Time consumption relative to the full model as the number of POD basis modes increases.

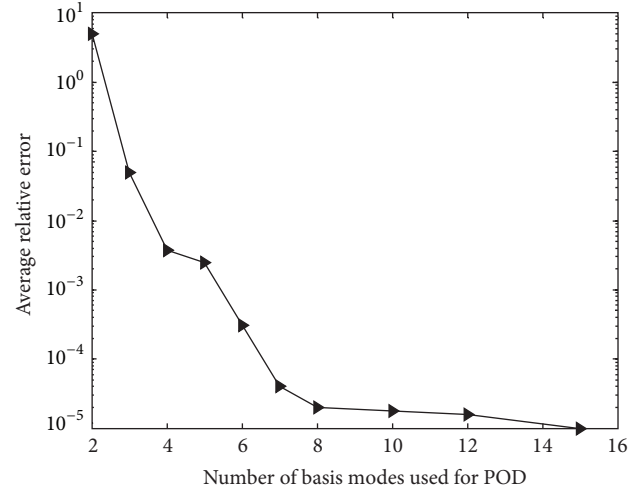


FIGURE 7: Relative error in the displacement field of the hyperelastic circular membrane as the number of POD basis modes increases.

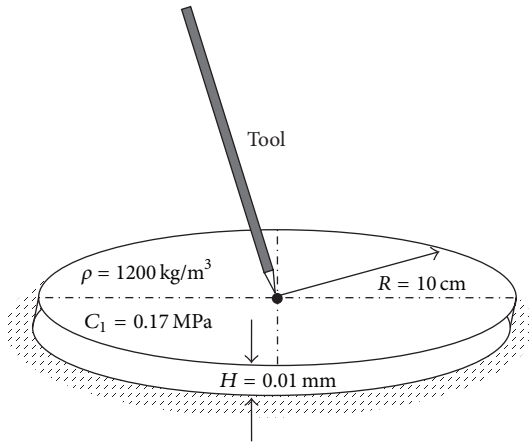


FIGURE 6: Hyperelastic circular membrane with fixed boundary conditions and concentrated force at the center of the top surface.

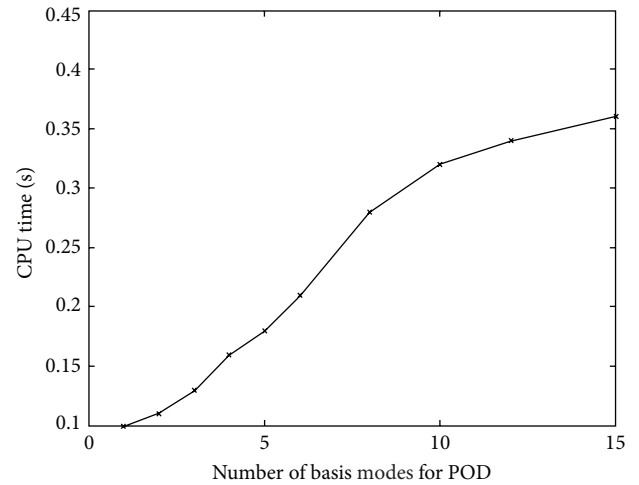


FIGURE 8: CPU time consumed in the solution of the hyperelastic circular membrane as the number of POD basis modes increases.

consumed was around 3% of the full-order model with a relatively small error as shown in Figure 3.

6.2. Circular Membrane. Here, we will consider a circular hyperelastic membrane of a radius $R = 10$ cm, thickness $H = 0.01$ mm, and density $\rho = 1200$ kg/m³, Figure 6. The boundary of the membrane is fixed, while the tool applies a concentrated load at the center of the top surface as follows:

$$u = u_{\text{tooltip}} = \begin{cases} 0.1t & t < 0.1 \\ 0, & t \geq 0.1 \end{cases} \quad \text{at } r = 0. \quad (35)$$

A Neo-Hookean hyperelastic model is assumed with $C_1 = 0.17$ MPa, and all of the initial conditions of the membrane are set to zero.

Figure 7 shows the relative error, (34), as the number of POD basis modes increases. It is obvious that the relative error decreases as the number of basis modes increases. The relative error of the reduced-order model with only

2 basis functions is relatively high; however, by increasing the number of basis functions, the error is dramatically reduced. The error with 8 basis functions is very small, and the change in error after that is negligible.

The CPU time consumption is shown in Figure 8, where it is shown that the CPU time was reduced dramatically by using small number of POD basis modes; however, as the number of basis modes increases, the time consumption increases as well.

Figure 9 shows the solution of the displacement of the hyperelastic circular membrane problem shown in Figure 6, and the solution is obtained using POD model order reduction technique with 8 basis functions after 0.1 sec.

7. Conclusion

In this paper, we have developed a point collocation-based method of finite spheres (PCMFS) approach with POD

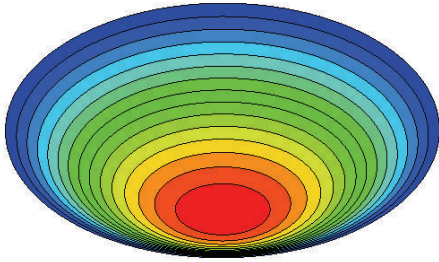


FIGURE 9: Solution of the displacement field of the hyperelastic circular membrane using POD and PCMFs.

model order reduction technique for the solution of nonlinear hyperelastic problems that arise in the simulation of soft tissue response. In this technique, an approximation is generated using the moving least squares method, while the point collocation method is used as the weighted residual technique. The advantage of this method is that numerical integration is not necessary which allows for efficient computations necessary for the simulation of applications such as virtual surgery.

POD model order reduction technique, used extensively in the field of large-scale dynamical systems, has been applied to reduce the computational cost associated with nonlinear hyperelastic problems found in soft tissue modeling. POD technique reduces the computational cost by generating an offline set of snapshots used to generate POD basis functions that is used during online computation to reduce the large-order original system by a smaller-order system reducing the computational cost.

The combination of the two methods was able to solve the boundary value problem in real time with relatively acceptable margin of error. The results showed that the computational time for the evaluation of the system matrices increases linearly with the number of nodes. For example, we were able to achieve relatively negligible error with only 8 basis functions with a time consumption of almost 3% of the time used in the full-order model.

The proposed technique can play a vital role in the development of physics-based virtual surgery environment that can account for nonlinear behavior of soft biological tissue; this method can be extended to more complicated material models in which more complicated phenomena such as deformation, incision, and cutting, as well as the reaction forces on the surgical tools, are modeled in real time.

References

- [1] M. J. Wagner and H. A. Thomas Jr., "Application of the medical knowledge general competency to emergency medicine," *Academic Emergency Medicine*, vol. 9, no. 11, pp. 1236–1241, 2002.
- [2] Y. Lim, *Physics based digital surgery using the point associated finite field approach [Ph.D. thesis]*, Rensselaer Polytechnic Institute, Troy, NY, USA, 2005.
- [3] E. Raposio, M. Fato, A. Schenone et al., "An "augmented-reality" aid for plastic and reconstructive surgeons," in *Proceedings of the Medicine Meets Virtual Reality (MMVR '5)*, pp. 232–235, Amsterdam, The Netherlands, 1997.
- [4] T. Krummel, "Surgical simulation and virtual reality: the coming revolution," *Annals of Surgery*, vol. 228, no. 5, pp. 635–637, 1998.
- [5] A. Levin, "Fewer crashes caused by pilots," Tech. Rep., USA Today, Washington, DC, USA, 2004.
- [6] S. F. Frisken-Gibson, "Using linked volumes to model object collisions, deformation, cutting, carving, and joining," *IEEE Transactions on Visualization and Computer Graphics*, vol. 5, no. 4, pp. 333–348, 1999.
- [7] D. Terzopoulost, J. Platt, A. Barr, and K. Fleischert, "Elastically deformable models," in *Proceedings of the 14th Annual Conference on Computer Graphics and Interactive Techniques (SIGGRAPH '87)*, vol. 21, no. 4, pp. 205–214, July 1987.
- [8] S. A. Cover, N. F. Ezquerra, R. Rowe, T. Gadacz, and J. F. O'Brien, "Interactively deformable models for surgery simulation," *IEEE Computer Graphics and Applications*, vol. 13, no. 6, pp. 68–75, 1993.
- [9] U. G. Kühnapfel, C. Kuhn, M. Hübner, H. G. Krumm, H. Maass, and B. Neisius, "The Karlsruhe endoscopic surgery trainer as an example for virtual reality in medical education," *Minimally Invasive Therapy and Allied Technologies*, vol. 6, no. 2, pp. 122–125, 1997.
- [10] Y. Lee, D. Terzopoulos, and K. Waters, "Realistic modeling for facial animation," in *Proceedings of the 22nd Annual ACM Conference on Computer Graphics and Interactive Techniques (SIGGRAPH '95)*, pp. 55–62, August 1995.
- [11] R. M. Koch, M. H. Gross, F. R. Carls, D. F. von Buren, G. Fankhauser, and Y. I. H. Parish, "Simulating facial surgery using finite element models," in *Proceedings of the 23rd Annual Conference on Computer Graphics and Interactive Techniques (SIGGRAPH '96)*, pp. 421–428, August 1996.
- [12] R. M. Kenedi, T. Gibson, J. H. Evans, and J. C. Barbenel, "Tissue mechanics," *Physics in Medicine and Biology*, vol. 20, no. 5, pp. 163–169, 1975.
- [13] K. Waters, "Physical model of facial tissue and muscle articulation derived from computer tomography data," in *Visualization in Biomedical Computing '92*, vol. 1808 of *Proceedings of SPIE*, pp. 574–583, October 1992.
- [14] S. Cotin, J. Pignon, H. Delingette, and G. Subsol, "A craniofacial surgery simulation test-bed," in *Visualization for Biomedical Computing (VBC '94)*, Rochester, Minn, USA, October 1994.
- [15] S. Platt and N. Badler, "Animating facial expressions," in *Proceedings of the 8th Annual Conference on Computer Graphics and Interactive Techniques (SIGGRAPH '81)*, vol. 15, pp. 245–252, August 1981.
- [16] A. Gelder, "Approximate simulation of elastic membranes by triangulated spring meshes," *Journal of Graphic Tools*, vol. 3, no. 2, pp. 21–42, 1998.
- [17] M. Bro-Nielsen, "Finite element modeling in surgery simulation," *Proceedings of the IEEE*, vol. 86, no. 3, pp. 490–503, 1998.
- [18] S. Cotin, H. Delingette, and N. Ayache, "Real-time elastic deformations of soft tissues for surgery simulation," *IEEE Transactions on Visualization and Computer Graphics*, vol. 5, no. 1, pp. 62–73, 1999.
- [19] H. Delingette, N. Ayache, and S. Cotin, "A hybrid elastic model for real-time cutting, deformations, and force feedback for surgery training and simulation," *The Visual Computer*, vol. 16, no. 8, pp. 437–452, 2000.
- [20] D. James and A. Pai, "Artdefo: accurate real time deformable objects," in *Proceedings of the 26th ACM Annual Conference on Computer Graphics and Interactive Techniques (SIGGRAPH '99)*, pp. 65–72, August 1999.

- [21] K. Miller, "Constitutive model of brain tissue suitable for finite element analysis of surgical procedures," *Journal of Biomechanics*, vol. 32, no. 5, pp. 531–537, 1999.
- [22] K. Miller and K. Chinzei, "Constitutive modelling of brain tissue: experiment and theory," *Journal of Biomechanics*, vol. 30, no. 11–12, pp. 1115–1121, 1997.
- [23] K. Miller and K. Chinzei, "Mechanical properties of brain tissue in tension," *Journal of Biomechanics*, vol. 35, no. 4, pp. 483–490, 2002.
- [24] K. Miller, K. Chinzei, G. Orsengo, and P. Bednarz, "Mechanical properties of brain tissue in-vivo: experiment and computer simulation," *Journal of Biomechanics*, vol. 33, no. 11, pp. 1369–1376, 2000.
- [25] M. Farshad, M. Barbezat, P. Flueler, F. Schmidlin, P. Graber, and P. Niederer, "Material characterization of the pig kidney in relation with the biomechanical analysis of renal trauma," *Journal of Biomechanics*, vol. 32, no. 4, pp. 417–425, 1999.
- [26] N. Ayache and H. Delingette, "Soft tissue modeling for surgery simulation," in *Computational Models for the Human Body*, pp. 453–550, Elsevier, 2004.
- [27] S. Blemker, V. Hing, R. Fedkiw, and J. Teran, "Finite volume methods for the simulation of skeletal muscle," in *Proceedings of the Eurographics/SIGGRAPH Symposium on Computer Animation (SCA '03)*, pp. 68–74, San Diego, Calif, USA, 2003.
- [28] K. Miller, G. Joldes, D. Lance, and A. Wittek, "Total Lagrangian explicit dynamics finite element algorithm for computing soft tissue deformation," *Communications in Numerical Methods in Engineering*, vol. 23, no. 2, pp. 121–134, 2007.
- [29] Z. A. Taylor, O. Comas, M. Cheng et al., "On modelling of anisotropic viscoelasticity for soft tissue simulation: numerical solution and GPU execution," *Medical Image Analysis*, vol. 13, no. 2, pp. 234–244, 2009.
- [30] S. M. BaniHani and S. De, "A comparison of some model order reduction methods for fast simulation of soft tissue response using the point collocation-based method of finite spheres," *Engineering with Computers*, vol. 25, no. 1, pp. 37–47, 2009.
- [31] Y. C. Yoon, S. H. Lee, and T. Belytschko, "Enriched meshfree collocation method with diffuse derivatives for elastic fracture," *Computers & Mathematics with Applications*, vol. 51, no. 8, pp. 1349–1366, 2006.
- [32] S. H. Lee and Y. C. Yoon, "Meshfree point collocation method for elasticity and crack problems," *International Journal for Numerical Methods in Engineering*, vol. 61, no. 1, pp. 22–48, 2004.
- [33] M. A. Puso, J. S. Chen, E. Zywickz, and W. Elmer, "Meshfree and finite element nodal integration methods," *International Journal for Numerical Methods in Engineering*, vol. 74, no. 3, pp. 416–446, 2008.
- [34] S. De, Y. J. Lim, M. Manivannan, and M. A. Srinivasan, "Physically realistic virtual surgery using the point-associated finite field (PAFF) approach," *Presence*, vol. 15, no. 3, pp. 294–308, 2006.
- [35] K. J. Bathe, *Finite Element Procedures*, Prentice-Hall, Englewood Cliffs, NJ, USA, 1996.
- [36] O. Zienkiewicz and R. Taylor, *The Finite Element Method Set*, Butterworth-Heinemann, London, UK, 6th edition, 2005.
- [37] Z. Gao, K. Lister, and J. P. Desai, "Constitutive modeling of liver tissue: experiment and theory," *Annals of Biomedical Engineering*, vol. 38, no. 2, pp. 505–516, 2010.
- [38] R. Ogden, *Non-Linear Elastic Deformations*, Halsted Press, New York, NY, USA, 1984.
- [39] R. Ogden, "Large deformation isotropic elasticity—on the correlation of theory and experiment for incompressible rubberlike solids," *Proceedings of the Royal Society of London A*, vol. 326, no. 1567, pp. 565–584, 1972.
- [40] A. C. Antoulas, *Approximation of Large-Scale Dynamical Systems*, Society for Industrial and Applied Mathematics (SIAM), Philadelphia, Pa, USA, 2005.
- [41] R. W. Freund, "Krylov-subspace methods for reduced-order modeling in circuit simulation," *Journal of Computational and Applied Mathematics*, vol. 123, no. 1–2, pp. 395–421, 2000.
- [42] E. Rudnyi and J. Korvink, "Review: automatic model reduction for transient simulation of MEMS-based devices," *Sensors Update*, vol. 11, no. 1, pp. 3–33, 2002.
- [43] M. Rewienski, *A trajectory piecewise-linear approach to model order reduction of nonlinear dynamical systems [Ph.D. thesis]*, MIT, Cambridge, Mass, USA, 2003.
- [44] E. Grimme, *Krylov projection methods for model reduction [Ph.D. thesis]*, University of Illinois at Urbana-Champaign, Champaign, Ill, USA, 1997.
- [45] K. Glover, "All optimal Hankel-norm approximations of linear multivariable systems and their L^∞ -error bounds," *International Journal of Control*, vol. 39, no. 6, pp. 1115–1193, 1984.
- [46] Y. C. Liang, H. P. Lee, S. P. Lim, W. Z. Lin, K. H. Lee, and C. G. Wu, "Proper orthogonal decomposition and its applications. I. Theory," *Journal of Sound and Vibration*, vol. 252, no. 3, pp. 527–544, 2002.
- [47] J. Lumley, G. Berkooz, and P. Holmes, "The proper orthogonal decomposition in the analysis of turbulent flows," *Annual Review of Fluid Mechanics*, vol. 25, pp. 539–575, 1993.
- [48] T. Kim, "Frequency-domain Karhunen-Lóeve method and its application to linear dynamic systems," *American Institute of Aeronautics and Astronautics Journal*, vol. 36, no. 11, pp. 2117–2123, 1998.
- [49] P. Holmes, J. L. Lumley, and G. Berkooz, *Turbulence, Coherent Structures, Dynamical Systems and Symmetry*, Cambridge University Press, New York, NY, USA, 1996.
- [50] J. L. Lumley, *Stochastic Tools in Turbulence*, Academic Press, New York, NY, USA, 1971.

Research Article

Homotopy Iteration Algorithm for Crack Parameters Identification with Composite Element Method

Ling Huang, Zhongrong Lv, Weihuan Chen, and Jike Liu

Department of Applied Mechanics, Sun Yat-sen University, Guangzhou, Guangdong 510006, China

Correspondence should be addressed to Zhongrong Lv; lvzhr@mail.sysu.edu.cn

Received 19 July 2013; Revised 12 October 2013; Accepted 12 October 2013

Academic Editor: Timon Rabczuk

Copyright © 2013 Ling Huang et al. This is an open access article distributed under the Creative Commons Attribution License, which permits unrestricted use, distribution, and reproduction in any medium, provided the original work is properly cited.

An approach based on homotopy iteration algorithm is proposed to identify the crack parameters in beam structures. In the forward problem, a fully open crack model with the composite element method is employed for the vibration analysis. The dynamic responses of the cracked beam in time domain are obtained from the Newmark direct integration method. In the inverse analysis, an identification approach based on homotopy iteration algorithm is studied to identify the location and the depth of a cracked beam. The identification equation is derived by minimizing the error between the calculated acceleration response and the simulated measured one. Newton iterative method with the homotopy equation is employed to track the correct path and improve the convergence of the crack parameters. Two numerical examples are conducted to illustrate the correctness and efficiency of the proposed method. And the effects of the influencing parameters, such as measurement time duration, measurement points, division of the homotopy parameter and measurement noise, are studied.

1. Introduction

Identification of crack parameters using the dynamic responses with finite element method (FEM) has been studied extensively for many years. In order to improve the degree of accuracy of vibration analysis, most of the approaches [1, 2] are based on densely refining finite element mesh. But these methods may lead to a large amount of computations. Unlike the classical FEM, Zeng [3] proposed a composite element method (CEM) combining the conventional FEM and classical theory (CT) to solve the structural dynamical problems. And Lu and Law [4] further improve the CEM using certain special boundary conditions of the beam. It is known that the CEM has two available approaches, the h -version and the c -version. As the former by increasing the number of element mesh is just like that of p -version of the FEM [3], the latter by increasing the number of analytical functions will reduce the number of degrees of freedom in the FEM. And the latter can obtain the fine approximate solution with less computational effort in structural dynamics. Thus, a super convergence equation of motion of the structure can be established by using the c -version of CEM.

There exist many reports on damage detection using structural dynamic response. Some of the methods are based on the time domain [5–8]. Cattarius and Inman [5] used the time histories of vibration response of the structure to identify damage in smart structures. Lu and Liu [6] made use of the dynamic responses of bridge under a moving vehicle to identify both the local damage of bridge and vehicular parameters. Lu and Law [7] proposed an approach for structural damage identification based on response sensitivity analysis. However, the response sensitivity approach is a local convergence approach, and it requires the initial values of the unknowns to be close to the true values. Then, Lu et al. [8] proposed a two-step approach based on mode shape curvature and response sensitivity analysis for crack identification.

As both the crack location and depth are unknowns in the identification, a method with large convergence range should be sought. The homotopy method [9–12] which is based on the concept of homotopy is a widely convergent method for solving system of equations. It has been extended for other algorithm and applied in many fields; for example, He [10] proposed a homotopy perturbation method, which combines the homotopy in topology and traditional perturbation

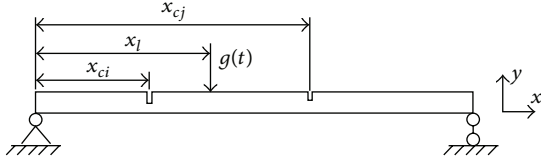


FIGURE 1: A simply supported beam with cracks.

method, to provide an approximate solution to a wide range of linear and nonlinear problems. Liao [11] proposed a homotopy analysis method for solving highly nonlinear problems in science, finance, and engineering areas. Alexander and Yorke [12] employed a homotopy continuation method to solve the fixed points and singularities of vector fields and bifurcation problems.

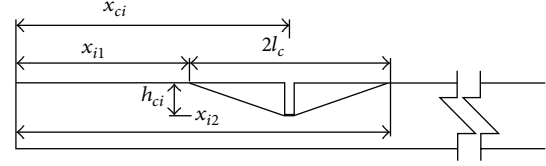
In this paper, an approach for identifying the parameters of cracks in a cracked beam based on homotopy iteration algorithm is presented. A fully open crack model with composite element model is adopted to establish the dynamics equation of the Euler-Bernoulli beam system. In inverse problem, the identification equation is derived by the minimization of the error between the calculated acceleration response and the simulated measured one. The equation is solved iteratively to identify the crack parameters. Meanwhile, Newton's method with the homotopy equation is used to track the correct path and improve the convergence of the crack parameters. A simply supported beam and a cantilever beam are studied to illustrate the accuracy and efficiency of the proposed method. Both single and multiple cracks in the beam can be identified successfully using several measured acceleration responses. And the effects of measurement time duration, measurement points, division of the homotopy parameter, and measurement noise on the identified results are investigated.

2. Forward Problem

2.1. Crack Model. Figure 1 shows a simple beam with multiple fully opened cracks along its length. It is assumed that the cracks have uniform depth across the width of the beam and that the mass distribution along the beam does not change. The stiffness, for the simplicity, is assumed to be varied linearly with a triangular reduction in a local region as Sinha et al. [13] proposed. That is, the crack only leads to local stiffness reduction in a specified length adjacent to the crack. The effective length of the stiffness reduction for the crack is $l_c = 1.5d$. As shown in Figure 2, the flexural rigidity $EI(x)$ adjacent to the i th crack can be written as

$$EI(x) = \begin{cases} EI_0 - E(I_0 - I_{ci}) \frac{(x - x_{i1})}{(x_i - x_{i1})}, & x_{i1} \leq x \leq x_{ci}, \\ EI_0 - E(I_0 - I_{ci}) \frac{(x_{i2} - x)}{(x_{i2} - x_i)}, & x_{ci} \leq x \leq x_{i2}, \end{cases} \quad (1)$$

where E is Young's modulus and $I_0 = wd^3/12$ and $I_{ci} = w(d - h_{ci})^3/12$ are the moments of inertia of the intact and

FIGURE 2: Variation on flexural rigidity $EI(x)$ adjacent to a crack.

cracked cross sections, respectively. w and d are the width and height of the beam, respectively. $x_{i1} = x_{ci} - l_c$ and $x_{i2} = x_{ci} + l_c$ are the positions where the reduction of the flexural rigidity begins and finishes, respectively. If the beam has multiple cracks, the same procedure can be followed to calculate the flexural rigidity of other cracks.

2.2. Dynamic Response of the Structure with CEM. As shown in Figure 1, the beam is discretized into one element together with several terms eigenfunction of classical theory. Lu and Law [4, 7] have proved that only using one finite element is effective in the c -version technique of CEM. And it can reduce the total number of degrees of freedom in the finite element model. For the crack identification, what is important is that we do not need to judge whether the cracks affect one or more elements stiffness as the crack(s) is always in one finite element for the entire beam. Otherwise, it needs to calculate the stiffness distribution due to the crack(s) along the beam in each iteration this one-beam-one-element strategy simplifies greatly the process in crack identification.

In the CEM, the displacement field d_{CEM} is combined with the FEM part and the CT part. The FEM part of the displacement field should satisfy the nodal boundary conditions, and it can be expressed as the product of the shape function matrix $\mathbf{N}(x)$ and the nodal displacement vector $q(t)$,

$$d_{FEM}(x, t) = \mathbf{N}(x) q(t), \quad (2)$$

where

$$\mathbf{N}(x) = \begin{bmatrix} 1 - 3\frac{x^2}{L^2} + 2\frac{x^3}{L^3}, x - 2\frac{x^2}{L} + \frac{x^3}{L^2}, \\ 3\frac{x^2}{L^2} - 2\frac{x^3}{L^3}, \frac{x^3}{L^2} - \frac{x^2}{L} \end{bmatrix}, \quad (3)$$

where L is the length of the beam.

The second part can be obtained by the linear combination of the multiplication of analytical shape function $\phi(x)$ with a vector of coefficient $c(t)$

$$d_{CT}(x, t) = \sum_{r=1}^n \phi_r(x) c_r(t), \quad (r = 1, 2, \dots, n), \quad (4)$$

where $\phi_r(x)$ is a special value which can be obtained according to the boundary conditions of the beam and n is the number of the mode functions used from the CT. Such that, for a simply supported beam, $\phi_r(x) = \sin(r\pi x/L)$ can be selected as Lu and Law [4] proposed. And the coefficient $c_r(t)$ denotes the contribution of the $\phi_r(x)$ in the total displacement field. For a uniform beam, less terms of the shapes

function in CT also can be obtained with accuracy results [4]. And the number of terms n can be determined by a frequency convergence test as the previous study by Lu and Law [7]. The frequency convergence criterion is defined as

$$\max_{r=1,2,\dots,10} \left| \frac{\Delta\omega_r^n}{\omega_r^n} \right| < \text{Tol}, \quad (5)$$

where ω_r^n is the estimation of the r th circular frequency with n -terms in the CT. $\Delta\omega_r^n = \omega_r^n - \omega_r^{n-1}$ is the difference of the r th circular frequency obtained with the n -terms and $(n-1)$ -terms. Tol is the tolerance value.

The displacement field of the CEM for a uniform Euler-Bernoulli beam element can be written as

$$d_{\text{CEM}}(x, t) = d_{\text{FEM}}(x, t) + d_{\text{CT}}(x, t) = \mathbf{S}(x) \mathbf{Q}(t), \quad (6)$$

where $\mathbf{S}(x) = [\mathbf{N}(x), \phi_1(x), \phi_2(x), \dots, \phi_n(x)]$ is the generalized shape function of CEM.

The stiffness matrix of the cracked beam can be obtained from the following equation:

$$\mathbf{K} = \int_0^L \frac{d^2 \mathbf{S}(x)^T}{dx^2} EI(x) \frac{d^2 \mathbf{S}(x)}{dx^2} dx. \quad (7)$$

For a beam with multiple cracks, as the whole crack beam is represented as a single finite element, the whole length of the beam can be divided according to the varied flexural rigidity. For $EI(x)$ adjacent to the i th crack can be obtained from (1); the global stiffness matrix \mathbf{K} can be obtained by superposition.

As the effect of crack on the mass of the beam is neglected and the consistent mass matrix of the cracked beam can be obtained from the following equation:

$$\mathbf{M} = \int_0^L \mathbf{S}(x)^T \rho A \mathbf{S}(x) dx, \quad (8)$$

where ρ is the mass density A is the area of the cross section.

After introducing the boundary condition, the equation of motion of the forced vibration of the cracked Euler-Bernoulli beam is expressed as

$$\mathbf{M}\ddot{\mathbf{Q}} + \mathbf{C}\dot{\mathbf{Q}} + \mathbf{K}\mathbf{Q} = \mathbf{G}(t). \quad (9)$$

In this study, Rayleigh damping model [14] is adopted; that is, $\mathbf{C} = a_1 \mathbf{M} + a_2 \mathbf{K}$, where a_1 and a_2 are two constants obtained from two different undamped natural frequencies, ω_i and ω_j , and their associated modal damping ratios, ξ_i and ξ_j , with the expression of $a_1 = 2\omega_j\omega_i(\omega_j\xi_i - \omega_i\xi_j)/(\omega_j^2 - \omega_i^2)$ and $a_2 = 2(\omega_j\xi_j - \omega_i\xi_i)/(\omega_j^2 - \omega_i^2)$. The vector of generalized acceleration $\ddot{\mathbf{Q}}$, velocity $\dot{\mathbf{Q}}$, and displacement \mathbf{Q} of the structure can be obtained from (9) by direct integration. Further, the vector of physical acceleration $\ddot{\mathbf{d}}(x)$, velocity $\dot{\mathbf{d}}(x)$, and displacement $\mathbf{d}(x)$ can be obtained from

$$\ddot{\mathbf{d}}(x) = \mathbf{S}(x) \ddot{\mathbf{Q}}, \quad (10a)$$

$$\dot{\mathbf{d}}(x) = \mathbf{S}(x) \dot{\mathbf{Q}}, \quad (10b)$$

$$\mathbf{d}(x) = \mathbf{S}(x) \mathbf{Q}. \quad (10c)$$

The generalized force vector is $\mathbf{G}(t) = \mathbf{S}(x_i)^T g(t)$, where $g(t)$ is an external force acting at the location of x_i from the left support.

3. Inverse Problem

3.1. Objective Function. The problem of crack identification can be treated as an optimization problem. In the identification, the unknowns consist of the crack location x_c and crack depth h_c ; that is, $\boldsymbol{\alpha} = [x_c, h_c]$. If there are m measured points in the beam structure, the measured acceleration response can be expressed as $\ddot{\mathbf{d}}^* = (\ddot{\mathbf{d}}_1, \ddot{\mathbf{d}}_2, \dots, \ddot{\mathbf{d}}_m)$. The objective function for the optimization problem can be derived by minimizing the error between the calculated acceleration response and the simulated measured one as

$$J = \frac{1}{2} \sum_{i=1}^{nt} \sum_{j=1}^m (\ddot{\mathbf{d}}(\boldsymbol{\alpha}, t) - \ddot{\mathbf{d}}^*(\boldsymbol{\alpha}, t))^2, \quad (11)$$

$$i = 1, 2, \dots, nt, \quad j = 1, 2, \dots, m,$$

where t denotes the the measured time instants, $nt = t/dt$ is the number of time step, and dt is the increment of time step.

The inverse problem can be solved by minimizing the objective function. Taking partial derivative with respect to the identification vector in (11), we have

$$f(\boldsymbol{\alpha}) = \begin{cases} \sum_{i=1}^{nt} \sum_{j=1}^m (\ddot{\mathbf{d}}(\boldsymbol{\alpha}, t) - \ddot{\mathbf{d}}^*(\boldsymbol{\alpha}, t)) \frac{\partial \ddot{\mathbf{d}}(\boldsymbol{\alpha}, t)}{\partial x_c} = 0, \\ \sum_{i=1}^{nt} \sum_{j=1}^m (\ddot{\mathbf{d}}(\boldsymbol{\alpha}, t) - \ddot{\mathbf{d}}^*(\boldsymbol{\alpha}, t)) \frac{\partial \ddot{\mathbf{d}}(\boldsymbol{\alpha}, t)}{\partial h_c} = 0, \end{cases} \quad (12)$$

where $\partial \ddot{\mathbf{d}}(\boldsymbol{\alpha}, t)/\partial x_c$ and $\partial \ddot{\mathbf{d}}(\boldsymbol{\alpha}, t)/\partial h_c$ are the acceleration response sensitivities with respect to the crack location and depth, respectively.

3.2. Homotopy Iteration Algorithm for Crack Identification. The basic idea of homotopy iteration algorithm is to introduce a parameter λ into the nonlinear equation $f(\boldsymbol{\alpha}) = 0$ to construct a family of homotopy mapping $H(\boldsymbol{\alpha}, \lambda)$, where $\lambda \in [0, 1]$ is named the homotopy parameter. The homotopy equation is assumed to be $H(\boldsymbol{\alpha}, \lambda) = \lambda f(\boldsymbol{\alpha}) + (1 - \lambda) f_0(\boldsymbol{\alpha})$ in this paper. When $\lambda = 1$, H is the mapping of $f(\boldsymbol{\alpha})$ as (12) shows, and, when $\lambda = 0$, H is assumed to be the mapping of $f_0(\boldsymbol{\alpha})$. And $f_0(\boldsymbol{\alpha})$ is set to be similar to $f(\boldsymbol{\alpha})$ but, related to the initial point, can be expressed as $f_0(\boldsymbol{\alpha}) = (\ddot{\mathbf{d}}(\boldsymbol{\alpha}, t) - \ddot{\mathbf{d}}(\boldsymbol{\alpha}_0, t)) \partial \ddot{\mathbf{d}}(\boldsymbol{\alpha}, t)/\partial \boldsymbol{\alpha}$, where $\boldsymbol{\alpha}_0$ is the arbitrarily selected initial value vector. In this way, a family of homotopy mapping H can be constructed instead of a single mapping f . Thus, the homotopy equation can meet the following equation:

$$H(\boldsymbol{\alpha}, \lambda) = \lambda f(\boldsymbol{\alpha}) + (1 - \lambda) f_0(\boldsymbol{\alpha}) = 0, \quad (13)$$

$$H(\boldsymbol{\alpha}, 0) = f_0(\boldsymbol{\alpha}) = 0, \quad (14)$$

$$H(\boldsymbol{\alpha}, 1) = f(\boldsymbol{\alpha}) = 0. \quad (15)$$

Equations (14) and (15) show that as the homotopy parameter λ increases from zero to one, the homotopy equation $H(\boldsymbol{\alpha}, \lambda)$

varies from $f_0(\boldsymbol{\alpha})$ to $f(\boldsymbol{\alpha})$. Hence, the parameters of the crack can be obtained by following the variations of parameter λ , and, when $H(\boldsymbol{\alpha}, \lambda) = 0$, the identification vector $\boldsymbol{\alpha}$ is in the homotopy path.

After obtaining the homotopy equation, the Newton iterative method is used to track the path in the process of identification. The solving procedure is explained as follows.

Step 1. Guess an initial value vector of crack parameters $\boldsymbol{\alpha}_0 = [x_{c0}, h_{c0}]$, divide the range of homotopy parameter $\lambda \in [0, 1]$ into n equal parts, and then obtain $d\lambda = 1/n$, let $\lambda_0 = 0$.

Step 2. Trace the homotopy path from the initial value $(\boldsymbol{\alpha}_0, \lambda_0)$ and give an increment $d\lambda$ to the homotopy parameter λ as $\lambda_1 = \lambda_0 + d\lambda$.

Step 3. Using Newton iterative method to calculate an updated vector of crack parameter $\boldsymbol{\alpha}_1 = [x_{c1}, h_{c1}]$ in the homotopy path, we have

$$\boldsymbol{\alpha}_1 = \boldsymbol{\alpha}_0 - \left(\frac{\partial H(\boldsymbol{\alpha}, \lambda_1)}{\partial \boldsymbol{\alpha}} \Big|_{\boldsymbol{\alpha}=\boldsymbol{\alpha}_0} \right)^{-1} H(\boldsymbol{\alpha}_0, \lambda_1), \quad (16)$$

where $\partial H(\boldsymbol{\alpha}, \lambda_1)/\partial \boldsymbol{\alpha}$ is the homotopy equation with respect to the crack parameters. The value of $H(\boldsymbol{\alpha}_0, \lambda_1)$ and $\partial H(\boldsymbol{\alpha}, \lambda_1)/\partial \boldsymbol{\alpha}$ will be introduced in next section.

Step 4. Check whether the updated crack parameter vector $\boldsymbol{\alpha}_1 = [x_{c1}, h_{c1}]$ is physically meaningful or not. If not, the result is considered diverged, then stop iteration and move to Step 1 to start with a new initial value or division of homotopy parameter. If otherwise, go to the next step.

Step 5. Let $\boldsymbol{\alpha}_0 = \boldsymbol{\alpha}_1$; repeat from Steps 3 to 4, until the obtained $(\boldsymbol{\alpha}_1, \lambda_1)$ in homotopy path satisfies the following convergence conditions:

$$\left\| \frac{\boldsymbol{\alpha}_1 - \boldsymbol{\alpha}_0}{\boldsymbol{\alpha}_1} \right\| \leq \text{Tol1}, \quad (17a)$$

where Tol1 is the first tolerance value for convergence and is taken as 1.0×10^{-3} in this study.

Step 6. Repeat the Newton iterative again, until the following convergence criterion is satisfied. That is, the identification parameters are assumed to in the homotopy path when $H(\boldsymbol{\alpha}_1, \lambda_1)$ meets the following criterion:

$$\|H(\boldsymbol{\alpha}_1, \lambda_1)\| \leq \text{Tol2}, \quad (17b)$$

where Tol2 is the second tolerance value and is taken to be 0.1 for all the study cases.

Step 7. The pair of unknowns $(\boldsymbol{\alpha}_1, \lambda_1)$ is taken as the new set of initial value $(\boldsymbol{\alpha}_0, \lambda_0)$ and repeat Steps 2 to 5 until the homotopy parameter λ reaches 1.0. The final $\boldsymbol{\alpha}_1$ would then be the required set of identification results.

3.3. Homotopy Equation and Its First Derivative. In order to obtain the homotopy equation, the acceleration response with

respect to the crack parameter should be obtained first. We take the derivative on both sides of (9) with respect to the crack location and crack depth; then we have

$$\begin{aligned} \mathbf{M} \frac{\partial \ddot{\mathbf{Q}}}{\partial x_c} + \mathbf{C} \frac{\partial \dot{\mathbf{Q}}}{\partial x_c} + \mathbf{K} \frac{\partial \mathbf{Q}}{\partial x_c} &= -a_2 \frac{\partial \mathbf{K}}{\partial x_c} \dot{\mathbf{Q}} - \frac{\partial \mathbf{K}}{\partial x_c} \mathbf{Q}, \\ \mathbf{M} \frac{\partial \ddot{\mathbf{Q}}}{\partial h_c} + \mathbf{C} \frac{\partial \dot{\mathbf{Q}}}{\partial h_c} + \mathbf{K} \frac{\partial \mathbf{Q}}{\partial h_c} &= -a_2 \frac{\partial \mathbf{K}}{\partial h_c} \dot{\mathbf{Q}} - \frac{\partial \mathbf{K}}{\partial h_c} \mathbf{Q}, \end{aligned} \quad (18)$$

where $\partial \ddot{\mathbf{Q}}/\partial x_c$, $\partial \ddot{\mathbf{Q}}/\partial h_c$, $\partial \dot{\mathbf{Q}}/\partial x_c$, $\partial \dot{\mathbf{Q}}/\partial h_c$, $\partial \mathbf{Q}/\partial x_c$, and $\partial \mathbf{Q}/\partial h_c$ are the vectors of generalized acceleration, velocity, and displacement sensitivities with respect to the crack location and depth, respectively. $\partial \mathbf{K}/\partial x_c$ and $\partial \mathbf{K}/\partial h_c$ are the first partial derivatives of the stiffness matrix with respect to the crack parameters. Since the flexural rigidity $EI(x)$ involves the crack location and depth and the global stiffness matrix \mathbf{K} can be obtained from (7), the derivatives $\partial \mathbf{K}/\partial x_c$ and $\partial \mathbf{K}/\partial h_c$ can be obtained directly. As the dynamic responses \mathbf{Q} and $\dot{\mathbf{Q}}$ have been calculated from (9), the right-hand side of (18) can be considered as a form of external force. Thus, the dynamic response sensitivity (i.e., the generalized acceleration response sensitivity, velocity response sensitivity, and displacement response sensitivity) can also be calculated from the Newmark integration method. Then, the physical acceleration response sensitivity can be obtained as

$$\frac{\partial \ddot{\mathbf{d}}}{\partial x_c} = \mathbf{S}(x) \frac{\partial \ddot{\mathbf{Q}}}{\partial x_c}, \quad (19a)$$

$$\frac{\partial \ddot{\mathbf{d}}}{\partial h_c} = \mathbf{S}(x) \frac{\partial \ddot{\mathbf{Q}}}{\partial h_c}. \quad (19b)$$

Furthermore, the objective function in (12) and homotopy equation in (13) can then be obtained.

To obtain the first derivative of the homotopy equation with respect to the crack parameters, we should apply the first derivative to both sides of (18) with respect to the crack parameters as

$$\begin{aligned} \mathbf{M} \frac{\partial^2 \ddot{\mathbf{Q}}}{\partial x_c^2} + \mathbf{C} \frac{\partial^2 \dot{\mathbf{Q}}}{\partial x_c^2} + \mathbf{K} \frac{\partial^2 \mathbf{Q}}{\partial x_c^2} \\ = -a_2 \frac{\partial^2 \mathbf{K}}{\partial x_c^2} \dot{\mathbf{Q}} - \frac{\partial^2 \mathbf{K}}{\partial x_c^2} \mathbf{Q} - 2 \left(a_2 \frac{\partial \mathbf{K}}{\partial x_c} \frac{\partial \dot{\mathbf{Q}}}{\partial x_c} + \frac{\partial \mathbf{K}}{\partial x_c} \frac{\partial \mathbf{Q}}{\partial x_c} \right), \\ \mathbf{M} \frac{\partial^2 \ddot{\mathbf{Q}}}{\partial x_c \partial h_c} + \mathbf{C} \frac{\partial^2 \dot{\mathbf{Q}}}{\partial x_c \partial h_c} + \mathbf{K} \frac{\partial^2 \mathbf{Q}}{\partial x_c \partial h_c} \\ = -a_2 \frac{\partial^2 \mathbf{K}}{\partial x_c \partial h_c} \dot{\mathbf{Q}} - \frac{\partial^2 \mathbf{K}}{\partial x_c \partial h_c} \mathbf{Q} - a_2 \frac{\partial \mathbf{K}}{\partial h_c} \frac{\partial \dot{\mathbf{Q}}}{\partial x_c} - \frac{\partial \mathbf{K}}{\partial h_c} \frac{\partial \mathbf{Q}}{\partial x_c} \\ - a_2 \frac{\partial \mathbf{K}}{\partial x_c} \frac{\partial \dot{\mathbf{Q}}}{\partial h_c} - \frac{\partial \mathbf{K}}{\partial x_c} \frac{\partial \mathbf{Q}}{\partial h_c}, \\ \mathbf{M} \frac{\partial^2 \ddot{\mathbf{Q}}}{\partial h_c^2} + \mathbf{C} \frac{\partial^2 \dot{\mathbf{Q}}}{\partial h_c^2} + \mathbf{K} \frac{\partial^2 \mathbf{Q}}{\partial h_c^2} \\ = -a_2 \frac{\partial^2 \mathbf{K}}{\partial h_c^2} \dot{\mathbf{Q}} - \frac{\partial^2 \mathbf{K}}{\partial h_c^2} \mathbf{Q} - 2 \left(a_2 \frac{\partial \mathbf{K}}{\partial h_c} \frac{\partial \dot{\mathbf{Q}}}{\partial h_c} + \frac{\partial \mathbf{K}}{\partial h_c} \frac{\partial \mathbf{Q}}{\partial h_c} \right), \end{aligned}$$

TABLE 1: Comparison of the convergence property with different number of terms in CT.

Number of term in CT	Natural frequencies in Hz ($x_c = 1000$ mm, $h_c = 1$ mm)							
	1	2	3	4	5	6	7	8
4	14.65	58.73	131.86	234.92	592.11	890.33	53510.81	58925.59
5	14.65	58.73	131.86	234.92	366.28	890.33	1252.84	58925.59
6	14.65	58.73	131.86	234.92	366.28	528.55	1252.83	1680.70
9	14.65	58.73	131.86	234.92	366.28	528.56	717.93	939.60
10	14.65	58.73	131.86	234.92	366.28	528.56	717.93	939.60

$$\begin{aligned}
& \mathbf{M} \frac{\partial^2 \ddot{\mathbf{Q}}}{\partial h_c \partial x_c} + \mathbf{C} \frac{\partial^2 \dot{\mathbf{Q}}}{\partial h_c \partial x_c} + \mathbf{K} \frac{\partial^2 \mathbf{Q}}{\partial h_c \partial x_c} \\
& = -a_2 \frac{\partial^2 \mathbf{K}}{\partial h_c \partial x_c} \dot{\mathbf{Q}} - \frac{\partial^2 \mathbf{K}}{\partial h_c \partial x_c} \mathbf{Q} - a_2 \frac{\partial \mathbf{K}}{\partial x_c} \frac{\partial \dot{\mathbf{Q}}}{\partial h_c} - \frac{\partial \mathbf{K}}{\partial x_c} \frac{\partial \mathbf{Q}}{\partial h_c} \\
& \quad - a_2 \frac{\partial \mathbf{K}}{\partial h_c} \frac{\partial \dot{\mathbf{Q}}}{\partial x_c} - \frac{\partial \mathbf{K}}{\partial h_c} \frac{\partial \mathbf{Q}}{\partial x_c},
\end{aligned} \tag{20}$$

where $\partial^2 \mathbf{K} / \partial x_c^2$, $\partial^2 \mathbf{K} / \partial x_c \partial h_c$, $\partial^2 \mathbf{K} / \partial h_c^2$, and $\partial^2 \mathbf{K} / \partial h_c \partial x_c$ are the second partial derivative of the stiffness matrix with respect to the crack parameters, and $\partial^2 \mathbf{K} / \partial x_c \partial h_c = \partial^2 \mathbf{K} / \partial h_c \partial x_c$. Since the response sensitivities $\partial \mathbf{Q} / \partial h_c$, $\partial \dot{\mathbf{Q}} / \partial x_c$, and $\partial \ddot{\mathbf{Q}} / \partial h_c$ have been calculated from (18), the second partial derivative of generalized acceleration response with respect to the unknown variables (x_c, h_c) can be calculated by the Newmark integration with (20). Then, the physical acceleration response sensitivity can be obtained as

$$\frac{\partial^2 \ddot{\mathbf{d}}}{\partial x_c^2} = \mathbf{S}(x) \frac{\partial^2 \ddot{\mathbf{Q}}}{\partial x_c^2}, \tag{21a}$$

$$\frac{\partial^2 \ddot{\mathbf{d}}}{\partial h_c^2} = \mathbf{S}(x) \frac{\partial^2 \ddot{\mathbf{Q}}}{\partial h_c^2}, \tag{21b}$$

$$\frac{\partial^2 \ddot{\mathbf{d}}}{\partial x_c \partial h_c} = \frac{\partial^2 \ddot{\mathbf{d}}}{\partial h_c \partial x_c} = \mathbf{S}(x) \frac{\partial^2 \ddot{\mathbf{Q}}}{\partial x_c \partial h_c}. \tag{21c}$$

Furthermore, the first derivative of the homotopy mapping in (13) with respect to the unknown vector $\partial H(\boldsymbol{\alpha}, \lambda) / \partial \boldsymbol{\alpha}$ can be obtained as

$$\frac{\partial H(\boldsymbol{\alpha}, \lambda)}{\partial \boldsymbol{\alpha}} = \begin{bmatrix} \lambda \frac{\partial f(\boldsymbol{\alpha})}{\partial x_c} + (1 - \lambda) \frac{\partial f_0(\boldsymbol{\alpha})}{\partial x_c} \\ \lambda \frac{\partial f(\boldsymbol{\alpha})}{\partial h_c} + (1 - \lambda) \frac{\partial f_0(\boldsymbol{\alpha})}{\partial h_c} \end{bmatrix}, \tag{22}$$

where

$$\begin{aligned}
\frac{\partial f(\boldsymbol{\alpha})}{\partial x_c} & = \left[\sum_{i=1}^{nt} \sum_{j=1}^m \left((\ddot{\mathbf{d}} - \ddot{\mathbf{d}}^*) \frac{\partial^2 \ddot{\mathbf{d}}}{\partial x_c^2} + \left(\frac{\partial \ddot{\mathbf{d}}}{\partial x_c} \right)^2 \right) \right], \\
\sum_{i=1}^{nt} \sum_{j=1}^m \left((\ddot{\mathbf{d}} - \ddot{\mathbf{d}}^*) \frac{\partial^2 \ddot{\mathbf{d}}}{\partial h_c \partial x_c} + \frac{\partial \ddot{\mathbf{d}}}{\partial x_c} \frac{\partial \ddot{\mathbf{d}}}{\partial h_c} \right) & \tag{23}
\end{aligned}$$

$$\begin{aligned}
\frac{\partial f(\boldsymbol{\alpha})}{\partial h_c} & = \left[\sum_{i=1}^{nt} \sum_{j=1}^m \left((\ddot{\mathbf{d}} - \ddot{\mathbf{d}}^*) \frac{\partial^2 \ddot{\mathbf{d}}}{\partial x_c \partial h_c} + \frac{\partial \ddot{\mathbf{d}}}{\partial h_c} \frac{\partial \ddot{\mathbf{d}}}{\partial x_c} \right) \right], \\
\sum_{i=1}^{nt} \sum_{j=1}^m \left((\ddot{\mathbf{d}} - \ddot{\mathbf{d}}^*) \frac{\partial^2 \ddot{\mathbf{d}}}{\partial h_c^2} + \left(\frac{\partial \ddot{\mathbf{d}}}{\partial h_c} \right)^2 \right) & \tag{24}
\end{aligned}$$

The first derivatives $\partial f_0(\boldsymbol{\alpha}) / \partial x_c$ and $\partial f_0(\boldsymbol{\alpha}) / \partial h_c$ can also be obtained in a similar way.

4. Numerical Simulations

4.1. A Simply Supported Beam. A uniform cross section simply supported beam with cracks is studied as shown in Figure 1. The parameters of the beam are: Young's modulus $E = 69.79$ GPa, mass density $\rho = 2600$ kg/m³, length $L = 2000$ mm, width $w = 50$ mm, and height $h = 25$ mm. An impulsive force acts at the 700 mm from the left support in the negative y -direction from $t = 0$ s to $t = 0.04$ s with

$$g(t) = \begin{cases} 10000tN, & (0 \text{ s} \leq t \leq 0.02 \text{ s}), \\ 10000(0.04 - t)N, & (0.02 \text{ s} < t \leq 0.04 \text{ s}). \end{cases} \tag{25}$$

In calculating the dynamic response, the time step is 0.001 s. Artificial measurement noise with different levels is added to the calculated responses to simulate the "measured" structural responses. All the time history data of 1.0 second are used in the identification unless otherwise specified. The two damping coefficients used for calculating Rayleigh damping matrix are both assumed to be 0.01.

Using the traditional FEM, the first eight frequencies of the beam are 14.65, 58.73, 131.85, 234.95, 366.31, 528.84, 718.45, and 941.15 Hz. Comparison with Table 1, one can find that when the number of term in CT is n , only the first n frequency is convergence for the uniform cross section beam. When only 10 modes are used, the first 8 natural frequencies can be obtained with good accuracy (the max error for the 8th natural frequency is only 0.17%). Indeed, when more terms of the harmonic functions are used, the accuracy can further be improved, but more computational time is needed in the calculation. When dynamic loads act on the beam, the dynamic responses of the beam will only include the first few lower modes; generally speaking, the contribution of the higher modes on the dynamic responses can be neglected. Thus, the number of the mode functions used from the CT is set to be 10 in the following study.

TABLE 2: Effect of the initial value on crack identification.

Scenarios	Initial value (mm)		True value (mm)		Identified results (mm)		Division of λ	Measurement points (mm)	No. of iteration
	x_{c0}	h_{c0}	x_c	h_c	x_c	h_c			
1	1500	2	1720	10	1720.000000	10.000000	5	600, 1100, 1600	31
2	1500	2	1000	10	999.999990	10.000000	5	600, 1100, 1600	38
3	1500	2	1000	1	1000.000234	1.000000	3	600, 1100, 1600	26
4	260	3	1000	1	999.999997	1.000000	21	600, 1100, 1600	146

TABLE 3: Effect of measurement time.

Scenarios	Identified results (mm)		Division of λ	Measurement time (s)	No. of iteration
	x_c	h_c			
1	1000.000234	1.000000	3	1	26
2	1000.000237	1.000000	3	2	30
3	1000.000187	1.000000	3	4	32

4.1.1. Effect of Initial Value on Crack Identification. In this case, single crack identification is conducted to illustrate the proposed method. Three measurement points located at 600 mm, 1100 mm, and 1600 mm from the left support are used in the crack identification. Totally, four Scenarios are studied as listed in Table 2. One can find that the crack parameters have been identified successfully with high accuracy in all Scenarios. It should be pointed out as the initial crack location is far away from the true crack location, the crack can also be identified successfully but the number of iteration will increase accordingly. And in general, finer division in the homotopy parameter λ should be considered as to track the correct path. Scenarios 3 and 4 show that the method is less affected by the initial values.

4.1.2. Effect of Measurement Time Duration. In this case, the effect of measurement time duration in crack identification is studied. The identification of Scenario 3 in Table 2 is reexamined; except the measurement time duration is taken to be 1.0 s, 2.0 s, and 4.0 s, respectively. The crack parameters are identified with satisfactory accuracy as shown in Table 3. It also can be notes that longer time duration has little effect on the degree of accuracy but will increase the number of iteration. And the process of iteration for this study is shown in Figure 3; one can see that longer measurement time will obtain more stable convergence pattern when tracking the approximate values in the homotopy path.

4.1.3. Effect of Measurement Points. In this case, how the measurement points affect the accuracy and the iterative process is studied. Three, four, and six measurement points are used for crack identification to give a comparison. And the other parameters are the same as the last case. The identification results are listed in Table 4. It can be found that increasing measurement points can improve the accuracy of the identification results. Figure 4 gives a comparison on the identified process of iteration. It can be noted that different number of measurement points has the similar convergence process. And the proposed method does not need a large number of measurement points.

4.1.4. Effect of Division of Homotopy Parameter. In this study, the effect of division of homotopy parameter on the identified results is discussed. Other parameters are the same as those in the last study except that the homotopy parameter is divided into 3, 4, and 5 parts. And the identified results for the study are listed in Table 5. We can find that increase of division parts of the homotopy parameter, the number of iteration will increase accordingly in general but it has little effect on the accuracy of identified results. Figure 5 shows the evolution of the crack parameters in the process of iteration for different division parts of the homotopy parameter; one can see that the convergence of Newton's method to track the homotopy path is similar.

4.1.5. Effect of Measurement Noise. In this section, the effect of measurement noise on the accuracy of identified results is taken into account. Again, the identification of Scenario 3 in Table 2 is studied. The effect of measurement noise is simulated as a normally distributed random error with zero mean and a unit standard deviation is added to the calculated acceleration as

$$\hat{\mathbf{d}} = \mathbf{d} + E_p \times N_{\text{oise}} \times \text{var}(\mathbf{d}), \quad (26)$$

where $\hat{\mathbf{d}}$ is the vectors of measured structural acceleration response, E_p is the noise level, N_{oise} is standard normal distribution vector with zero mean and unit standard deviation, and $\text{var}(\cdot)$ is the variance of the time history.

The relative errors of crack location and depth identification are defined as

$$\text{Relative error} = \left\| \frac{\boldsymbol{\alpha}_{\text{id}} - \boldsymbol{\alpha}_{\text{true}}}{\boldsymbol{\alpha}_{\text{true}}} \right\| \times 100\%, \quad (27)$$

where $\boldsymbol{\alpha}_{\text{id}}$ and $\boldsymbol{\alpha}_{\text{true}}$ are the identified and true values, respectively. Table 6 gives a comparison of the identified results for 0%, 1%, 5%, and 15% noise level, respectively. This study shows that the crack parameters have been identified successfully even with 15% measurement noise. With the increase of the measurement noise level, identification errors will become larger and the max identification error is 8.93% in the location of crack and 5.24% in the crack depth.

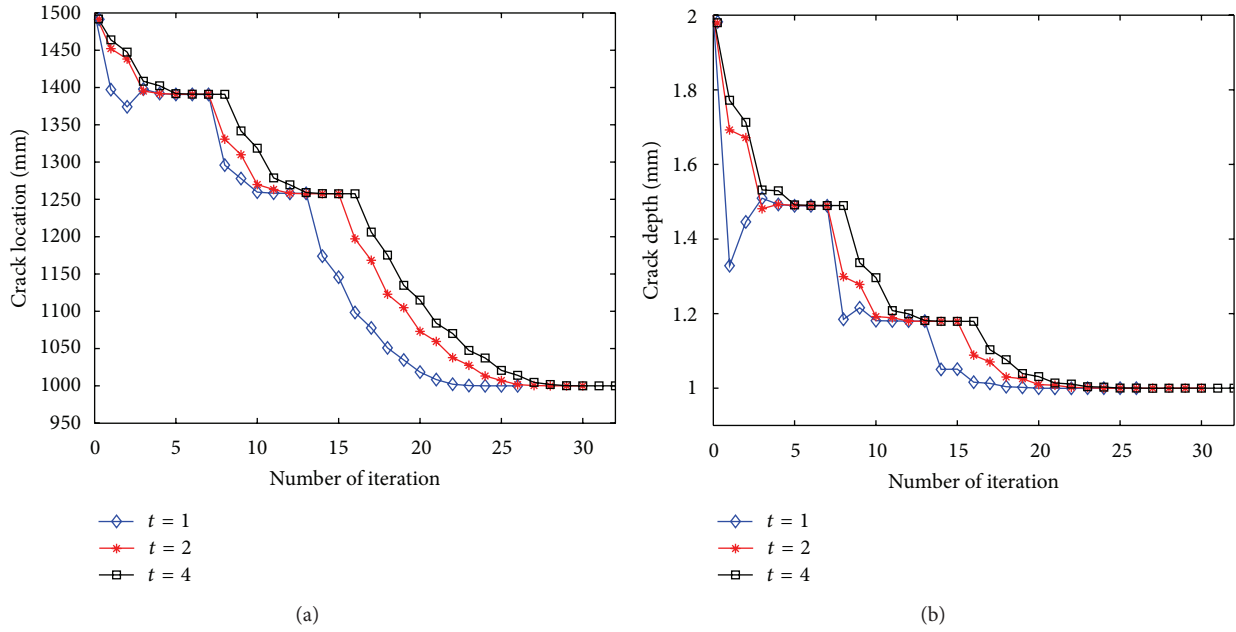


FIGURE 3: Effect of measurement time duration.

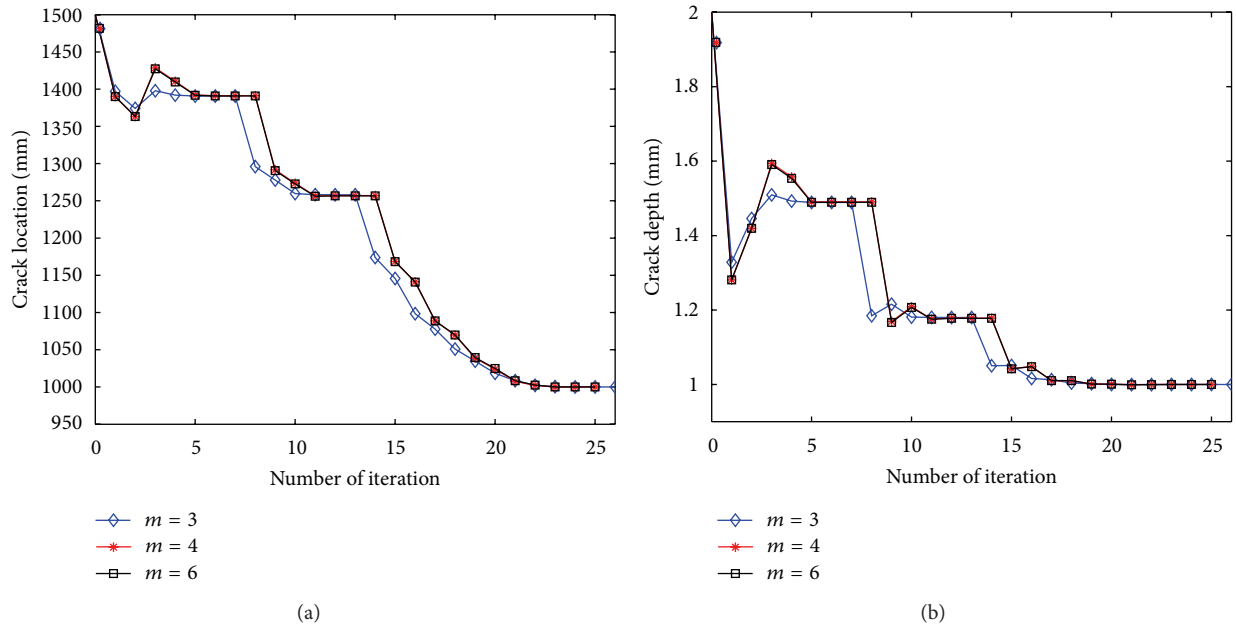


FIGURE 4: Effect of measurement points.

4.1.6. *Identification of Multiple Cracks.* The same simply supported beam is studied with two cracks in this Section. The cracks are assumed to be located at 450 mm and 1000 mm from the left support of the beam, respectively. The depths of the crack are 5 mm and 1 mm, respectively. In the identification, the initial values of locations for these two cracks are set to be 500 mm and 1500 mm, respectively, and depths are both set to be 2 mm. Six measurement points as the Scenario 3 in Table 4 are used in this case. And the setting of other parameters is shown in Table 7. The identification

results and the relative errors for the cases with 0% and 5% noise levels are considered. It can be noted that the identified results for the two cracks are as good as those for a single crack when the measurement noise is free. Comparing the identified results with measurement noise and the free noise one, we can find that the effect of measurement noise on crack identification is noticeable, but the identified results are still satisfactory. For 5% noise level, the maximum relative errors are 1.82% and 0.28% in the crack location and depth for the first crack, respectively and 6.49% and 7.22% for the second

TABLE 4: Effect of measurement points.

Scenarios	Identified results (mm)		Measurement points (mm)	No. of iteration
	x_c	h_c		
1	1000.000234	1.000000	600, 1100, 1600	26
2	1000.000005	1.000000	400, 800, 1200, 1600	25
3	999.999999	1.000000	300, 600, 900, 1200, 1500, 1800	25

TABLE 5: Effect of division of homotopy parameter.

Scenarios	Identified results (mm)		Division of λ	Measurement time (s)	No. of iteration
	x_c	h_c			
1	1000.000234	1.000000	3	1	26
2	1000.000003	1.000000	4	1	28
3	999.9999346	1.000000	5	1	30

TABLE 6: Effect of measurement noise.

Scenarios	Noise	Identified results (mm)/rel. (%)		Division of λ	No. of iteration
		x_c	h_c		
1	Nil	1000.000234/0.00	1.000000/0.00	3	26
2	1%	1021.498303/2.15	1.003232/0.32	3	22
3	5%	1070.401667/7.04	1.022658/2.27	3	23
4	15%	1089.318837/8.93	1.052358/5.24	3	19

Note: "Rel. (%)" denotes relative error.

TABLE 7: Identification of two cracks in a simply supported beam.

Scenarios	Noise	Identified results (mm)/rel. (%) in crack 1		Identified results (mm)/rel. (%) in crack 2		Division of λ	Measurement time (s)	No. of iteration
		x_{c1}	h_{c1}	x_{c2}	h_{c2}			
1	Nil	450.000000/0.00	5.000000/0.00	999.999997/0.00	1.000000/0.00	5	1	78
2	5%	441.804646/1.82	4.986154/0.28	1064.867252/6.49	1.072199/7.22	7	1	74

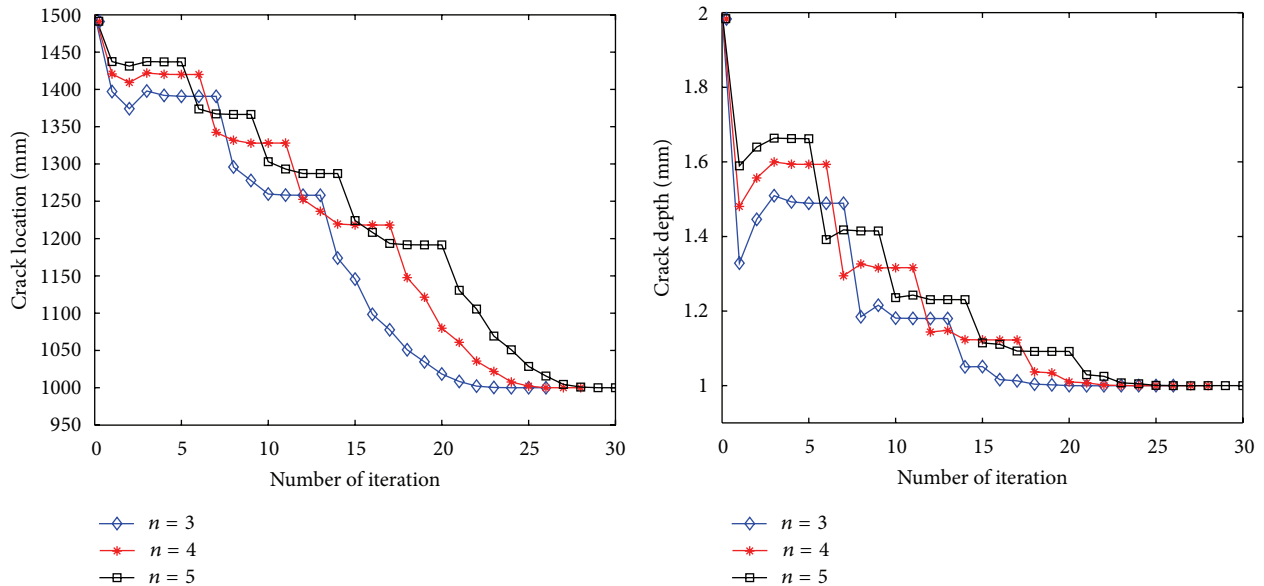


FIGURE 5: Effect of division of homotopy parameter.

TABLE 8: Crack identification in a cantilever beam.

	Initial	True	Identified results	
			2s	4s
Single crack				
Crack location x_c (mm)	750	250	250.000162	250.000259
Crack depth h_c (mm)	3	1	1.000001	1.000001
Division of λ	—	—	26	20
No. of iteration	—	—	92	96
Two cracks				
Crack locations x_{c1}/x_{c2} (mm)	360/700	250/600	249.603356/599.789017	250.009037/600.005717
Crack depths h_{c1}/h_{c2} (mm)	2/7.8	1/6.5	0.997240/6.498047	1.000067/6.500058
Division of λ	—	—	16	15
No. of iteration	—	—	137	137

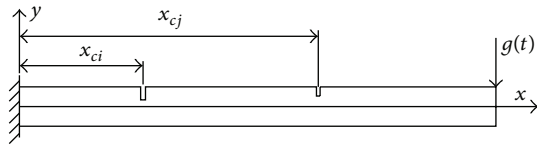


FIGURE 6: A cantilever beam with cracks.

crack, respectively. These results further illustrate the effectiveness of the proposed method.

4.2. A Cantilever Beam. A uniform cross section cantilever beam with cracks is studied as another example. As Figure 6 shows, the physical parameters of the beam are: elastic modulus of material $E = 69.79$ GPa, mass density $\rho = 2600$ kg/m³, length $L = 1000$ mm, width $w = 50$ mm and height $h = 25$ mm. when calculating the dynamic response, a sinusoidal force $g(t) = 40 \sin(15\pi t)N$ acts at the free end of the beam. Four measurement points located at 300 mm, 450 mm, 600 mm, and 750 mm from the clamped end are used to record the acceleration data. The two damping coefficients used for calculating Rayleigh damping matrix are both assumed to be 0.01. The time step is 0.005 s and the time duration is taken to be 2.0 s and 4.0 s, respectively. The number of the mode functions used from the CT is also set to be 10, and the way to choose the number of term is the same as the simply supported beam. Both single crack and two cracks are simulated in this case. Good identification results are listed in Table 8. For a single crack identification, the measurement of time duration may have little effect on the degree of accuracy as Section 4.1.2 shows. But for two cracks, it can improve the accuracy of the identified results in general as the unknown parameters increases in the identification. This case further illustrates the effectiveness of the proposed method.

5. Discussions

The homotopy iteration algorithm is to divide the range of homotopy parameter $\lambda \in [0, 1]$ into multiple subintervals; then the Newton algorithm is used to search the best convergence solution in each subinterval to obtain the updated crack parameters and another homotopy equation. Assuming that

the homotopy parameter is divided into N parts, we will have $N + 1$ homotopy equations as $\alpha = 0, 1/N, \dots, 1$. When the division of homotopy parameter is only one, the homotopy iteration algorithm decreases to a simple Newton algorithm. But the Newton algorithm is with local convergence and is easy to divergent. Thus, the division of homotopy parameter is an integer greater than or equal to 2. And with the range between the initial parameters and the true parameters increasing, the finer division of homotopy parameter should be considered to improve the convergence. But in some subdivision, the Newton algorithm to track the path may be divergent to the crack depth very close to zero or the height of the beam. Because in these two conditions, the homotopy equation and its first derivative are so small that it leads to misjudgment. Thus, the new division or initial parameters should be considered. But according to authors' calculation experience, when the subdivision increases to some value (greater than 30), the misjudgment will still occur as the above two conditions exist. That is why increasing the subdivision over some larger value does not modify the convergence properties of the algorithm.

6. Conclusions

In this paper, an open crack model with the CEM for Euler-Bernoulli beam system is adopted to establish the dynamics equation in the forward problem. In the inverse problem, an identification approach based on homotopy iteration algorithm is presented to identify the parameters of cracks. Numerical simulation shows that the proposed method is less affected by the initial values and is effective and accurate for crack identification when the measurement noise is free. With the increase of the measurement noise, the identification errors will become larger, but the identified results are still satisfactory. The study also shows that more measurement points can obtain more accuracy of the identification results in general but has the similar convergence process.

Conflict of Interests

The authors declare that there is no conflict of interests regarding the publication of this paper.

Acknowledgments

This work is supported in part by the NSFC (11172333 and 11272361), the Fundamental Research Funds for the Central Universities (13lgzd06), and the General Financial Grant from the China Postdoctoral Science Foundation (2013M531893). Such financial aids are gratefully acknowledged.

References

- [1] M. I. Friswell and J. E. Mottershead, *Finite Element Model Updating in Structural Dynamics*, Kluwer Academic, Dodrecht, The Netherlands, 1995.
- [2] A. G. Peano, "Hierarchies of conforming finite elements for plane elasticity and plate bending," *Computers and Mathematics with Applications*, vol. 2, no. 3-4, pp. 211-224, 1976.
- [3] P. Zeng, "Composite element method for vibration analysis of structure," *Journal of Sound and Vibration*, vol. 218, no. 4, pp. 619-696, 1998.
- [4] Z. R. Lu and S. S. Law, "Discussions on 'composite element method for vibration analysis of structure,'" *Journal of Sound and Vibration*, vol. 305, no. 1-2, pp. 357-361, 2007.
- [5] J. Cattarius and D. J. Inman, "Time domain analysis for damage detection in smart structures," *Mechanical Systems and Signal Processing*, vol. 11, no. 3, pp. 409-423, 1997.
- [6] Z. R. Lu and J. K. Liu, "Identification of both structural damages in bridge deck and vehicular parameters using measured dynamic responses," *Computers and Structures*, vol. 89, no. 13-14, pp. 1397-1405, 2011.
- [7] Z. R. Lu and S. S. Law, "Dynamic condition assessment of a cracked beam with the composite element model," *Mechanical Systems and Signal Processing*, vol. 23, no. 2, pp. 415-431, 2009.
- [8] X. B. Lu, J. K. Liu, and Z. R. Lu, "A two-step approach for crack identification in beam," *Journal of Sound and Vibration*, vol. 332, no. 2, pp. 282-293, 2013.
- [9] B. C. Eaves, F. J. Gould, H. O. Peitgen, and M. J. Todd, *Homotopy Methods and Global Convergence*, Plenum Press, New York, NY, USA, 1983.
- [10] J. H. He, "Homotopy perturbation method: a new nonlinear analytical technique," *Applied Mathematics and Computation*, vol. 135, no. 1, pp. 73-79, 2003.
- [11] S. J. Liao, "On the homotopy multiple-variable method and its applications in the interactions of nonlinear gravity waves," *Communications in Nonlinear Science and Numerical Simulation*, vol. 16, no. 3, pp. 1274-1303, 2011.
- [12] J. C. Alexander and J. A. Yorke, "The homotopy continuation method: numerically implementable topological procedures," *Transactions of the American Mathematical Society*, vol. 242, pp. 271-284, 1978.
- [13] J. K. Sinha, M. I. Friswell, and S. Edwards, "Simplified models for the location of cracks in beam structures using measured vibration data," *Journal of Sound and Vibration*, vol. 251, no. 1, pp. 13-38, 2002.
- [14] K. J. Bathe, *Finite Element Procedures in Engineering Analysis*, Prentice Hall, Upper Saddle River, NJ, USA, 1982.

Research Article

An Efficient Approach for Identifying Constitutive Parameters of the Modified Oyane Ductile Fracture Criterion at High Temperature

Sergei Alexandrov,¹ Yusof Mustafa,² and Mohd Yazid Yahya³

¹ A. Yu. Ishlinskii Institute for Problems in Mechanics, Russian Academy of Sciences, 101-1 Prospect Vernadskogo, Moscow 119526, Russia

² Faculty of Mechanical Engineering, Universiti Teknologi Malaysia, 81310 Skudai, Johor Darul Ta'zim, Malaysia

³ Centre for Composite, Universiti Teknologi Malaysia, 81310 Skudai, Johor Darul Ta'zim, Malaysia

Correspondence should be addressed to Sergei Alexandrov; sergei.alexandrov@spartak.ru

Received 13 September 2013; Revised 6 November 2013; Accepted 6 November 2013

Academic Editor: Timon Rabczuk

Copyright © 2013 Sergei Alexandrov et al. This is an open access article distributed under the Creative Commons Attribution License, which permits unrestricted use, distribution, and reproduction in any medium, provided the original work is properly cited.

The paper presents the theoretical part of a method for identifying constitutive parameters involved in the modified Oyane ductile fracture criterion at high temperature. Quite a general rigid viscoplastic model is adopted to describe material behavior. The ductile fracture criterion is in general path-dependent and involves stresses. Therefore, the identification of constitutive parameters of this criterion is a difficult task which usually includes experimental research and numerical simulation. The latter requires a precisely specified material model and boundary conditions. It is shown in the present paper that for a wide class of material models usually used to describe the behavior of materials at high temperatures, the criterion is significantly simplified when the site of fracture initiation is located on traction free surfaces. In particular, this reduced criterion does not involve stresses. Since there are well established experimental procedures to determine the input data for the reduced criterion, the result obtained can be considered as a theoretical basis for the efficient method for identifying constitutive parameters of the modified Oyane ductile fracture criterion at high temperature. The final expression can also be used in computational models to increase the accuracy of predictions.

1. Introduction

Empirical ductile fracture criteria are widely used by practically working engineers to predict the initiation of ductile fracture in metal forming processes. Reviews of such criteria for cold metal forming processes are provided in [1–3]. Most of these criteria include a path-dependent integral whose integrand contains invariants of the stress tensor. Therefore, the identification of constitutive parameters of ductile fracture criteria in general requires numerical simulation of forming processes which is impossible without a precisely specified material model and boundary conditions. These input data affect the result of numerical simulation. An alternative method of identifying constitutive parameters of two widely used cold ductile fracture criteria has been proposed in [4, 5]. This method is applicable when the fracture initiation occurs at traction free surfaces and the final

expressions are finite relations between two in-surface strains or the equivalent strain and two in-surface strains. In the case of hot forming, many experimental results indicate a sharp drop of the strain to fracture at a certain level of temperature and strain rate [6–8]. In the range of temperatures and strain rates where this drop does not occur, hot ductile fracture criteria are often accepted as modifications of cold ductile fracture criteria in which constitutive parameters depend on temperature and strain rate [6, 9–13]. In particular, the criterion proposed in [14] for cold metal forming has been modified in [10, 13] to account for temperature and strain rate effects. Experimental verification of the applicability of this modified ductile fracture criterion to several materials has been provided in these papers as well. An efficient method for identifying constitutive parameters involved in the original criterion [14] has been proposed in [4]. However, this method is based on a rigid hardening material model

which is not adequate for describing hot metal forming. In the present paper, the method [4] is extended to quite a general viscoplastic model.

2. Constitutive Equations

Rigid viscoplastic solids are often used to describe the behavior of material in hot metal forming processes (see, e.g., [15]). The constitutive equations of such solids are the yield condition and its associated flow rule. A widely adopted yield condition is

$$\sigma_{\text{eq}} = \sigma_0 \Phi(\xi_{\text{eq}}, \varepsilon_{\text{eq}}), \quad (1)$$

where σ_0 is a reference stress, σ_{eq} is the equivalent stress, ξ_{eq} is the equivalent strain rate, and ε_{eq} is the equivalent strain. The quantities σ_{eq} , ξ_{eq} , and ε_{eq} are defined by

$$\sigma_{\text{eq}} = \sqrt{\frac{3}{2}} \sqrt{\tau_{ij} \tau_{ij}}, \quad \xi_{\text{eq}} = \sqrt{\frac{2}{3}} \sqrt{\dot{\xi}_{ij} \dot{\xi}_{ij}}, \quad \frac{d\varepsilon_{\text{eq}}}{dt} = \xi_{\text{eq}}, \quad (2)$$

where σ_{ij} are the components of the stress tensor, $\dot{\xi}_{ij}$ are the components of the strain rate tensor, t is the time, $\tau_{ij} = \sigma_{ij} - \sigma \delta_{ij}$ are the components of the stress deviator tensor, $\sigma = (\sigma_{ij} \delta_{ij})/3$ is the hydrostatic stress, and δ_{ij} is Kronecker's symbol. With no loss of generality it is possible to assume that $\Phi(0, 0) = 1$. Then, σ_0 is the yield stress in uniaxial tension at $\xi_{\text{eq}} = 0$ and $\varepsilon_{\text{eq}} = 0$. The flow rule associated with the yield condition (1) results in

$$\dot{\xi}_{ij} = \lambda \tau_{ij}, \quad (3)$$

where λ is a nonnegative multiplier. Using (1) this multiplier can be eliminated in (3) to give

$$\dot{\xi}_{ij} = \frac{3}{2} \frac{\xi_{\text{eq}} \tau_{ij}}{\sigma_0 \Phi(\xi_{\text{eq}}, \varepsilon_{\text{eq}})}. \quad (4)$$

The ductile fracture criterion applicable at high temperatures and strain rates is [13]

$$\int_0^{t_f} \left(1 + \frac{\sigma}{B \sigma_{\text{eq}}} \right) \xi_{\text{eq}} dt = C(\xi_{\text{eq}}, T), \quad (5)$$

where t is the time, t_f is the value of t at the instant of fracture initiation, and B is a material constant. C depends on the equivalent strain rate and temperature, T . The ductile fracture criterion (5) is a modification of the criterion proposed in [14] for cold metal forming processes. It is worthwhile of noting that the model chosen demands that the principal axes of the stress and strain rate tensors coincide.

3. Free Surface Fracture

Assume that fracture initiates at a point of a traction free surface. It is evident that one of the principal stress directions is orthogonal to this surface. Therefore, one of the principal strain rate directions is also orthogonal to this surface and

an infinitesimal material fiber coinciding with this principal direction at the initial instant is fixed in the material. Let ξ_1 be the principal strain rate associated with this direction. In this special case

$$\varepsilon_1 = \int_0^t \xi_1 dt, \quad (6)$$

where ε_1 is the principal logarithmic strain. Equation (6) is valid at any large strain. The principal stress orthogonal to the free surface vanishes; $\sigma_1 = 0$. It follows from this equation that

$$\sigma = -\tau_1 \quad (7)$$

at the free surface. Substituting (7) into (5) and using (1) give

$$\int_0^{t_f} \left[1 - \frac{\tau_1}{B \sigma_0 \Phi(\xi_{\text{eq}}, \varepsilon_{\text{eq}})} \right] \xi_{\text{eq}} dt = C(\xi_{\text{eq}}, T). \quad (8)$$

It follows from (4) that

$$\frac{2}{3} \xi_1 = \frac{\xi_{\text{eq}} \tau_1}{\sigma_0 \Phi(\xi_{\text{eq}}, \varepsilon_{\text{eq}})}. \quad (9)$$

Replacing the integrands in (8) by means of (9) leads to

$$\int_0^{t_f} \left[\xi_{\text{eq}} - \frac{2}{3} \frac{\xi_1}{B} \right] dt = C(\xi_{\text{eq}}, T). \quad (10)$$

Using (2) and (6) integration in this equation can be carried out analytically to give

$$\varepsilon_{\text{eq}}^f - \frac{2}{3} \frac{\varepsilon_1^f}{B} = C(\xi_{\text{eq}}, T), \quad (11)$$

where $\varepsilon_{\text{eq}}^f$ and ε_1^f are the values of ε_{eq} and ε_1 , respectively, at the instant of fracture initiation. Let ε_2 and ε_3 be the in-surface principal logarithmic strains and let ε_2^f and ε_3^f be their values at the instant of fracture initiation, respectively. It follows from the incompressibility equation that $\varepsilon_3^f + \varepsilon_2^f + \varepsilon_1^f = 0$. Using this equation, ε_1^f can be eliminated in (11) to give

$$\varepsilon_{\text{eq}}^f + \frac{2}{3} \frac{(\varepsilon_2^f + \varepsilon_3^f)}{B} = C(\xi_{\text{eq}}, T). \quad (12)$$

This relation is the fracture criterion at the free surface. Its remarkable property is that the left hand side of (12) is independent of stress components. The in-surface finite strains at the instant of fracture initiation can be found using high speed photography [12]. The equivalent strain is in general path-dependent. Therefore, the strain path should be determined to calculate $\varepsilon_{\text{eq}}^f$. However, since the material is supposed to be incompressible, it is sufficient to find the dependence of ε_2 on ε_3 [16]. This dependence can be found using high speed photography.

4. Conclusions

The main result of the present paper is that the ductile fracture criterion (5) involving stresses reduces to (12) when the initiation of fracture occurs at a point of a traction free surface. Equation (12) is simply a relation between the equivalent strain and two in-surface strains. Therefore, there is no need to find experimentally and numerically the state of stress at the site of fracture initiation. On the contrary, (12) can be used in numerical codes. This should increase the accuracy of predictions because there is no need to calculate the state of stress at the site of fracture initiation. As an example, it is instructive to apply (12) to theoretical/experimental results obtained in [17]. In this work the finite element method and compression of cylindrical specimens of Ti40 alloy were used to identify the constitutive parameters of the fracture criterion (5) at $B = 2/3$. As a result, it has been found (in our nomenclature) that

$$\int_0^{t_f} \left(1 + \frac{3\sigma}{2\sigma_{eq}} \right) \xi_{eq} dt = 2.227 - 0.0493 \ln Z. \quad (13)$$

Here Z is the Zener-Hollomon parameter which is a temperature compensated strain rate. Using (12), it is possible to control the accuracy of (13) by means of simpler methods than those applied in [17]. In particular, (13) takes the following form:

$$\varepsilon_{eq}^f + \varepsilon_2^f + \varepsilon_3^f = 2.227 - 0.0493 \ln Z. \quad (14)$$

According to experimental results presented in [17] the equivalent strain to fracture is a linear function of $\ln Z$. These data are in agreement with (14) if and only if strain paths in the experiment are linear or, at least, close enough to linear. Of course, this condition should be verified by experiment. However, it is worthwhile of noting that strain paths in cold upsetting are usually convex down [18–20].

Equation (12) has been derived for quite a general viscoplastic model. Therefore, there is no need to specify the model to apply this equation in conjunction with experimental data. Finally, boundary conditions have no effect on this equation. Obviously, some boundary conditions such as a friction boundary condition have a great effect on the initiation of ductile fracture. However, all these possible effects are automatically taken into account in the measured values of the in-surface principal strains. To summarize, it is believed that the aforementioned mathematical properties of the ductile fracture criterion considered provide a theoretical basis for an efficient theoretical/experimental method for the identification of constitutive parameters of the ductile fracture criterion [13] at high temperature.

The general method of analysis used in the present paper has been also adopted in [21] to reduce the modified Cockcroft-Latham ductile fracture criterion to a simple form not involving stresses. However, the basic assumptions and final results are quite different. In particular, in the case of the modified Cockcroft-Latham ductile fracture criterion the general method is applicable if and only if the site of fracture initiation coincides with the point of intersection of two

planes of symmetry and a traction free surface. On the other hand, (12) is valid at any point of a traction free surface. This difference may affect the choice of specimens for experiment. Moreover, (12) involves the equivalent strain which is a path-dependent integral whereas the final expression in [18] is a relation between two finite in-surface strains at the instant of fracture initiation. This difference may affect the choice of experimental techniques to measure kinematic variables.

The main assumption to derive (12) from the fracture criterion (5) is that the site of fracture initiation is located at a traction free surface. This condition is satisfied in many sheet forming processes. Therefore, the simplified ductile fracture criterion in the form of (12) can be directly adopted to predict the initiation of ductile fracture in such processes.

Acknowledgments

The research described in this paper has been supported by the Grants RFBR-13-08-00969 and NSH-3842.2012.1.

References

- [1] A. G. Atkins, "Fracture in forming," *Journal of Materials Processing Technology*, vol. 56, no. 1–4, pp. 609–618, 1996.
- [2] M. A. Shabara, A. A. El-Domiaty, and A. Kandil, "Validity assessment of ductile fracture criteria in cold forming," *Journal of Materials Engineering and Performance*, vol. 5, no. 4, pp. 478–488, 1996.
- [3] R. Hambli and M. Reszka, "Fracture criteria identification using an inverse technique method and blanking experiment," *International Journal of Mechanical Sciences*, vol. 44, no. 7, pp. 1349–1361, 2002.
- [4] D. Vilotić, M. Planč, S. Grbić, S. Alexandrov, and N. Chikanova, "An approach to determining the workability diagram based on upsetting tests," *Fatigue and Fracture of Engineering Materials and Structures*, vol. 26, no. 4, pp. 305–310, 2003.
- [5] S. Alexandrov and D. Vilotić, "A theoretical-experimental method for the identification of the modified Cockcroft-Latham ductile fracture criterion," *Proceedings of the Institution of Mechanical Engineers C*, vol. 222, no. 9, pp. 1869–1872, 2008.
- [6] S. Alexandrov, P. T. Wang, and R. E. Roadman, "A fracture criterion of aluminum alloys in hot metal forming," *Journal of Materials Processing Technology*, vol. 160, no. 2, pp. 257–265, 2005.
- [7] O. Sabokpa, A. Zarei-Hanzaki, and H. R. Abedi, "An investigation into the hot ductility behavior of AZ81 magnesium alloy," *Materials Science and Engineering A*, vol. 550, pp. 31–38, 2012.
- [8] J. Deng, Y. C. Lin, S. S. Li, J. Chen, and Y. Ding, "Hot tensile deformation and fracture behaviors of AZ31 magnesium alloy," *Materials and Design*, vol. 49, pp. 209–219, 2013.
- [9] N. Ogawa, M. Shiomi, and K. Osakada, "Forming limit of magnesium alloy at elevated temperatures for precision forging," *International Journal of Machine Tools and Manufacture*, vol. 42, no. 5, pp. 607–614, 2002.
- [10] X. Zhang, W. Zeng, Y. Shu, Y. Zhao, H. Yu, and Y. Zhou, "Fracture criterion of Ti40 alloy based on the Zener-Hollomon parameter at hot forming," *Rare Metal Materials and Engineering*, vol. 37, no. 4, pp. 604–608, 2008.
- [11] J. T. Yeom, J. H. Kim, J. H. Kim, J. K. Hong, and J. S. Lee, "Hot forging design of cam for vessel engine using finite element

- analysis and ductile fracture criteria,” *Steel Research International*, vol. 81, pp. 298–301, 2010.
- [12] Y. Zhu, W. Zeng, F. Zhang, Y. Zhao, X. Zhang, and K. Wang, “A new methodology for prediction of fracture initiation in hot compression of Ti40 titanium alloy,” *Materials Science and Engineering A*, vol. 553, pp. 112–118, 2012.
- [13] J. He, Z. Cui, F. Chen, Y. Xiao, and L. Ruan, “The new ductile fracture criterion for 30Cr2Ni4MoV ultra-super-critical rotor steel at elevated temperatures,” *Materials and Design*, vol. 52, pp. 547–555, 2013.
- [14] M. Oyane, T. Sato, K. Okimoto, and S. Shima, “Criteria for ductile fracture and their applications,” *Journal of Mechanical Working Technology*, vol. 4, no. 1, pp. 65–81, 1980.
- [15] Y.-M. Guo, Y. Yokouchi, and H. Suzuki, “Analysis of hot forward-backward extrusion by the visco-plastic finite-element method,” *Journal of Materials Processing Technology*, vol. 38, no. 1-2, pp. 103–113, 1993.
- [16] S. Alexandrov, D. Vilotic, Z. Konjovic, and M. Vilotic, “An improved experimental method for determining the workability diagram,” *Experimental Mechanics*, vol. 53, pp. 699–711, 2013.
- [17] X.-M. Zhang, W.-D. Zeng, Y. Shu et al., “Fracture criterion for predicting surface cracking of Ti40 alloy in hot forming processes,” *Transactions of Nonferrous Metals Society of China*, vol. 19, no. 2, pp. 267–271, 2009.
- [18] H. A. Kuhn, P. W. Lee, and T. Erturk, “Fracture criterion for cold forming,” *Journal of Engineering Materials and Technology of the ASME*, vol. 95, pp. 213–218, 1973.
- [19] S. I. Oh and S. Kobayashi, “Workability of aluminum alloy 7075-t6 in upsetting and rolling,” *Journal of Engineering for Industry-Transactions of the ASME*, vol. 98, no. 3, pp. 800–806, 1976.
- [20] J. J. Shah and H. A. Kuhn, “An empirical formula for workability limits in cold upsetting and bolt heading,” *Journal of Applied Metalworking*, vol. 4, no. 3, pp. 255–261, 1986.
- [21] S. Alexandrov and Y. R. Jeng, “An efficient method for the identification of the modified Cockcroft-Latham fracture criterion at elevated temperature,” *Archive of Applied Mechanics*, vol. 83, no. 12, pp. 1801–1804, 2013.

Research Article

Study on Analog Theory of Rock Mass Simulation and Its Engineering Application

Sun Shaorui, Lu Yexu, Xu Yuanyuan, Liu Jin, and Wei Jihong

College of Earth Science and Engineering, Hohai University, Nanjing 210098, China

Correspondence should be addressed to Sun Shaorui; ssrfish@hhu.edu.cn

Received 3 May 2013; Revised 24 August 2013; Accepted 10 October 2013

Academic Editor: Stephane P. A. Bordas

Copyright © 2013 Sun Shaorui et al. This is an open access article distributed under the Creative Commons Attribution License, which permits unrestricted use, distribution, and reproduction in any medium, provided the original work is properly cited.

During construction of 3D geological models, it is difficult to determine the uniform between geological model and true model. As a comprehensive index, rock quality designation (RQD) is reliable to assess the rationality of geological models. Unfortunately, The RQD of rockmass is determined completely by the deterministic threshold value and directions of the scan lines presently. To avoid this drawback, the modified method of the RQD value based on the threshold value and 3D space is proposed in this paper. Simultaneously, the analogue-simulation method based on rupture mechanism and classification of discontinuities is proposed. The elliptical discontinuity is considered for general discontinuity, and the special discontinuities, such as bedding, fault, and interlayer are dealt with individually. The accuracy of the 3D model is verified by the modified RQD. The 3D model of the rockmass is analogue simulated through repetitively obtaining data from the interval confidence of geometrical parameters of discontinuities, which are determined by a mass of data derived from field investigation. Besides, the dam base of the Xiangjiaba hydropower station is taken as an example, and the 3D model of the dam base is analog-simulated; its stability is evaluated by DDA method. The safety coefficient of the dam base is obtained by utilizing the overload method.

1. Introduction

At present, 3D geological simulation methods have been developed from model construction to practical computation [1, 2]. 3D geological models have been easily accepted as efficient methods to understand the engineering characteristics of rock masses, as these models are constructed with discontinuities and structural bodies as 3D networks. The discrete-element method (DEM), which was firstly developed by Cundall, has been widely used to construct 3D geological models in rock engineering applications. Jing [3] has introduced additional aspects of the DEM in different related engineering problems. Andersson and Dverstorp [4], Elsworth [5], Long et al. [6], and Smith and Schwartz [7] have also widely used the discrete fracture network (DFN) to research the behavior of rock masses. Although these software programs have been successfully used to simulate the behavior of rock fractured systems, the aforementioned research methods and their application to engineering problems are still limited to simplify the representations of the critical discontinuities of rock masses. In addition, the uniformity between constructed

and true models lacks the validation methods, which will cause the constructed model to be unreliable. For some particular types of discontinuities, such as fault, fracture zone, and interlayer, there is no way to realize in these methods. Therefore, 3D geological simulation method in this study can overcome these drawbacks through analogue simulation technique considering particular discontinuities.

Rock quality designation (RQD) has been widely used to classify the discontinuity of rock masses and assess the intactness of rock masses. In previous studies, the applications of RQD have been mainly based on a deterministic threshold value and a single scanline direction. Priest and Hudson [8] have studied RQD and proposed a relationship between the fracture frequency and RQD. Harrison [9] has presented equations derived by analyzing fracture frequencies with different distributions, which may expand the range of RQD values. Sen and Kazi [10] and Şen [11] have studied RQD along a scanline with any specific orientation and established a relationship between the RQD value and fracture frequency along the chosen orientation. Zhang and Einstein [12], Jiang et al. [13], and Milne et al. [14] have studied the relationships

between RQD and rock mass parameters, such as fracture frequency, deformation modulus, volumetric joint count, and permeability coefficient. Snow [15] has pointed out that RQD and fracture frequency decrease with depth increasing. However, after many years of research, RQD has gradually come to favor the methods of quantitative and multiple indexes, and it has become more and more widely known that rock structure has a great influence on rock quality. Because of anisotropy and nonhomogeneity of rock mass, the previous evaluation methods of the RQD have some drawbacks, such as deterministic threshold value and scanline. The new method in this paper considers the different threshold values and measure methods from the angle of full space. The general RQD proposed in this paper evaluates rock mass quality based on many RQD balls with the different measure threshold values. Therefore, the general RQD is adopted to overcome the drawbacks of traditional evaluation method of the RQD.

The discontinuous deformation analysis (DDA) method has been widely used to assess the stability of rock mass engineering. The method has been developed for 2D problems by Shi and Goodman [16] and expanded to 3D by Shi [17] and Jiang and Yeung [18]. Some researchers, such as Yeung et al. [19], Hatzor and Feintuch [20], MacLaughlin and Berger [21], Doolin and Sitar [22], and Tsesarsky et al. [23], have confirmed the verification and validation of DDA by comparing the predictions from the method with analytical solutions, as well as with other numerical methods and laboratory and field measurements. In addition, DDA can also be viewed as a mature and reliable method to apply in the stability analysis of rock engineering; for example, Hatzor et al. [24] and Sitar et al. [25] have used DDA to investigate slope stability, and Kim et al. [26], Wu et al. [27], and Tsesarsky and Hatzor [28] have used it to analyze tunneling stability in discontinuous rock masses. In the past study on DDA method, the orientation of discontinuity is constant when DDA method is used to conduct numerical simulation. It is unreasonable for the true geometrical characteristics of natural discontinuity. Meanwhile, variable orientation of discontinuity can produce many polyhedrons with different shape compared with that of constant orientation. Additionally, another problem for the DDA method is that the particular discontinuities cannot be considered. Therefore, in order to avoid two drawbacks, both the particular types of discontinuities by improving preprocess program and the variable orientation of natural discontinuity are considered for the simulation method in this study.

At present, a wide variety of rock quality assessment methods have taken rock structure into account; however, it is necessary to determine how to adapt the rock structure model into the adaptive mechanical model for providing the basic data for model experiments and rock masses intactness assessment. The 3D structure model of rock masses is typically acquired by using discontinuities and spacing, block size, and other rock intactness indexes. There are three issues involved in the acquaintance of rock structure: (i) how to gain the reasonable values for the geometrical characteristics of the discontinuities. It remains open to discuss how to describe the whole rock masses through the representative data from

field measurements, when simulating the space geometry of discontinuities, and the effects of the geometrical characteristics of the rock are partially caused by tectonic movement and so forth. The second issue is (ii) how to reasonably understand the rock masses formed by discontinuities. Rock masses are the combination of discontinuities and structural body. Under the condition that the geometrical characteristics of the rock masses have been confirmed, it is worth considering how to simulate the rock masses using these characteristics and how to compare the simulated rock masses with the virtual ones. Furthermore, there are several different beliefs concerning how to define the index reflecting the intactness of rock masses. (iii) How to build the connection between the numerical computational and the geological models constructed using the 3D network simulation method is the third one. Currently, most numerical computational methods which take rock as a continuous medium are not effective in distinguishing the characteristics of rock masses. Even if the discontinuous analysis method is adopted in some cases, the general means will not compensate for the deficiencies in the numerical calculation of engineering; thus it is necessary to establish the relationships between the 3D geological models and discontinuous deformation analysis methods.

2. Basic Principles and Methodologies

2.1. Simulation Method of Discontinuities. Despite the fact that the technique of discontinuous network simulation (DNS) has been greatly improved in recent years, this method is not particularly accurate, due to its hypothesis. It assumes that the spatial shape of the discontinuities is circular, while this is not necessarily true. In addition, the technique of the DNS ignores the effects of the large-scale discontinuities, taking only the grade IV and V discontinuities into account. It is easy to understand that the application and decision of the 3D simulation technique are restricted, and, as matter of a fact, the grade IV and V discontinuities are the ones which play controlling roles in the local stabilization of rock masses. In this paper, the large-scale discontinuities are firstly considered during the construction of the 3D geological model. The production of the grade IV and V discontinuities is based on the 3D model, including the large scale discontinuities such as fault and weak interlayers. Through a large amount of the field observations and research regarding the shape of the discontinuities, it is believed that the discontinuities should not be categorized into a single circular shape, due to the fact that the production of the discontinuities is affected mainly by the tectonic movement. As known, the stress ellipsoid is applied to structure geology for explaining rock failure and deformation of rock masses based on the definition of mathematics and the physical meaning. Therefore, the shape of discontinuities directly affected by tectonic stress should not be circular in shape, but elliptical, generally due to the inequality of the values of the maximum and minimum principal stresses. Based on this view, the elliptical shape would be adopted to corresponding discontinuities affected by tectonic stress, and the steps of the DNS are as follows: (i) take samples of the discontinuities through field measurements;

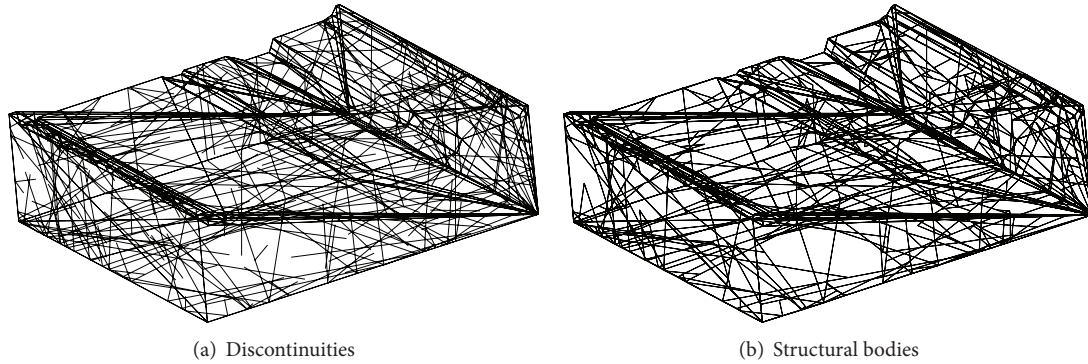


FIGURE 1: Map of the DNS for the Xiangjiaba hydropower station dam base.

(ii) create probabilistic models of geometrical parameters of the discontinuities such as orientation, spacing, and trace length; (iii) make use of the Monte-Carlo random simulation technique to obtain random data from the confidence interval of geometrical parameters of discontinuities; (iv) construct the large-scale discontinuities in the 3D model, such as the fault, bedding, and interlayer; (v) construct the grade IV and V discontinuities in the 3D model; and (vi) create a complete network map of the DNS and form its boundaries. The boundaries formed by the discontinuities are shown in Figure 1(a), while Figure 1(b) shows the boundaries of the dam base formed by the structural bodies.

2.2. Verification of the DNS

2.2.1. RQD and Its Deficiencies. Rock masses are discontinuous, inhomogeneous, and anisotropic in terms of their discontinuous geometry; thus it is a difficult task to simulate the whole characteristics of rock masses. At present, ROD, a method used to evaluate the intactness and quality of rock masses, is the main means of simulating the discontinued properties of rock. The intactness coefficient of rock masses deals with the anisotropic property from the whole rock mass. However, RQD makes an objective appraisal of the intactness of the rock mass using the scanlines, such as borehole, tunnel, and field outcrop. The advantages and disadvantages of the method are described as follows.

- (i) It is not proper to use the RQD method to merely evaluate the quality of rock mass through a borehole which narrowly shows the condition of rock masses, because the rock mass has the property of anisotropy. In addition, the RQD method proposed by DEER in 1964 gave the deterministic value of 10 cm, which is defective at measuring the intactness of rock masses, and increases the amount of calculation if it is used to evaluate the stability of the rock mass, due to the production of a mass of structural elements separated by discontinuities. For example, the actual direction of a scanline in the project is often vertical in the borehole and horizontal in the tunnel, and the RQD value of single direction scanline cannot reflect the intact degree of the rock masses quality if considering the anisotropy of the rock masses. In addition, a

threshold value of 10 cm is nevertheless an arbitrarily selected value. Therefore, if the variable threshold can have a dramatic effect on the computed RQD, it is appropriate that the assessment of the RQD can be further investigated in order to determine a method for selecting the threshold value, rather than always relying on the customary value. In order to avoid these dimensional effects, another threshold value should be adopted according to the specific engineering project.

- (ii) The rock masses are constituted by blocks of different sizes and shapes, which are formed by the separation of the discontinuities. When analyzing the stability of the rock masses in the project using the DDA method, every structural element will be formed by a closed loop constituted by several traces, and the traces which do not constitute a closed loop will be deleted or trimmed. Therefore, the RQD values are not reasonable due to the different quantity traces in the measure scanlines intersecting with the redundant traces, and thus both should be taken into account during the analysis of RQD. The dam base model formed by structural elements should be reliable from the perspectives of theory and field investigation.

2.2.2. Modified Approach of RQD Evaluation. Two main approaches for RQD evaluation are proposed as follows. (1) Improve the gauge of threshold value. In order to conveniently calculate using the DDA method and satisfy the reasonable threshold value of the rock mass intactness, ten gauges of threshold values, spaced every 1.0 m, from 1.0 m to 10.0 m, are used to evaluate the intactness of the rock masses, thus creating a combination of the intactness and measurement indexes. (2) Change the single direction to 3D space. Based on the perspective of rock mass anisotropy, an all-sided gauge of the threshold value is adopted to measure the RQD in 3D space rather than in the vertical or horizontal direction.

Four RQD balls formed in four different threshold values are shown in Figure 2. As seen, the shape of the RQD ball is circular when the threshold value is smaller, and the characteristic of the rock mass approaches isotropy; on the contrary, the larger the threshold value is, the more

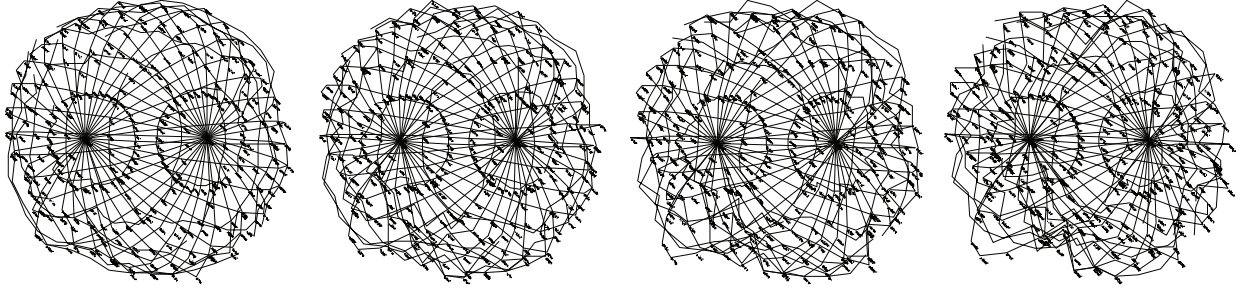


FIGURE 2: 3D RQD of the Xiangjiaba hydropower station dam base rock masses.

disproportionate the shape is, and the rock mass anisotropy may be clearly seen. These results show that the RQD ball is indeed capable of representing the characteristics of rock mass structures.

2.2.3. RQD Verification Methods. In order to verify the reasonability of 3D geological model of DNS, the actual measured RQD is compared with the simulated one. The steps of the measurement method are as follows.

- (i) Calibration of the borehole: according to the simulated rock masses, the RQD of the rock masses in the actual position of the drill hole is evaluated, and the results with those of the actual measurements are compared. The error between the actual measured values and the simulated values of the geometrical parameters must not be avoided. RQD is used to calibrate the simulated model by adjusting the geometrical parameters of the discontinuities, because RQD is a comprehensive index, which contains the geometrical characteristics of discontinuities, such as orientation, spacing, and trace length, to reflect the intactness of rock masses. Therefore, it is necessary to verify the RQD by adjusting the geometrical characteristic of the discontinuities until the results satisfy the demands.
- (ii) Calibration of the block characteristic of the rock masses: contrast the size and magnitude of the block formed from the 3D model with those of the actual field investigation. The span of the block may be satisfied by adjusting the geometrical parameters of the discontinuities.

It is believed to be very difficult to simultaneously satisfy the two aforementioned aspects. In general, the first one aspect is fulfilled, and then the other assessment aspect is calibrated accordingly.

2.3. Basic Theory of Discontinuous Deformation Analysis (DDA). Recently, the basic theory of DDA begins to reach maturity in correlative research and has made significant development in engineering application. The key contents of DDA are discussed below. Blocks in DDA are connective and form a block system by the contact constraint between two



FIGURE 3: Location of dam base zone.

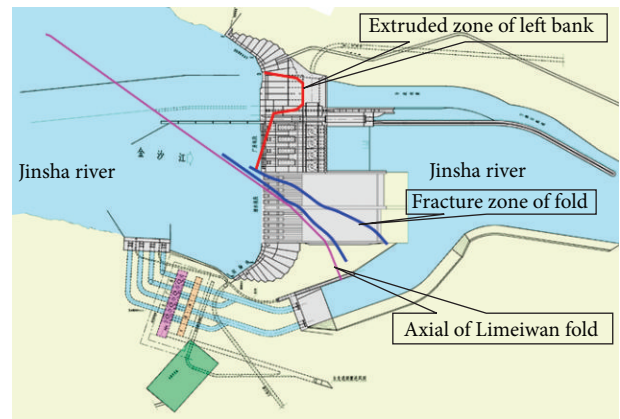


FIGURE 4: Layout of dam base zone.

blocks. Within representing the number of blocks in the block system, the following equations are listed together in

$$\begin{pmatrix} K_{11} & K_{12} & K_{13} & \cdots & K_{1n} \\ K_{21} & K_{22} & K_{23} & \cdots & K_{2n} \\ K_{31} & K_{32} & K_{33} & \cdots & K_{3n} \\ \vdots & \vdots & \vdots & \ddots & \vdots \\ K_{n1} & K_{n2} & K_{n3} & \cdots & K_{nn} \end{pmatrix} \begin{pmatrix} D_1 \\ D_2 \\ D_3 \\ \vdots \\ D_n \end{pmatrix} = \begin{pmatrix} F_1 \\ F_2 \\ F_3 \\ \vdots \\ F_n \end{pmatrix}. \quad (1)$$

Every block possesses six degrees of freedom. Each element $[K_{ij}]$ given in the coefficient matrix in (1) is a 6×6

TABLE 1: Statistical results of geometrical parameters of discontinuities.

No.	Orientation		Statistical indexes	Model	Mean	Standard variation	Samples
	Dip/°	Dip angle/°					
(1)	45.54~115.54	8.46~58.46	Spacing/m	Log-normal	0.60	0.79	360
			Dip/°	Normal	85.24	13.32	374
			Dip angle/°	Uniform	36.77	11.44	374
			Trace length/m	Log-normal	23.80	19.76	374
			Spacing/m	Log-normal	11.10	32.64	23
(2)	170.0~190.0	64.61~89.61	Dip/°	Normal	181.46	6.33	28
			Dip angle/°	Normal	81.21	7.17	28
			Trace length/m	Uniform	2.01	0.34	28
			Spacing/m	Log-normal	5.29	24.44	49
			Dip/°	Uniform	345.84	8.84	58
(3)	326.57~360.00	41.47~76.47	Dip angle/°	Uniform	60.22	8.56	58
			Trace length/m	Log-normal	2.07	1.49	58
			Spacing/m	Log-normal	3.50	12.64	54
			Dip/°	Uniform	292.48	16.96	63
			Dip angle/°	Uniform	43.47	6.07	63
(4)	262.01~327.01	24.81~69.81	Trace length/m	Log-normal	0.95	0.54	63
			Spacing/m	Log-normal	2.20	7.66	22
			Dip/°	Normal	60.44	7.95	27
			Dip angle/°	Log-normal	69.33	9.83	27
			Trace length/m	Log-normal	3.64	2.12	27

TABLE 2: Physical-mechanical parameters of rock masses in the dam base.

Materials	Density/kN/m ³	Modulus/GPa	Poisson's ratio	f'	c'/MPa
Concrete	24.0	17.60	0.167		
Bed rock (II)	26.0	15.00	0.220	1.20	1.40
Bed rock (III ₁)	26.0	7.00	0.250	0.99	1.00
Bed rock (III ₂)	26.0	5.50	0.280	0.86	0.80
Bed rock (III ₂ ~IV)	26.0	4.00	0.290	0.77	0.65
Soft layers P_n	20.0	0.75	0.400	0.35	0.10

TABLE 3: Intactness assessment of rock masses of Xiangjiaba hydropower station dam base.

Rock quality grade	Degree of weathering	Intactness of rock masses			Location of distribution
		Velocity of acoustic wave/m/s	RQD in the tunnel/%	RQD in the borehole/%	
I	Unweathered	>5000	>90	>85	Depth of dam base
II	Unweathered to weak weathering	4000–5000	75–90	60–85	Zones 1, 2, 4
	Moderate weathering (lower) to weak weathering	3500–4000	62.5–75	45–60	Zones 1, 4, 5, 6
III	Moderate weathering (upper)	3000–3500	50–62.5	30–45	Zone 6
	Weak weathering to unweathered				Zone 3
IV	Weak weathering to unweathered	2000–3000	25–50	5–30	Zones 3, 5 Influence band of fault and concentrated joint band
V		<2000			Shattered fault zone and weak interlayer

Notes: The zone of the dam base is divided by six sub-zones, which are arranged in order from the right bank to left bank of the Jinsha River.

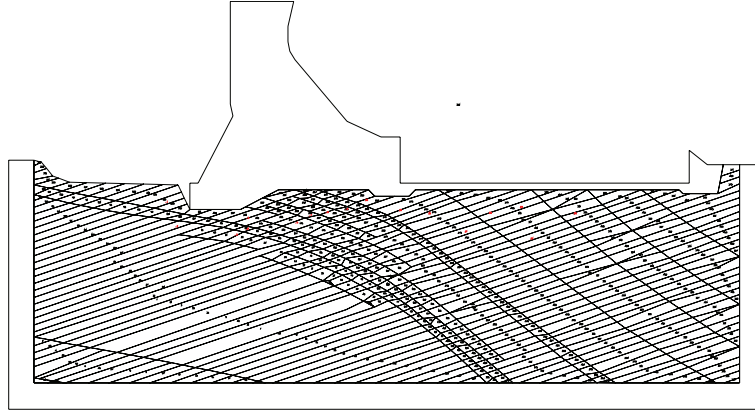


FIGURE 5: Computation model of dam base of Xiangjiaba hydropower station.

submatrix; $[D_i]$ and $[F_i]$ are 6×1 submatrices; D_i represents the deformation variable of block i ; and F_i is the load which is placed on the six deformation variables of block i . The six variables of each block are listed in

$$(u_0, v_0, r_0, \varepsilon_x, \varepsilon_y, \gamma_{xy}), \quad (2)$$

where (u_0, v_0) is the rigid body displacement of the special point (x_0, y_0) in the block; angle r_0 , shown with the radian, is an angle of rotation around the center point (u_0, v_0) in the block; $\varepsilon_x, \varepsilon_y$ are the normal strain; and γ_{xy} is the shear strain.

DDA is based on the principle of the minimum potential energy; the total potential energy Π is the sum of all of the potential energy. Use the equation below to calculate each stress and force potential energy, as well as their respective differentials. The equation of the matrix $[K_{ij}]$ is shown in

$$\frac{\partial^2 \Pi}{\partial d_{ri} \partial d_{si}} = 0, \quad r, s = 1, \dots, 6. \quad (3)$$

All the terms in (3) form a 6×6 submatrix, which is the submatrix $[K_{ij}]$ in (1). It may be clearly seen that (3) and the coefficient matrix are symmetrical. The equation of the matrix $[F_i]$ is shown in

$$-\frac{\partial \Pi(0)}{\partial d_{ri}} = 0, \quad r = 1, \dots, 6. \quad (4)$$

All the terms of (4) form a 6×6 submatrix, which will be added into the submatrix $[F_i]$.

Many components of the total stiffness matrix are provided by the single block and block systems, including the elastic, initial stress, point load, volume force, inertia force, initial displacement, bolt connection, normal contact force, tangent contact force, and friction force submatrices. The role played by each part of the total stiffness matrix in every situation may be clarified, provided that the appropriate potential energy expression is performed for each situation, and (3) or (4) is used. The simulation process is realized by a modified source code, which is considered to be the influence of the weak interlayer, based on the original code programming described by Shi [16, 17].

3. Case study

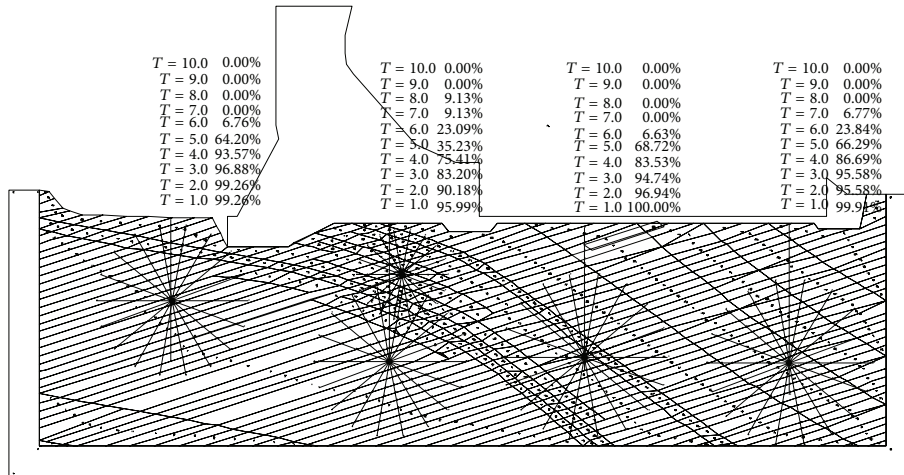
3.1. Engineering Geology Survey. The Xiangjiaba hydropower station is the final planned stepped hydropower station along the Jinsha River (Figure 3). Figure 4 shows the dam base of the Xiangjiaba hydropower station. The engineering geological conditions of the dam site zone are very complex: the river bed contains 15 small faults, which may be divided into two groups; the first group discontinuity which its strike is NNW, contains seven faults with the orientation of $280 \sim 300^\circ / \text{SW} \angle 70 \sim 80^\circ$; the other, strike NE, contains six faults with the orientation of $30^\circ \sim 50^\circ / \text{NW} \angle 65^\circ \sim 80^\circ$.

In the dam site zone, the joint and fissure developments differ from each other due to their different tectonic locations. If the zone is divided based on tectonic location, the stratum steep-dip is located within the core of the fold. The right side of the bed and the right bank are both on the SW limbs of the fold, and the left side of the bed and the left bank are both on the NE limbs. The joint and fissure develop greatly, with the strikes of the superiority jointing groups being $40 \sim 70^\circ$ and $320 \sim 340^\circ$, the former of which are fissures with medium- to high-dip angles, and the latter are joints with low-dip angles. The density of the joint and fissure is 10–20 per m. The joints on the left bank develop better than those on the right bank; there are two superiority jointing groups on the left bank, which have strikes of $280 \sim 300^\circ$ and $60 \sim 80^\circ$ and the density is 2–5 per m; and there are two superiority joint groups in the right with strikes of $60 \sim 80^\circ$ and $280 \sim 300^\circ$ and the density is 1–3 per m. The geometrical characteristics and corresponding probability distribution models of the main discontinuities are listed in Table 1.

3.2. Calculation Parameters and Analysis. The material parameters used for calculation in the DDA method are shown in Table 2.

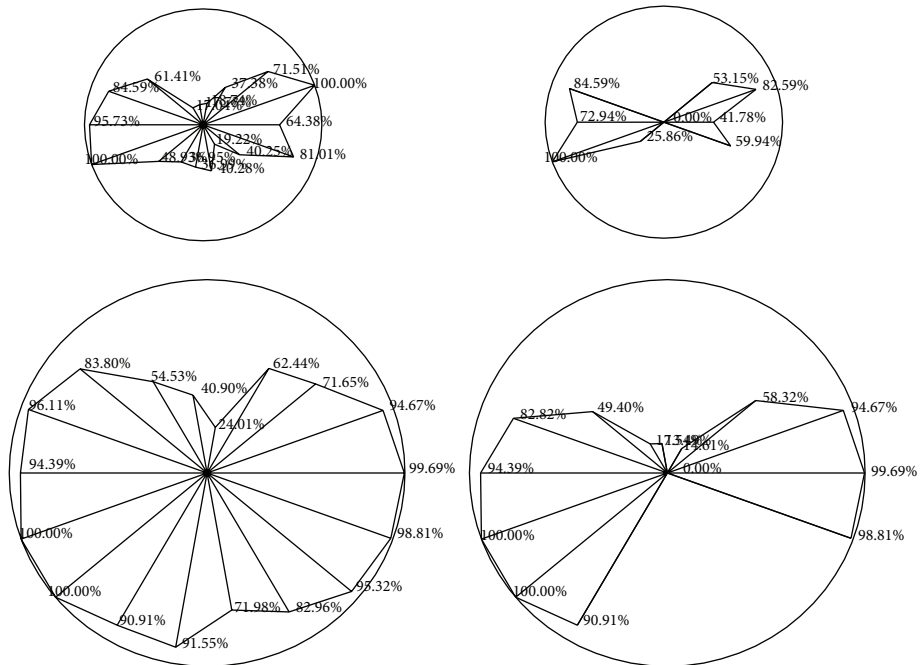
3.3. Analysis of the Calculation Results

3.3.1. Computation Model. Figure 5 shows the section of the 3D geological model of the dam base which is constructed by the DNS techniques. It may be seen that the combination of



T = 10.0	0.00%	T = 10.0	0.00%	T = 10.0	0.00%	T = 10.0	0.00%
T = 9.0	0.00%	T = 9.0	0.00%	T = 9.0	0.00%	T = 9.0	0.00%
T = 8.0	0.00%	T = 8.0	9.13%	T = 8.0	0.00%	T = 8.0	0.00%
T = 7.0	0.00%	T = 7.0	23.09%	T = 7.0	0.00%	T = 7.0	6.77%
T = 6.0	6.76%	T = 6.0	35.23%	T = 6.0	6.63%	T = 6.0	23.84%
T = 5.0	64.20%	T = 5.0	75.41%	T = 5.0	68.72%	T = 5.0	66.29%
T = 4.0	93.57%	T = 4.0	83.20%	T = 4.0	83.53%	T = 4.0	86.69%
T = 3.0	96.88%	T = 3.0	90.18%	T = 3.0	94.74%	T = 3.0	95.58%
T = 2.0	99.26%	T = 2.0	95.99%	T = 2.0	96.94%	T = 2.0	95.58%
T = 1.0	99.26%	T = 1.0	100.00%	T = 1.0	100.00%	T = 1.0	99.94%

(a) Location and scale of RQD method application



(b) Results of RQD method at different locations

FIGURE 6: RQD map of the dam base controlled by the rock mass discontinuities.

the discontinuities and soft layers is taken into account when building the dam base.

In Figure 5, it is quite clear that there are many soft layers in the rock masses of the dam base, as well as in the soft interlayer distributed throughout the entire dam base zone. Based on the results of the field engineering geological survey, these soft layers showing the shape of the knee buckling are found below the dam base and will lead to detrimental results.

3.3.2. *Assessment of Rock Masses Quality.* It may be concluded from Figure 5 that two types of superiority discontinuities exist in the rock masses with the exception of the soft layers. In addition, the discontinuities tend to develop better upstream than downstream. In order to reasonably evaluate

the rock masses dissected by the discontinuities, a comprehensive method which evaluates the rock masses from all directions must be used.

Table 3 shows the intactness assessment system of rock masses of the dam base. As seen, the RQD in the center of dam base is lower than that in the sides. This indicates that the rock masses in the center of the dam base are broken due to tectonic movement. In addition, the RQD in the tunnel is larger than that in the borehole. This phenomenon is proven by the constructed 3D model in Figure 6.

(1) *Evaluation of RQD.* The evaluation results of the rock mass quality are shown in Figure 6(a). It may be concluded that the RQD method is arbitrary and is able to evaluate the

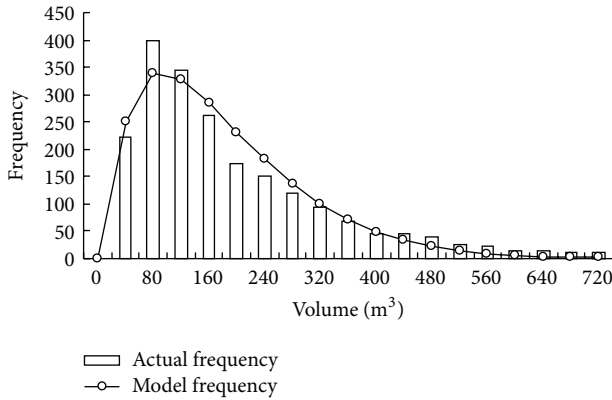


FIGURE 7: Actual and model distribution of the rock block size.

rock mass quality from any direction. Meanwhile, as a typical measurement, the borehole is still used to evaluate the rock mass quality. Vertically below the dam surface, the value of the ROD shown by the borehole is smaller than that above the surface, and the RQD values of all other parts of the dam have little differences among them. When the threshold value is 7.0, the RQD value is typically 0; when the threshold value of the RQD is smaller, the RQD value approaches 100%, while the RQD value of the rock masses below the dam remains at about 95%.

Figure 6(b) shows the RQD values under two threshold values, namely, 3.0 m and 5.0 m, at two different locations. Regardless of where the rock masses are located, the RQD is anisotropic. In the NNE direction the rock mass quality is higher, while in the NNW direction the quality is lower, and while the threshold value is larger, the RQD value tends to be 0. For the rock masses near the contact surface vertically below the dam base, the RQD value decreases with the threshold value decreasing.

(2) *Rock Block Characteristic Analysis.* Figure 7 shows the statistics of the rock mass volumes. As seen, the majority of the volume of the rock blocks is less than 300 m^3 , the lowest rock volume is 6.5 m^3 , the highest is 5367.8 m^3 , and the average value is 207.0 m^3 . The model is consistent with the Weibull distribution, and the model resembles the actual data accurately.

3.3.3. *Discontinuous Deformation Analysis.* As seen in Figure 8(a), in order to analyze the deformation of the dam base rock masses during the service period, the measure points are arranged in the dam base or at locations where the fissures are likely to be produced. Then the horizontal displacement, vertical displacement, horizontal velocity, and vertical velocity are analyzed, and the results are shown in Figures 8(b) to 8(e).

Similar trends with different measure points are seen in both Figures 8(b) and 8(c). The displacement of the forepart of the dam is larger than the ones in the center and rear parts of the dam. In the displacement of point 4, the measure points in the forepart are larger than those in all the remaining parts, and the highest value is 20 cm. The highest value of

displacement in the rear part of the dam ranges from 15 to 17 cm. The base of the dam may be divided into four parts; one of these measure points has the largest displacement, namely, point 4; the points 5, 6, 18, 20, and 25 form the second group, their displacements ranging from 12.5 to 17.5 cm; the third group contains points 7, 8, and 19, their displacements ranging from 11 to 12.5 cm; and the fourth group contains points 9, 22, and 23, the displacements of which are all approximately 10 cm.

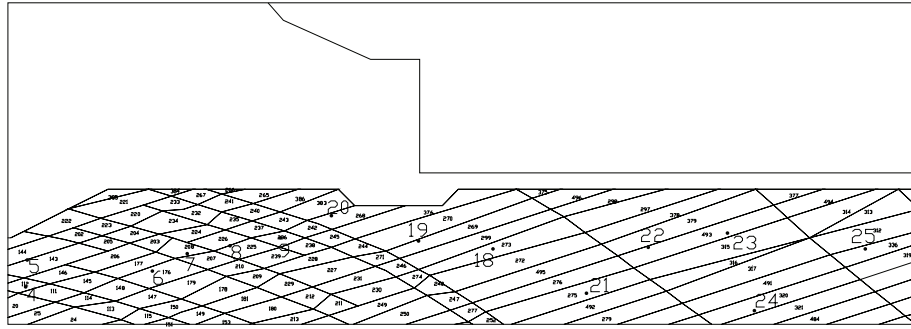
As seen in Figure 8(d), the altering regularity of the X-velocity developed with time ranges between 1.5 and 4.0 s; points 8 and 9 have velocities in the opposite direction as the other points; the curves vary widely beginning from 1.5 s; the maximum velocity value is greater than 4.0 cm/s; and beginning from 5 s, the trends of every point are similar. As a whole, the range of the forepart of the dam is larger than that of the rear part; the changing regularity of the curves is similar from 1.5 to 5.0 s, with the exception of point 25, the curve of which is lower than the others. In the end, the respective velocities of all the points tend to zero. The curve of the Y-velocity shown in Figure 8(e) alters regularly, from 0 to 4.5 s; beginning from 4.5 s, the displacements of the points in the dam base begin to change, and the one in the forepart is more evident than that in the rear. The reason for this phenomenon is that the dam deforms toward the rear due to the water pressure, and the rock masses of the forepart are uplifted, resulting in rock mass relaxation.

3.3.4. *Failure Analysis of Dam Base.* It is convenient to examine the actual damage of the rock masses through the DDA program. The results are calculated via 1000 calculation steps in DDA and are shown in Figure 9, in which the small circles at the top represent the damage degree. The DDA program considers the effects of many groups of discontinuities, and the direction of the discontinuities alters widely due to the knee buckling shape.

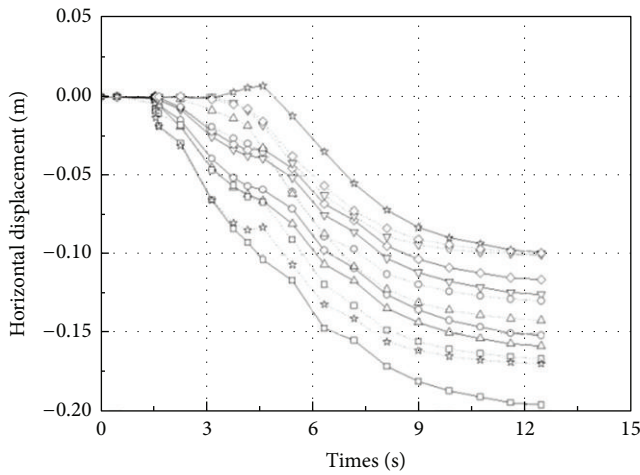
According to the overload method used in the DDA program, the rock mass failure of the dam base is classified as tensile fracture damage. The large circles in Figure 9 show that the discontinuities have a relatively large opening, due to the deformation of the dam base. In Figure 10, the curve of the horizontal displacement flattens out as the overload multiples reach 7.0 times, and when the overload multiples range from 7.0 to 7.5 times, the curve of the vertical displacement ceases to change. The main reasons for this phenomenon include the fact that the rock masses of the dam base readjust after being damaged, and the rocks in the rear of the dam act as a resistance. Therefore it may be concluded that the damage of the rock masses of the dam base is simulated very effectively using the DDA method in the service period, and the failures and discontinuities in the contact part of the dam base may be easily observed.

4. Conclusions

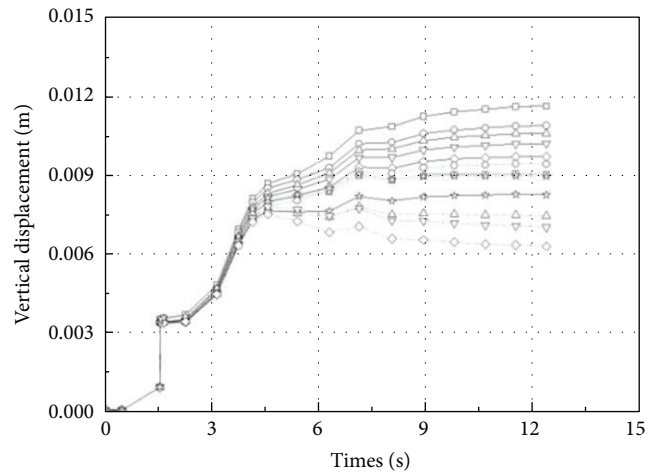
RQD is one of the most important indexes for assessing the intactness of rock masses which depend on the geometrical characteristics of their discontinuities. In this paper it is



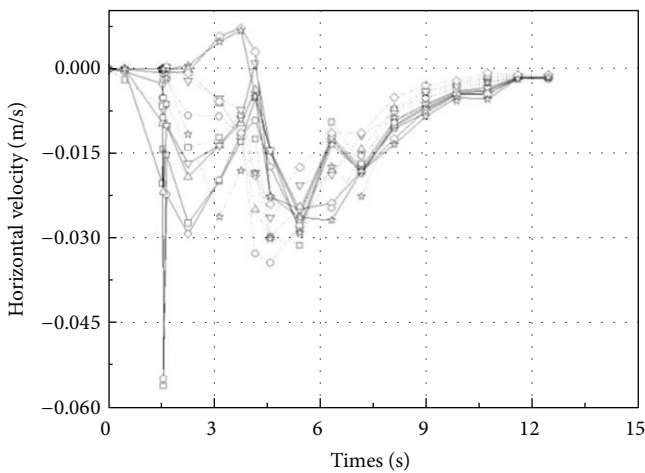
(a) Measure points in the dam base



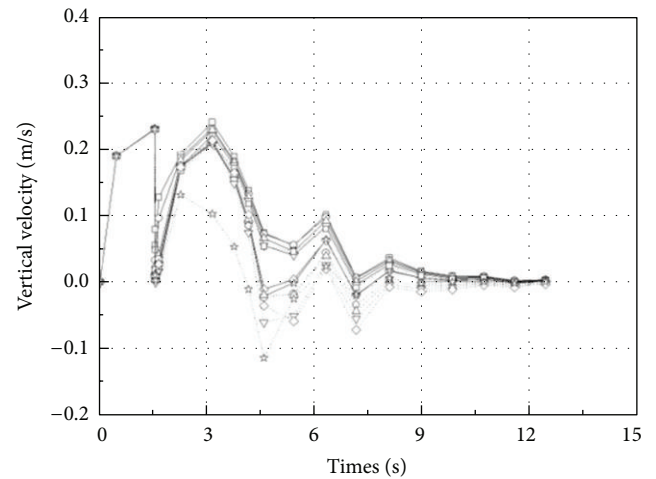
(b) X-displacement with time of measure points



(c) Y-displacement with time of measure point



(d) X-velocity with time of measure points



(e) Y-velocity with time of measure points



FIGURE 8: Displacement and velocity with time of different measure points in the dam base.

shown that the use of the optimal RQD threshold value greatly extends the range of RQD values. A series of methods is used to assess rock quality, construct a 3D model, and evaluate the stability of the dam base. The conclusions of the study are as follows.

- (1) Based on the mechanism of the geological mechanics, the elliptical discontinuities are used to simulate the rock structure, and this method is applied to the dam base of Xiangjiaba hydropower station. This study shows that the effects of the rock structure are caused

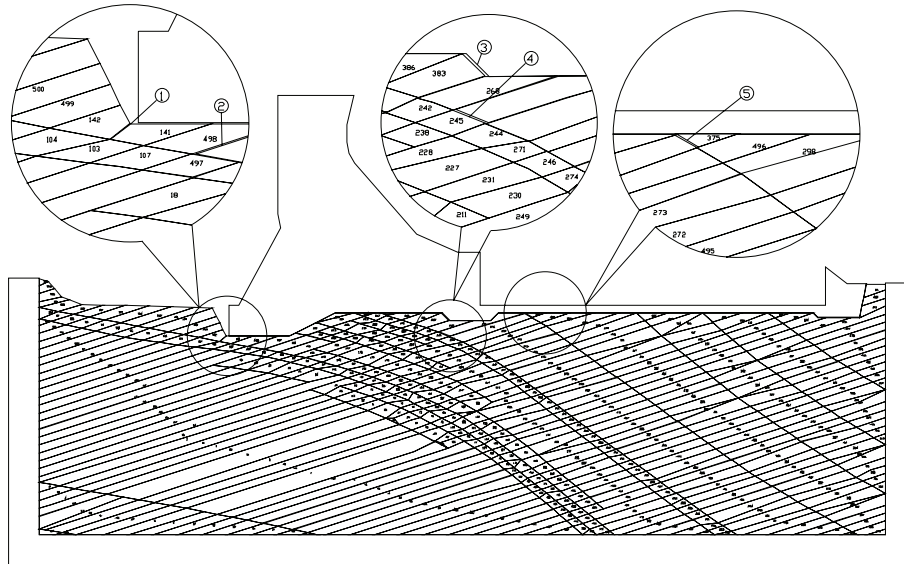


FIGURE 9: Fracture of rock masses in the dam base.

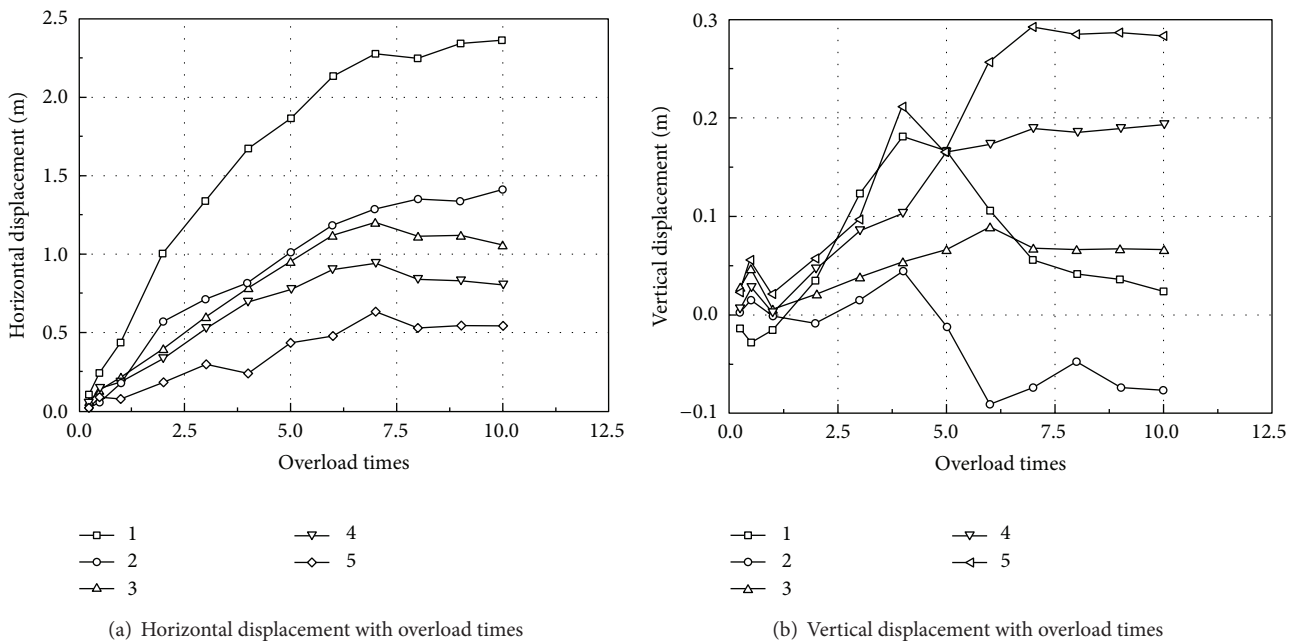


FIGURE 10: Relationship between overload and displacement of the measure points.

by the special discontinuities during the simulation, and this method is very valid for application to the simulation of the rock structure.

- (2) Based on the anisotropic characteristic of the rock masses, the modified RQD method with the threshold value and 3D space is applied to confirm the rationality of the 3D simulation and evaluate the rock mass quality of the dam base.
- (3) Based on the 3D structure of the dam base, the ground profile applied in the discontinuous deformation analysis is obtained by cutting the model and the

rock mass quality and the strain characteristic of the dam base are analyzed. The overload method is used to consider the failures occurring near the contact surface of the dam base and the rock masses, and the stability coefficient of the dam is determined through calculation.

Acknowledgments

This study is financially supported by the Natural Science Foundation of China (Grants nos. 41002089 & 41102162) and Jiangsu Overseas Research & Training Program for

University Prominent Young and Middle-aged Teachers and Presidents. The authors would also like to acknowledge the editors and reviewers of this paper for their very helpful comments and valuable remarks.

References

- [1] D. H. Zhong, M. C. Li, L. G. Song, and G. Wang, "Enhanced NURBS modeling and visualization for large 3D geoen지니어링 applications: an example from the Jinping first-level hydropower engineering project, China," *Computers and Geosciences*, vol. 32, no. 9, pp. 1270–1282, 2006.
- [2] H. H. Zhu, X. Y. Zhuang, Y. C. Cai, and G. Ma, "High rock slope stability analysis using the enriched meshless Shepard and least squares method," *International Journal of Computational Methods*, vol. 8, no. 2, pp. 209–228, 2011.
- [3] L. Jing, "Formulation of discontinuous deformation analysis (DDA)—an implicit discrete element model for block systems," *Engineering Geology*, vol. 49, no. 3-4, pp. 371–381, 1998.
- [4] J. Andersson and B. Dverstorp, "Conditional simulations of fluid flow in three-dimensional networks of discrete fractures," *Water Resources Research*, vol. 23, no. 10, pp. 1876–1886, 1987.
- [5] D. Elsworth, "A hybrid boundary element-finite element analysis procedure for fluid flow simulation in fractured rock masses," *International Journal for Numerical and Analytical Methods in Geomechanics*, vol. 10, no. 6, pp. 569–584, 1986.
- [6] J. C. S. Long, P. Gilmour, and P. A. Witherspoon, "A model for steady fluid flow in random three-dimensional networks of disc-shaped fractures," *Water Resources Research*, vol. 21, no. 8, pp. 1105–1115, 1985.
- [7] L. Smith and F. W. Schwartz, "An analysis of the influence of fracture geometry on mass transport in fractured media," *Water Resources Research*, vol. 20, no. 9, pp. 1241–1252, 1984.
- [8] S. D. Priest and J. A. Hudson, "Discontinuity spacings in rock," *International Journal of Rock Mechanics and Mining Sciences and*, vol. 13, no. 5, pp. 135–148, 1976.
- [9] J. P. Harrison, "Selection of the threshold value in RQD assessments," *International Journal of Rock Mechanics and Mining Sciences*, vol. 36, no. 5, pp. 673–685, 1999.
- [10] Z. Sen and A. Kazi, "Discontinuity spacing and RQD estimates from finite length scanlines," *International Journal of Rock Mechanics and Mining Sciences and*, vol. 21, no. 4, pp. 203–212, 1984.
- [11] Z. Şen, "Theoretical RQD-porosity-conductivity-aperture charts," *International Journal of Rock Mechanics and Mining Sciences and Geomechanics*, vol. 33, no. 2, pp. 173–177, 1996.
- [12] L. Zhang and H. H. Einstein, "Using RQD to estimate the deformation modulus of rock masses," *International Journal of Rock Mechanics and Mining Sciences*, vol. 41, no. 2, pp. 337–341, 2004.
- [13] X. W. Jiang, L. Wan, X. S. Wang, X. Wu, and X. Zhang, "Estimation of rock mass deformation modulus using variations in transmissivity and RQD with depth," *International Journal of Rock Mechanics and Mining Sciences*, vol. 46, no. 8, pp. 1370–1377, 2009.
- [14] D. Milne, J. Hadjigeorgiou, and R. Pakalnis, "Rock mass characterization for underground hard rock mines," *Tunnelling and Underground Space Technology*, vol. 13, no. 4, pp. 383–391, 1998.
- [15] D. T. Snow, "Rock fracture spacings, openings, and porosities," *Journal of the Soil Mechanics and Foundations Division*, vol. 94, no. 1, pp. 73–91, 1968.
- [16] G. H. Shi and R. E. Goodman, "Two dimensional discontinuous deformation analysis," *International Journal for Numerical and Analytical Methods in Geomechanics*, vol. 9, no. 6, pp. 541–556, 1985.
- [17] G. H. Shi, "Three dimensional discontinuous deformation analysis," in *Rock Mechanics in the National Interest: Proceedings of the 38th U.S. Rock Mechanics Symposium*, pp. 1421–1428, A.A. Balkema, Rotterdam, The Netherlands, 2001.
- [18] Q. H. Jiang and M. R. Yeung, "A model of point-to-face contact for three-dimensional discontinuous deformation analysis," *Rock Mechanics and Rock Engineering*, vol. 37, no. 2, pp. 95–116, 2004.
- [19] M. R. Yeung, Q. H. Jiang, and N. Sun, "Validation of block theory and three-dimensional discontinuous deformation analysis as wedge stability analysis methods," *International Journal of Rock Mechanics and Mining Sciences*, vol. 40, no. 2, pp. 265–275, 2003.
- [20] Y. H. Hatzor and A. Feintuch, "The validity of dynamic block displacement prediction using DDA," *International Journal of Rock Mechanics and Mining Sciences*, vol. 38, no. 4, pp. 599–606, 2001.
- [21] M. M. MacLaughlin and E. A. Berger, "A decade of DDA validation: development and application of discontinuous modeling for rock engineering," in *Proceedings of the 6th International Conference on Analysis of Discontinuous Deformation*, pp. 13–31, A.A. Balkema, Rotterdam, The Netherlands, 2003.
- [22] D. M. Doolin and N. Sitar, "Displacement accuracy of discounting deformation analysis method applied to sliding block," *Journal of Engineering Mechanics*, vol. 128, no. 11, pp. 1158–1168, 2002.
- [23] M. Tsesarsky, Y. H. Hatzor, and N. Sitar, "Dynamic displacement of a block on an inclined plane: analytical, experimental and DDA results," *Rock Mechanics and Rock Engineering*, vol. 38, no. 2, pp. 153–167, 2005.
- [24] Y. H. Hatzor, A. A. Arzi, Y. Zaslavsky, and A. Shapira, "Dynamic stability analysis of jointed rock slopes using the DDA method: King Herod's Palace, Masada, Israel," *International Journal of Rock Mechanics and Mining Sciences*, vol. 41, no. 5, pp. 813–832, 2004.
- [25] N. Sitar, M. M. MacLaughlin, and D. M. Doolin, "Influence of kinematics on landslide mobility and failure mode," *Journal of Geotechnical and Geoenvironmental Engineering*, vol. 131, no. 6, pp. 716–728, 2005.
- [26] Y. I. Kim, B. Amadei, and E. Pan, "Modeling the effect of water, excavation sequence and rock reinforcement with discontinuous deformation analysis," *International Journal of Rock Mechanics and Mining Sciences*, vol. 36, no. 7, pp. 949–970, 1999.
- [27] J. H. Wu, Y. Ohnishi, and S. Nishiyama, "Simulation of the mechanical behavior of inclined jointed rock masses during tunnel construction using discontinuous deformation analysis (DDA)," *International Journal of Rock Mechanics and Mining Sciences*, vol. 41, no. 5, pp. 731–743, 2004.
- [28] M. Tsesarsky and Y. H. Hatzor, "Tunnel roof deflection in blocky rock masses as a function of joint spacing and friction—a parametric study using discontinuous deformation analysis (DDA)," *Tunnelling and Underground Space Technology*, vol. 21, no. 1, pp. 29–45, 2006.

Research Article

Explicit Dynamic Finite Element Method for Failure with Smooth Fracture Energy Dissipations

Jeong-Hoon Song,¹ Thomas Menouillard,² and Alireza Tabarraei³

¹ Department of Civil and Environmental Engineering, University of South Carolina, Columbia, SC 29208, USA

² STUCKY Ltd., Rue du Lac 33, 1020 Renens VD 1, Switzerland

³ Department of Mechanical Engineering and Engineering Science, University of North Carolina at Charlotte, Charlotte, NC 28223, USA

Correspondence should be addressed to Jeong-Hoon Song; jhsong@cec.sc.edu

Received 19 July 2013; Accepted 1 October 2013

Academic Editor: Timon Rabczuk

Copyright © 2013 Jeong-Hoon Song et al. This is an open access article distributed under the Creative Commons Attribution License, which permits unrestricted use, distribution, and reproduction in any medium, provided the original work is properly cited.

A numerical method for dynamic failure analysis through the phantom node method is further developed. A distinct feature of this method is the use of the phantom nodes with a newly developed correction force scheme. Through this improved approach, fracture energy can be smoothly dissipated during dynamic failure processes without emanating noisy artifact stress waves. This method is implemented to the standard 4-node quadrilateral finite element; a single quadrature rule is employed with an hourglass control scheme in order to decrease computational cost and circumvent difficulties associated with the subdomain integration schemes for cracked elements. The effectiveness and robustness of this method are demonstrated with several numerical examples. In these examples, we showed the effectiveness of the described correction force scheme along with the applicability of this method to an interesting class of structural dynamic failure problems.

1. Introduction

It has been shown that the extended finite element method (XFEM) [1, 2] can be successfully applied to several types of internal discontinuity problems, focusing on failure problems. For example, the XFEM has been applied to arbitrary branched and intersecting cracks [3], three dimensional crack propagation [4, 5], cohesive crack models [6] and dynamic shell [7], and 2D [8] fracture problems.

Although the standard XFEM has been successfully applied to dynamic fracture problems by Belytschko et al. [8], they mostly considered fracture problems with a single initial notch and/or simple crack geometry. This limitation arises from the difficulty in the representation of a complicated crack geometry and with the numerical integration. To circumvent this difficulty, Xu and Needleman [9], Ortiz and Pandolfi [10], Repetto et al. [11], and Cirak et al. [12] proposed the interelement crack model; but this interelement crack model can have mesh sensitivity problems as pointed out in Belytschko et al. [8] and Song et al. [13].

Our motivation in presenting this paper is to illustrate a new method which is efficient for dynamic propagation of multiple cracks and fragmentation problems but nevertheless free from mesh sensitivity by using intra-element discontinuities. In this method, we use an element superposition concept to represent cracked elements which was proposed by Song et al. [14].

In addition, we describe a method to deal with the description of the crack tip element in terms of stiffness. It aims at characterizing the release of the crack tip element when the crack propagates. An additional correction force introduced by Menouillard and Belytschko [15] takes into account this crack tip element and makes the new additional degrees of freedom release continuously. This artificial correction force will be used to smooth the stress near the crack tip because no tip enrichment is used in our XFEM discretization.

Menouillard et al. [16] developed a mass lumping strategy for the XFEM formulation and more particularly for the

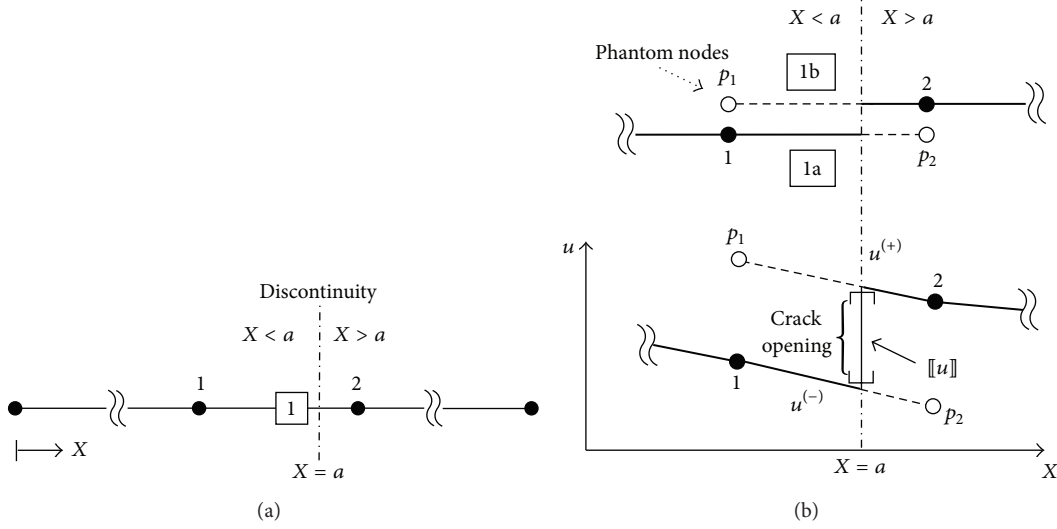


FIGURE 1: Representation of a discontinuity in a one-dimensional finite element: (a) problem description of a one-dimensional rod and (b) representation of a discontinuity with the phantom node method; solid circles denote real nodes and hollow circles denote phantom nodes.

discontinuous enrichment part. They found that the enrichment does not significantly decrease the stable time step. Then, Menouillard et al. [17] used another decomposition of the enriched shape function developed by A. Hansbo and P. Hansbo [18] which is used in the phantom node method developed by Song et al. [14] and Song and Belytschko [19].

The outline of this paper is as follows. The governing equation and its weak form are given in Section 2. The representation of a discontinuity in a cracked element with a phantom node method is presented in Section 3. Section 4 presents a new method for smoothly releasing the newly cracked element near the tip by taking into account the position of the tracked crack tip in the tip element. Several numerical examples are given in Section 5. Section 6 presents the conclusions of this paper.

2. Governing Equations and Weak Form

For a two-dimensional dynamic problem, the strong form of the linear momentum equation in a total Lagrangian description is

$$\frac{\partial P_{ji}}{\partial X_j} + \rho_0 b_i - \rho_0 \ddot{u}_i = 0 \quad \text{in } \Omega_0, \quad (1)$$

where \mathbf{P} is the nominal stress tensor, ρ_0 is the initial mass density, and \mathbf{b} is the body force vector. The boundary conditions are

$$n_j^0 P_{ji} = \bar{t}_i^0 \quad \text{on } \Gamma_t^0 \quad (2)$$

$$u_i = \bar{u}_i \quad \text{on } \Gamma_u^0 \quad (3)$$

$$n_j^0 P_{ji}^- = -n_j^0 P_{ji}^+ = \tau_i^{0c} ([[u_i]]) \quad \text{on } \Gamma_c^0, \quad (4)$$

where \mathbf{n}^0 is the unit normal vector to the boundary, $\boldsymbol{\tau}^{0c}$ is the cohesive traction across the crack surfaces, $\bar{\mathbf{t}}^0$ is the applied

traction on the Neumann boundary Γ_t , and $\bar{\mathbf{u}}$ is the applied displacement on the Dirichlet boundary Γ_u^0 ; $\Gamma_u^0 \cup \Gamma_t^0 = \Gamma^0$, $\Gamma_u^0 \cap \Gamma_t^0 = \emptyset$. Superscript plus and minus signs refer to the two sides of the discontinuity. The spaces of admissible function are

$$\mathcal{U} = \{ \mathbf{u}(\mathbf{X}, t) \mid \mathbf{u}(\mathbf{X}, t) \in C^0, \mathbf{u}(\mathbf{X}, t) = \bar{\mathbf{u}}(t) \quad \text{on } \Gamma_u^0, \mathbf{u} \text{ discontinuous on } \Gamma_c \}, \quad (5)$$

$$\mathcal{U}_0 = \{ \delta \mathbf{u}(\mathbf{X}, t) \mid \delta \mathbf{u}(\mathbf{X}, t) \in C^0, \delta \mathbf{u}(\mathbf{X}, t) = 0 \quad \text{on } \Gamma_u^0, \delta \mathbf{u} \text{ discontinuous on } \Gamma_c \}. \quad (6)$$

The weak form of the momentum equation is given by for $\mathbf{u}(\mathbf{X}, t) \in \mathcal{U}$

$$\delta W^{\text{kin}} = \delta W^{\text{int}} - \delta W^{\text{ext}} + \delta W^{\text{coh}} \quad \forall \delta \mathbf{u}(\mathbf{X}) \in \mathcal{U}_0, \quad (7)$$

where δW^{int} is the internal work, δW^{ext} is the external work performed by the applied loads, δW^{kin} is the kinetic work performed by inertia forces, and δW^{coh} is the work performed by the cohesive traction on the crack surface Γ_c . These quantities are defined as

$$\delta W^{\text{kin}} = \int_{\Omega_0} \delta \mathbf{u} \cdot \rho_0 \ddot{\mathbf{u}} d\Omega_0, \quad (8)$$

$$\delta W^{\text{int}} = \int_{\Omega_0} \frac{\partial \delta \mathbf{u}}{\partial \mathbf{X}} : \mathbf{P} d\Omega_0, \quad (8)$$

$$\delta W^{\text{ext}} = \int_{\Omega_0} \delta \mathbf{u} \cdot \rho_0 \mathbf{b} d\Omega_0 + \int_{\Gamma_t^0} \delta \mathbf{u} \cdot \bar{\mathbf{t}}^0 d\Gamma_t^0, \quad (9)$$

$$\delta W^{\text{coh}} = - \int_{\Gamma_c} \delta [[\mathbf{u}]] \cdot \boldsymbol{\tau}^c d\Gamma_c, \quad (9)$$

where $\bar{\mathbf{t}}$ is the normalized traction prescribed on Γ_t^0 and $\boldsymbol{\tau}^c$ is the cohesive traction applied on the discontinuity surface; an updated Lagrangian form is used for the cohesive work in (9).

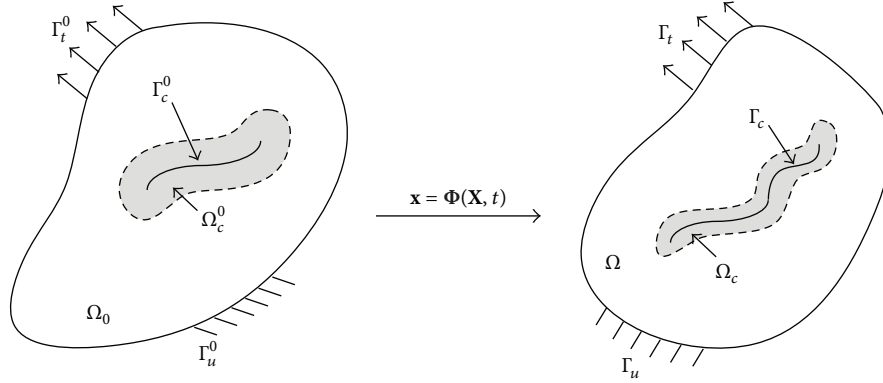
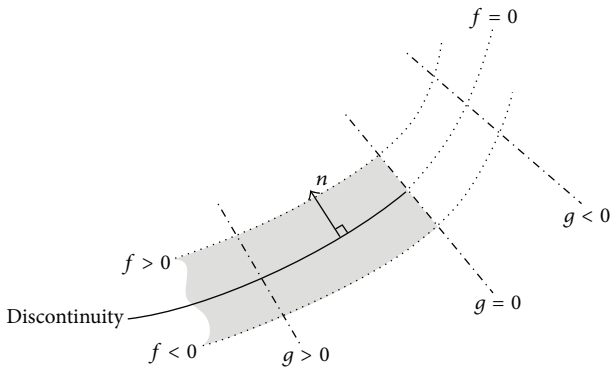


FIGURE 2: Representation of a two-dimensional body with an internal discontinuity in the initial and the current domains.


 FIGURE 3: Two-dimensional discontinuity representation by two implicit functions $f(\mathbf{X})$ and $g(\mathbf{X}, t)$.

3. Representation of a Discontinuity with Phantom Nodes

We first illustrate the modeling of a one-dimensional cracked element with phantom nodes and then give the general description for the modeling of the two-dimensional case, subsequently. Consider a one-dimensional rod and let a crack be located inside of element 1 at $X = a$, as shown in Figure 1(a).

The displacement field in cracked element 1 can be seen to consist of two separated displacement fields as shown in Figure 1(b): the displacement field of element 1a for $X < a$, and element 1b for $X > a$. To construct new elements 1a and 1b from the element 1, we add new nodes which are replicas of the original nodes; we called these nodes phantom nodes.

We define phantom nodes by the following:

$$I \text{ is a phantom node in } \begin{cases} \text{element 1a} & \text{if } \mathbf{X}_I - a > 0 \\ \text{element 1b} & \text{if } \mathbf{X}_I - a < 0. \end{cases} \quad (10)$$

We can now rewrite the displacement field of element 1 as a set of two superimposed elements with phantom nodes

$$\begin{aligned} \mathbf{u}^1(\mathbf{X}, t) &= \mathbf{u}^{1a}(\mathbf{X}, t) + \mathbf{u}^{1b}(\mathbf{X}, t) \\ &= \underbrace{[u_1^{1a} N_1 + p_2^{1a} N_2]}_{\mathbf{u}^{1a}} H(-(X-a)) \\ &\quad + \underbrace{[p_1^{1b} N_1 + u_2^{1b} N_2]}_{\mathbf{u}^{1b}} H(X-a), \end{aligned} \quad (11)$$

where a superscript and subscript denote the element and node number, respectively, \mathbf{N}_I are the shape functions, p is the nodal unknown of the phantom node, and $H(x)$ is the Heaviside step function defined by

$$H(x) = \begin{cases} 1 & x \geq 0 \\ 0 & x < 0. \end{cases} \quad (12)$$

The displacement jump across the crack is given by

$$\begin{aligned} [[u]]_{X=a} &= \lim_{\varepsilon \rightarrow 0} [\mathbf{u}^{1a}(X+\varepsilon) - \mathbf{u}^{1b}(X-\varepsilon)]_{X=a} \\ &= \{u_1^{1a} N_1(a) + p_2^{1a} N_2(a)\} \\ &\quad - \{p_1^{1b} N_1(a) + u_2^{1b} N_2(a)\} \\ &= (\mathbf{u}_I^{1a} - \mathbf{u}_I^{1b}) N_I(a). \end{aligned} \quad (13)$$

This procedure for cracked elements is similar to the standard XFEM nodal enriching scheme. However, the phantom nodes method simplifies the implementation of cracked elements within the context of existing finite element codes, since it is only necessary to add an extra element with phantom nodes and modify the element connectivity matrices.

3.1. Phantom Node Method in Two Dimensions. Consider an initial domain Ω_0 as shown in Figure 2. The motion is described by $\mathbf{x} = \Phi(\mathbf{X}, t)$, where \mathbf{X} and \mathbf{x} denote material and spatial coordinates, respectively. In the current domain, the image of the initial domain Ω_0 is denoted by Ω . We allow

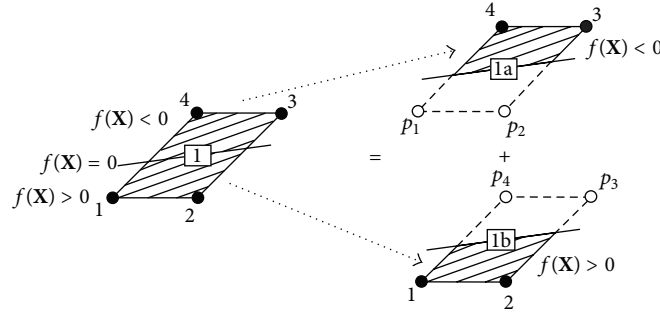


FIGURE 4: Representation of a cracked element in two dimensions; solid circles denote real nodes and hollow circles denote phantom nodes.

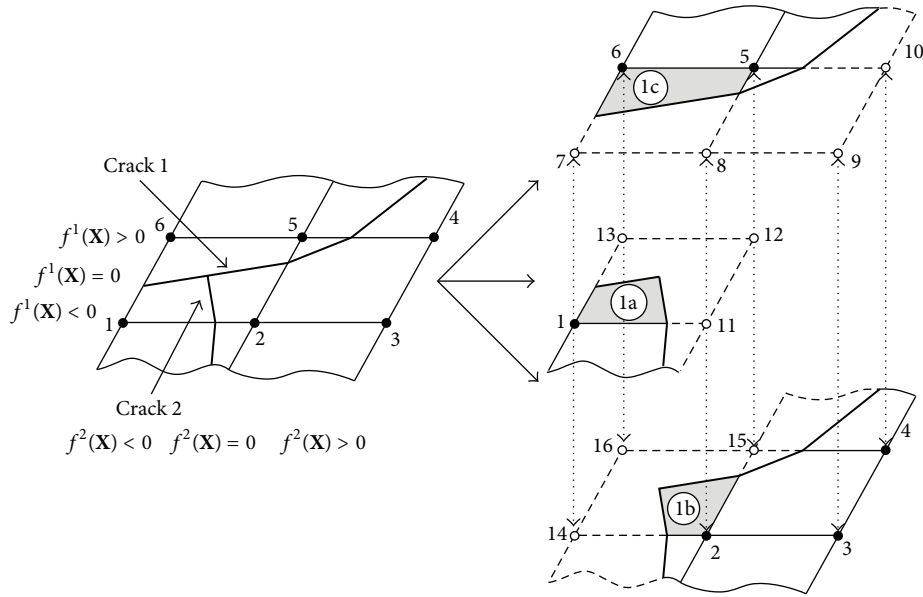


FIGURE 5: Decomposition of an element into three elements 1a, 1b, and 1c in order to model crack branching; solid and hollow circles denote the original nodes and the added phantom nodes, respectively.

this domain to contain internal discontinuities Γ_c which is enveloped by a region Ω_c .

Inside of the region Ω_c , we define two local level set functions $f(\mathbf{X})$ and $g(\mathbf{X}, t)$, where $f(\mathbf{X})$ and $g(\mathbf{X}, t)$ are signed distance functions which describe the crack surface and tip geometry, respectively. The isozero line of the function $f(\mathbf{X})$, that is, $f(\mathbf{X}) = 0$, corresponds to the crack surface Γ_c , and the function $g(\mathbf{X}, t)$ is defined so that $g(\mathbf{X}, t) > 0$ along the crack surface and vanishes at the crack tip; see Figure 3. By using a set of these level set functions, we can implicitly define the crack geometry by

$$\mathbf{X} \in \Omega_c^0 \quad \text{if } f(\mathbf{X}) = 0 \quad g(\mathbf{X}, t) > 0, \quad \mathbf{X} \in \Omega_c^0. \quad (14)$$

For the numerical representation, instead of employing an implicit definition of the crack surface, generally we can approximate the path of an internal discontinuity by

$$\sum_I f_I N_I(\mathbf{X}) = 0, \quad (15)$$

where $f_I = f(\mathbf{X})$ and $f(\mathbf{X}) = \min_{\bar{\mathbf{X}} \in \Gamma_c} \|\mathbf{X} - \bar{\mathbf{X}}\|$. As a consequence of (15), the surface of discontinuity can be represented by $f(\mathbf{X}_I)$ at the nodes of the cracked elements [20, 21]. Note that for the element-by-element cracking scheme which is employed in this study, we can replace the function $g(\mathbf{X}, t)$ by a list of cracked elements.

For a two-dimensional element, the superposed displacement fields in the cracked element can be developed in a similar manner to the one-dimensional case. Consider cracked element 1 and replace the element with element 1a and 1b as shown in Figure 4.

The displacement field of this superimposed element is

$$\mathbf{u}(\mathbf{X}, t) = \underbrace{\sum_{I=1}^{n^N} \mathbf{u}_I^{1a}(t) N_I(\mathbf{X}) H(-f(\mathbf{X}))}_{\mathbf{u}^{1a}(\mathbf{X}, t)} + \underbrace{\mathbf{u}_I^{1b}(t) N_I(\mathbf{X}) H(f(\mathbf{X}))}_{\mathbf{u}^{1b}(\mathbf{X}, t)}. \quad (16)$$

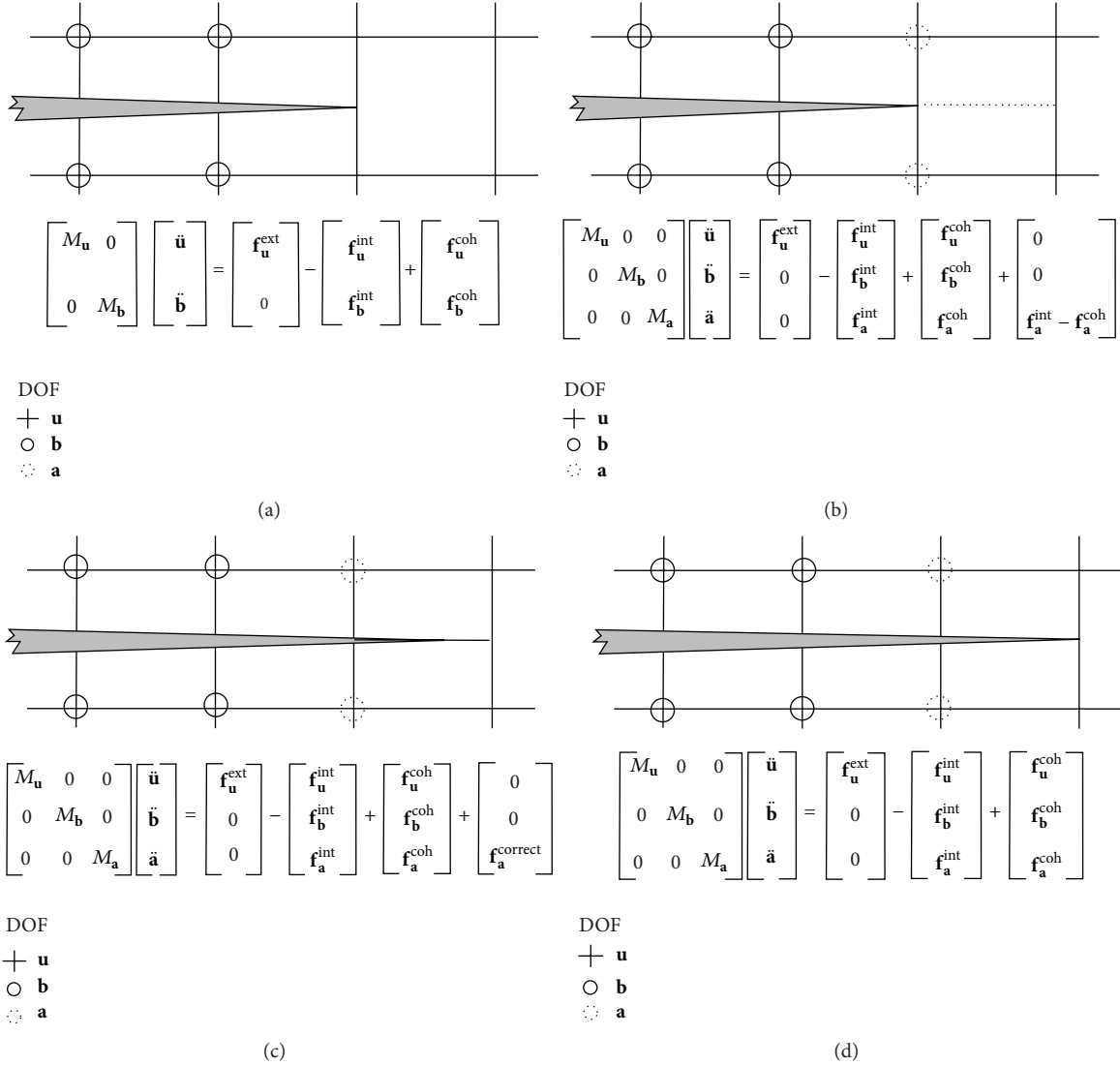


FIGURE 6: Evolution from the state (a) to (d) through the intermediate states (b) and (c) where the correction force decreases. M_u denotes the mass matrix related to the standard degrees of freedom \mathbf{u} , M_b to the existing discontinuous degree of freedoms \mathbf{b} , and M_a to the new discontinuous degrees of freedom \mathbf{a} . \mathbf{f}^{ext} denotes the external force, \mathbf{f}^{coh} denotes the cohesive force, and \mathbf{f}^{int} denotes the internal forces related to the different kinds of degrees of freedom (i.e. \mathbf{u} , \mathbf{b} , and \mathbf{a} , respectively, denoted by a cross, a continuous circle, and a dotted circle).

The explicit value of the displacement jump is given by

$$\begin{aligned} \llbracket \mathbf{u} \rrbracket &= \lim_{\varepsilon \rightarrow 0} [\mathbf{u}^{1a}(\mathbf{X} + \varepsilon \nabla f) - \mathbf{u}^{1b}(\mathbf{X} - \varepsilon \nabla f)] \\ &= [N_I H(-f(\mathbf{X})) \mathbf{u}_I^{1a} - N_I H(f(\mathbf{X})) \mathbf{u}_I^{1b}]_{\mathbf{X} \in \Gamma_c} \quad (17) \\ &= (\mathbf{u}_I^{1a} - \mathbf{u}_I^{1b}) N_I(a). \end{aligned}$$

The concept of element overlapping method can be easily extended to modeling of an arbitrary crack junction or branching problems. When the original crack 1 branches into a new crack 2 or a crack 1 junctions with a crack 2, as shown in Figure 5, the element can be replaced with three overlapping

elements and the discontinuous displacement fields can be represented by

$$\begin{aligned} \mathbf{u}(\mathbf{X}, t) &= \mathbf{u}^{1a}(\mathbf{X}, t) + \mathbf{u}^{1b}(\mathbf{X}, t) + \mathbf{u}^{1c}(\mathbf{X}, t) \\ &= \sum_{I \in S_1} \mathbf{u}_I N_I H(-f^1(\mathbf{X})) H(-f^2(\mathbf{X})) \\ &\quad + \sum_{I \in S_2} \mathbf{u}_I N_I H(-f^1(\mathbf{X})) H(f^2(\mathbf{X})) \quad (18) \\ &\quad + \sum_{I \in S_3} \mathbf{u}_I N_I H(f^1(\mathbf{X})) H(-f^2(\mathbf{X})), \end{aligned}$$

where $f^1(\mathbf{X})$ and $f^2(\mathbf{X})$ are level set functions for crack 1 and 2, respectively.

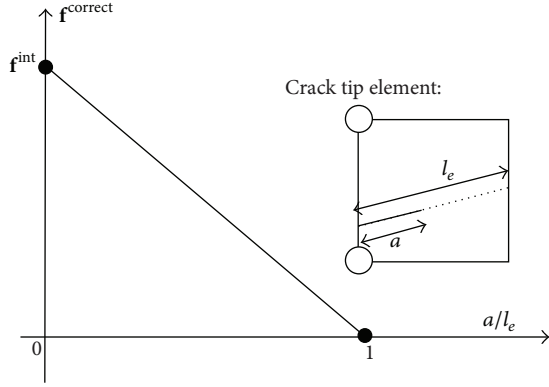


FIGURE 7: Law of the correction force as a function of the fracture ratio of the crack tip element (i.e., the position of the crack tip in the element).

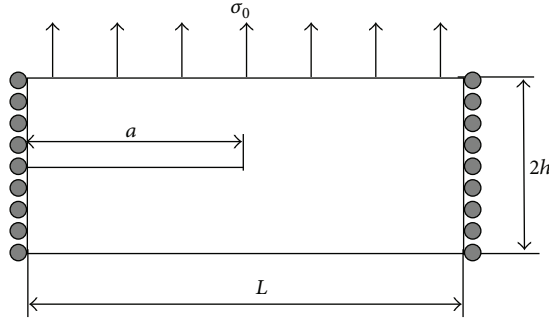


FIGURE 8: Geometry and loading of the semi-infinite plate example.

If the crack branching angle between crack 1 and crack 2 is acute, that is, both cracks cut the element edge of nodes 2 and 5 in Figure 5, the phantom node method cannot resolve this case and in this case, minimal remeshing is required to properly model crack branching.

4. Correction Force

In this section, we aim at developing a method to deal with the release of the crack tip element when the crack propagates through. It is to avoid sudden element release near the crack tip during propagation and thus avoid unphysical stress wave propagation due to the crack propagation.

Figure 6(a) shows the crack tip element with the associated phantom nodes. When the crack tip reaches the next element, the new crack tip element is suddenly released (see the sudden passage from Figures 6(a) to 6(d)) because the corresponding internal force takes a significant value when the phantom nodes are injected (i.e., $\mathbf{f}_a^{\text{int}}$ is nonzero in Figure 6(d)). Our proposed method makes a progressive release of the crack tip element. This even happens with the cohesive force. Figures 6(b) and 6(c) show the crack tip element on a dotted line and the additional correction force acting in the momentum equation, which aims at releasing smoothly the element when the crack tip travels through from one edge to the next one. Thus the modified discrete

TABLE I: Flowchart for numerical computation procedures.

Steps	Numerical computation procedures
1	Apply initial conditions including initial boundary conditions and prestress
2	Compute initial forces: $\mathbf{f}_0 = \mathbf{f}_0^{\text{ext}} - \mathbf{f}_0^{\text{int}}$
3	Compute acceleration: $\mathbf{a}_n = \mathbf{M}_n^{-1} \mathbf{f}_n$
4	Time update: $t_{n+1} = t_n + \Delta t_{n+(1/2)}$
5	First partial update for nodal velocities: $\mathbf{v}_{n+(1/2)} = \mathbf{v}_n + (t_{n+(1/2)} - t_n) \mathbf{a}_n$
6	Apply velocity boundary conditions at $t_{n+(1/2)}$
7	Update nodal displacements: $\mathbf{d}_{n+1} = \mathbf{d}_n + \Delta t_{n+(1/2)} \times \mathbf{v}_{n+(1/2)}$
8	Compute strain and stress
9	Check fracture criterion and insert phantom nodes
10	Compute forces at time: $\mathbf{f}_{n+1} = \mathbf{f}_{n+1}^{\text{ext}} - \mathbf{f}_{n+1}^{\text{int}} + \mathbf{f}_{n+1}^{\text{coh}} + \mathbf{f}_{n+1}^{\text{correct}}$
11	Compute acceleration: $\mathbf{a}_{n+1} = \mathbf{M}_{n+1}^{-1} \mathbf{f}_{n+1}$
12	Second partial update for nodal velocities: $\mathbf{v}_{n+1} = \mathbf{v}_{n+(1/2)} + (t_{n+1} - t_{n+(1/2)}) \mathbf{a}_{n+1}$
13	Update counter n
14	Output: if simulation is not completed, go to Step 4

momentum equation for the newly added degrees of freedom becomes

$$\mathbf{f}^{\text{kin}} = \mathbf{f}^{\text{int}} - \mathbf{f}^{\text{ext}} + \mathbf{f}^{\text{coh}} - \mathbf{f}^{\text{correct}}, \quad (19)$$

where $\|\mathbf{f}^{\text{correct}}\|$ tends to zero when the crack tip reaches the new edge, and thus the element becomes completely cut by the discontinuity (see Figure 6(d)). Note that \mathbf{f}^{coh} is not displayed in Figure 6. The initial value of the correction force (when the crack tip is on the previous edge) is such that the sum of the four forces in the equation above is zero as it is shown in Figure 6(b). At this point, the correction force is the same as the internal force, and thus no acceleration occurs yet on the new additional degrees of freedom, denoted by \mathbf{a} in Figure 6. The flowchart for numerical computation procedures is described in Table 1.

The evolution of the correction force is shown in Figure 7 which describes the magnitude of the correction force as a function of the crack tip position in the tip element. Indeed the correction force goes from the initial internal force to zero when the crack tip propagates from one edge to another. Between these two crack tip positions, the correction force is taken to be linear in our simulation. However this is not a restriction to use a linear law. In other words, the correction force is only applied to the newly added degrees of freedom, for example, the additional degrees of freedom of the crack tip element (see Figure 7). The law is

$$\mathbf{f}_e^{\text{correct}}(t) = \left(1 - \frac{a(t)}{l_e}\right) \mathbf{f}_e^{\text{int}}(t_{\text{inj}}), \quad (20)$$

where t_{inj} is the time the corresponding degrees of freedom are injected, $a(t)$ is the crack propagation speed, and l_e is the characteristic length of finite elements.

The continuity of the internal force related to the new additional degrees of freedom gives the same property to the

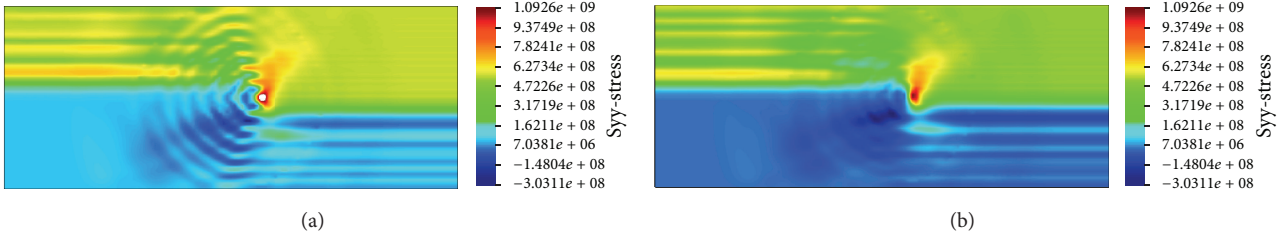


FIGURE 9: Stress field in the fine mesh: (a) without correction and (b) with correction force.

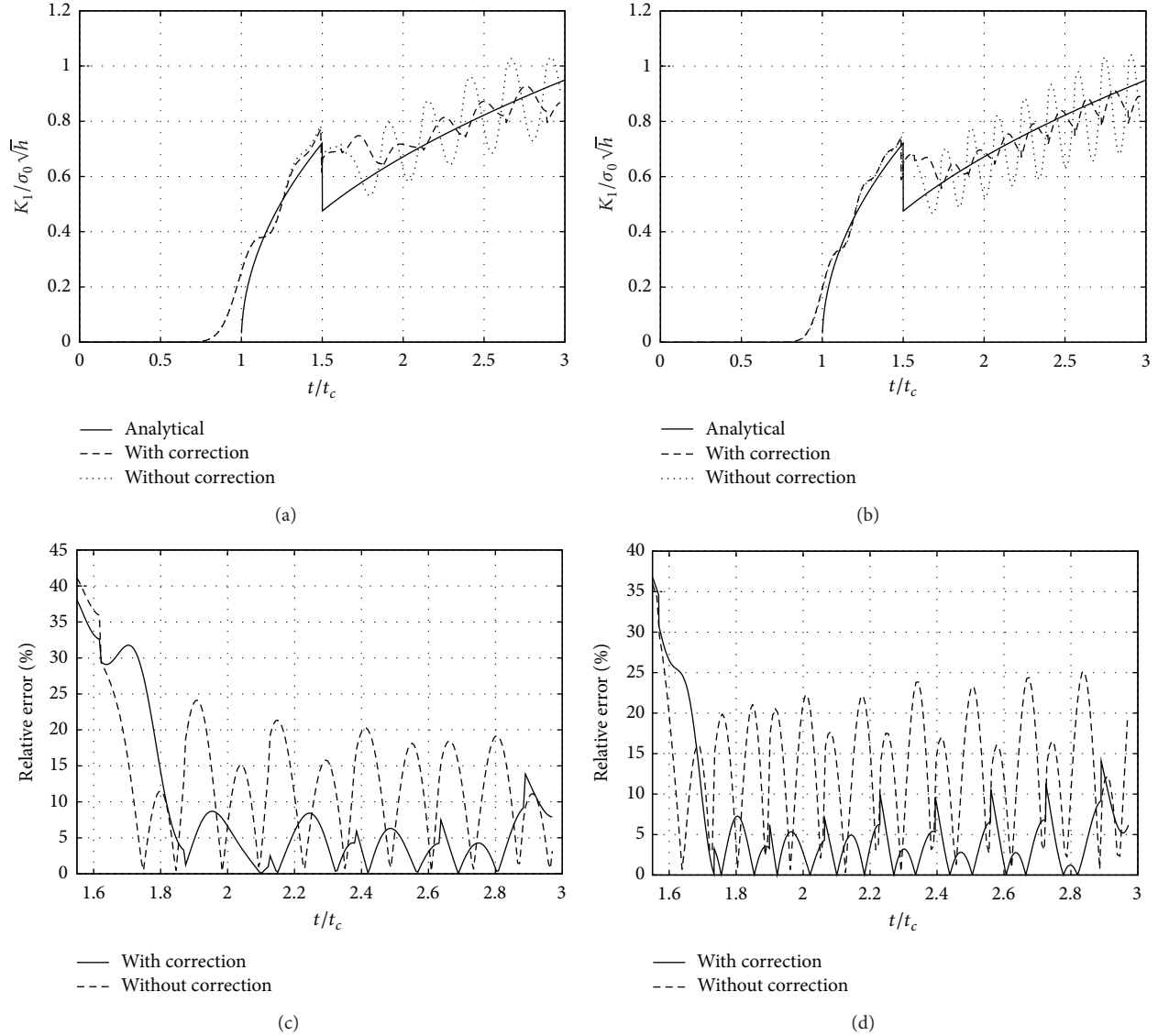


FIGURE 10: Normalized stress intensity factor as a function of time computed on the (a) coarse mesh and (b) fine mesh; relative error on stress intensity factor as a function of time on the (c) coarse mesh and (d) fine mesh.

acceleration through the momentum equation. Therefore, the velocity and displacement remains quite continuous in time when additional degrees of freedom are injected, and thus the property of continuity in time remains in the strain and stress field too, and a continuous progressive release of the tip element occurs.

5. Numerical Examples

5.1. *Moving Semi-Infinite Mode I Crack.* The example considered in this section is an infinite plate with a semi-infinite crack [22] loaded as shown in Figure 8. A theoretical solution of this problem for a given crack velocity is given in Freund

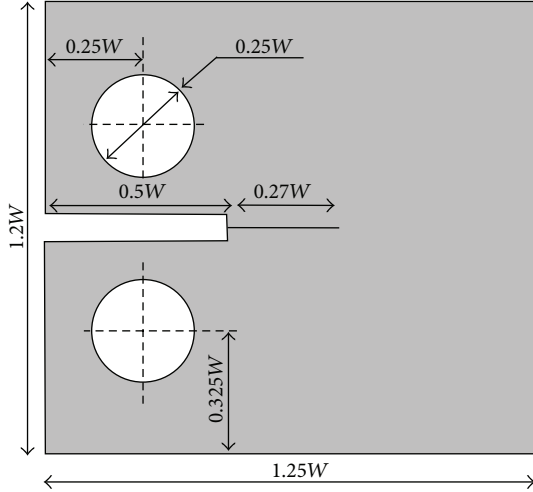


FIGURE 11: Compact tension specimen geometry ($W = 0.05$ m) and the thickness is $W/2$.

[23]. According to the geometry described in Figure 8, the analytical solution is valid until time $t \leq 3t_c = 3h/c_1$ (where c_1 is the dilatational wave speed). Beyond that, the reflected stress wave reaches the crack tip and the analytical solution is no longer valid. The dimensions of the structure are the following: the length is $L = 10$ m, the initial crack length $a = 5$ m, and the vertical position of the crack is $h = 2$ m. Two regular meshes are used: 78×39 and 120×59 4-node elements. The material properties are Young's modulus $E = 210$ GPa, Poisson's ratio $\nu = 0.3$, and density $\rho = 8,000$ kg/m³. The tensile stress applied on the top surface is $\sigma_0 = 500$ MPa. The crack velocity is imposed to be zero until $1.5 t_c$ and $1,500$ m/s after. The mode I stress intensity factor is normalized by the factor $\sigma_0 \sqrt{h}$.

We study the effect of the correction force on the accuracy of the stress intensity factor of a moving crack. The analytical relation between the stress intensity factor K_I and the velocity \dot{a} of the crack is given by [23]

$$K_I(\dot{a}, t) = \begin{cases} 0 & \text{if } t < t_c \\ \frac{2\sigma_0}{1-\nu} \sqrt{\frac{c_1(t-t_c)(1-2\nu)}{\pi}} & \text{if } t_c \leq t < 1.5t_c \\ \frac{2\sigma_0}{1-\nu} \sqrt{\frac{c_1(t-t_c)(1-2\nu)}{\pi}} \times \frac{1-(\dot{a}/c_r)}{1-(\dot{a}/2c_r)} & \text{if } 1.5t_c \leq t, \end{cases} \quad (21)$$

where the Rayleigh wave speed is $c_r = 2,947$ m/s and the dilatational wave speed is $c_1 = 5,944$ m/s.

Figure 9 shows the stress contour at the end of the computation for the two cases, that is, with and without the correction force. One can notice that the correction force makes the stress fields smoother in the structure when the crack propagation occurs and eliminates majority of the released stress waves due to the abrupt injection of phantom

node as shown in Figure 9(a). In contrary spurious stress waves appear in Figure 9(a) due to the crack propagation and the sudden release of the crack tip elements.

Figures 10(a) and 10(b), respectively, present the normalized stress intensity factor as a function of time for the coarse mesh and fine mesh, respectively, with and without the correction force. Both figures underline that the correction force improves the result during propagation by decreasing the magnitude of the oscillations due to the released crack tip element. Indeed the number of oscillations are directly related to the number of newly cracked elements. To evaluate the improvement, Figures 10(c) and 10(d) show the relative error between the computations using the correction force and not for the coarse and fine meshes. The error is decreased from 20% to 5% by adding the correction force on the newly added degrees of freedom during the crack propagation.

5.2. Stiffened Compact Tension Specimen. The stiffened compact tension specimen is used in various experiments [24, 25]. The particularity of the stiffened test is that an additional part of material opposite to the initial crack has the effect of a stiffener. With such a configuration, the crack will not be able to propagate straight toward the stiffener, but an instability will make the crack propagate up or down as a curve. Figure 11 presents the geometry of the specimen without showing the stiffened part; the stiffened part is glued on the right edge of the specimen as shown in Figure 12(b). A J_2 plasticity theory is used to model the behavior of the specimen. The material properties are Young's modulus $E = 69$ GPa, Poisson's ratio $\nu = 0.3$, density $\rho = 2,780$ kg/m³, yield stress $\sigma_0 = 275$ MPa, and hardening slope $h = 640$ MPa. A constant velocity of 1.8 m/s is applied at the center of two steel bars located in each hole of the specimen.

Figure 12(a) shows the final fracture pattern of the specimen at the end of the computation. The numerical result shown in Figure 12(a) agrees well with the experimental result obtained by Galanis [24] as shown in Figure 12(b). The computed load-deflection curve is also in good agreement with the experiments as shown in Figure 13.

5.3. Dynamic Multiple Crack Branchings in a Square Plate. For dynamic fracture problems, crack branching due to a dynamic instability is a common phenomenon. Several experimental results on crack branching have been previously reported [26–30]. However, because of difficulties in the representation of branched crack paths, only a few numerical results have been reported [8, 9, 31] and so forth. Note that Belytschko et al. [8] allowed the original crack to branch only once; Xu and Needleman [9] used an element edge crack model which is less complex than intraelement crack models but has a certain mesh sensitivity; for the issues regarding mesh sensitivity, refer to Belytschko et al. [8]. Also, Rabczuk and Belytschko [31] discretely modeled the crack with the meshfree cracked particle method. In the following, we examine the performance of the proposed method in a crack branching problem.

We consider a 0.1 m by 0.04 m prenotched specimen as shown in Figure 14. Tensile traction, $\sigma = 1$ MPa, is applied on

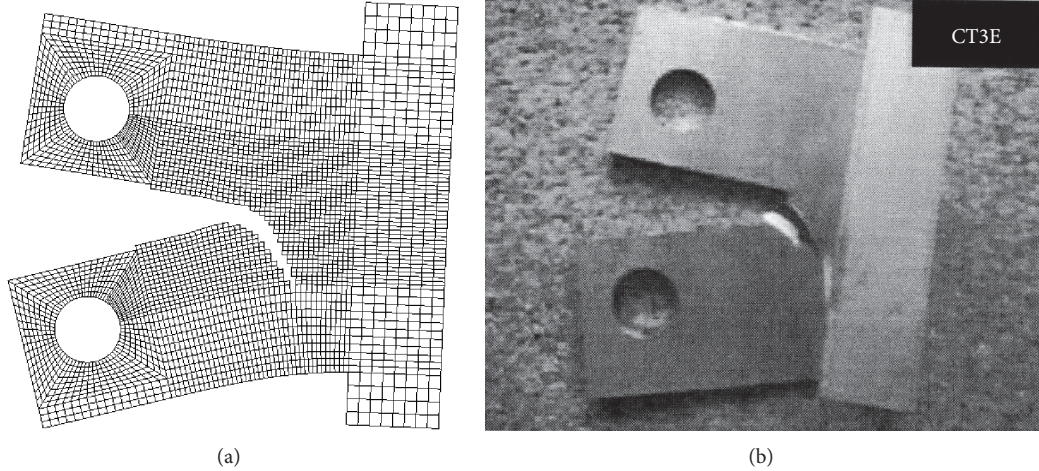


FIGURE 12: (a) Deformed mesh and (b) experimental postmortem specimen [24].

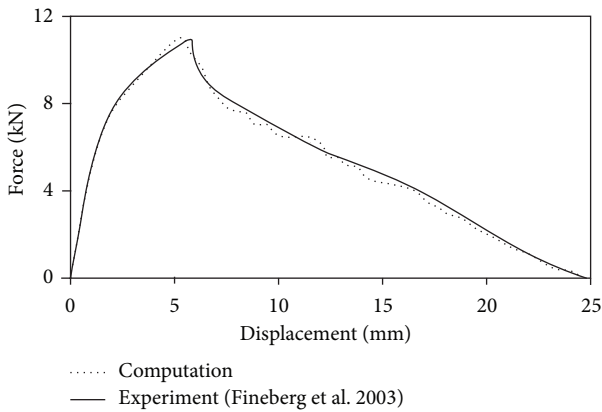


FIGURE 13: Comparison of the load deflection curve between the experimental data [24] and computational results.

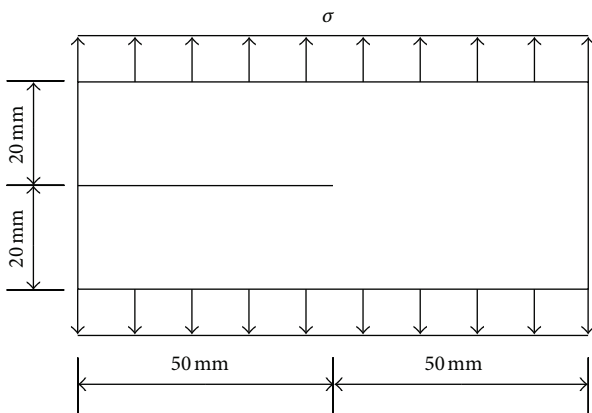


FIGURE 14: Plate with an initial notch under tensile stress.

both the top and bottom edges as a step function in time. We discretized the domain with 100×51 uniform quadrilateral elements and used explicit time integration with a Courant number of 0.1. Material softening is modeled with a Lemaitre

damage law [32] and a linear cohesive law was imposed once a discontinuity developed. To capture the crack branching phenomena, we monitored the maximum principal stress criterion at several additional points around the crack tip. If the Lemaitre damage criterion is satisfied and the maximum principal directions show relatively different crack growth angles, we initiate crack branches.

The pattern of multiple crack branchings with damage evolution is shown in Figure 15. The numerical simulation is executed until one of the crack tips reaches the boundary of the specimen: $t = 56.02 \mu\text{s}$. The maximum crack tip speed is around 1250 m/s and the Rayleigh wave speed is 2100 m/s. The overall dynamic crack branching pattern agrees with the results which were already reported by Rabczuk and Belytschko [31].

5.4. Thick Cylinder under Internal Pressure. We consider a thick cylinder under high internal pressure. The inner and outer radii of the cylinder are 80 mm and 150 mm, respectively. An internal pressure, $p = p_0 e^{-t/t_0}$, is applied with $p_0 = 10 \text{ GPa}$ and $t_0 = 0.1 \text{ ms}$. The material properties are $\rho = 7800 \text{ kg/m}^3$, $E = 210 \text{ GPa}$, and $\nu = 0.30$. Also, we induced a $\pm 5\%$ perturbation to the elastic modulus to introduce some asymmetry for initiating the cracks. We modeled the thick cylinder with 20,000 uniform quadrilateral elements.

Because of the high internal pressure, the fragmentation process occurs only in the first $5.0 \mu\text{s}$; then each fragments moves outward in the radial direction with no further cracks initiating. Figure 16 shows the magnified deformed mesh at different time steps. In this simulation, we obtained 6 relatively big fragments and 10 strip shape fragments; for a clear illustration of the fragments, see Figure 17.

This overall pattern of cylinder fragmentation is similar to that already reported by Rabczuk and Belytschko [31]. However, the finite element simulation shown here does not exhibit the small fragments seen in [31]. It is also found that the reduced 4-node quadrilateral finite element with the hourglass control scheme is quite sensitive to mesh distortion; it would be desirable to use the smoothed finite elements

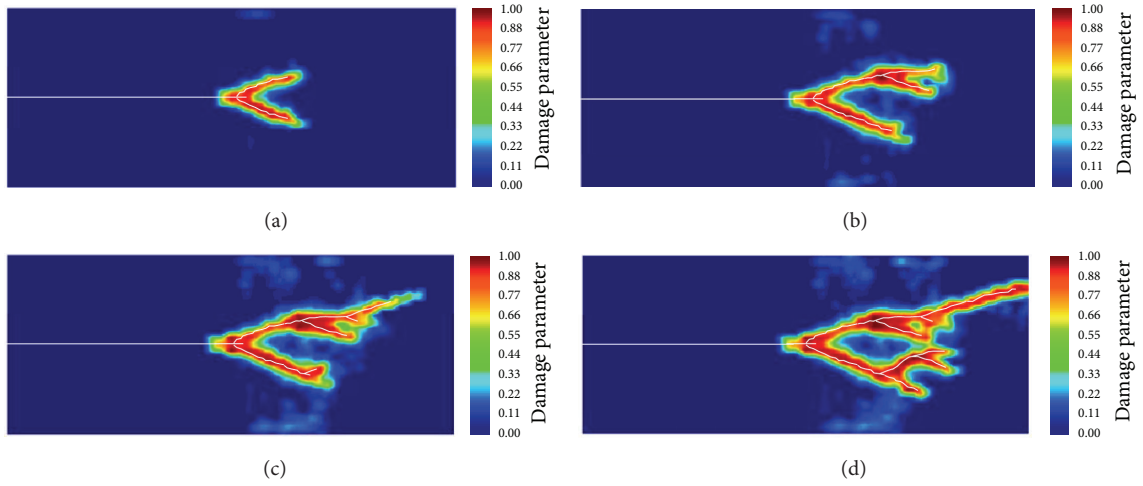


FIGURE 15: The pattern of crack branching and damage evolution at different time steps: (a) $t = 30.14 \mu\text{s}$, (b) $t = 45.24 \mu\text{s}$, and (c) $t = 56.02 \mu\text{s}$.

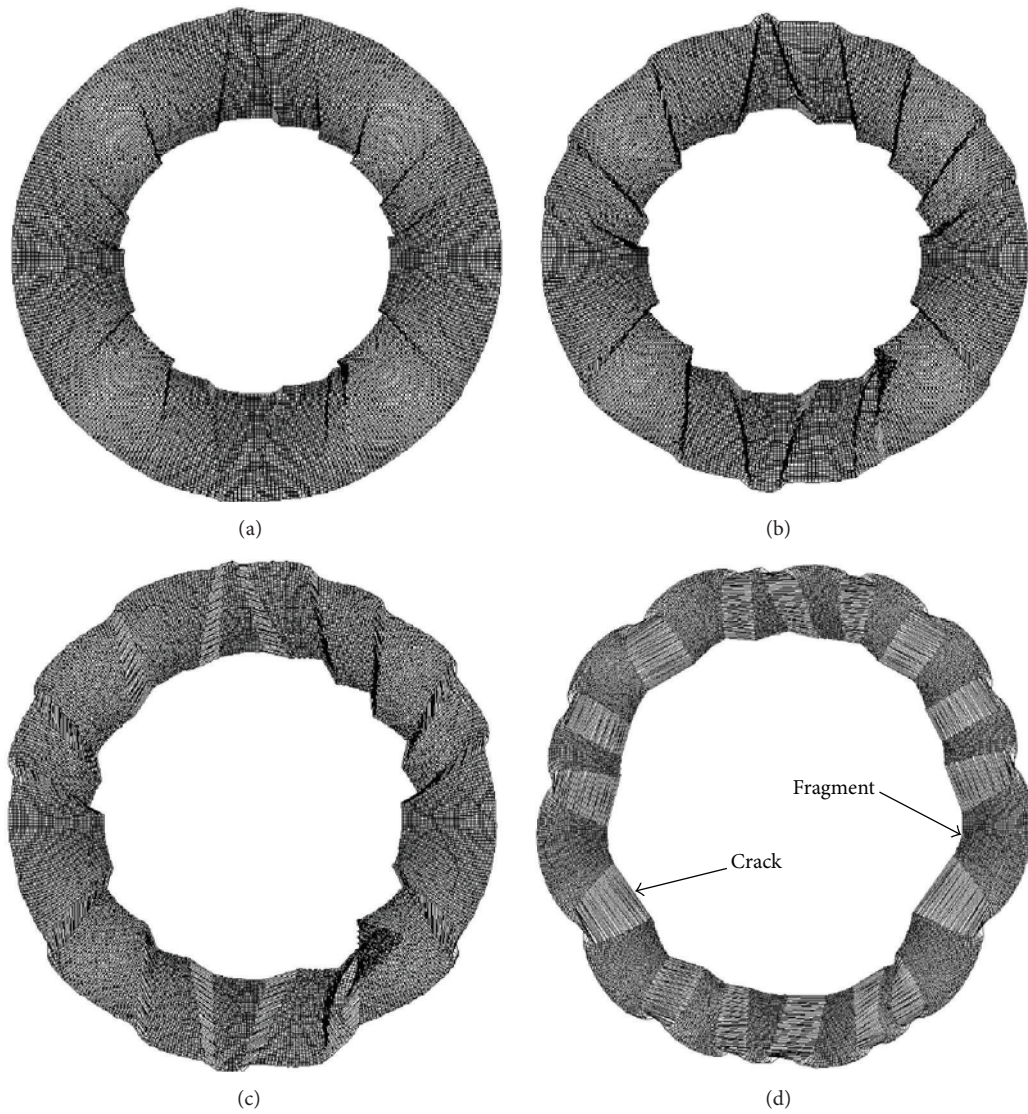


FIGURE 16: Deformed shape of the thick cylinder under internal pressure at different time steps: (a) $t = 1.78 \mu\text{s}$, (b) $t = 3.42 \mu\text{s}$, (c) $t = 6.40 \mu\text{s}$, and (d) $t = 13.50 \mu\text{s}$; the long elements are cracked as indicated in (d).

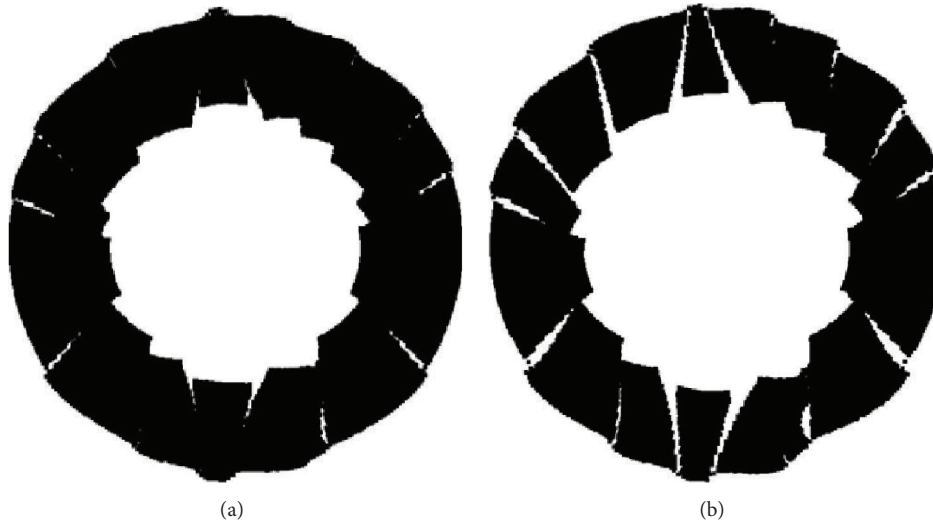


FIGURE 17: Shape of the fragments of the thick cylinder under internal pressure at different time steps: (a) $t = 3.72 \mu\text{s}$ and (b) $t = 6.71 \mu\text{s}$.

[33] or the method proposed by Areias and Rabczuk [34] for this type of simulations, that is, problems with severe mesh distortion.

6. Conclusion

A numerical method for the simulation of the dynamic propagation of multiple cracks is presented. The method employs the phantom node method with a one point integration scheme. Though the phantom node method is another form of the standard XFEM, it provides us with a simple implementation within the framework of the standard FEM. Also, by using one point integration with hourglass control, we can decrease the computational cost and circumvent the subdomain integration which is generally used for cracked elements. Moreover a correction force can handle the progressive opening of the crack tip element due to the crack propagation, and this improves the results in terms of stress intensity factors. To evaluate the applicability of the proposed method, several numerical examples which have a certain complexity in the representation of crack geometry have been analyzed. The smooth crack propagation obtained with a correction force is first checked from an energy point of view. Then the accuracy of the method is shown by computing the stress intensity factors for a dynamic mode I crack propagation. The simulation of a compact tension specimen with a stiffener is in good agreement with the experiment observations. We simulated a dynamic multiple crack branching problem and found that the method is particularly successful in this type of simulations. In the simulation of a multiple crack propagation problem, the numerical example shows that the proposed model can simulate the growth, interconnection and, finally, failure of a plate containing multiple cracks. Also, the simulation of a fragment processes is quite effectively analyzed. An attractive feature of this method is its low computational cost and

simplicity within the context of the conventional explicit finite element method.

Conflict of Interests

The authors declare that there is no conflict of interests regarding the publication of this paper.

Acknowledgment

The support of the Office of Naval Research under Grants N00014-13-1-0386 and N00014-11-1-0925 are gratefully acknowledged.

References

- [1] T. Belytschko and T. Black, "Elastic crack growth in finite elements with minimal remeshing," *International Journal for Numerical Methods in Engineering*, vol. 45, no. 5, pp. 601–620, 1999.
- [2] N. Moës, J. Dolbow, and T. Belytschko, "A finite element method for crack growth without remeshing," *International Journal for Numerical Methods in Engineering*, vol. 46, no. 1, pp. 131–150, 1999.
- [3] C. Daux, N. Moës, J. Dolbow, N. Sukumar, and T. Belytschko, "Arbitrary branched and intersecting cracks with the extended finite element method," *International Journal for Numerical Methods in Engineering*, vol. 48, no. 12, pp. 1741–1760, 2000.
- [4] P. M. A. Areias and T. Belytschko, "Analysis of three-dimensional crack initiation and propagation using the extended finite element method," *International Journal for Numerical Methods in Engineering*, vol. 63, no. 5, pp. 760–788, 2005.
- [5] Q. Duan, J. H. Song, T. Menouillard, and T. Belytschko, "Element-local level set method for three-dimensional dynamic crack growth," *International Journal for Numerical Methods in Engineering*, vol. 80, no. 12, pp. 1520–1543, 2009.

- [6] G. Zi and T. Belytschko, "New crack-tip elements for XFEM and applications to cohesive cracks," *International Journal for Numerical Methods in Engineering*, vol. 57, no. 15, pp. 2221–2240, 2003.
- [7] P. M. A. Areias, J. H. Song, and T. Belytschko, "Analysis of fracture in thin shells by overlapping paired elements," *Computer Methods in Applied Mechanics and Engineering*, vol. 195, no. 41–43, pp. 5343–5360, 2006.
- [8] T. Belytschko, H. Chen, J. Xu, and G. Zi, "Dynamic crack propagation based on loss of hyperbolicity and a new discontinuous enrichment," *International Journal for Numerical Methods in Engineering*, vol. 58, no. 12, pp. 1873–1905, 2003.
- [9] X.P. Xu and A. Needleman, "Numerical simulations of fast crack growth in brittle solids," *Journal of the Mechanics and Physics of Solids*, vol. 42, no. 9, pp. 1397–1434, 1994.
- [10] M. Ortiz and A. Pandolfi, "Finite-deformation irreversible cohesive elements for three-dimensional crack-propagation analysis," *International Journal for Numerical Methods in Engineering*, vol. 44, no. 9, pp. 1267–1282, 1999.
- [11] E. A. Repetto, R. Radovitzky, and M. Ortiz, "Finite element simulation of dynamic fracture and fragmentation of glass rods," *Computer Methods in Applied Mechanics and Engineering*, vol. 183, no. 1-2, pp. 3–14, 2000.
- [12] F. Cirak, M. Ortiz, and A. Pandolfi, "A cohesive approach to thin-shell fracture and fragmentation," *Computer Methods in Applied Mechanics and Engineering*, vol. 194, no. 21-24, pp. 2604–2618, 2005.
- [13] J.-H. Song, H. Wang, and T. Belytschko, "A comparative study on finite element methods for dynamic fracture," *Computational Mechanics*, vol. 42, no. 2, pp. 239–250, 2008.
- [14] J. H. Song, P. M. A. Areias, and T. Belytschko, "A method for dynamic crack and shear band propagation with phantom nodes," *International Journal for Numerical Methods in Engineering*, vol. 67, no. 6, pp. 868–893, 2006.
- [15] T. Menouillard and T. Belytschko, "Correction Force for releasing crack tip element with XFEM and only discontinuous enrichment," *European Journal of Computational Mechanics*, vol. 18, no. 5-6, pp. 465–483, 2009.
- [16] T. Menouillard, J. Réthoré, A. Combescure, and H. Bung, "Efficient explicit time stepping for the extended finite element method (X-FEM)," *International Journal for Numerical Methods in Engineering*, vol. 68, no. 9, pp. 911–939, 2006.
- [17] T. Menouillard, J. Réthoré, N. Moës, A. Combescure, and H. Bung, "Mass lumping strategies for X-FEM explicit dynamics: application to crack propagation," *International Journal for Numerical Methods in Engineering*, vol. 74, no. 3, pp. 447–474, 2008.
- [18] A. Hansbo and P. Hansbo, "A finite element method for the simulation of strong and weak discontinuities in solid mechanics," *Computer Methods in Applied Mechanics and Engineering*, vol. 193, no. 35, pp. 3523–3540, 2004.
- [19] J. H. Song and T. Belytschko, "Dynamic fracture of shells subjected to impulsive loads," *Journal of Applied Mechanics, Transactions of ASME*, vol. 76, Article ID 051301, 2009.
- [20] G. Ventura, J. X. Xu, and T. Belytschko, "A vector level set method and new discontinuity approximations for crack growth by EFG," *International Journal for Numerical Methods in Engineering*, vol. 54, no. 6, pp. 923–944, 2002.
- [21] G. Ventura, E. Budyn, and T. Belytschko, "Vector level sets for description of propagating cracks in finite elements," *International Journal for Numerical Methods in Engineering*, vol. 58, no. 10, pp. 1571–1592, 2003.
- [22] K. Ravi-Chandar, *Dynamic Fracture*, Elsevier Science, New York, NY, USA, 2004.
- [23] L. B. Freund, *Dynamic Fracture Mechanics*, Cambridge University Press, Cambridge, UK, 1990.
- [24] K. P. Galanis, *Fracture of aluminum naval structures [Ph.D. thesis]*, Massachusetts Institute of Technology, 2007.
- [25] K. P. Galanis and V. J. Papazoglou, "Effect of stiffening configurations on fracture of aluminium structures," *Strain*, vol. 45, no. 2, pp. 131–138, 2009.
- [26] M. Ramulu and A. S. Kobayashi, "Mechanics of crack curving and branching—a dynamic fracture analysis," *International Journal of Fracture*, vol. 27, no. 3-4, pp. 187–201, 1985.
- [27] E. Sharon, S. P. Gross, and J. Fineberg, "Local crack branching as a mechanism for instability in dynamic fracture," *Physical Review Letters*, vol. 74, no. 25, pp. 5096–5099, 1995.
- [28] E. Sharon and J. Fineberg, "Microbranching instability and the dynamic fracture of brittle materials," *Physical Review B*, vol. 54, no. 10, pp. 7128–7139, 1996.
- [29] K. Ravi-Chandar, "Dynamic fracture of nominally brittle materials," *International Journal of Fracture*, vol. 90, no. 1-2, pp. 83–102, 1998.
- [30] J. Fineberg, E. Sharon, and G. Cohen, "Crack front waves in dynamic fracture," *International Journal of Fracture*, vol. 119, no. 3, pp. 247–261, 2003.
- [31] T. Rabczuk and T. Belytschko, "Cracking particles: a simplified meshfree method for arbitrary evolving cracks," *International Journal for Numerical Methods in Engineering*, vol. 61, no. 13, pp. 2316–2343, 2004.
- [32] J. Lemaitre and J. L. Chaboche, *Mechanics of Solid Materials*, Cambridge University Press, Cambridge, UK, 1990.
- [33] N. Nguyen-Thanh, T. Rabczuk, H. Nguyen-Xuan, and S. P. A. Bordas, "A smoothed finite element method for shell analysis," *Computer Methods in Applied Mechanics and Engineering*, vol. 198, no. 2, pp. 165–177, 2008.
- [34] P. Areias and T. Rabczuk, "Finite strain fracture of plates and shells with configurational forces and edge rotation," *International Journal For Numerical Methods in Engineering*, vol. 94, no. 12, pp. 1099–1122, 2013.

Research Article

Explicit Dynamic Finite Element Method for Predicting Implosion/Explosion Induced Failure of Shell Structures

Jeong-Hoon Song,¹ Patrick Lea,² and Jay Oswald³

¹ Department of Civil and Environmental Engineering, University of South Carolina, Columbia, SC 29208, USA

² Theoretical and Applied Mechanics, Northwestern University, Evanston, IL 60208, USA

³ School for Engineering of Matter, Transport and Energy, Arizona State University, Tempe, AZ 85287, USA

Correspondence should be addressed to Jeong-Hoon Song; jhsong@cec.sc.edu

Received 30 July 2013; Accepted 3 September 2013

Academic Editor: Timon Rabczuk

Copyright © 2013 Jeong-Hoon Song et al. This is an open access article distributed under the Creative Commons Attribution License, which permits unrestricted use, distribution, and reproduction in any medium, provided the original work is properly cited.

A simplified implementation of the conventional extended finite element method (XFEM) for dynamic fracture in thin shells is presented. Though this implementation uses the same linear combination of the conventional XFEM, it allows for considerable simplifications of the discontinuous displacement and velocity fields in shell finite elements. The proposed method is implemented for the discrete Kirchhoff triangular (DKT) shell element, which is one of the most popular shell elements in engineering analysis. Numerical examples for dynamic failure of shells under impulsive loads including implosion and explosion are presented to demonstrate the effectiveness and robustness of the method.

1. Introduction

In this work, we describe a method for modeling fractured discrete Kirchhoff triangular (DKT) shell elements [1] based on the extended finite element method (XFEM) [2, 3]. One of the underlying key concepts in the XFEM is the partition of unity approach [4, 5]. In the partition of unity approach, the approximation basis is spanned by the standard finite element approximation space and extended by the products of the standard finite element shape functions with special local characteristic functions which are constructed from knowledge about the solution. The XFEM has since been developed for two-dimensional dynamic fracture problems [6, 7], static shell fractures [8], and implicit dynamic shell fracture problems [9].

Even though numerous references are available for continuum shell elements, the literature on dynamic crack propagation in shells is quite limited. Cirak et al. [10, 11] have developed a method for dynamic crack propagation in Kirchhoff type shells based on interelement cohesive crack methods [12–14]; in the interelement cohesive crack methods, the crack is limited to propagation along the element edges with local remeshing.

Mehra and Chaturvedi [15] used the smooth particle hydrodynamics (SPH) method for simulations of tearing of thick plates. Combescure et al. [16] and Maurel and Combescure [17] recently developed SPH shell formulations for explicit dynamic method and successfully applied the method to the prediction of dynamic fractures in shell structures.

The described implementation scheme is mainly based on the XFEM, but its actual implementation follows the phantom node method [7, 18] that has been developed by the author of this paper. In this approach [7, 18], the element which contains the crack is replaced by two superposed elements with additional nodes. Though this discontinuity representation scheme uses the same linear combination of enrichment functions as the conventional XFEM, it allows for considerable simplifications in fractured thin shell element formalisms and furthermore is applicable to arbitrary large deformations.

An elementwise progression of the crack is also employed; that is, the crack tip is always on an element edge. The elementwise crack propagation scheme may cause some noise during the crack propagation with coarse meshes. However, in Song et al. [7], it is shown that such noise diminishes with

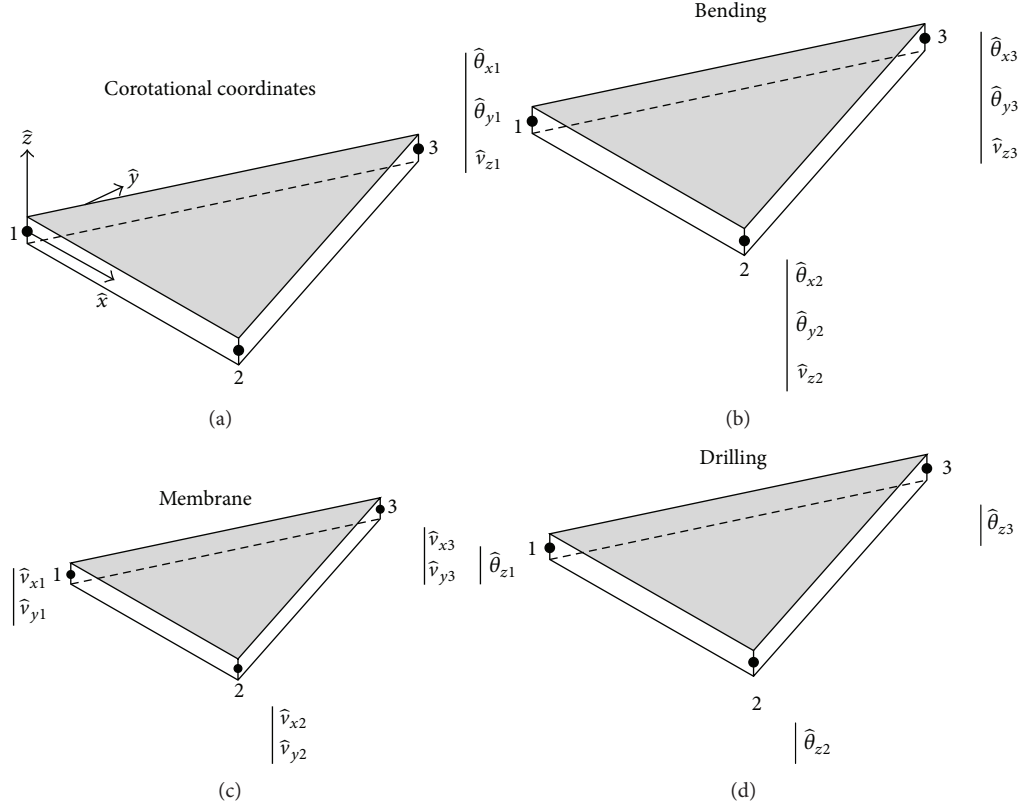


FIGURE 1: Kinematic data of the DKT triangular element: (a) the corotational coordinates, (b) the bending degrees of freedom, (c) the in-plane membrane degrees of freedom, and (d) the drilling degrees of freedom.

mesh refinements, and the crack propagation speeds converge to the progressive crack propagation results [6, 19, 20].

2. Discrete Kirchhoff Triangular Shell Element

The main advantage of the DKT shell element is that a mesh can easily be generated from any kind of surfaces. The geometry of the element is described by three linear shape functions in the reference coordinates. The kinematic of the DKT shell elements is described by superimposing the membrane, the bending, and the rotational (drilling) behavior of shells with different corresponding degrees of freedoms (DOFs) as shown in Figure 1.

However, for further explanation on the salient features of the DKT element, henceforth, we will use β instead of θ for the rotation as shown in Figure 2; note that this is only for a clear illustration purpose. In this notation, β_x is the rotation whose displacement is along the axis x .

The discrete Kirchhoff assumption [1] is the following: the normal rotations must be equal to the first derivative of the transverse displacement. These constraints are imposed at a discrete number of points, which leads to the relation between the normal rotations and the displacements at the element joints. Let us consider the constraints in terms of x and y directions as

$$\begin{aligned} \beta_x(\xi) + w_x &= 0, \\ \beta_y(\xi) + w_y &= 0, \end{aligned} \quad (1)$$

where $\beta_x = \theta_y$ and $\beta_y = -\theta_x$. This sign difference is due to the orientation of the rotation, which will generate in-plane displacements. However, with a linear discretization, these conditions cannot be verified within the entire domain of the shell finite element. One alternative approach is that they can be only verified at some discrete parts of the shell elements, such as a midpoint of each side of the DKT elements; this is the implication of the discrete Kirchhoff assumption in the DKT shell elements.

To verify the discrete Kirchhoff assumption, one has to add additional shape functions which do not change the nodal values of any field but only are allowed to modify the values on the midpoint. Thus, the rotational DOFs are discretized by

$$\beta_x = \sum_{i=1}^3 N_i \cdot \beta_{xi} + \sum_{i=4}^6 P_i \cdot C_i \cdot \alpha_i, \quad (2)$$

$$\beta_y = \sum_{i=1}^3 N_i \cdot \beta_{yi} + \sum_{i=4}^6 P_i \cdot S_i \cdot \alpha_i. \quad (3)$$

As shown in Figure 3, the discrete Kirchhoff constraints along each side $i-j$ are introduced at the midpoint k :

$$\beta_s(\xi) + w_s = 0, \quad (4)$$

where s is the absciss along the side of the element.

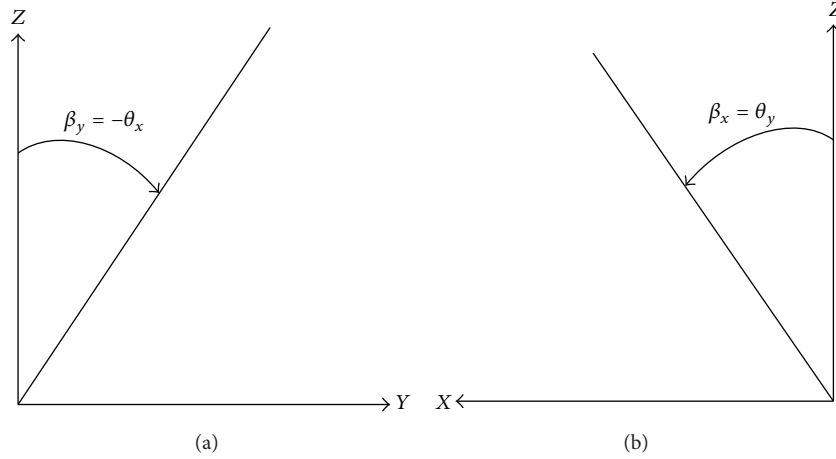
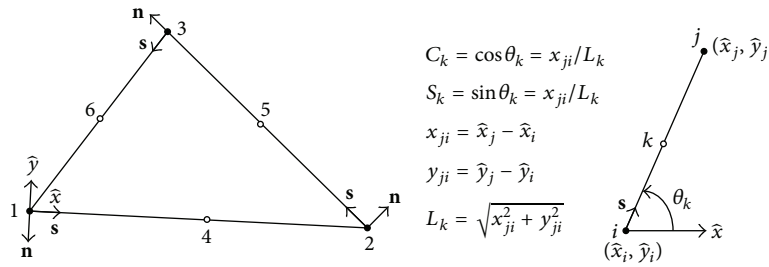

 FIGURE 2: Positive directions of β_x and β_y and correspondence between the rotations θ_x and θ_y and β_x and β_y .


FIGURE 3: Geometry and local tangential-normal coordinate system of the DKT element.

The different functions P_i appearing in (2) and (3) are given by

$$P_4 = 4(1 - \xi - \eta)\xi, \quad (5)$$

$$P_5 = 4\eta\xi, \quad (6)$$

$$P_6 = 4(1 - \xi - \eta)\eta. \quad (7)$$

Note that, in (2) and (3), C and S define cosinus and sinus values of the current geometry in the reference coordinates as shown in Figure 4. The particular values for the reference triangular element are $C_4 = 1$, $S_4 = 0$, $C_5 = -\sqrt{2}/2$, $S_5 = \sqrt{2}/2$, $C_6 = 0$, and $S_6 = -1$. These values are the cosinus and sinus of the vector representing the side of the reference triangular element. Thus, for example, at the node 4 in Figure 3, we can show that x is the same in terms of substituting (2) and (4). Furthermore, for this particular edge that has the midpoint at $(0, 1/2)$, we could further develop the following relation:

$$\begin{aligned} -w_s &= \beta_s \left(\frac{1}{2}, 0 \right) \\ &= \beta_x \left(\frac{1}{2}, 0 \right) = \frac{\beta_{x1} + \beta_{x2}}{2} + \alpha_4 \quad (8) \\ &= -w_x = -\frac{w_2 - w_1}{2}. \end{aligned}$$

So, the expression of α_4 is given as

$$\alpha_4 = w_1 - w_2 - \frac{\beta_{x1}}{2} - \frac{\beta_{x2}}{2}. \quad (9)$$

Similarly, we can determine the other unknowns α_5 and α_6 as

$$\alpha_6 = w_1 - w_3 - \frac{\beta_{y1}}{2} - \frac{\beta_{y3}}{2}, \quad (10)$$

$$\alpha_5 = -\sqrt{2}w_3 + \sqrt{2}w_2 + \frac{\sqrt{2}}{4}(\beta_{x2} + \beta_{x3} - \beta_{y2} - \beta_{y3}).$$

However, the other three unknowns α_4 , α_5 , and α_6 in the formalism of the rotation should be determined by solving system equations given by

$$4 \cdot \begin{bmatrix} 1 - 2\xi - \eta & -\frac{\sqrt{2}}{2}\eta & 0 \\ 0 & \frac{\sqrt{2}}{2}\xi & \xi + 2\eta - 1 \\ -\frac{\xi}{2} & \frac{\sqrt{2}}{4}(\eta - \xi) & \frac{\eta}{2} \end{bmatrix} \cdot \begin{bmatrix} \alpha_4 \\ \alpha_5 \\ \alpha_6 \end{bmatrix} = \begin{bmatrix} \beta_{x,x} \\ \beta_{y,y} \\ \frac{1}{2}(\beta_{x,y} + \beta_{y,x}) \end{bmatrix}. \quad (11)$$

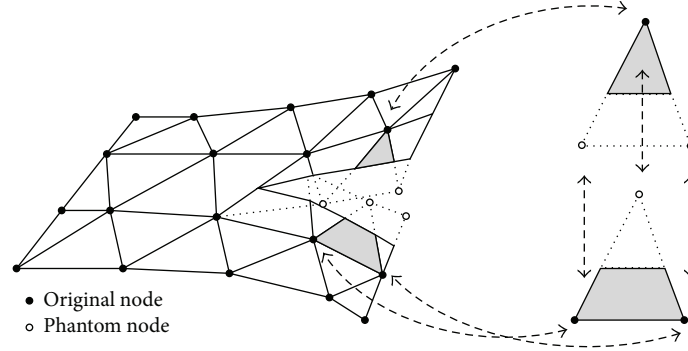


FIGURE 4: Representation of the crack by the XFEM and the phantom node method with DKT elements.

Throughout this procedure, that is, determining three unknowns α_4 , α_5 , and α_6 , the Kirchhoff assumption is enforced in the middle of each side of the shell element. Note that the nodal value is still intact because of the shape functions P_i which are zero at the nodes.

3. Representation of Fractured Shell Element

Based on the phantom node approach [7, 18], the DKT shell element which contains a crack is replaced by two superposed DKT elements with additional phantom nodes as shown in Figure 4.

As with the standard approach to phantom nodes [7, 18], cracks will be inserted elementwise at propagation and the crack surface will be limited to normal to the shells midsurface. While the equations here will be for the phantom node method, the equivalence between phantom node method and XFEM is shown by Song et al. [7].

The discontinuous velocity fields in the midsurface of the fractured shell elements can be described by

$$\begin{aligned} \mathbf{v}_{\text{mid}} = & \sum_{i=1}^3 N_i (H(-f(\mathbf{x}, t))) \mathbf{v}_i \\ & + \sum_{j=1}^3 N_j (H(f(\mathbf{x}, t))) \mathbf{v}_j, \end{aligned} \quad (12)$$

where i and j are the first and second halves of the pair of overlapping element, respectively, $f(\mathbf{x})$ is an implicit function that can describe the geometry of the crack surface in the midsurface of the shell with iso-zero line, that is; crack path in the midsurface of shell can be represented by $f(\xi) = 0$, and $H(x)$ is the step function given by

$$H(x) = \begin{cases} 1, & x \geq 0, \\ 0, & x < 0. \end{cases} \quad (13)$$

The velocity fields can also be expressed in corotational coordinates as is common in shell, but we have omitted it for

brevity. The velocity equation for the DKT shells does not vary from that of the other shell elements but the rotations do. Keeping with the notation from the last section the rotations in x and y can be expressed as

$$\begin{aligned} \beta_x = & \sum_{i=1}^3 N_i (H(-f(\mathbf{x}, t))) \beta_{xi} \\ & + \sum_{i=4}^6 P_i (H(-f(\mathbf{x}, t))) C_i \cdot \alpha_i \\ & + \sum_{j=1}^3 N_j (H(-f(\mathbf{x}, t))) \beta_{xj} \\ & + \sum_{j=4}^6 P_j (H(-f(\mathbf{x}, t))) C_j \cdot \alpha_j, \end{aligned} \quad (14)$$

$$\begin{aligned} \beta_y = & \sum_{i=1}^3 N_i (H(-f(\mathbf{x}, t))) \beta_{yi} \\ & + \sum_{i=4}^6 P_i (H(-f(\mathbf{x}, t))) S_i \cdot \alpha_i \\ & + \sum_{j=1}^3 N_j (H(-f(\mathbf{x}, t))) \beta_{yj} \\ & + \sum_{j=4}^6 P_j (H(-f(\mathbf{x}, t))) S_j \cdot \alpha_j, \end{aligned} \quad (15)$$

where again an overlapping pair (elements i and j) is used. One advantage of using the phantom node method with DKT shells is that the procedure for finding α 's does not need to be varied from the standard method. This greatly simplifies the implementation of the XFEM for DKT elements, leaving (5)–(11) unchanged.

4. Computation Procedures

4.1. Time Integration: Newmark Scheme. In this work, Newmark scheme for the explicit time integration is used. The time integration procedure is written as

$$U_{t+\Delta t} = U_t + \Delta t \cdot \dot{U}_t + \frac{\Delta t^2}{2} \ddot{U}_t, \quad (16)$$

$$\dot{U}_{t+\Delta t} = \dot{U}_t + \frac{1}{2} \Delta t (\ddot{U}_t + \ddot{U}_{t+\Delta t}), \quad (17)$$

$$M \cdot \ddot{U}_{t+\Delta t} = F_{\text{ext}} - F_{\text{int}}, \quad (18)$$

where U_t (\dot{U}_t and \ddot{U}_t , resp.) denotes the displacement (velocity and acceleration, resp.) at time t . Δt is the time integration step, M is the mass matrix, and F_{ext} (F_{int} , resp.) is the external (internal, resp.) forces at time t .

A diagonal mass matrix is frequently used in this explicit time integration scheme because it allows us to avoid a matrix inversion for solving (14); that is, no matrix inversion appears in this scheme. Consequently, the main advantage of using explicit time integration scheme is to speed up the computation and use less memory by storing only vectors instead of matrices to the computer.

However, this explicit integration scheme is conditionally stable, and the stability condition is defined in terms of a maximum time step Δt_c ; we usually name it a critical time step since it is the largest time step that can be used. The critical time step is evaluated from the eigenvalue analysis with the mass M and stiffness matrix K since

$$\Delta t_c = \frac{2}{\omega_{\text{max}}}, \quad (19)$$

where ω_{max} is the maximum frequency determined by solving eigenvalue of problems in (16):

$$\det(K - \omega^2 M) = 0. \quad (20)$$

The stability of explicit time integration for the XFEM is defined by the same condition on the mass and the stiffness; the computation frequency must be greater than the greatest vibration frequency of the structure.

4.2. Computation of Lumped Mass Matrix for Cracked Elements. In the explicit dynamic analysis method, constructions of lumped mass are essential to ensure the computation of nodal accelerations without implicit solution procedures. However, the mass lumping scheme for cracked elements which employ the XFEM approach is not obvious. To circumvent such difficulties, several methods have been proposed: implicit (in cracked elements)-explicit (in continuum elements) time integration scheme [6] and modified mass lumping schemes [21, 22].

In this study, the lumped mass for regular DOFs is diagonalized by the conventional row sum mass lumping technique, but, for the cracked elements, we used the mass lumping scheme that was proposed by Menouillard et al. [22]. Thus, the diagonal term i of the mass corresponding to the

enriched DOFs also depends on the enrichment function H as follows:

$$M_i = \frac{m}{n_{\text{node}}} \frac{1}{\|\Omega_e\|} \int_{\Omega} H^2 d\Omega_e, \quad (21)$$

where m is the total actual mass of the element, n_{node} is the number of nodes of the element, and $\|\Omega_e\|$ is the measure of the finite element domain Ω_e . For the particular case of discontinuous enriched functions such as Heaviside function, the term of the mass matrix corresponding to an enriched node is in fact just a fraction of the regular finite element term; in other words, the lumped mass matrix for the enriched nodes is written as follows:

$$M_i = \frac{m}{n_{\text{node}}} \frac{A_i}{A}, \quad (22)$$

where A is the volume or area of the regular element and A_i represents the fraction ratio of the cut element. One imperative advantage of this mass lumping scheme is that this method does not significantly decrease the critical time step of the continuum element [22].

5. Material Model and Modeling of Fracture

5.1. Damage Plasticity Model. A damage plasticity model that can account for the effects of stress triaxiality and Lode angle was proposed by Xue [23] and Xue and Wierzbicki [24]. In this constitutive model, damage of a material point is accessed by measuring the accumulation of the following damage increment:

$$dD = m \left(\frac{\varepsilon_p}{\varepsilon_f} \right)^{m-1} \frac{d\varepsilon_p}{\varepsilon_f}, \quad (23)$$

where D is damage parameter, ε_p is the plastic strain, ε_f is a reference strain envelope, and m is a material constant. The reference strain envelope is a function of the pressure and the Lode angle:

$$\varepsilon_f = \varepsilon_{f0} \mu_p(p) \mu_{\theta}(\theta_L), \quad (24)$$

where ε_{f0} is the initial reference strain, p is the pressure, and θ_L is the Lode angle. The functions μ_p and μ_{θ} are defined as

$$\begin{aligned} \mu_p(p) &= 1 - q \log \left(1 - \frac{p}{p_{\text{lim}}} \right), \\ \mu_{\theta}(\theta_L) &= \gamma + (1 - \gamma) \left(\frac{6|\theta_L|}{\pi} \right)^k, \end{aligned} \quad (25)$$

where q and p_{lim} are material constants and γ and k are parameters determining the shape of the strain envelope. The weakening effect caused by the damage was also considered in this model:

$$\sigma = w(D) \sigma_M = (1 - D^{\beta}) \sigma_M, \quad (26)$$

where σ_M is the stress of the undamaged material, $w(D)$ is the weakening function, and β is another material constant.

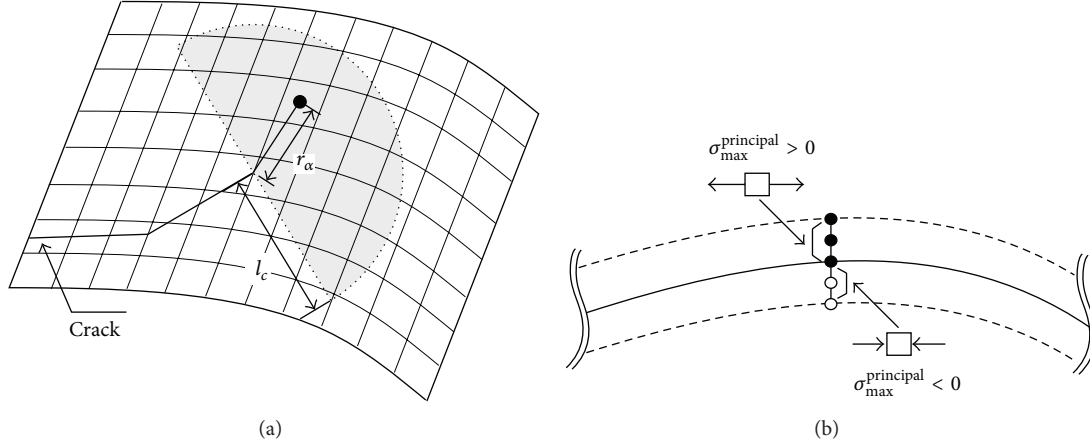


FIGURE 5: Schematic of averaging domain for the evaluation of the fracture criterion: (a) the size of averaging domain and (b) possible principal stress states through the shell depth.

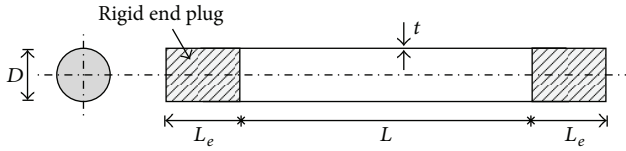


FIGURE 6: Setup for implosion induced failure of cylinder.

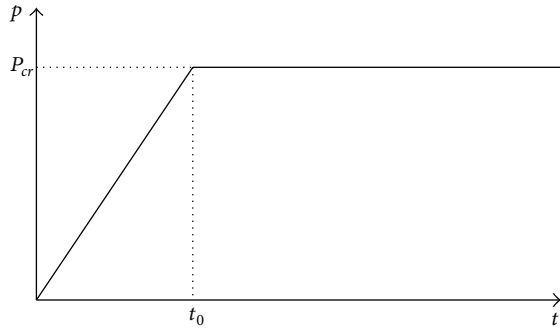


FIGURE 7: Loading curve used in the simulation of Texas experiments.

5.2. Fracture Criterion. A critical strain based fracture criterion is used to determine the onset point of a poststrain localization behavior of a material, that is, fracture. When the strain at a crack tip material point reaches a fracture threshold, we inject a strong discontinuity ahead of the previous crack tip according to maximum principle tensile strain direction of an averaged strain $\boldsymbol{\varepsilon}^{\text{avg}}$. For the computation of the averaged strain, $\boldsymbol{\varepsilon}^{\text{avg}}$, we used a pointwise weighted averaging scheme which is given by

$$\boldsymbol{\varepsilon}^{\text{avg}} = \frac{\sum_{\alpha} w(r_{\alpha}) \boldsymbol{\varepsilon}_{\alpha}}{\sum_{\alpha} w(r_{\alpha})}, \quad (27)$$

where $w(r)$ is the cubic spline weight function, r_{α} is the distance from the crack tip to the material points α , r_c ($\approx 3h_e$) is the size of the averaging domain, and h_e is the size of the crack

tip element; see Figure 5. Note that, for the computation of the averaged strain $\boldsymbol{\varepsilon}^{\text{avg}}$, we only included material points which show tension dominant states as shown in Figure 5(b).

5.3. Dissipation of Fracture Energy. In this study, a cohesive crack model is prescribed along the newly injected strong discontinuity surfaces until the crack opening is fully developed, that is, until cohesive traction has vanished. The roles of a prescribed cohesive model can be summarized as follows.

- (1) It can be a remedy to spurious mesh-dependent pathological behaviors by providing a bounded solution at the crack tip. For linear elastic fracture simulations, if the crack tip is not smoothly closed with cohesive forces, finite element solutions are unbounded at the crack tip due to the crack tip stress singularity and a crack path is determined by the surrounding mesh resolution. Also, for fracture in plastic bulk materials, the crack tip stress singularity can be slightly alleviated by plasticity. However, the finite element solutions still depend on the mesh resolution.
- (2) If the crack opening displacement is not governed by a cohesive model, the normal stress component to the crack surface suddenly drops to zero due to lack of fracture energy dissipations; note that injecting a strong discontinuity without prescribing cohesive force is the same as creating two free surfaces without dissipating new surface initiation energies. In this case, the total system suffers from an excessive accumulation of elastic energy and this excessively accumulated energy accelerates the crack propagation speed; more discussions on the relationship between crack propagation speed and dissipated fracture energy can be found in Rabczuk et al. [27].

In this study, we only prescribe the normal traction of a linear cohesive model since the early stage of crack initiation due to implosion or explosion is mostly due to mode I fracture behavior.

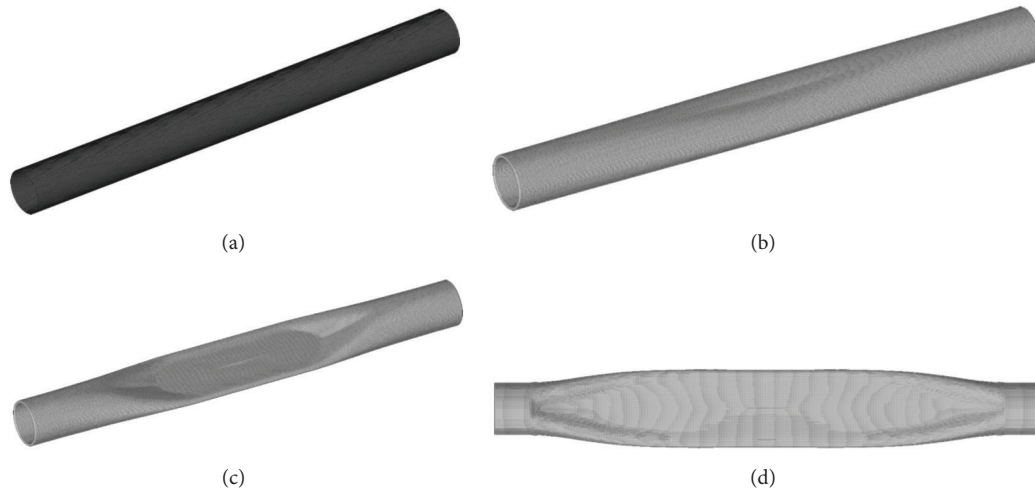


FIGURE 8: Snapshots of numerical results of IMP26 experiment: (a) initial configuration and the mesh, (b) deformed configuration at time $t = 1.48$ ms; the center of the cylinder begins to collapse, (c) deformed configuration at time $t = 1.78$ ms; buckling region enlarges toward the two ends, and (d) final deformed configuration; the cylinder buckles in mode 2.

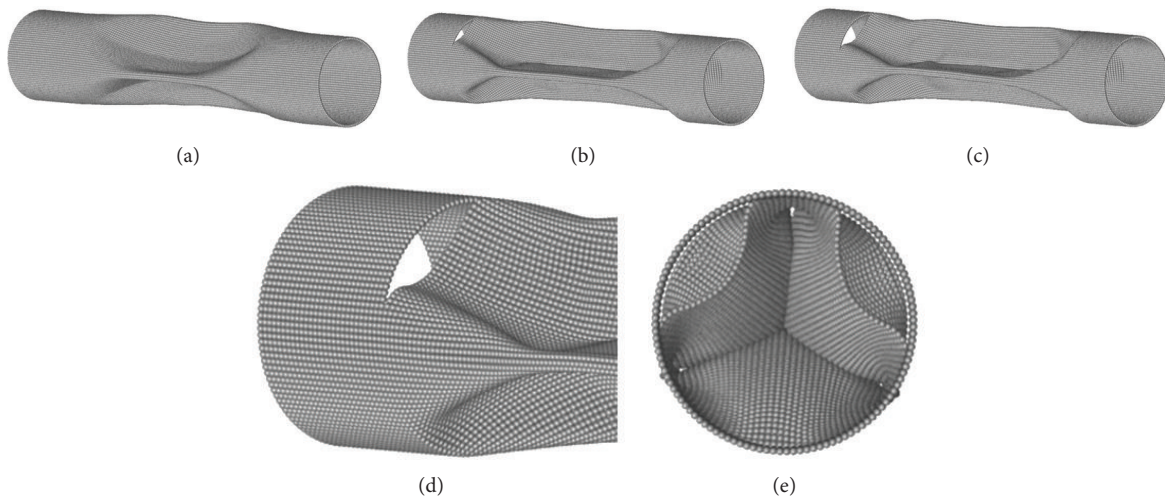


FIGURE 9: Snapshots of numerical results of IMP25 experiment: (a) deformed configuration at time $t = 0.92$ ms; cylinder collapses at mode 3, (b) deformed configuration at time $t = 1.08$ ms; cracks initiated at the two ends, (c) the final deformed configuration, (d) local zoom view of the crack, and (e) view from the axial direction.

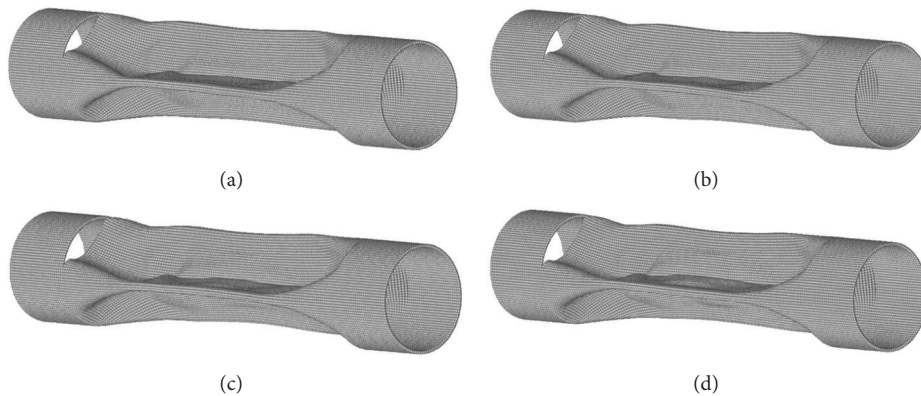


FIGURE 10: Comparison of final configurations of cylinders with different imperfection magnitudes: (a) 0.05% imperfection, (b) 0.1% imperfection, (c) 0.5% imperfection, and (d) 1.0% imperfection.

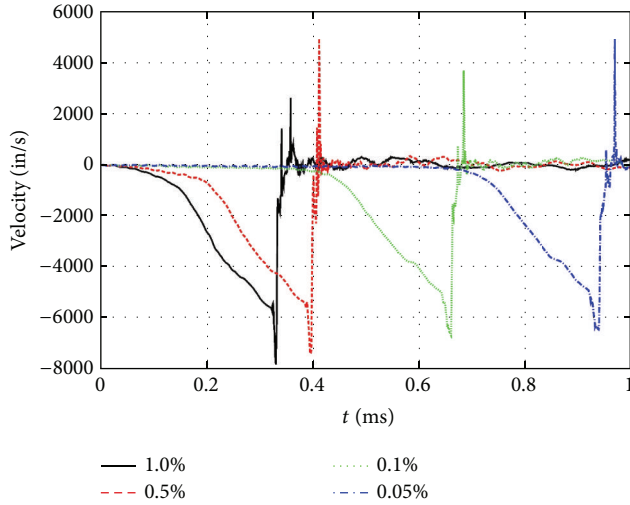


FIGURE 11: Comparisons of time history of nodal velocity at the center node with different amplitudes of imperfection.

6. Numerical Examples

6.1. Implosion Induced Dynamic Failure of Cylinder. The cylinder is of length L with two extension parts of length L_e at the ends; see Figure 6. Rigid plugs are perfectly bonded to the extension parts. The thickness of the cylinder is t , and the diameter is D . In the experiments, the specimens are loaded with hydrostatic pressure and the pressure was increased until the cylinders buckled. It was observed in the experiment that specimens will buckle in some specific modes, which have a dependence on the geometry.

In this example, we focused on predicting final fracture pattern of two experiments. The first specimen is denoted by IMP26 experiment, where $L = 366.8$ mm, $D = 38.085$ mm, and $t = 0.701$ mm. The length of the extension parts is $L_e = 25.4$ mm. The material of the cylinder is aluminum alloy (AL) 6061-T6. In the experiment, the result indicated a mode 2 implosion, but there was no fracture observed. The second specimen, denoted by IMP25, is $L = 143$ mm plus two 25.4 mm extension parts at the ends, $D = 38.087$ mm, and $t = 0.701$ mm. Because it has a much shorter length than that of IMP26, IMP25 specimen buckled in a higher mode, that is, mode 3 buckling, and showed fracture on the interfaces of the end plugs and the main specimen.

For numerical analysis, we modeled IMP26 and IMP25 specimens with 49200 and 24000 shell elements, respectively. The average element size is about 1 mm. The material behavior of AL6061-T6 is modeled with the damage plasticity [23, 24] with Young's modulus $E = 69.5$ GPa, the density $\rho = 2780$ kg/m³, Poisson ratio $\nu = 0.3$, yield stress $\sigma_{y0} = 276$ MPa, and the hardening modulus $E_T = 634$ MPa.

The following coordinate system was used: the x -axis is along the axis of the cylinder, and the y - and z -axes are in the radial direction. A uniform surface pressure loading was applied on all the shell elements. Another set of concentrated forces along the axis direction were applied to the nodes on the rim of the two ends. These forces served to compress the

cylinder along its longitudinal axis. The summation of the magnitude of these concentrated forces is equivalent to the total force exerted on the end plug due to the pressure. All the nodes in the two extension parts are only allowed to move along the x -axis, and all the other DOFs of these nodes, including the translational DOFs u_y and u_z and the rotational DOFs θ_x , θ_y , and θ_z , are constrained. The employment of the applied concentrated forces and the sliding boundary conditions is to model the effect of the plug.

A bilinear load curve for the pressure was used in both simulations. The pressure started at zero and was increased to p_{cr} , that is, the experimental critical buckling pressure, in time t_0 and then was kept constant at p_{cr} until the end of simulation. The schematic of time history of the pressure is shown in Figure 7; $p_{cr} = 1.15$ MPa for IMP26 experiment and $p_{cr} = 2.83$ MPa for IMP25 experiment. We used the parameter $t_0 = 5.0 \times 10^{-5}$ s in both simulations.

Geometry imperfection is introduced into the radius to evoke circumferential buckling easily. The actual radius with imperfection has the form $r = r_0(1 - a \cos n\theta)$, where r_0 is the unperturbed radius, a is the imperfection magnitude, and θ is the circumferential angle. n is the number of wavelengths in the circumferential direction, $n = 2$ for IMP26 simulation, and $n = 3$ for IMP25 simulation. It should be noted that the buckling mode in numerical results does not depend on the imperfection mode. We also tested the IMP25 simulation with injection of mode 2 imperfection and obtained very similar results.

Figures 8(a)–8(d) show four snapshots of the numerical results for IMP26. The center of the specimen yielded first and then buckled in mode 2. The buckling region evolved toward the two ends, and the specimen entirely collapsed. $a = 0.1\%$ was used in the simulation of IMP26, which is close to 0.107%, the maximum ovalization measured in the experimental specimen.

In IMP25 simulation, we allowed an injection of the discontinuity near the interface of the main part and the extension part of the specimen. We also observed large plastic strain, large damaged or unstable material points along the central buckling lines. However, this may be due to the repulsive forces generated during the contact, so no crack was allowed to initiate in these regions.

Several imperfection magnitudes a from 0.05% to 1% were tested in IMP25 simulation. The maximum oval imperfection measured in the experiment is 0.043%. It should be noted there should not be imperfection as large as 1% in the actual specimen, and this is only to examine the effect of the imperfection.

Figure 9 shows four snapshots of IMP25 results of $a = 0.05\%$ at different times. The central part of the cylinder collapses first, and then the collapse region enlarges toward the ends. Some cracks were initiated at the ends and propagated along the circumferential direction.

The final configurations of different imperfection magnitudes are compared in Figure 10. No large effect can be observed for imperfection magnitudes though the crack opening of $a = 1.0\%$ looks larger than that of $a = 0.05\%$. The time histories of velocity y of finite element node 11670 (at the center of cylinder) are plotted and compared in Figure 11.

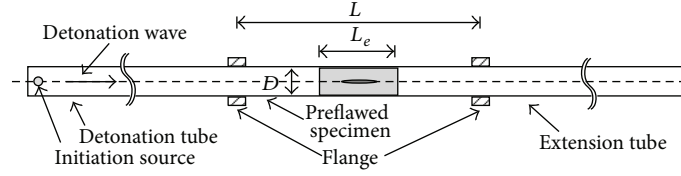


FIGURE 12: Preflawned cylinder with gaseous detonation loading.



FIGURE 13: Experimental results of Shepherd experiment [25, 26]: (a) both the forward and backward tips curved and (b) backward tip curving and forward tip bifurcation.

Let the collapse time be defined as the time to reach the peak velocity. It can be observed that smaller imperfection leads to longer collapse time, but the peak velocity of all the imperfections does not show an obvious dependence on the imperfection magnitude.

6.2. Explosion Induced Failure of Cylinder. Chao [25] and Chao and Shepherd [26] performed a series of experiments with gaseous detonation loading. The schematic setting of the experiment is shown in Figure 12. The preflawned cylinder was linked to a detonation tube and an extension tube. The initial surface notch was located at the center of the cylinder. All the tubes were filled with explosive gas. The detonation source point is located inside the detonation tube, 1.52 m away from the left end of the preflawned tube.

The pressure wave was initiated at the source point and then passed the specimen and the extension tube, causing the original surface notch to form a crack cutting through the cylinder wall and propagate.

Chao [25] and Chao and Shepherd [26] launched 9 shots with the above specimen with the initial notch length $L_c = 25.4$ mm. The length of the specimen is $L = 0.61$ m, the diameter $D = 0.038$ m, and the shell thickness $t = 0.89$ mm. They found two types of fracture behaviors. One was that both the forward and the backward crack tips curved after they were formed and went straight for a short distance, as shown in Figure 13(a). The other type of results also showed a backward crack curving but the forward crack tip bifurcated and finally cut the specimen into two segments. The configuration of the second fracture pattern is shown in Figure 13(b).

The specimen is modeled with 40680 shell elements. The left and the right ends of the numerical models were fully clamped in the simulation. The following fitted exponential-decay curve [28] was used to represent the detonation pressure:

$$p(x, t) = \begin{cases} 0, & 0 < t < t_{cj}, \\ p_{cj} \exp\left(-\frac{t - t_{cj}}{T}\right), & t > t_{cj}, \end{cases} \quad (28)$$

where x is the distance away from the initiation point along the axial direction, t is time, p_{cj} is the peak value of the

pressure wave, $t_{cj} = x/v_{cj}$ is the time for the wave to travel from the initiation point to the evaluation point, v_{cj} is the velocity of the wave, and the time parameter $T = 3.0t_{cj}$. In the current simulation, $p_{cj} = 6.1$ Mpa and $v_{cj} = 2404$ m/s. The pressure was applied to all the elements from the internal side. The material properties are Young's modulus $E = 2780$ kg/m³, Poisson ratio $\nu = 0.3$, initial yield $\sigma_{y0} = 275$ MPa, and hardening modulus $E_T = 640$ MPa.

The configurations at different times of numerical results are shown in Figures 14 and 15. The stress concentration can be seen in front of the crack tip. The crack tips went straight at the early stage of propagation. Both the forward and the backward tips curved after around 0.3 ms. The forward crack tip shows sharper curving at about 90 degrees to the axis. The backward crack tip shows a slanted path.

The final fracture patterns are shown in Figure 15. The crack propagation paths are similar to the experimental results shown in Figure 13. The difference is that our results show a little shorter crack length, which may be due to the difference of the loading and boundary conditions between numerical modeling and real experiment.

7. Conclusion

We described a new finite element method for prediction of dynamic fractures in thin shells. The method is incorporated within an explicit time integration scheme and able to represent the crack paths free from initial mesh topologies. For the representation of discontinuities due to cracks, the described method employs a simplified version of the conventional XFEM based on the phantom node method. In this approach, the cracked shell element is treated by two superimposed elements with newly added phantom nodes on the cracked portions.

The method is implemented for the DKT shell element. This facilitates the implementation of the method into standard finite element programs. Another attractive feature of the method is that it provides an easy mesh generation and a relatively low computational cost and this allows large scale nonlinear dynamic fracture problems to be solved efficiently.

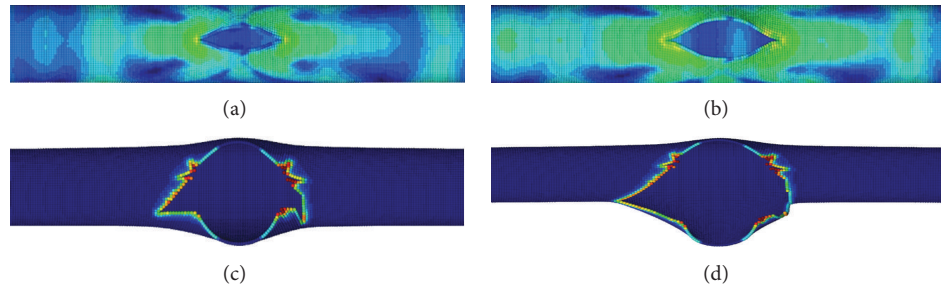


FIGURE 14: Numerical results of Shepherd experiment at different times: deformed configurations with effective stress contour plots at (a) time $t = 0.255$ ms and (b) time $t = 0.3$ ms and with damage plot at (c) time $t = 0.42$ ms and (d) time $t = 0.54$ ms.

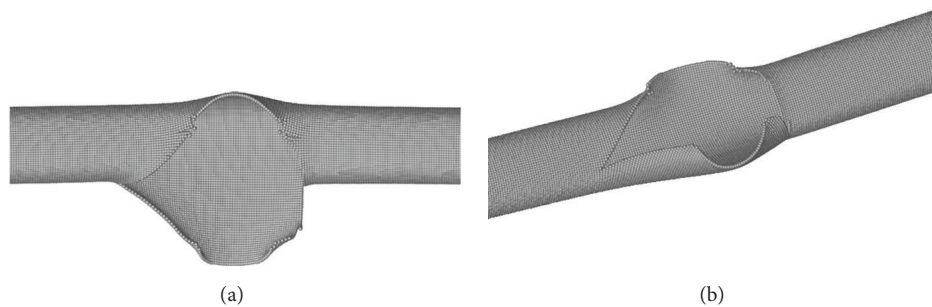


FIGURE 15: Final configurations of Shepherd experiment. (a) Top view. (b) Side view.

Conflict of Interests

The authors declare that there is no conflict of interests regarding the publication of this paper.

Acknowledgment

The support of the Office of Naval Research under Grants nos. N00014-13-1-0386 and N00014-11-1-0925 is gratefully acknowledged.

References

- [1] J. L. Batoz, K. J. Bathe, and L. W. Ho, "Study of three-node triangular plate bending elements," *International Journal for Numerical Methods in Engineering*, vol. 15, no. 12, pp. 1771–1812, 1980.
- [2] T. Belytschko and T. Black, "Elastic crack growth in finite elements with minimal remeshing," *International Journal for Numerical Methods in Engineering*, vol. 45, no. 5, pp. 601–620, 1999.
- [3] N. Moës, J. Dolbow, and T. Belytschko, "A finite element method for crack growth without remeshing," *International Journal for Numerical Methods in Engineering*, vol. 46, no. 1, pp. 131–150, 1999.
- [4] J. M. Melenk and I. Babuška, "The partition of unity finite element method: basic theory and applications," *Computer Methods in Applied Mechanics and Engineering*, vol. 139, no. 1–4, pp. 289–314, 1996.
- [5] I. Babuška and J. M. Melenk, "The partition of unity method," *International Journal for Numerical Methods in Engineering*, vol. 40, no. 4, pp. 727–758, 1997.
- [6] T. Belytschko, H. Chen, J. Xu, and G. Zi, "Dynamic crack propagation based on loss of hyperbolicity and a new discontinuous enrichment," *International Journal for Numerical Methods in Engineering*, vol. 58, no. 12, pp. 1873–1905, 2003.
- [7] J.-H. Song, P. M. A. Areias, and T. Belytschko, "A method for dynamic crack and shear band propagation with phantom nodes," *International Journal for Numerical Methods in Engineering*, vol. 67, no. 6, pp. 868–893, 2006.
- [8] P. M. A. Areias and T. Belytschko, "Non-linear analysis of shells with arbitrary evolving cracks using XFEM," *International Journal for Numerical Methods in Engineering*, vol. 62, no. 3, pp. 384–415, 2005.
- [9] P. M. A. Areias, J. H. Song, and T. Belytschko, "Analysis of fracture in thin shells by overlapping paired elements," *Computer Methods in Applied Mechanics and Engineering*, vol. 195, no. 41–43, pp. 5343–5360, 2006.
- [10] F. Cirak, M. Ortiz, and A. Pandolfi, "A cohesive approach to thin-shell fracture and fragmentation," *Computer Methods in Applied Mechanics and Engineering*, vol. 194, no. 21–24, pp. 2604–2618, 2005.
- [11] F. Cirak, R. Deiterding, and S. P. Mauch, "Large-scale fluid-structure interaction simulation of viscoplastic and fracturing thin-shells subjected to shocks and detonations," *Computers and Structures*, vol. 85, no. 11–14, pp. 1049–1065, 2007.
- [12] X.-P. Xu and A. Needleman, "Numerical simulations of fast crack growth in brittle solids," *Journal of the Mechanics and Physics of Solids*, vol. 42, no. 9, pp. 1397–1434, 1994.
- [13] G. T. Camacho and M. Ortiz, "Computational modelling of impact damage in brittle materials," *International Journal of Solids and Structures*, vol. 33, no. 20–22, pp. 2899–2938, 1996.
- [14] M. Ortiz and A. Pandolfi, "Finite-deformation irreversible cohesive elements for three-dimensional crack-propagation

- analysis,” *International Journal for Numerical Methods in Engineering*, vol. 44, no. 9, pp. 1267–1282, 1999.
- [15] V. Mehra and S. Chaturvedi, “High velocity impact of metal sphere on thin metallic plates: a comparative smooth particle hydrodynamics study,” *Journal of Computational Physics*, vol. 212, no. 1, pp. 318–337, 2006.
- [16] A. Combescure, B. Maurel, and S. Potapov, “Modelling dynamic fracture of thin shells filled with fluid: a fully SPH model,” *Mecanique & Industries*, vol. 9, no. 2, pp. 167–174, 2008.
- [17] B. Maurel and A. Combescure, “An SPH shell formulation for plasticity and fracture analysis in explicit dynamics,” *International Journal for Numerical Methods in Engineering*, vol. 76, no. 7, pp. 949–971, 2008.
- [18] J.-H. Song and T. Belytschko, “Dynamic fracture of shells subjected to impulsive loads,” *Journal of Applied Mechanics*, vol. 76, no. 5, pp. 1–9, 2009.
- [19] J. Réthoré, A. Gravouil, and A. Combescure, “An energy-conserving scheme for dynamic crack growth using the eXtended finite element method,” *International Journal for Numerical Methods in Engineering*, vol. 63, no. 5, pp. 631–659, 2005.
- [20] T. Rabczuk, G. Zi, A. Gerstenberger, and W. A. Wall, “A new crack tip element for the phantom-node method with arbitrary cohesive cracks,” *International Journal for Numerical Methods in Engineering*, vol. 75, no. 5, pp. 577–599, 2008.
- [21] T. Menouillard, J. Réthoré, A. Combescure, and H. Bung, “Efficient explicit time stepping for the eXtended finite element method (X-FEM),” *International Journal for Numerical Methods in Engineering*, vol. 68, no. 9, pp. 911–939, 2006.
- [22] T. Menouillard, J. Réthoré, N. Moës, A. Combescure, and H. Bung, “Mass lumping strategies for X-FEM explicit dynamics: application to crack propagation,” *International Journal for Numerical Methods in Engineering*, vol. 74, no. 3, pp. 447–474, 2008.
- [23] L. Xue, “Damage accumulation and fracture initiation in uncracked ductile solids subject to triaxial loading,” *International Journal of Solids and Structures*, vol. 44, no. 16, pp. 5163–5181, 2007.
- [24] L. Xue and T. Wierzbicki, “Ductile fracture initiation and propagation modeling using damage plasticity theory,” *Engineering Fracture Mechanics*, vol. 75, no. 11, pp. 3276–3293, 2008.
- [25] T. W. Chao, *Gaseous detonation-driven fracture of tubes [Ph.D. dissertation]*, California Institute of Technology, Pasadena, Calif, USA, 2004.
- [26] T. W. Chao and J. E. Shepherd, “Fracture response of externally flawed aluminum cylindrical shells under internal gaseous detonation loading,” *International Journal of Fracture*, vol. 134, no. 1, pp. 59–90, 2005.
- [27] T. Rabczuk, J.-H. Song, and T. Belytschko, “Simulations of instability in dynamic fracture by the cracking particles method,” *Engineering Fracture Mechanics*, vol. 76, no. 6, pp. 730–741, 2009.
- [28] W. M. Beltman and J. E. Shepherd, “Linear elastic response of tubes to internal detonation loading,” *Journal of Sound and Vibration*, vol. 252, no. 4, pp. 617–655, 2002.